Summer 7-15-2022

COMPUTATIONAL, SYNTHETIC AND SPECTROSCOPIC STUDIES ON DONOR ACCEPTOR TRANSITION METAL COMPLEXES

Ranjana Dangi
The University of New Mexico

Ranjana Dangi
Candidate

Chemistry and Chemical Biology
Department

This dissertation is approved, and it is acceptable in quality and form for publication:

Approved by the Dissertation Committee:

Professor Martin L. Kirk, Chairperson

Dr. Brian Gold

Dr. Changjian Feng

Dr. Dongchang Chen

COMPUTATIONAL, SYNTHETIC AND SPECTROSCOPIC STUDIES ON DONOR ACCEPTOR TRANSITION METAL COMPLEXES

by

RANJANA DANGI

B.Sc. Chemistry and Microbiology, Tribhuvan University, 2005
M.Sc. Chemistry, Tribhuvan University, 2009

DISSERTATION

Submitted in Partial Fulfillment of the
Requirements for the Degree of

Doctor of Philosophy
Chemistry

The University of New Mexico
Albuquerque, New Mexico

July 2022

DEDICATION

To my parents, Narendra Bahadur Dangi, Tirtha Maya Dangi and all my well wishers

ACKNOWLEDGEMENTS

My sincere gratitude and appreciation go to my PhD advisor Professor Martin L. Kirk for his guidance and mentorship. I always appreciate the patience and professionalism he has to mentor students on research projects. I can review myself the time I joined and now. The professionalism, techniques, and the knowledge I have earned will remained as my precious earnings in my life.

I would like to extend my sincere gratitude to former and current graduate students and postdoctoral fellows of Kirk research group; Dr. Ben Stein, Dr. Chao Dong, Dr. Dominic Kofl Kersi and Dr. Diana Habel-Rodriguez, I appreciate them for their guidance during my early days when I was learning every single detail about synthesis and computational techniques. My colleagues Khadnand KC, Amrit Pokhrel, Ju Chen, Laura Jane Ingersol, Sangita Poudel, and Shiyue Gao, Jesse Lepluart, Josh Mengell and Caroline Mangione; thank you everyone being there with me. Post-doctoral fellows: Dr. Jing Yang, Dr. Logan Giles, Dr. Benjamin William, Dr. Cass Richers and Dr. Munendra Yadav for informing me with their specific areas of expertise, allowing me to complete the project at hand.

I would not be here today without the unconditional support and belief from my family. My mother, Tirtha Maya Dangi, the support you have given me during this journey is incredible. My father, my brothers and my sister were always there for me every moment of need, despite being across the globe. Your emotional support has been invaluable during my PhD journey. Finally, I would like to extend my sincere thanks to my wonderful kids and husband for their love, support, and sacrifice during my PhD work. My

sons Andrew and Adriel, and my dear husband Purbendra, thank you for everything you have done.

COMPUTATIONAL, SYNTHETIC AND SPECTROSCOPIC STUDIES ON DONOR ACCEPTOR TRANSITION METAL COMPLEXES

By

Ranjana Dangi

B.Sc. Chemistry and Microbiology, Tribhuvan University, 2005

M.Sc. Chemistry, Tribhuvan University, 2009

Ph.D. Chemistry, University of New Mexico, 2022

ABSTRACT

I

Fundamental advances in our ability to design and construct electronic components at the nanoscale will require new design paradigms. One proposed nanoscale electronic component is the molecular rectifier. Molecular and molecule-based electronic components are advantageous due to their ease of synthetic manipulation, and the fact that the size dimensions of molecules are inherently at the nanoscale (0.5 - 3nm). Our group has shown how the Donor-Bridge-Acceptor biradical approach can be used to derive key structure-property relationships that allow insight into the choice of bridge fragments for molecular rectification by using constitutional isomers of the donor-bridge-acceptor biradical (NN-Th-Py-SQ) (S=1/2 *ortho*-semiquinonate, SQ; S=1/2 nitronlynitroxide, NN; Th = thiophene; Py = pyridine). These NN-bridge-SQ complexes serve as constant bias analogs for molecular current rectifying devices. The efficiency of rectification is given by the rectification ratio (RR = $g_{forward}/g_{reverse}$; where g = conductance). The experimental and calculated RRs for (NN-Th-Py-SQ) isomers is 1.58 and 1.24

respectively at ±2.56V applied bias. Low RRs are obtained for this system since the Py and Th π-systems have not been effectively decoupled.

II

The conductance was calculated through Au_n-S-Bridge-S-Au_n (Bridge = conjugated organic σ/π- system) constructs by using the Quantum ATK computational software and those results are compared to experimentally-determined magnetic exchange coupling parameters in a series of $Tp^{Cum,Me}$Zn(SQ-Bridge-NN) complexes. In these systems, $Tp^{Cum,Me}$ = hydro-tris(3-cumenyl-1- methylpyrazolyl)borate ancillary ligand, Zn = diamagnetic zinc(II), SQ = semiquinone (S = 1⁄2), and NN = nitronylnitroxide radical (S = 1⁄2). A nonlinear functional relationship between the biradical magnetic exchange coupling, $J_{D\rightarrow A}$, and the computed conductance, g_{mb}, was determined based on our analysis. Monomer and dimer bridge fragments do not lie on the same $J_{D\rightarrow A}$ vs. g_{mb}, curve. A scale invariance exists between the monomeric and dimeric bridges which shows that the two data sets are related by a proportionate scaling of $J_{D\rightarrow A}$. The ratio of distance dependent decay constants for conductance (β_g) and magnetic exchange coupling (β_J) does not equal unity, which indicates that inherent differences in the tunneling energy gaps, $\Delta\varepsilon$, and the bridge-bridge electronic coupling, H_{BB}, are not directly transferrable properties as they relate to exchange and conductance. The observed results are described in valence bond terms, accompanied by resonance structure contributions to the ground state bridge wavefunction being different for SQ-Bridge-NN and Au_n-S-Bridge-S-Au_n systems.

III

A new idea for decoupling donor and acceptor π-systems in a molecular rectifier is to employ a transition metal as the decoupling fragment. In another project, we have used square planar complex of Nickel (II), Palladium (II), and Platinum (II) using a dioxolane donor and a bipyridine acceptor ligand, of which wavefunctions are localized on the HOMO and LUMO, respectively. The RRs are observed to be markedly higher (RR as high as 7.6) using this molecular motif. The increasing RRs from Ni to Pt is due to more delocalized transmission eigenstate lying within the bias window.

IV

We have designed a series of emissive Platinum(II) complexes to obtain insight into vibronic control of excited state lifetimes and highlight new (diimine)Pt(dichalcogenolene) complexes that possess low-energy dichalcogenolene → diimine charge-separated excited states. We have used a combination of electronic absorption and transient spectroscopies, spectroscopic computations, and group theoretical arguments to understand the dependence of specifically designed static distortions on excited state lifetimes. Our results indicate that we can control $T_1 \rightarrow S_0$ lifetimes by nearly two orders of magnitude, providing deep insight into the nature of molecular vibrations that enhance vibronic spin-orbit coupling contributions to spin-forbidden decay processes

V

Radical-elaborated Pt(II) D-A complexes using a catecholate donor ligand have also been synthesized. The radical spin density is delocalized onto the acceptor catecholate moiety through a metal oxygen dπ-pπ orbital pathway. Low temperature EPR has been utilized to investigate the extent of spin delocalization mediated by the Pt ion, where the dipolar

contribution of the Pt hyperfine anisotropy is compared with calculated spin-Hamiltonian parameters. Intermolecular magnetic interaction between radical spins has been determined by magnetic susceptibility experiments and reveal a pairwise dimeric antiferromagnetic exchange interaction of $J = -12\ cm^{-1}$. To probe the magnitude of the spin delocalization, another radical was appended to the acceptor moiety. This biradical molecule has been successfully synthesized and further work is in progress to collect and analyze all spectroscopic data.

TABLE OF CONTENTS

List of Figures xvi

List of Tables xxv

Chapter 1. Spectroscopic Techniques and Principles 1

1.1 Introduction 1

1.2 Electronic Absorption Spectroscopy 1

1.2.1 Beer-Lambert Law 1

1.2.2 Born-Oppenheimer Approximation and Franck-Condon Principle 3

1.2.3 Selection Rules 5

1.2.4 Effect of Temperature 7

1.2.5 Electronic Transitions in Metal Complexes 8

1.3 Electron Paramagnetic Resonance 10

1.3.1 Zeeman Effect 11

1.3.2 Origin of g-anisotropy 13

1.3.3 Hyperfine Interaction 15

1.3.4 Spin Population and Relaxation 18

1.4 X-ray Absorption Spectroscopy 20

1.4.1 Metal K-edge XAS 20

1.4.2 Ligand K-edge XAS 23

1.4.3 Sulfur K-edge XAS 24

1.4.4 Working Principle and Synchrotron Radiation Source 25

1.5 References 26

Chapter 2. A Study on Relating Exchange Coupling and Conductance Properties of Donor-Bridge-Acceptor Transition Metal Complexes 31

2.1 Literature Review 31

2.2 Single Molecule Rectifier: Computational Study on the Rectification Behavior of $Tp^{Cum,Me}$Zn(SQ-py-thp-NN) and $Tp^{Cum,Me}$Zn(SQ-thp-py-NN) 32

2.2.1 Introduction 32

2.2.2 Transport Calculation 36

2.2.3 Results and Discussion 38

2.2.4 Molecular Design and Structure 38

2.2.5 Exchange Couplings and Rectification Ratios 39

2.2.6 Mechanism of Rectification in T-P Bridges 45

2.2.7 Computational Assessment of Molecular Electron Transport Through T-P 47

2.2.8 Analysis of the Transport Calculation Results 49

2.2.9 Conclusion 53

2.3 Transferrable Property Relationships Between Magnetic Exchange Coupling and Molecular Conductance 54

2.3.1 Introduction 55

2.3.2 Molecular Electronic Structure Calculations 60

2.3.3 Transport Calculations 60

2.3.4 Results and Discussions 61

2.3.4.1 Exchange Coupling in SQ-Bridge-NN Complexes 61

2.3.4.2 Exchange Coupling within the Context of a Valence Bond Configuration Interaction Model 62

2.3.4.3 Magnetic Exchange and Conductance 66

2.3.4.4 Magnetic Exchange and Conductance: Resonance Structures .. 77

2.3.5 Conclusion 79

2.4 Transition Metals as a Decoupling Unit: Donor-Acceptor Pt(II) Complexes as a Single Molecule Rectifier 81

2.4.1 Introduction 81

2.4.2 Experimental Methods 84

2.4.3 Results and Discussions 86

2.4.3.1 I-V Curve Analysis and Rectification Ratios 86

2.4.3.2 Analysis of Transmission Spectrum 91

2.4.3.3 Analysis of Transmission Eigen Channel and Molecular Projected Self-consistent Hamiltonian (MPSH) States 101

2.4.3.4 Correlation Between Transmission Eigen States and Molecular Self-consistent Hamiltonian (MPSH) States 108

2.4.3.5 Evaluation of HOMO-LUMO Gap 114

2.4.3.6 Projected Device Density of States (PDDOS) 118

2.4.4 Conclusion 120

2.5 References 122

Chapter 3: Vibronic Spin-Orbit Coupling Contribution to Spin Forbidden Radiative Decay 139

3.1 Introduction 139

3.2 Synthesis, Characterization and Spectroscopy of (2,2'-biquinoline)Pt(II) (1,2 benzeneodithiol), (biq)Pt(bdt) 146

3.2.1 Background 146

3.2.2 Synthesis and Characterizations 147

3.2.3 Electronic Structure and Spin-Orbit Coupling Matrix-Element Calculation..... 150

3.2.4 Experimental Details 151

3.2.5 Results and Discussions 154

3.2.6 Conclusion..... 166

3.3 Synthesis, Characterization and Spectroscopy of (3,3'-methyl 2,2'-bipyridine (dmbpy)Pt(II)(1,2 benzenedithiol); (dmbpy)Pt(bdt)..... 167

3.3.1 Background 167

3.3.2 Synthesis and Characterization of 3,3'-methyl-2,2'-bipyridine Ligand 168

3.3.3 Synthesis and Characterization of (3,3'-methyl-2,2'-bipyridine)Pt(II)Cl_2, (dmbpy)$PtCl_2$ 169

3.3.4 Synthesis and Characterization of (3,3'-methyl-2,2'-bipyridine)Pt(II) (1,2-benzenedithiol) 173

3.3.5 Experimental Details 175

3.3 6 Results and Discussions 176

3.3.7 Conclusion 184

3.4 A Study of Orbital Topology Control on Ground State Recovery Pathway 187

3.4.1 Background 187

3.4.2 Synthesis and Characterization of the 3,3'-iso-biquinoline (i-biq) Ligand 189

3.4.3 Synthesis of (3,3'-iso-biquinoline)Pt(II)Cl_2, (i-biq)$PtCl_2$ 190

3.4.4 Synthesis of (3,3'-iso-biquinoline)Pt(II)(1,2-benzene dithiol) (i-biq)Pt(bdt) Complex 191

3.4.5 Experimental Methods 193

3.4.6 Results and Discussions 193

3.4.6.1 Electronic Absorption Spectroscopy 193

3.4.6.2 Photoluminescence and Kinetic Data 195

3.4.6.3 S K-edge X-ray Absorption Spectroscopy 200

3.4.7 Conclusions 204

3.5 References 205

Chapter 4: A Study of Spin Delocalization in Radical Co-ordinated Pt(II) Donor Acceptor Complexes. 213

4.1 Introduction 213

4.2 Background 214

4.3 Synthesis, Characterization and Spectroscopy of (1,5-diisopropyl 6-oxoverdazyl) Pt(II)(1,2 benzenedithiol), (PyVD)Pt(bdt) 218

4.3.1 Synthesis of 1,5-diisopropyl-3-pyridin-2yl-6-oxoverdazyl Radical (PyVD) 218

4.3.2 Synthesis of (PyVD)$PtCl_2$ 220

4.3.3 Synthesis and Spectroscopy of (1,5-diisopropyl 6-oxoverdazyl-radical)Pt(II)(1,2 benzene dithiol) (PyVD)Pt(bdt) 222

4.4 Synthesis, Characterization and Spectroscopy of (1,5-diisopropyl, 6-oxoverdazyl) Pt(II)(catecholate), (PyVD)Pt(cat) 225

4.4.1 Synthesis and Characterization 225

4.4.2 Experimental and Characterization Methods 226

4.4.3 Results and Discussions 227

4.4.3.1 X-ray Crystallography 227

4.4.3.2 Electronic Absorption Spectroscopy 233

4.4.3.3 Solvatochromatic Effect 236

4.4.3.4 Electron Paramagnetic Resonance 239

4.4.3.5 Magnetism 245

4.4.4 Conclusion 248

4.5 Synthesis, Characterization and Spectroscopy of Biradical System 248

4.5.1 Synthesis and Characterization 248

4.5.2 X-ray Crystallography 249

4.5.3 Results and Discussions 254

4.5.3.1 Electronic Absorption Spectroscopy 254

4.5.3.2 Electron Paramagnetic Resonance Spectroscopy 255

4.5.3.3 Magnetism 257

4.5.4 Conclusion 258

4.6 References 258

Appendix A: XYZ Coordinates of Optimized Geometry for Chapter 1 265

Appendix B: Mass Spectrometric Data for Chapter 2 and Chapter 3 272

Appendix C: NMR Spectroscopic Data for Chapter 3 279

Appendix D: X-ray Crystallographic Data for Chapter 3 and Chapter 4 279

List of Figures

Figure 1.1: Schematic representation of potential energy surfaces. Left; potential surfaces representing without nuclear distortion and right; with nuclear distortions 4

Figure 1.2: Summary of various electronic transitions in octahedral transition metal complexes 8

Figure 1.3: Depicting the removal of degeneracy of m_s = ±1/2 spin states by the application of an external magnetic field 13

Figure 1.4: Schematic representation of L-edge (left) and K-edge (right) transitions in XAS 21

Figure 1.5: XAS spectrum showing energy region of pre-edge XANES, and EXAFS from lower to higher energy respectively 23

Figure 2.1: Schematic representation of a single molecule rectifier where the molecule is sandwiched between two gold electrodes 33

Figure 2.2: Bond line drawings and thermal ellipsoidal plots (left and right) for SQ-T-P-NN and SQ-P-T-NN with corresponding single-molecule rectifier device cartoons(center) 35

Figure 2.3: Variable-temperature magnetic susceptibility data for the complexes SQ-P-T-NN (Top, A) and SQ-T-P-NN (Bottom, B) 40

Figure 2.4: Room temperature electronic absorption spectra. Low energy intense band in both isomeric complexes is showing the charge transfer from SQ to B-NN LUMO (left) and TD-DFT calculated EDDMs indicating the nature of electron transfer 42

Figure 2.5: DFT computed T-P HOMO and NN HOMO wave functions that mix with the frontier NN orbitals (Left), VBCI model for SQ-P-T-NN illustrating the bridge HOMO and LUMO(Right) 45

Figure 2.6: Calculated I-V curve at +/- 4 eV applied bias (left). DFT calculated wave function of 90° torsion angles of T-P bridge component with 90º torsion angles (right) along with bond line drawing of 90° rotated pyridine-thiophene ring..... 47

Figure 2.7: Results of transport calculations on T-P bridge molecule under forward and reverse bias direction. I-V curve calculated at ±4 eV applied bias. Vertical dashed lines indicate the intrinsic bias of SQ-PT-NN and SQ-TP-NN = charge transfer energy(left) 48

Figure 2.8: Zero bias transmission spectrum calculated as a function of the energy in eV and the computed transmission probability. Dotted line shows the Fermi Energy of electrodes 50

Figure 2.9: Zero bias calculated transmission eigenstates on at −0.32 eV and 2.23 eV(top) 52

Figure 2.10: (A) Metal-Bridge-Metal junctions corresponding to biradical complexes. (B) Bridges common to M-B-M junctions and Donor-Bridge-Acceptor complexes. (C) Ferromagnetic exchange parameters $J_{D\rightarrow A}$ are shown along with corresponding bridge fragment 58

Figure 2.11: Diagram illustrating of how bridge-mediated electronic coupling is related to conductance and magnetic exchange coupling 60

Figure 2.12: Diagrammatically showing the one electron transitions that contribute to the magnetic exchange coupling, NN-Bridge (HOMO) ⟶ SQ(SOMO) and SQ(SOMO) ⟶ NN-Bridge (LUMO) in SQ-Bridge-NN biradicals 63

Figure 2.13: Resonance structures illustrating enhanced H_{BB}, H_{DB}, H_{BA} couplings in D-B-A biradicals (SQ-Ph-Ph-NN) 64

Figure 2.14 Device Configuration of the Au-S-phenylene-S-Au construct used for further transport calculations 66

Figure 2.15: Illustration of the HOMO contribution in the conductance mechanism. The biased Au(yellow) electrodes are filled to the chemical potential of the electrodes. The variable bias window is highlighted in light pink color where $\Delta E_{Gap} = V_{bias}$ 68

Figure 2.16: Transmission function calculated at zero biased applied voltage for [M-Ph-M] with bridge fragment and calculated percentage contribution of individual MPSH states for these transmission channel (left). Yellow region is defined as the bias window of 2V at an applied bias of ±2 V 69

Figure 2.17: Computed current vs exchange coupling for the monomeric (red circle) and dimeric (blue circle). Separate empirical power law functions have been fit to the data with similar exponents 72

Figure 2.18: Computed value of current (nA) calculated at +2V applied bias voltage and exchange coupling (in cm^{-1}) for the phenylene bridges (red circles) and thiophene (blue circles). The fit of data to the equation is shown by the red(phenylene) and blue(thiophene) lines 73

Figure 2.19: Resonance Raman enhancement pattern of SQ-Ph_2-NN biradical di-bridge collected in the solid state (top) and electron difference density map (EDDM) generated

from the optimized geometry and performing a TD-DFT calculation using the optimized geometry (bottom) 79

Figure 2.20: Bond line drawings of dichalcogenolenes Pt(II) Diimine complexes (center), wavefunctions of Highest Occupied Molecular Orbitals (HOMO; left) and Lowest Unoccupied Molecular Orbitals (LUMO; right) 83

Figure 2.21: Transition metal complexes under study for their rectifier properties. Cat-Ni-bpy (left), Cat-Pd-bpy (middle) and Cat-Pt-bpy (right). The points where sulfur atom is covalently attached before geometry optimization is indicated with red solid dots 84

Figure 2.22: Device configuration converted from the optimized bulk configuration of Cat-Ni-bpy(top), Cat-Pd-bpy(middle) and Cat-Pt-bpy(bottom) 86

Figure 2.23: IV-curve obtained by integrating $T\ (E,\ V)$ with absolute current calculated under an applied bias voltage of ±2 V. Cat-Ni-bpy (red), Cat-Pd-bpy(blue) and Cat-Pt-bpy (green) 89

Figure 2.24: Plot of calculated rectification ratios vs applied bias. Cat-Ni-bpy (black line and circle) has clearly exhibited the highest rectification ratio at ±1.2 V and Cat-Pd-bpy (blue line and circle) and Cat-Pt-bpy (red line and sphere) have their maximum rectification at ±2 V bias 90

Figure 2.25: Overlay of transmission function at equilibrium for cat-Ni-bpy (red dotted line), Cat-Pd-bpy (green solid line) and Cat-Pt-bpy (blue dotted dashed line). At equilibrium 92

Figure 2.26: Total transmission function calculated at ± 2 V applied bias. Current is expressed in nA units. Cat-Ni-bpy (top), Cat-Pd-bpy (middle) and Cat-Pt-bpy (bottom). Dotted green arrow in each case is indicating the increasing positive biased voltage and red dotted arrow is for the increasing negative bias voltage 94

Figure 2.27: Overlay of transmission function calculated at ±1.2 V applied biased. Red spectrum is calculated for +1.2 V and blue spectrum is calculated for -1.2 V reverse bias and forward bias respectively 95

Figure 2.28: Overlay of transmission function calculated at 0 (red solid line), ±1.2 V (blue solid line), ±2 V (green solid line). Direction of arrow is indicating the corresponding at 0.28 eV transmission peak going out of and entering to the bias window, respectively, in the top and bottom plots 96

Figure 2.29: Transmission function calculated at ± 0.4 V (left) and ± 2 V (right) for (bpy)M(Cat) complexes of Nickel, Palladium, and Platinum; top to bottom respectively. Data is depicting the negligible differences with a small, applied bias and significant differences is when the applied bias is increased to ± 2 V 100

Figure 2.30: Iso-surface (isovalue =0.029) plot of transmission eigen channel calculated from the transmission spectrum at equilibrium with corresponding energy. Top on the blue background is Cat-Ni-bpy; Middle on light yellow background is Cat-Pd-bpy; and the Bottom on the light green background is Cat-Pt-bpy 103

Figure 2.31: Molecular projected self-consistent Hamiltonian (MPSH) states calculated at equilibrium condition for Cat-M-bpy complexes 107

Figure 2.32: Molecular frontier orbitals wavefunction of (bpy)Pt(cat) complex generated from fully optimized geometry and plotted by Chem-Craft 107

Figure 2.33: Molecular projected sel-consistent Hamiltonian (MPSH) eigen state at −1.2 V (top row) for Ni and −2 V for Pd (middle row) and Pt (bottom row) complexes. Plotted at same iso value of (0.27) 113

Figure 2.34: Transmission eigen channel calculated at the bias point of maximum rectification ratio. Value for iso-surface (0.29) has kept same for all of them for comparison purpose. it corresponds to the 1.2 V for Ni, 2 V for Pd and 2 V for the palladium complex at top 114

Figure 2.35: Calculated HOMO-LUMO gap for positive and negative bias voltages ... 116

Figure 2.36: Heat map depicting the projected local density of states for Platinum complex calculated at +2 V bias, zero bias and −2 V bias from left to right respectively. The weight scale has shown on the right side of the plot 119

Figure 2.37: Transmission eigen states calculated at the energy corresponding to the peaks position of PDDOS in positive bias plot of palladium at (top) and platinum (Pt) at bottom 120

Figure 2.38: Overlay of transmission function forward and reverse bias with individual contribution from the metal, catecholate, bipyridine on PDDOS at forward and reverse bias and reverse bias for platinum, palladium, and nickel respectively 121

Figure 3.1: DFT calculated molecular wavefunction map of (bpy)Pt(O,S), (bpy)Pt(S,S), (bpy)Pt(O,Se) and (bpy)Pt(S,Se) respectively. Platinum d-orbital has notably rotated toward the more covalent dichalcogenolenes in the mixed dichalcogene complexes 141

Figure 3.2: Jablonski Diagram showing the excited state photo-processes after absorption of electromagnetic radiation by the molecule 144

Figure 3.3: Metal d-orbital rotation by introducing the static distortions along three vibrational rotational axes to lower the symmetry 145

Figure 3.4: Synthetic scheme of (bdt)Pt(biq) complex. Top; synthesis of $(DMSO)_2PtCl_2$, middle; synthesis of $biqPtCl_2$ and bottom; synthesis of (bdt)Pt(biq) 149

Figure 3.5: Room temperature electronic absorption spectrum of (bdt)Pt(biq) complex as solution in dry degassed methylene dichloride. It is depicting the ligand-to-ligand charge transfer transition at 13,300cm^{-1} associated with the molar extinction coefficient value of 5000 Lmol^{-1}cm^{-1} 156

Figure 3.6: Resonance Raman profile of (bdt)Pt(biq) by exciting the molecule at 407 nm, 458 nm, 488 nm, 514 nm, 568 nm, 647 nm wavelengths and the enhancement modes are shown with different color codes; 1613 cm^{-1} mode in blue, 1459 cm^{-1} mode in green, 1342 cm^{-1} mode in black 157

Figure 3.7: The assignment of vibrational modes contributing the LL'CT band on the resonance Raman profile plot. Left hand side; HOMO, EDDM and LUMO of (bdt)Pt(biq) are from bottom to top. The bond line drawing and arrows pointing the normal vibrational mode (middle) 158

Figure 3.8: Room temperature emission spectrum of (bdt)Pt(biq) collected in solution of dry degassed dichloromethane (CH_2Cl_2). The emission maximum wavelength is observed at 980 nm 159

Figure 3.9: Optimized structure obtained from electronic structure calculation by using gaussian method 160

Figure 3.10: Transient absorbance (TA) difference data collected at room temperature in the degassed solution of dichloromethane following 450 nm wavelength. The gate width 5 ns centered at 600 nm 161

Figure 3.11: Kinetic absorption trace at 525 nm by exciting the molecule at 450 nm. The solution was prepared by using dry dichloromethane (CH_2Cl_2) 164

Figure 3.12: Overlay of experimental peak fitting (red solid line) gaussian resolved peak (green dotted line) and computed oscillator strength (brown sticks) of XAS S k-edge data collected in solid state 166

Figure 3.13: Depicting the molecular orbital involved in first peak of (bdt)Pt(biq) complex S K-edge data. Sulfur 1S orbital is on the left, while LUMO is on the right 166

Figure 3.14: Exhibited the molecular orbital involve on the more intense second transition 167

Figure 3.15: Crystal structure of the (dmbpy)$PtCl_2$. Respective atoms have been depicted in the standard color indication. Numbering of the constituent atoms is done by Mercury software for crystallography data 172

Figure 3.16: Crystal packing diagram of the (dmbpy)$PtCl_2$. The crystal was grown in the dry ethyl acetate by using a slow evaporation method at room temperature 172

Figure 3.17: Depicting the dominant orbital involved in LL'CT process in (bdt)Pt(dmbpy). HOMO is on left and LUMO is in right, has weight percentage of 68 as obtained from TD DFT calculation 177

Figure 3.18: Room temperature electron absorption spectrum of (bdt)Pt(dmbpy). The x-coordinates represents the energy in wavenumber and the y-coordinates represents the molar extinction coefficient value calculated by serial dilution method by using dry degassed dichloromethane solvent 178

Figure 3.19: Room temperature electronic absorption spectrum collected in the degassed solution of dichloromethane at different known concentration (top). The different concentration of solution was achieved by the serial dilution method 179

Figure 3.20: Emission spectrum, collected at room temperature in dry degassed THF as solvent 180

Figure 3.21: Static distortion induced orbital rotation in (bdt)Pt(dmbpy) complex along molecular z-coordinates resulting in a non-zero first order spin-orbit coupling matrix element 181

Figure 3.22: Emission lifetime measured data (red) recorded at room temperature in degassed THF by using 450 nm diode laser as an excitation source and the emission counts were made at 800 nm 182

Figure 3.1: Overlay of experimental peak fitting (blue solid line) gaussian resolved peak (green dotted line) and computed oscillator strength (blue sticks) of XAS S K-edge data collected in solid state sample of (bdt)Pt(bmbpy) in the Synchrotron facility at Stanford University..... 183

Figure 3.2: Computed orbitals of 1s sulfur and LUMO of the complex (bdt)Pt(dmbpy) associated for the lower energy weak transition at 2471.7 eV..... 185

Figure 3.3: The acceptor orbitals responsible for pre-edge peak observed in 2472 eV of the XAS S Kedge spectrum of (bdt)Pt(dmbpy) complex..... 186

Figure 3.26: Comparison of frontier molecular orbital (HOMOs on left and LUMOs on right, DFT optimized geometry at the center) of (bpy)Pt(S,S) (parent complex), (bpy)Pt(O,S) (complex having static distortion along x-axis), (biq)Pt(S,S) (static distortion along y-axis) and (dmbpy)Pt(S,S) (static distortion along z-axis) from top to bottom .. 187

Figure 3.27: Room temperature electronic absorption spectrum of (bdt)Pt(i-biq) recorded in HITACHI, UV-vis-near IR spectrometer. Sample was prepared in distilled THF 183

Figure 3.28: TD-DFT calculation results of (biq)Pt(bdt) (Top) and (i-biq)Pt(bdt) (bottom) 183

Figure 3.29: Room temperature emission spectrum recorded in CH_2Cl_2. Excitation wavelength was set as 485 nm with absorption value of 0.45. Emission maximum was observed at 780 nm 186

Figure 3.4: Electronic absorption (black solid line) and emission spectrum (red solid line) overlay of (bdt)Pt($\boldsymbol{i}$-biq) (in terms of wavenumber unit for energy at x-axis) complex recorded at room temperature by using FLS 980 fluorescence spectrometer 188

Figure 3.5: Overlay of emission data recorded by using FLS 980 fluorometer in THF solution for ($\boldsymbol{i}$-biq) ligand (blue solid line) and (bdt)Pt($\boldsymbol{i}$-biq) complex (red solid line) excited at 400 nm and 480 nm respectively 190

Figure 3.6: Room temperature data recorded by using FLS 980 exhibiting the mono-exponential decay of excited state lifetime of 9 ns, χ^2 value is 0.948 and B (pre-exponential factor) value is 1006 200

Figure 3.7: Depicting the acceptor orbital involved in first transition from sulfur 1s orbital. Left hand side orbitals are the 1s for two sulfur atoms. Right hand side is showing the molecular LUMO (top) and LUMO+1 (bottom 201

Figure 3.8: Overlay of experimental peak fitting (red solid line) gaussian resolved peak (green dotted line) and computed oscillator strength (brown sticks) of XAS S K-edge data collected in solid state sample of (bdt)Pt(i-biq) in the Synchrotron facility at Stanford University..... 202

Figure 3.9: (bdt)Pt(i-biq), computed orbital contributions. Exhibiting the molecular orbitals involved in the second intense peak at 2472.2 eV of S K-edge plot. Sulfur 1S orbitals are shown in left hand side of the figure whereas molecular LUMO+5, Pt d_{x2-y2} orbital is shown in right..... 203

Figure 4.1: Frontier orbitals SOMOs and LUMOs of NN radical (top) and verdazyl radical (VD) (bottom) plotted by sing Chem-Craft program on optimized ground state electronic structure. Both SOMOs share the common features 219

Figure 4.2. Room Temperature Electronic absorption spectrum of (PyVD)Pt(bdt) expressed in absorbance vs energy on wavenumber. The sample solution was prepared in acetonitrile 225

Figure 4.3: X-ray crystallographic structure of (PyVD)Pt(Cat. For clarity, color coding is as follows: carbon = green color, oxygen = red color and nitrogen = blue, platinum = gray. (Bottom) showing distortion from planarity..... 230

Figure 4.4: Depicting the crystallization in dimeric form in (top) inter molecular interaction distance is shown by black dotted line between two platinum atoms. Displaying the nature of crystal packing in one unit cell (bottom), red, green, and black dotted lines represent the distance between two dimer, inter-dimeric distance, and distance between two molecules 231

Figure 4.5: Electronic absorption spectrum of (PyVD)Pt(Cat) expressed in molar extinction coefficient vs energy in wavenumbers. The sample solution was prepared in Acetonitrile. Inset: DFT calculated orbitals involved in one electron promotions for three visible features 236

Figure 4.6: CASSCF result summary calculated at (5e, 5O) active space. (Top) orbitals in active space (bottom) electronic configuration in ground state and first excited state 236

Figure 4.7: Solvatochromic effect studied on (PyVD)Pt(Cat) complex considering the lowest energy charge transfer transition band with series of solvents: heptane, toluene, tetrahydrofuran, ethyl acetate, acetonitrile, and dimethyl sulfoxide. The charge transfer band has been remarkably shifted to lower energy on moving from polar solvent to non-polar solvent 238

Figure 4.8: Frequency calculated result shows the quinoidal stretch indicated by red arrow on (PyVD)Pt(Cat) responsible for the structural feature at low energy band in heptane solvent 239

Figure 4.9: Plot of solvent polarity index vs energy of lowest energy intense feature in EAS data 239

Figure 4.10: Diagram representing the spin delocalization pathway (left). Spin density distribution map plotted on the optimized ground state geometry (right) 241

Figure 4.11: 298K solution isotropic EPR data of PyVD ligand recorded in DCM, experimental (red) and simulation (blue). Simulation parameters are presented in set along with bond line drawing of ligand PyVD 241

Figure 4.12: Room temperature solution electron paramagnetic resonance spectrum of (PyVD)Pt(Cat) in toluene. The experimental data and the simulated data are presented in red and blue. Simulation parameters are listed in set 242

Figure 4.13: EPR data of (PyVD)Pt(Cat) recorded at 77K in 2-methyl THF. Red solid line corresponds to the experimental, and black solid line simulated data sets. Black, brown, and blue arrows are indicating the three Pt A-tensor values 244

Figure 4.14: A-tensor and g-tensor orientation on the molecular frame (right), molecular beta-LUMO wavefunction (right) with the yellow arrow pointing the direction of maximum A-tensor as represented by the red line in tensor orientation 245

Figure 4.15: $\chi T \; vs \; T$ plot of (PyVD)$PtCl_2$ recorded at variable temperature at 0.1 tesla applied magnetic field on microcrystalline solid sample. Red dots are the data points and blue solid line is the optimized fit to the data 247

Figure 4.16: $\chi T \; vs \; T$ plot of (PyVD)Pt(Cat) recorded at variable temperature at 0.1 tesla applied magnetic field on powder solid sample. Red dots are the data points and blue solid line is the optimized fit to the data 248

Figure 4.17: $\chi_{para} \; vs \; T$ plot of (PyVD)Pt(Cat) recorded at variable temperature at 0.1 tesla applied magnetic field on powder form of sample. Blue dots are the data points and red solid line is the optimized fit to the data 248

Figure 4.18: (Top) ORTEP drawing of X-ray crystallographic structure of (PyVD)Pt(CatVD). Elements are color coded by representative color. (Bottom) has demonstrated the labeling of selected atoms of interest 251

Figure 4.19: Crystal packing in unit cell. 252

Figure 4.20: X-ray crystallographic structure of (PyVD)Pt(Cat) demonstrating Pt-Pt (3.201Å) (gray colored solid sphere) intermolecular interaction in dimeric complex ... 252

Figure 4.21: EAS data recorded at 298K in acetonitrile. Orbitals involved have been shown on respective peaks by purple arrows 255

Figure 4.22: 298K solution EPR data of (PyVD)Pt(CatVD) recorded in toluene, experimental data (red) and simulated data (blue). Only A_{pt} value was used during simulation. Simulation parameters and spin density map are presented in set 257

Figure 4. 23: 77K EPR in frozen solution showing half field transition 257

List of Tables

Table 1.1: Intensities of the absorption bands in 3d metal series 6

Table 1.2: Metal d-orbital rotation effects 17

Table 1.3: Contribution of dipolar interaction of nucleus with a single d electron on anisotropic hyperfine 17

Table 1.4: Frequently used microwave frequencies and corresponding magnetic field strengths 19

Table 2.1: Experimentally observed and calculated values of decay constants, barrier heights, tunneling energy gaps and bridge coupling ratios comparison 75

Table 2.2: Table showing the calculated rectification ratios at different applied bias voltage which have been used to calculate the transmission spectrum and the corresponding current at each bias voltage in both forward and reverse bias direction 89

Table 2.3: Contribution from individual molecular projected self-consistent Hamiltonian (MPSH) state molecular orbital, perturbed by the metallic electrodes connected to it at the specific transmission peak at zero bias transmission spectrum Cat-Ni-bpy (top) Cat-Pd-bpy (middle) and Cat-Pt-bpy (bottom) 107

Table 2.4: Contribution from individual molecular projected self-consistent Hamiltonian (MPSH) state, molecular orbital perturbed by the metallic electrodes connected to it at the specific transmission peak at -1.2 V bias transmission spectrum Cat-Ni-bpy (top), and -2 V for Cat-Pd-bpy (middle) and Cat-Pt-bpy (bottom) 111

Table 2.5: Calculated HOMO-LUMO gap under 0V to ±2V. Top; Cat-Ni-bpy, middle; Cat-Pd-bpy and bottom; Cat-Pt-bpy 116

Table 3.1: Crystal structure and refinement of (dmbpy)$PtCl_2$ 172

Table 3.2: Selected bond lengths of (dmbpy)$PtCl_2$ 172

Table 3.3: Selected bond angles of (dmbpy)$PtCl_2$ 173

Table 3.4: Selected torsion angles of (dmbpy)$PtCl_2$ 174

Table 3.5: Comparison of lifetime, calculated spin-orbit coupling matrix element, Stokes shift value and absorption maximum in dichloromethane for (bpy)Pt(S,S) (bpy)Pt(O,S), (biq)Pt(S,S) and (dmbpy)Pt(S,S) complexes. 187

Table 3.6: Calculated values of singlet and triplet transition energies (in cm^{-1}) for (biq)Pt(bdt)and (i-biq)Pt(bdt) 200

Table 4.1: Observed band assignment based on the TD-DFT calculation and electron density difference map (EDDMs) associated with selected electronic transitions (green for going and red for accepting orbitals) 226

Table 4.2: Selected bond lengths obtained from X-ray crystallography of (PyVD)Pt(Cat) 233

Table 4.3: Selected bond angles from X-ray crystallographic structure of (PyVD)Pt(Cat) 233

Table 4.4: Selected torsion angles from the X-ray crystallography of (PyVD)Pt(Cat) . 233

Table 4.5: 77K EPR spin Hamiltonian parameters 242

Table 4.6: Crystal data and structure refinements (PyVD)Pt(CatVD) 252

Table 4.7: Selected bond lengths from the X-ray crystal structure of (PyVD)Pt(CatVD) 253

Table 4.8: Selected bond angles from the X-ray crystal structure of (PyVD)Pt(CatVD) 254

Table 4.9: Selected torsion angles from the X-ray crystal structure of (PyVD)Pt(CatVD) 254

ACRONYM GLOSSARY

ATK	atomistic tool kit
cm^{-1}	wavenumber
L	liter
Mol^{-1}	per mole
ε	molar absorptivity
C	concentration
DFT	density functional theory
SOMO	singly occupied molecular orbital
HOMO	highest occupied molecular orbital
LUMO	lowest unoccupied molecular orbital
Bpy	bipyridine
(i)-biq	isobiquinoline
Dmbpy	dimethyl bipyridine
S	sulfur
O	oxygen
N	nitrogen
MEC	molar extinction coefficient
EPR	electron paramagnetic resonance
EAS	electronic absorption spectroscopy
EDDM	electron density difference map
CASSCF	complete active space self-consistent field
ES	excited state
GS	ground state
ISC	inter-system crossing
IC	internal conversion
NR	non-radiative
IV	current voltage
E_L	left electrode
E_R	right electrode
V	voltage
I	current
eV	electron volt
nm	nanometer
biq	biquinoline
VD	verdazyl
Pt	platinum
Cat	catecholate
SQ	semi-quinone
bdt	1,2 benzenedithiol
SD	spin density
MPSH	molecular projected self-Hamiltonian

Chapter 1

1.1 Techniques and Principles

Spectroscopic techniques are an essential part of research for recording and analyzing data. Throughout this study, many spectroscopic techniques are used to record the data on the target molecules. Here in this chapter, the most frequently used techniques are summarized with their experimental procedure and working principles.

1.2 Electron Absorption Spectroscopy

Electronic absorption spectroscopy applies the principle of absorption of electromagnetic radiation by the molecule. This technique measures the amount of light transmitted through the sample. Efficiency of light absorbed by a sample at certain wavelength is given by the absorbance (A) or transmittance (T) as shown in equation 1.1.[1] Where, I_0 = intensity of incident light; I = intensity of light after passing through the sample.

$$\%T = \frac{I}{I_0} 100\% \qquad (1.1)$$

1.2.1 Beer-Lambert Law and Oscillator Strength

In simple cases, absorbance of electromagnetic radiation by the sample follows the Beer-Lambert law as depicted in equation 1.2. Beer-Lambert law is useful to quantify the concentration of sample solution. The deviation from linearity of dependence of absorbance on concentration may indicate the formation of aggregates, may

concentration of sample is very high and/or the presence of significant amount of other absorbing species.[1]

$$log_0\left(\frac{I}{I_0}\right) = A = \varepsilon bc \qquad (1.2)$$

The absorption intensity (A) is defined as the maximum height of an absorption peak according to equation (1.2). Absorbance is correlated with the molar extinction coefficient or molar absorptivity (ε = L•Mol^{-1}•cm^{-1}), optical path length of sample (b = cm) and the concentration of sample (c = Mol•L^{-1}) as shown in equation (1.2). Higher concentration of the sample results higher absorbance value. The molar extinction coefficient has physical significance, as it is an intrinsic property of the molecule. It is proportional to the square root of the transition dipole moment integral which describes the electronic transition between ground and excited states of the molecule after absorbing a photon.

The molar extinction coefficient is utilized to calculate the oscillator strength (f), which determines the likelihood of absorbing photons. The oscillator strength is directly related to the integral of the absorbance according to equation (1.3).[2]

$$f = 4.32 \times 10^{-9} \int \varepsilon(\bar{\nu}) d\bar{\nu} = 9.6 \times 10^{-9} \times \varepsilon(\bar{\nu}) \times \Delta\bar{\nu} \qquad (1.3)$$

Here, ($\Delta\bar{\nu}$) is defined as the full width at the half of the maximum absorption in wavenumber), and (f) is dimensionless quantity.[3 4 5]

1.2.2 Born-Oppenheimer Approximation and Franck-Condon Principle

Analysis of electronic absorption spectra often uses these two different principles, the Born Oppenheimer approximation, and the Franck-Condon principle. A transition dipole moment is induced by the incident photon of light, more specifically defined as the electric dipole moment that is associated with the electronic transition between two states of the molecule.

$$\Psi_{total} = \Psi_{electronic} \times \Psi_{nuclear} \quad (1.4)$$

$$E_{total} = E_{electronic} + E_{vibrational} + E_{rotational} \quad (1.5)$$

According to the Born-Oppenheimer approximation, the electronic and nuclear components of the wavefunctions are accounted for separately due to their large difference in the mass. The separation is shown in equation (1.4). Equation (1.5) treats the electronic, vibrational, and rotational energies as independent from each other. Equation (1.6) has demonstrated the large-scale order differences of energies, thus the Born-Oppenheimer approximation can be approximated according to equation (1.7).[6]

$$E_{electronic} \approx 1000^{*} E_{vibrational} \approx 1000000^{*} \mathrm{E}_{rotational} \quad (1.6)$$

$$E_{total} = E_{electronic} + E_{vibrational} \quad (1.7)$$

The Frank-Condon principle helps us to better understand experimental absorption spectra by assigning the most intense transition as the one with most vibrational wavefunction overlap, which is most probable transition. Electronic transitions take place at very short time scale (about 10^{-15} s)[1 3], thus there is little nuclear movement is expected from a transition between the ground state and an excited state during an electronic transition. That little movement does occur is observed as vibronically structured spectra. The ground and electronic state potential energy diagrams with vibrational levels as shown in Figure 1.1.

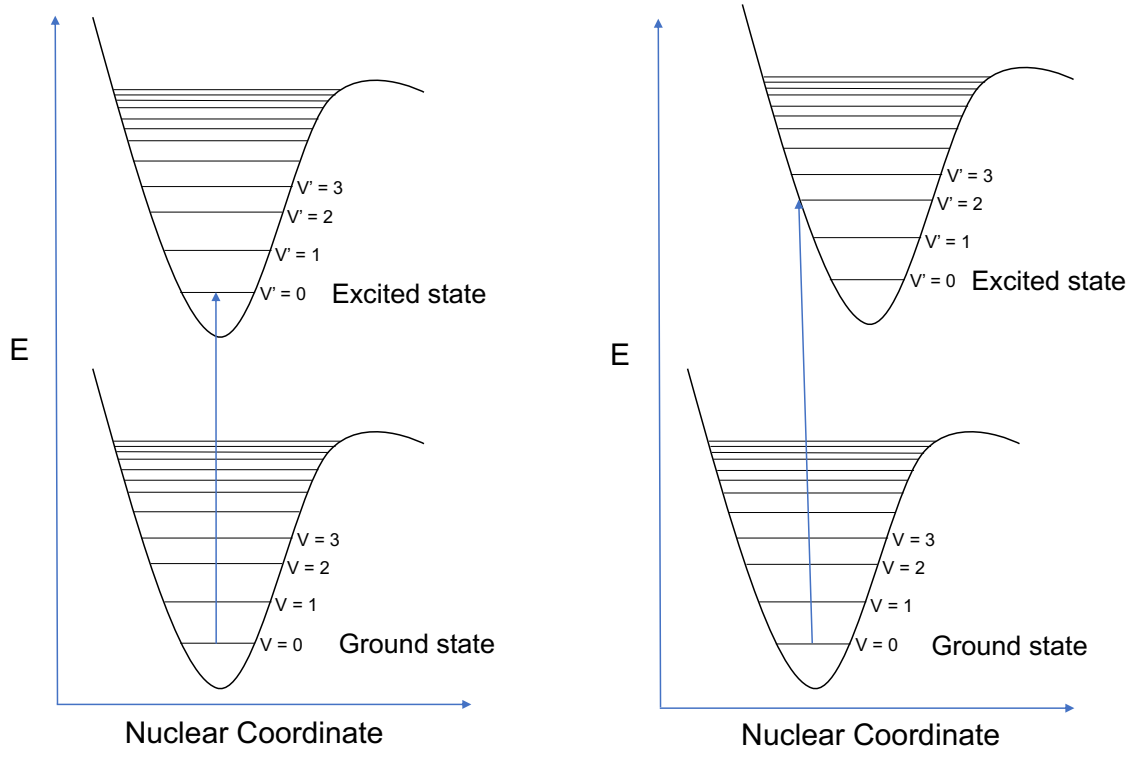

Figure 1.1: Schematic representation of potential energy surfaces. (left) potential surfaces representing without nuclear distortion and (right) with nuclear distortions.

The strength of the transition dipole (R) correlates with the overlap integral of ground (Ψ_b) and excited state (Ψ_a) wave functions as explained by equation (1.8). Applying the Born-Oppenheimer approximation expands equation (1.8) with the separation of the electronic transition moment and the vibrational overlap. The first and second integrals, respectively, in the equation (1.9) are derived from Figure 1.1.[4] The second integral in equation (1.9) must be non-zero for there to be an allowed transition. Observations of formally dipole forbidden transitions are due to vibronic and spin-orbit coupling.[7]

$$R = \int \Psi_b \, \hat{\mu} \, \Psi_a dt = \langle \Psi_b | \hat{\mu} | \Psi_a \rangle \tag{1.8}$$

$$R = \left\langle \Psi_{el}^{g} \Psi_{vib}^{g} \middle| \hat{\mu} \middle| \Psi_{el}^{e} \, \Psi_{vib}^{e} \right\rangle = \int \Psi_{el}^{g} \Psi_{el}^{e} dr \int \Psi_{vib}^{g} \Psi_{vib}^{e} dR \tag{1.9}$$

1.2.3 Selection Rules

There are two main selection rules to explain allowed and forbidden electronic transitions in transition metal complexes. The spin selection rule, $\Delta S = 0$, and the Laporte (orbital) selection rule $\Delta l = \pm 1$. The spin selection rule allows the electronic transitions between two states of the same spin multiplicity. Thus, the electronic transition from a singlet ground state to a triplet excited state, and repopulation of ground state from lowest excited triplet state, are spin forbidden transitions. Spin selection rule can be modulated by the spin-orbit coupling. Such as, 4d and 5d heavy metals with large spin-orbit coupling

constants effectively relax the spin selection rule. Nonetheless, the intensity of spin forbidden transitions is typically very weak as depicted in Table 1.1.[8]

Table 1.1: Intensities of the absorption bands in 3d metal series.[8]

Molecular extinction coefficient ε_{max} ($Lmol^{-1}cm^{-1}$)	Types of electronic transitions
<1	Spin forbidden and Laporte forbidden
20-100	Spin allowed and Laporte forbidden
C.250	Spin forbidden and Laporte allowed
1000-50000	Spin allowed and Laporte allowed

The Laporte selection rule is applicable to the molecule possessing an inversion center, also known as centrosymmetric molecules. Electronic transitions, $p(u) \longrightarrow p(u)$ and $d\ (g) \longrightarrow d\ (g)$ are Laporte forbidden in centrosymmetric molecules since electronic transitions must change the parity as represented by the equation (1.10).

$$\Gamma(\Psi_a) \times \Gamma(\mu)\Gamma(\Psi_b) \subset A_1(g) \qquad (1.10)$$

More specifically, transitions that are g (gerade) to g or u (ungerade) to u are Laporte forbidden and the transitions that involve the change in parity of orbitals are Laporte allowed, that is $g \longrightarrow \mathrm{u}$ and $u \longrightarrow g$. Thus, the $d \rightarrow d$, transitions, also termed as ligand field transitions, in octahedral (O_h) complexes are observed to be weak because they are Laporte forbidden due to the presence of inversion symmetry.[9] As we know, tetrahedral (T_d) complexes don't possess a center of symmetry, and $p \longrightarrow p$ and $d \longrightarrow d$ electronic transition are dipole allowed. The Laporte selection rule can be altered by

dynamic or static distortions from the perfect centrosymmetric symmetry. Electronic and vibrational coupling by asymmetric vibrations is also an effective way to relax the parity selection rules by allowing the mixture of wave functions of d-orbitals and p-orbitals as in equation (1.9) and equation (1.11).

$$\Gamma(\Psi_a) \times \Gamma(\mu) \times \Gamma(\Psi_b) \times \Gamma(\Psi_{vib}^e) \subset A_1(g) \qquad (1.11)$$

1.2.4 Effect of Temperature

At room temperature, the metal complexes exhibit broad absorption bands of electronic transitions with long tails. This is not a common feature in low temperature measurements. At low temperatures, the band becomes more resolved and sharper. These bands can become very structured in Shpolskii matrices at low temperatures (e.g., liquid helium). The sharpness of an absorption peak (phonon-less transition) is due to the minimization of lattice and solvent interactions by isolating the individual molecule. The molar extinction coefficient of the 0-0' transition band will increase significantly at low temperature since the lowest vibrational level of the ground state is more populated compared to higher vibrational levels Figure 1.1.[10] However, the total oscillator strength remains unchanged. The intensity of electronic transitions that occur due to relaxed Laporte forbiddeness by vibronic coupling (molecular vibrations) decreases with lowering the temperature since the 0-0' transition is forbidden. Different possible electronic transitions are schematically demonstrated in Figure 1.2. Differences in the intensity of electronic transitions can be seen on Table 1.1.

1.2.5 Electronic Transitions in Metal Complexes

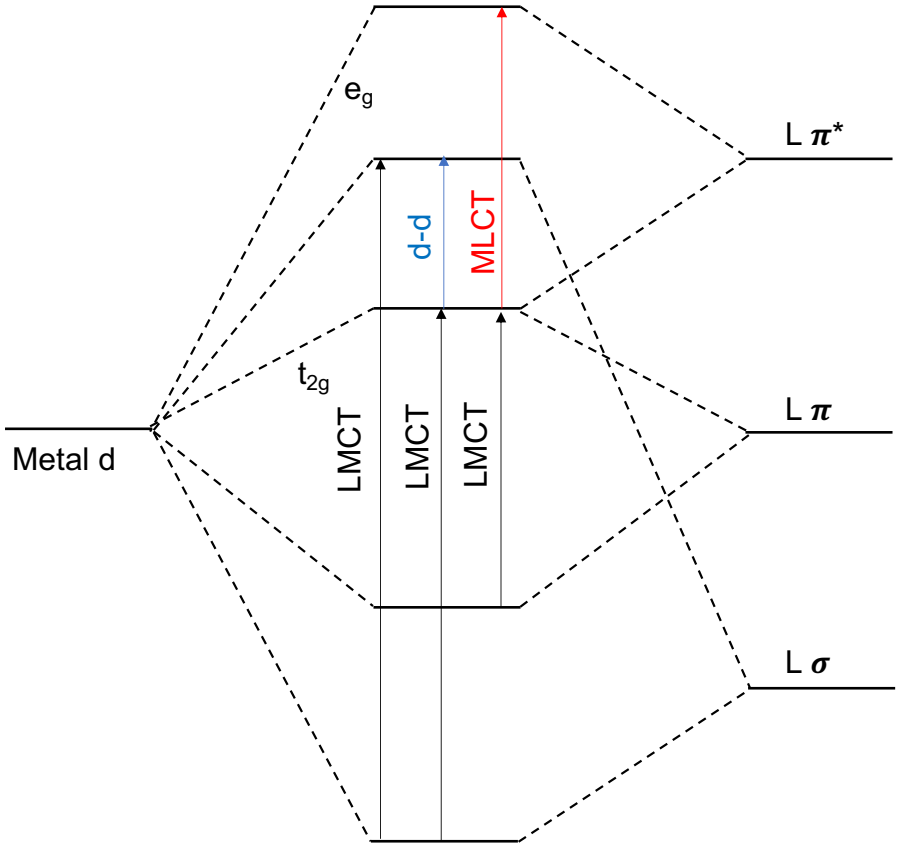

Figure 1.2**:** Schematic summarization of various electronic transitions in octahedral transition metal complexes. Black solid arrow is depicting metal to ligand charge transfer type of transitions, blue solid arrow depicts the ligand field (d-d) transitions and red solid arrow is indicting the metal to ligand charge transfer transition. (Left) showing metal d-orbital and (right) showing ligand orbitals.

Typically, electronic transitions that belong to transition metal complexes are ligand field transitions (d-d), metal-to-ligand charge transfer transitions (MLCT) and ligand-to-metal charge transfer transitions (LMCT).[11] Another type of transition we have observed in our experimentally recorded data of donor-acceptor complexes is ligand-to-ligand charge transfer transition (LLCT), when the promotion of electron occurs from a donor orbital that is predominantly ligand in nature to an acceptor orbital that predominantly ligand in character but localized on a different ligand. When the metal is in a higher

oxidation state and the coordinating ligand has a lone pair of electrons, the complex exhibits LMCT transitions. MLCT transitions occur when the ligand has low-lying π* orbitals. This is the case in common ligands such as 2,2' bipyridine, SCN^-, CN^-, and CO.[11] Ligand field transitions occur at low energy (d-d) and are weak in intensity compared to the charge transfer transition (LMCT, MLCT and LLCT). Further analysis of the energy of ligand field transitions provides the energy of ligand field splitting parameter Dq.[12] The relative intensity of charge transfer transitions is expressed in terms of oscillator strength $\left(f_{\Psi_e\Psi_g}\right)$ as expressed in equation (1.12).[3]

$$f_{\Psi_e\Psi_g} = 4.32 \times 10^{-9} \int \varepsilon(\bar{\nu})\, d\bar{\nu} \qquad (1.12)$$

Where ε is molar extinction coefficient and $\bar{\nu}$ is the frequency in wavenumbers. The transition dipole moment integral is depicted in equation (1.13).

$$\mu_{eg} = \langle \Psi_e | \mu | \Psi_g \rangle \qquad (1.13)$$

The oscillator strength in equation (1.12) is proportional to the square of the transition dipole moment integral as depicted in equation (1.14) which expresses the strength of the ground state (Ψ_g) and excited state (Ψ_e) wavefunctions coupling.

$$f_{\Psi_e\Psi_g} = \frac{2m_e}{\hbar^2}\left(E_{\Psi_e} - E_{\Psi_g}\right)\left|\langle \Psi_e | \mu | \Psi_g \rangle\right|^2 \qquad (1.14)$$

Here, m_e is the free electron mass, $\hbar$ is the reduced Planck constant, and E_{Ψ_e} and E_{Ψ_g} are the energies of the excited state and ground state respectively. The electric dipole moment operator (μ) transforms as x, y, and z in the character table for the given point group. For the allowed electric dipole transition, the integral of transition dipole matrix element must be non-zero, which is possible when the triple product of the ground state, excited state and electric dipole moment operator contains the totally symmetric representation. Conversely, in the case of forbidden electric dipole transitions, the integral of dipole moment operator is zero, and the triple product does not contain the totally symmetric representation.[13] [14] [15] Nonetheless, the dipole transitions gain allowedness by the dynamic and static spin-orbit coupling.

1.3 Electron Paramagnetic Resonance Spectroscopy

Electron paramagnetic resonance (EPR) spectroscopy is a frequently used technique that utilizes the absorption of microwave radiation by molecules, ions, and atoms bearing unpaired spin. It is a very effective tool to study the nature of paramagnetic reaction intermediates and obtain mechanistic information when radicals are formed, geometric and electronic structure information of organic radicals, spin-bearing transition metal complexes and biological molecules with unpaired electrons. We can obtain important geometric and the electronic structure information by the analysis and study of the EPR spin-Hamiltonian parameters. EPR and nuclear magnetic resonance (NMR) spectroscopies share some similarity. In NMR two energy states arise from the interaction of the nuclear magnetic moment ($I = \pm {}^1/_2$) under the applied field and an observed transition between them occurs when this energy is in resonance with the rf field. In EPR

spectroscopy, two energy states are split in a magnetic field ($m_s = \pm {}^1/_2$), defining the Zeeman effect, and a transition is observed when this energy splitting is in resonance with a microwave field (detailed in section 1.3.1). [3] [16] [17]

1.3.1 The Zeeman Effect

An electron spins along its axis, generating its own magnetic field. The dipole moment of the electron has shown in equation (1.15),

$$\mu = g\mu_B S \tag{1.15}$$

where, μ_B is the Bohr magneton, S is the spin angular momentum, and g is defined as the g-factor (splitting factor). We can extract structural information in paramagnetic molecules from the nature of the g-value. The g-value of a free electron is 2.0023, and any deviation from this value depends on how the spin interacts with the external field, which in turn, depends on the chemical environment of the spin bearing species.[18] When an unpaired spin magnetic moment interacts with the external magnetic field, the separation of energy levels into two spin states takes place as shown in Figure 1.3. The spin state (β) is anti-parallel to the external magnetic field and is stabilized and it becomes the lower energy state. The higher energy level spin state (α) is associated with the spin magnetic moment parallel to the external magnetic field thus it is more destabilized. This effect is defined as the Zeeman effect. The Zeeman Hamiltonian for the interaction of an electron with an applied magnetic field oriented along the molecular z-axis can be written as in equation (1.16).[19]

$$\widehat{H} = g\beta H\widehat{S_z} \quad (1.16)$$

The definition of other parameters is same as in equation (1.16) except for $\widehat{S_z}$, which represents the spin operator in the z-direction. Absorption of electromagnetic radiation induces a transition between two spin states. The transition energy between the two spin states is given by equation (1.17) and is schematically depicted in Figure 1.3.[3]

$$\Delta E = g\beta H \quad (1.16)$$

The EPR transitions are possible only when resonance criteria have been met and selection rules are satisfied:

1. Resonance occurs when the photon energy matches with the energy difference between two levels of spin states as depicted in Figure 1.3
2. Reorientation of the electron magnetic dipole moment must be induced by the oscillating magnetic field perpendicular to the applied magnetic field during the transition between two levels.

The selection rules are different based on consideration of spin. First, spin existing as isolated from the chemical environment (Rules 1,2) and second spin interacting with nearby magnetic nuclei (Rule 3).

1. For isolated spins the transitions are allowed when $\Delta m_s = \pm 1$,
2. In case of strong spin-spin interaction, the allowed transitions occur between $\Delta m_s = \pm 1$ and $\Delta m_s = \pm 2$,
3. When the unpaired spin interacts with magnetic nuclei, then the allowed transitions are between the levels, $\Delta m_s = \pm 1$, and $\Delta m_I = 0$.

In EPR spectroscopy, the resonance condition can theoretically be achieved by two ways; by either sweeping the microwave frequency and holding the applied magnetic field constant, or by keeping the microwave frequency constant with scanning of the magnetic field. In practice, the field sweep method is much more common, based on the sensitivity of the microwave cavity and the range of variations of parameters.[20]

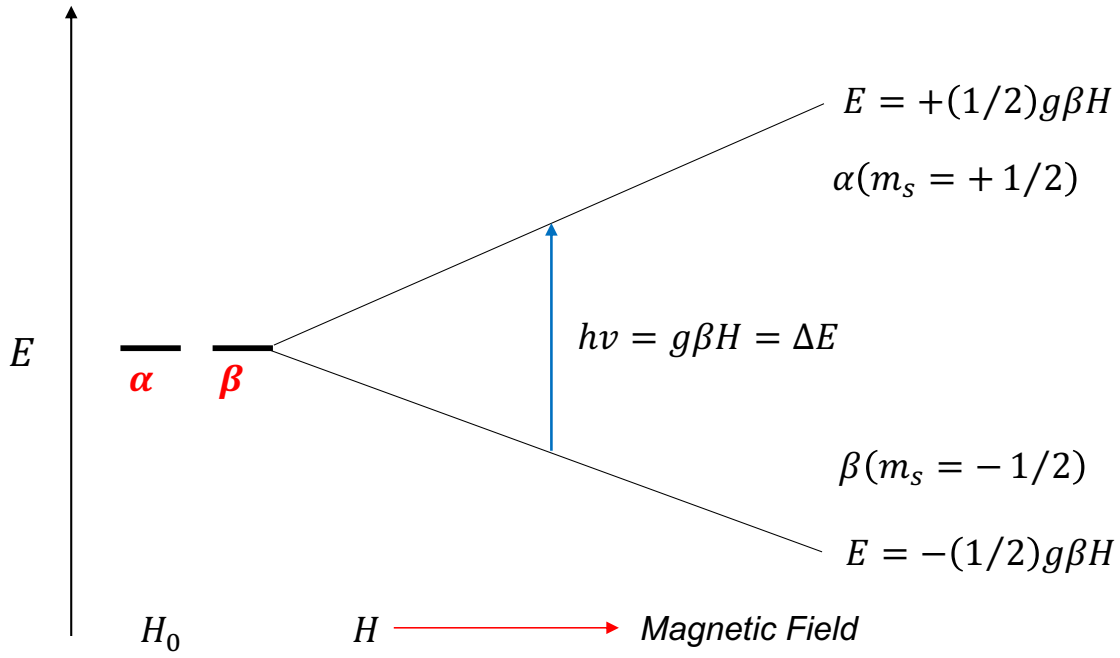

Figure 1.3: Depicting the removal of degeneracy of ±1/2 spin states by the application of external magnetic field. Blue solid arrow represents position of resonance with field, H_0 (no applied magnetic field) and H is the magnetic fields. E; represents the energy of corresponding spin states.

1.3.2 Origin of g-tensor Anisotropy

The g-tensor, also known as the g-matrix, is similar to the gyromagnetic ratio in NMR. It provides the information of magnetic moment of an atom via its spin (S) or angular

momentum (J) as shown in equation (1.18).[21] The physical origin of the g-tensor is from the interaction of the unpaired electron spin with the applied magnetic field.[22]

$$\vec{\mu} = -\beta < \Psi_g | \vec{L} + g_e \vec{S} | \Psi_g > \quad (1.17)$$

In general, ground state orbital angular momentum is close to zero since spin is often quenched by the ligand field. However, the orbital angular momentum of the ground state is achieved by the spin-orbit coupling ($\lambda \vec{L} \bullet \vec{S}$) between specific excited states and the ground state, as described in equation (1.19). This mixing of orbital angular momentum between excited states and the ground state causes the g-value to deviate from its free electron value. Thus, the g-value represented by equation (1.20), provides significant information about the electronic structure of the molecule.

$$\vec{\mu} = -\beta [< \Psi_g | g_e \vec{S} | \Psi_g > + < \Psi_g | \lambda \vec{L} \bullet \vec{S} | \Psi_e >] \quad (1.18)$$

$$h\nu = (g_e + \delta g)\beta H = g\beta H \quad (1.19)$$

The g-tensor can also be described by a 3×3 matrix representation, called the g-matrix, allowing for more detailed description via the Cartesian coordinate system, $g = \begin{bmatrix} g_x & 0 & 0 \\ 0 & g_y & 0 \\ 0 & 0 & g_z \end{bmatrix}$. If all the g-values are the same ($g_x = g_y = g_z$) in the molecule then the system is called isotropic. Low symmetry molecules at room temperature in solution also display isotropic g-values since room temperature provides enough thermal energy for

rapid rotation of the molecule to average the anisotropic effect. Another scenario when the g value is parallel to the unique axis ($g_z = g_\parallel$) and the remaining two g-values are equal and perpendicular ($g_{x,y} = g_\perp$) yields an axial system. A rhombic system will be observed when all three g-values are different ($g_x \neq g_y \neq g_z$) as viewed in the EPR spectrum.[3]

The g-values of the ground state are obtained by solving equation (1.21),

$$g_i = 2 - 2\lambda \sum_{e \neq g} \frac{< \Psi_g | \overrightarrow{L_\iota} | \Psi_e > < \Psi_e | \overrightarrow{L_\iota} | \Psi_g >}{E_g - E_e} \qquad (1.20)$$

where, $i = x, y, z$.[23] Different elements have different spin-orbit coupling constants (λ). It is expressed as, $\lambda = \pm \xi / 2S$ (ξ is one electron spin-orbit coupling constant represented by + for half-filled and – for less than half-filled systems, S is total spin of the transition metal ion). Heavy transition metal atoms have large values of λ, thus resulting in a large deviation of the g-value from the free electron g value of 2.0023. In general, more than half-filled d-electron systems exhibit g-values greater than 2.0023, and systems with less than a half-filled d-electron configuration exhibit g-values less than 2.0023.[3] The energy difference in the denominator of equation (1.21) can be obtained from electronic absorption spectroscopy.

1.3.3 Hyperfine Interaction (A-tensor)

In EPR, hyperfine splitting occurs by the interaction of unpaired electron spin with the nuclear spin of nearby magnetic nuclei. Electron-nuclear hyperfine interaction is

possible because of coupling of electron spin with nuclear spin. The spin-Hamiltonian is modified by the hyperfine interaction as given in equation (1.22).[3]

$$H = \beta H \bullet g \bullet \vec{S} + A \bullet I \bullet \vec{S} \qquad (1.21)$$

Here, A is defined as the hyperfine tensor that is represented by a 3×3 matrix. The hyperfine units are usually expressed in units of 10^{-4} cm^{-1} or in MHz. Based on the origin of the hyperfine coupling, it is categorized into isotropic or anisotropic components in a molecule with an axis of trigonal or higher symmetry. This is represented by equation (1.23). In the case of low symmetry molecules, a rhombic hyperfine tensor is observed.

$$A = \begin{bmatrix} A_{\perp} & 0 & 0 \\ 0 & A_{\perp} & 0 \\ 0 & 0 & A_{\perp} \end{bmatrix} = \begin{bmatrix} A_{iso} & 0 & 0 \\ 0 & A_{iso} & 0 \\ 0 & 0 & A_{iso} \end{bmatrix} + \begin{bmatrix} A_{aniso} & 0 & 0 \\ 0 & A_{aniso} & 0 \\ 0 & 0 & A_{aniso} \end{bmatrix} \qquad (1.22)$$

The hyperfine term is included in the spin Hamiltonian as depicted in equation (1.24). According to equation (1.24), the Zeeman split lines in the EPR spectrum further split into ($2NI$+1) lines due to the coupling of the magnetic moment of spin with the magnetic nuclei.

$$h\nu = g\beta\mathrm{H} + \mathrm{A}m_S m_I \qquad (1.23)$$

There are various contributions that contribute to the A-tensor. The first contribution comes from the direct Fermi contact term, which is the result of the symmetry allowed mixing of the s-orbital into the ground state. It is a purely isotropic hyperfine interaction. There is also the indirect Fermi contact term that is due to the polarization of s-electrons by the interaction with unpaired d-electron in the ground state. Another contribution comes from the direct and indirect dipolar coupling. Indirect couplings come from the spin

and orbital angular momentum of the unpaired electron and interacting nuclear momentum. The direct dipolar couplings dominate the anisotropic A-tensor (values are given in Table 1.3 based on the interaction of nucleus with single electron in metal d-orbital). There is also spin-orbit coupling between the nuclear spin and orbital angular momentum of the electron that contributes to the A-tensor because of metal d-orbital rotation as shown in Table 1.2.[20] An analysis of the A-tensor can also be helpful to obtain important electronic and geometric structure information on metal ligand covalency and spin density delocalization in the molecule.

Table 1.2: d-orbital rotation effects. [24]

	Orbital Angular Momentum Operator(L)		
	X	Y	Z
Initial Orbital	Final Orbital		
$d_{x^2-y^2}$	$-id_{yz}$	$-id_{xz}$	$2id_{xy}$
d_{z^2}	$-i\sqrt{3}\, d_{yz}$	$i\sqrt{3}\, d_{yz}$	0
d_{xy}	$-id_{xz}$	$-id_{yz}$	$-2id_{x^2-y^2}$
d_{xz}	$-id_{xy}$	$id_{x^2-y^2} - i\sqrt{3}\, d_{z^2}$	$-id_{yz}$
d_{yz}	$id_{x^2-y^2} + i\sqrt{3}\, d_{z^2}$	id_{xy}	$-id_{xz}$

Table 1.3: Contribution of dipolar interaction of nucleus with a single d electron on anisotropic hyperfine coupling.

	X	Y	Z
Z^2	4	4	-2
$x^2 - y^2$	-2	-2	4
yz	4	-2	-2
xz	-2	4	-2
xy	-2	-2	4

1.3.4 Spin Population and Relaxation

As demonstrated in Figure 1.3, under an applied magnetic field, Zeeman splitting of alpha (α) and beta (β) spins generate two separate energy levels for the two spin states. The room temperature Boltzmann spin population of the two-level system is shown in equation (1.25).

$$\frac{N_{upper}}{N_{lower}} = e^{\frac{-\Delta E}{K_B T}} = e^{-\frac{g\beta H}{K_B T}} = 1 - \frac{g\beta H}{K_B T} = 0.9986 \qquad (1.24)$$

Small spin population differences between the upper and lower levels contribute to weaker observed EPR signals. In the absence of a relaxation phenomenon, the difference in the spin population of the two energy levels is proportional to the applied external magnetic field and inversely proportional to temperature as presented in equation (1.26) which affects the intensity of the EPR signal.

$$N_{lower} - N_{upper} = N_{lower}[(1 - (1 - \frac{g\beta H}{K_B T})] = \frac{Ng\beta H}{K_B T} \qquad (1.25)$$

Spin population relaxation can happen because of both spin-lattice and spin-spin relaxation.[20 22] The spin-lattice (longitudinal relaxation Γ_{1e}) is responsible for the observed spin population difference in the two energy levels by dissipating the energy to the lattice. Longer spin-lattice relaxation times cause a decrease in intensity of the EPR signal. A

factor that contributes the line broadening (line width) is the spin-spin relaxation (transverse relaxation Γ_{2e}) which occurs from dipolar interactions and energy exchange with the higher spin states or lower energy nucleus. The spin-spin relaxation time is shorter than the spin-lattice relaxation time.[20]

In the case of high magnetic fields, as shown in Table 1.4, the Zeeman interaction is very large compared to the hyperfine terms. Thus, the Zeeman interaction plays the dominant role in recorded EPR spectra. Higher frequency EPR is useful to resolve two partially overlapping lines that are magnetic field dependent. Lower field experiments (S-band and L-band) are useful for resolving the complex splitting pattern as well.[25]

Table 1.4: Frequently used microwave bands and corresponding magnetic field strengths [25].

Microwave band	Frequency (GHz)	B_0(Gauss)
L	1.1	392
S	3.0	1070
X	9.5	3389
Q	35	12485
W	90	32152

1.4 X-ray Absorption Spectroscopy (XAS)

X-ray absorption spectroscopy involves the absorption of X-ray that promotes a core electron transition to a higher energy vacant orbital and to the continuum. It is a specialized technique to obtain electronic and geometric structural information of the target molecule, such as metal-ligand bond distance with high accuracy, type and number of metal atoms and ligands in a sample, and overall geometry of the molecule.[26] [27] The

X-ray energy is tunable to be element specific, thus it is an element specific probe to study the molecule of our interest.

Based on the type of core electron ejected and amount of X-ray energy utilized, the XAS technique is generally categorized into two types: K-edge and L-edge, and both are depicted in Figure 1.4. K-edge XAS is when a core (1s) electron is promoted to vacant excited states or the continuum, producing a photoelectron. K-edge XAS can be further categorized into metal K-edge (section1.4.1) and ligand K-edge (detailed in section 1.4.2). L-edge XAS is when ejection of core (2s or 2p) electrons takes place, producing a photoelectron. [28] [29] L-edge XAS utilizes soft X-rays (0.1-2 keV), to provide direct information on metal-ligand covalency in transition metal coordination complexes.[27]

1.4.1 Metal K-edge XAS

In metal K-edge XAS, an electron from the K-Shell, (1s electron) of metal is excited into a valence orbital or the continuum by using X-ray energies greater than 4 KeV. Metal K-edge XAS spectroscopy is a direct method to obtain the electronic structure, geometric

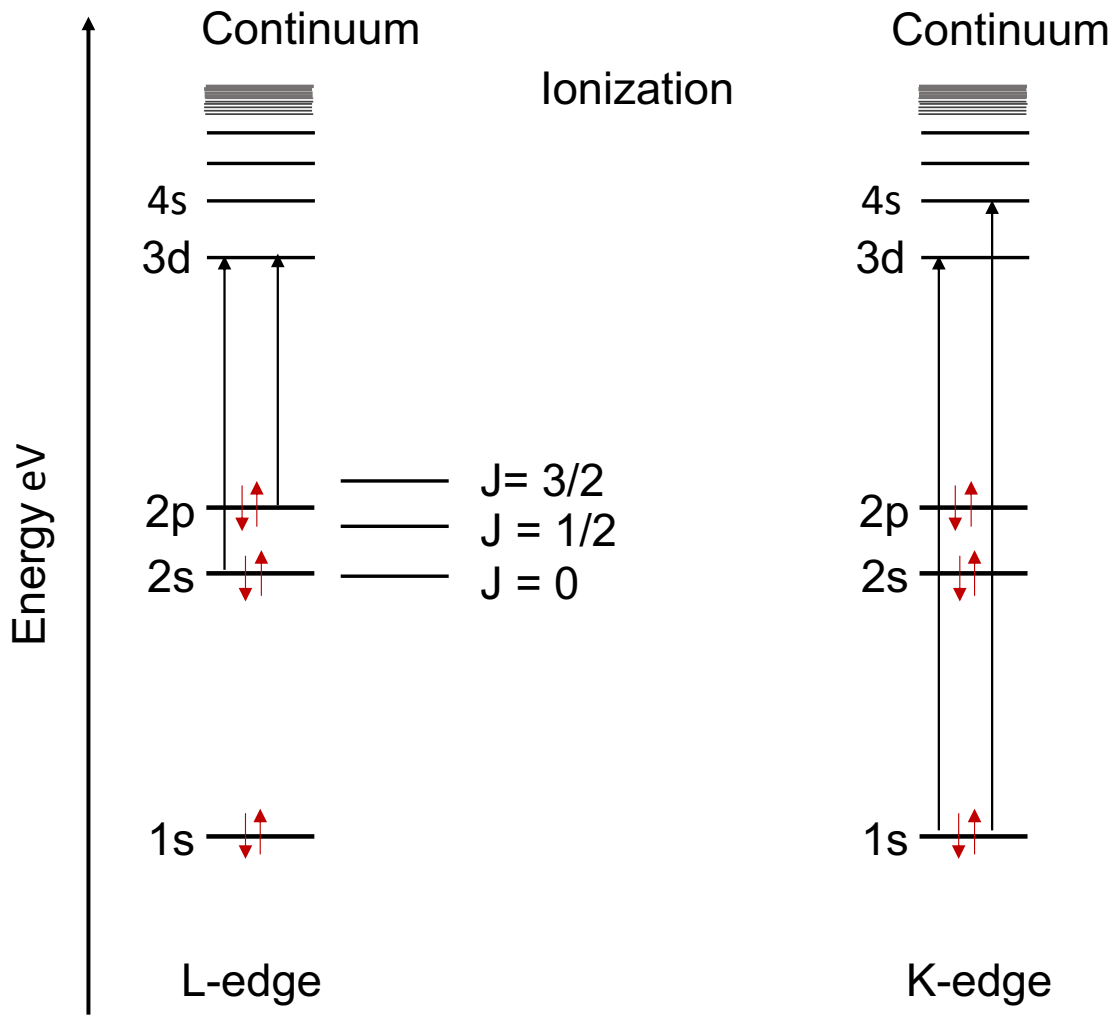

Figure 1.4: Schematic representation of L-edge (left) and K-edge (right) transitions in XAS.

structure, bond length, coordination numbers and types of coordinated atoms in metal complexes. The metal K-edge spectrum is divided into two regions, high and low energy. X-ray absorption near edge structure (XANES) covers the lower energy region of the spectrum and the extended X-ray absorption fine structure (EXAFS) component covers the higher energy region of the spectrum as shown in Figure 1.5. These two regions belong to different types of transitions and hold complementary information. The XANES region covers the near edge and rising edge. Among them, the near edge or pre-edge

peak is associated with the transition from 1s to an (n)d orbital. It is a quadrupole allowed transition ($\Delta I \pm 2$). The intensity of the near edge peak can increase by mixing of the metal d-orbital with a metal p-orbital, and the intensity also changes with symmetry and coordination number. The pre-edge feature is reflective of the number of holes in the 3d manifold. Thus, there is significant variation of pre-edge features between a metal with a single hole or multiple holes in the 3d manifold. Electron-electron repulsion and ligand field effects result in multiplet splittings.[27] Another intense peak in the XANES region is the rising edge. The intensity is gained by the electric dipole allowed transition from 1s to np orbitals. Its energy shifts according to the oxidation state of the metal. Therefore, it is frequently used to quantify the effective nuclear charge of the involved atom.

The higher region of the metal K-edge is the EXAFS region, which represents the transitions from the 1s orbital K-shell to the continuum. This region is ~36 eV above the threshold energy. Observed oscillations arise from the constructive and destructive interference of forward- and backscattered photoelectrons, which behave as a wave.[27] EXAFS provides key information about the number, nature, and distance of the ligand atoms from the absorbers.[26]

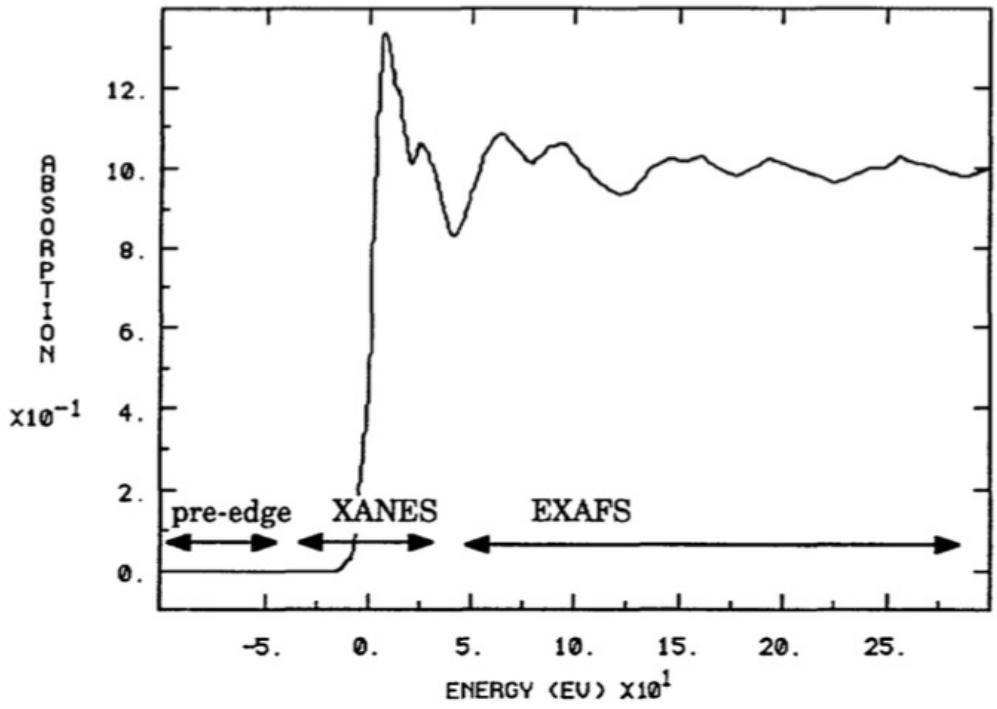

Figure 1.5: XAS-spectrum showing energy region of pre-edge XANES and EXAFS from lower to the higher respectively (Figure is adapted from reference 22). [30]

1.4.2 Ligand K-edge XAS

Ligand X-ray absorption edge spectra provides greater insight into the coordinating ligand. Several metals, such as Mo, Cu, Fe, Ni, are studied by the metal K-edge XAS to provide a direct probe of metal ligand covalency and bonding. Among the ligand K-edge studies, sulfur and chlorine-based ligands are the most ubiquitous[31]. Ligand K-edge XAS is a powerful tool that provides direct information on metal ligand covalency and the nature of the bonding interactions. In this research study, sulfur K-edge spectroscopy has been employed. All further discussion on ligand K-edge XAS will be directed toward sulfur K-edge spectroscopy. S K-edge XAS is the technique that has been used to quantitatively determine metal-sulfur covalency in the different molecules synthesized.

1.4.3 Sulfur K-edge XAS

Use of the tunable synchrotron radiation specific to the sulfur element (~2472 eV), is used to excite the sulfur 1s electron into the unoccupied sulfur 3p orbitals, and further into the continuum. We generally observe variable intensity pre-edge features in the ligand K-edge X-ray absorption spectra of transition metal complexes. The allowedness of these transitions is increased upon the mixing of the formerly filled 3p orbital of sulfur with the metal d orbital, since the 3p orbital of sulfur is directly involved in the bonding with the transition metal.[31] [32] The intensity of sulfur K-edge pre-edge spectra quantifies the amount of sulfur character in the metal d orbital, since the transition associated with the pre-edge is localized on the sulfur atom. The intensity of the pre-edge features can be obtained quantitatively by using equation (1.27).

$$I\left[S\left(1s \rightarrow \psi^{*}_{\beta-LUMO}\right)\right] = \beta^{2} I[S(1s \rightarrow 3p)] \qquad (1.26)$$

Here, $\psi^{*}_{\beta-LUMO}$ is the ground state wavefunction of the lowest unoccupied molecular orbital (LUMO) set in the metal complex and β^{2} corresponds to the amount of sulfur character in the LUMO wavefunction. The value for β^{2} can be determined by analyzing the total integrated area under the sulfur K-edge pre-edge peaks and the dipole integral (I_s), which is proportional to the intensity of the electric-dipole allowed transition.[32] Specifically, for the study of our (bpy)Pt(E, E') systems, the amount of sulfur character per hole is responsible for the intensity of pre-edge peak as expressed in equation (1.28), which is further detailed in chapter 3.

$$D_0 = \frac{h}{3N} c_i^2 I_{s(1s\rightarrow 3p)} \quad (1.27)$$

Here, D_0 is the integrated area under the per-edge peak, h is number of holes (unoccupied orbitals), N is the number of absorbers (N=2 for the (bpy)Pt(E, E') systems). More details of the application and analysis of S K-edge data is presented and discussed in Chapter 3.

1.4.4 Experimental Principles and the Synchrotron Radiation Source

X-ray absorption spectroscopy uses high energy photons obtained from a tunable synchrotron light source which is generated from accelerated electrons. This is the working principle for the generation of synchrotron radiation based on the thermionic principle.[33] Electrons are ejected from the heated metal and enter a linear accelerator (LINAC) where the velocity of the electrons is dramatically increased by using a high voltage field to the limit where the velocity of electrons becomes comparable with velocity of light. An accelerated stream of electrons in the LINAC circulates around a booster ring of bending magnets. The energy of the electrons is further increased by the high magnetic field. Then, the synchrotron light enters the wigglers, a storage ring which has clusters of opposing magnetic poles placed vertically in two layers. Magnetic poles are there to achieve tunability of synchrotron light by changing the number of poles. Oscillating light passes to the different magnetic poles and propagates in one direction obtained from the wigglers. The SSRL beam line used for our samples in this Dissertation is BL 7-3, which has 20 magnetic poles at magnetic field of 2 Tesla, and the energy range is 5-33 KeV.

After the interaction of synchrotron light with a sample molecule, the intensity of transmitted light is represented by the Beer-Lambert law as presented in equation 1.27.

$$I_t = I_0 e^{-\mu(E)X} \quad (1.28)$$

Here, the parameters, I_t, I_0 and x are the intensity of transmitted light, intensity of the incident light, and the thickness of the sample, respectively.

$$ln\frac{I_0}{I_t} = \mu(E) \quad (1.29)$$

$$ln\frac{I_f}{I_t} = \mu(E) \quad (1.30)$$

1.5 References

(1) Valeur, B. Molecular Fluorescence Principles and Applications. *Molecular Fluorescence* **2001**, 399.

(2) Harris, D. C.; Bertolucci, M. D. *Symmetry and Spectroscopy: An Introduction to Vibrational and Electronic Spectroscopy*; Dover Publications: New York, 1989.

(3) Drago, R. S.; Drago, R. S. *Physical Methods for Chemists*, 2nd ed.; Saunders College Pub: Ft. Worth, 1992.

(4) Solomon, E. I. Electronic Absorption-Charge Transfer Transitions. *Comments on Inorganic Chemistry* **1984**, *3* (5), 249–260. https://doi.org/10.1080/02603598408080075.

(5) Solomon, E. I. Spectroscopic Methods in Bioinorganic Chemistry: Blue to Green to Red Copper Sites. *Inorg. Chem.* **2006**, *45* (20), 8012–8025. https://doi.org/10.1021/ic060450d.

(6) Noggle, J. H. *Physical Chemistry*, 3rd ed.; HarperCollins College Publishers: New York, 1996.

(7) Dong, C. Spectroscopic and Computational Studies of Molybdenum Enzymes and Models, 2015.

(8) ED, J. L; Joint Ed, R. G. W. *Modern Coordination Chemistry*; 1967.

(9) Shriver, D. *Inorganic Chemistry, 3e + Cd + Study Guide /Solutions Manual.*; W H Freeman: Place of publication not identified, 1999.

(10) Lever, A. B. P. *Inorganic Electronic Spectroscopy*, 2nd ed.; Studies in physical and theoretical chemistry ; 33.; Elsevier: Amsterdam, 1984.

(11) Shriver, D. F.; Atkins, P. W. *Inorganic Chemistry: Third Edition*; Oxford University Press, 1999.

(12) Solomon, E. I. *Inorganic Electronic Structure and Spectroscopy*; 2006.

(13) Cummings, S. D.; Eisenberg, R. Tuning the Excited-State Properties of Platinum (II) Diimine Dithiolate Complexes. *Journal of the American Chemical Society* **1996**, *118* (8), 1949–1960.

(14) Cummings, S. D.; EISENBERG, R. Inorg. Chem. *Inorganic Chemistry* **1995**, No. 34, 2007.

(15) Kubo, K.; Nakano, M.; Tamura, H.; Matsubayashi, G. X-Ray Crystal Structure and Electrical Conductivity of [Pt(2,2′-Bipyridine)(C8H4S8)][BF4] [C8H4S82−=2-{(4,5-Ethylenedithio)-1,3-Dithiole-2-Ylidene}-1,3-Dithiole-4,5-Dithionate(2-)]. *Inorganica*

Chimica Acta **2002**, *336*, 120–124. https://doi.org/10.1016/S0020-1693(02)00844-7.

(16) Mabbs, F. E.; Collison, D. *Electron Paramagnetic Resonance of Transition Metal Compounds*; 1992.

(17) Weltner, W. *Magnetic Atoms and Molecules*; Scientific and Academic Editions: New York, 1983.

(18) Balagopalakrishna, C.; Kimbrough, J. T.; Westmoreland, T. D. Electronic Structural Contributions to *g* Values and Molybdenum Hyperfine Coupling Constants in Oxyhalide Anions of Molybdenum(V). *Inorg. Chem.* **1996**, *35* (26), 7758–7768. https://doi.org/10.1021/ic951142a.

(19) Collison, D.; Enemarkb, J. H.; Wexlerb, P. A. Crystal and Molecular Structure of [SnLCI,]. The Single- Crystal Electron Paramagnetic Resonance Spectra of [MoE(L)CI,] and [MoO(L)(NCS),] Diluted in [SnLCI,] [E = 0 or S; L = Tris(3,5-Dimethylpyrazolyl)Hydroborate] t. *J. CHEM. SOC. DALTON TRANS.* **1994**, 9.

(20) Atherton, N. M. *Principles of Electron Spin Resonance*; Ellis Horwood series in physical chemistry; Ellis Horwood: Chichester, 1993.

(21) Abragam, A.; Bleaney, B. *Electron Paramagnetic Resonance of Transition Ions*; Oxford classic texts in the physical sciences; Oxford University Press: Oxford, 2012.

(22) Weil, J. A.; Bolton, J. R. *Electron Paramagnetic Resonance: Elementary Theory and Practical Applications*, 2nd ed.; Wiley-Interscience: Hoboken, N.J, 2007.

(23) Solomon, E. I. Electron Paramagnetic Resonance (EPR). *Comments on Inorganic Chemistry* **1984**, *3* (5), 230–238. https://doi.org/10.1080/02603598408080073.

(24) *Physical Methods in Bioinorganic Chemistry: Spectroscopy and Magnetism*; Que, L., Ed.; University Science Books: Sausalito, Calif, 2000.

(25) *Multifrequency Electron Paramagnetic Resonance: Data and Techniques*; Misra, S. K., Ed.; Wiley-VCH: Weinheim, 2014.

(26) Solomon, E. I. "Functional Insight from Physical Methods on Metalloenzymes." *Inorg. Chem.* **2005**, *44* (4), 723–726. https://doi.org/10.1021/ic040127f.

(27) Baker, M. L.; Mara, M. W.; Yan, J. J.; Hodgson, K. O.; Hedman, B.; Solomon, E. I. K- and L-Edge X-Ray Absorption Spectroscopy (XAS) and Resonant Inelastic X-Ray Scattering (RIXS) Determination of Differential Orbital Covalency (DOC) of Transition Metal Sites. *Coordination Chemistry Reviews* **2017**, *345*, 182–208. https://doi.org/10.1016/j.ccr.2017.02.004.

(28) Yano, J.; Yachandra, V. K. X-Ray Absorption Spectroscopy. *Photosynth Res* **2009**, *102* (2–3), 241–254. https://doi.org/10.1007/s11120-009-9473-8.

(29) Koningsberger, D. C.; Mojet, B. L.; van Dorssen, G. E.; Ramaker, D. E. XAFS Spectroscopy; Fundamental Principles and Data Analysis. 13.

(30) Alp, E. E.; Mini, S. M.; Ramanathan, M. X-Ray Absorption Spectroscopy: EXAFS and XANES - A Versatile Tool to Study the Atomic and Electronic Structure of Materials. 12.

(31) Rose Williams, K.; Hedman, B.; Hodgson, K. O.; Solomon, E. I. Ligand K-Edge X-Ray Absorption Spectroscopic Studies: Metal-Ligand Covalency in Transition Metal Tetrathiolates. *Inorganica Chimica Acta* **1997**, *263* (1–2), 315–321. https://doi.org/10.1016/S0020-1693(97)05663-6.

(32) Sarangi, R.; DeBeer George, S.; Rudd, D. J.; Szilagyi, R. K.; Ribas, X.; Rovira, C.; Almeida, M.; Hodgson, K. O.; Hedman, B.; Solomon, E. I. Sulfur K-Edge X-Ray Absorption Spectroscopy as a Probe of Ligand−Metal Bond Covalency: Metal vs Ligand Oxidation in Copper and Nickel Dithiolene Complexes. *J. Am. Chem. Soc.* **2007**, *129* (8), 2316–2326. https://doi.org/10.1021/ja0665949.

(33) David Johnson, P. Synchrotron Radiation. In *Experimental Methods in Physical Sciences*; Vol. 29, pp 23–43.

Chapter 2

Using Donor Bridge Acceptor Transition Metal Complexes to Probe Molecular Rectification and Conductance.

2.1 Literature Review

Molecular electronics involves studying and applying combinations of molecules and molecular building blocks to enable the construction of electronic components at the nanoscale. Characteristics of molecular electronic materials depend on their molecular organization in space.[1] The concept of molecular electronics has developed from the proposed idea in the early 1970s that a molecule connected between the metal electrodes that could rectify a current.[2] Since then, the development of functional molecular electronics with a single molecule has been a compelling field among researchers. The purpose of using a molecular component in these electronic devices is to further miniaturize these devices without compromising performance.[3] Molecular and molecule-based electronic components have an advantage in the field of nanotechnology due to their ease of synthetic manipulation, and the fact that the size dimensions of molecules are inherently at the nanoscale. The main focus of our study in the field of molecular electronics is to understand the movement of electron through single molecules, and this results in significant experimental and theoretical challenges. Among them, the major one is the fluctuation of actual conductance data using single molecule and difficulty to obtain the actual geometry of the molecule that contributes to an individual data point.[4] Over four decades, research on single molecule electronics has progressed significantly to overcome these challenges. Molecular electronics has broad subareas for fundamental research. Here, our is focused on the single molecule rectifier and molecular conductance through molecular bridges.[5]

2.2 Single molecule rectifier: A study on the rectification behavior of $Tp^{Cum,Me}Zn$(SQ-py-thp-NN) and $Tp^{Cum,Me}Zn$(SQ-thp-py-NN)

(This study is adapted from the paper published in 2017 in Chemical Science: M. L. Kirk, D. A. Shultz; J. Zhang, R. Dangi, L. Ingersol, J. Yang, N. S. Finney, R. D. Sommer, L. Wojtas, Heterospin Biradicals Provide Insight into Molecular Conduction and Rectification, Chemical Science, **2017**, 8, 5408 – 5415. DOI: 10.1039/c7sc00073a).[6]

2.2.1 Introduction

Aviram and Ratner stated that an intrinsic functionality of a molecule could be utilized as a device in 1974.[2] They have presented their proposed concept of molecular rectifier design by considering organic donor (D) and acceptor (A) moieties having aromatic π-systems that are covalently attached to metallic electrodes. The preferred metals to use as an electrode to connect this wire are gold or platinum in order to avoid the degradation or oxidation of the metallic electrode.[6] In Aviram and Ratner's single molecule rectifier design, decoupling of the π-system was achieved by using a σ-only bonding molecular fragment connecting the wired donor and acceptor in their proposed molecular electronic concept. In the single molecule rectifier, the molecule would mimic the band structure of a semiconductor by using the electron rich and electron deficient features of the molecular moieties connected to the electrodes through chemically different orbitals. The purpose of this is to allow one-way flow of current with respect to the Fermi energy of the electrodes.[6] The efficiency of the single molecular rectification design is characterized by the Rectification Ratio (RR), which is the ratio of the absolute current flowing in conducting and insulating directions at the same applied bias voltage.[7]

The performance of these single molecule rectifier is not very satisfying compared to their semiconductor counterparts.

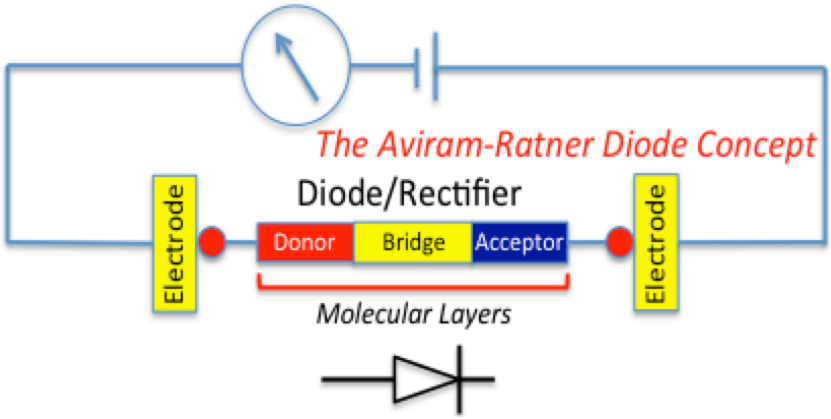

Figure 2.1: Schematic representation of single molecule ratifier where a molecule is sandwiched between two gold electrodes. Arrow is indicating the current rectifying direction.

The reported molecular rectifier performance (RR) is typically lower than 10.[7] In 2015, Van Dyke and Ratner proposed three new design principles to improve the performance of the single molecule rectifier. The first rule proposed by Van Dyke and Ratner is focused on the utilization of the asymmetric anchoring group to chemically connect the molecule to electrodes, an electron deficient group is used to promote the LUMO alignment and an electron rich group is used to promote the HOMO alignment on the opposite end of the molecule. The second rule is to utilize the anchoring group to promote the frontier orbital in the close vicinity of the electrode Fermi levels. Finally, the third rule involves the utilization of the decoupling unit to effectively decouple the π-conjugation between the donor and acceptor moieties without a large reduction in the conduction.[8]

Our study here is focused on applying the third rule proposed by Van Dyke and Ratner in order to analyze the molecular rectifier design by using organic donor-acceptor fragments as decoupler units. Donor-Bridge-Acceptor molecular systems, despite being a phenomenal rectifier design, allows for a high level of control of the active rectifying component. However, the nature of the coupling of D-B-A complex with metallic electrodes has not been fully understood. The contact geometry of the molecule strung between the metallic electrodes in a device configuration is not precisely known.[9] The prediction of molecular orientation normally assisted by performing thousands of individual experiments to measure the conductance properties of the single molecule and then constructing conductance histograms.[9] In these experiments, the challenge will always remain to assess the geometric orientation of the molecule relative to the metallic electrodes and the geometry of the molecule associated with the preferred direction of current flow.

In our work, these ambiguities related to geometry of the molecule have been eliminated by replacing the metallic electrode equivalents with spin bearing organic radicals, where the structures have been characterized by the X-ray crystallography as shown in Figure 2.*2*. These spin bearing radicals are covalently connected to the D-A bridging molecular fragment, which would serve as a rectifier in a device configuration.[10] The pyridine-thiophene/thiophene-pyridine (P-T/T-P) bridges are covalently connected to a semiquinone (SQ) at one end and nitronylnitroxide at the other end, and thus form constitutional isomers. This satisfies the charge transfer in both the positive and negative bias directions. The same molecule is attached between electrodes in a device configuration as depicted in Figure 2.*2*.

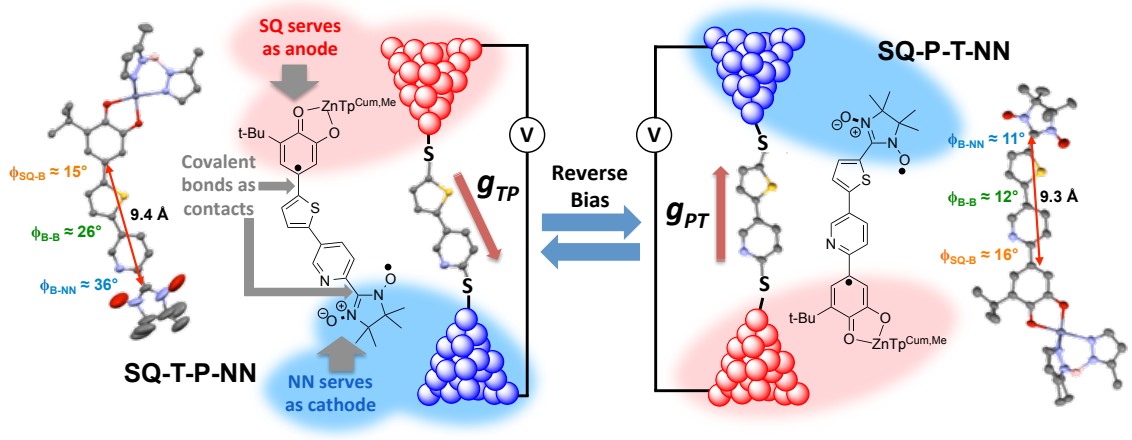

Figure 2.2: Bond line drawings and thermal ellipsoidal plots (left and right) for SQ-T-P-NN and SQ-P-T-NN with corresponding single -molecule rectifier devices (center).(This figure is adapted from the paper published in 2017 Chemical Science: M. L. Kirk, D. A. Shultz; J. Zhang, R. Dangi, L. Ingersol, J. Yang, N. S. Finney, R. D. Sommer, L. Wojtas, Heterospin Biradicals Provide Insight into Molecular Conduction and Rectification, Chemical Science, **2017**, 8, 5408 – 5415. DOI: 10.1039/c7sc00073a).

Here, the SQ and NN moieties function as molecular analogs of the biased electrodes. Different bridge-radical torsion angles model aspects associated with asymmetrical anchor group attachment, while the electron-deficient pyridine bound to the electron-rich thiophene constitutes the D-A bridge fragment. This ensures asymmetrical orbital alignment with electrodes, fulfilling the proposed idea by Van Dyck and Ratner in 2015.[8] Bond torsions within the molecular system serve to partially decouple the bridge fragments. A relatively large dipole moment of 1.94 D is calculated for the bridge, and this satisfies the proposed principle by Aviram and Ratner[2] (σ-bond as a decoupler) and the decoupling rule presented by Van Dyke and Ratner.[7] Intrinsic unimolecular rectification is an inherent property of the molecule in which the energy levels of the molecule shift with the applied bias voltage. In this study, we have also performed single-molecule electron transport calculations and compared them with the experimental observations obtained

from electronic absorption spectroscopy, magnetic susceptibility, and molecular electronic structure computations on structurally known geometries.

2.2.2 Transport Calculations

The Quantum ATK 2016.0 v16.0 software program was used to perform the transport calculations.[11] [12] [13] The device configuration consists of three major sections: the left gold electrode, the molecular fragment (central scattering region) and the right gold electrode. Both the electrodes are comprised of a 3 × 3 array of Au (111) atoms, altogether 81 atoms per electrode. For the specified electrode the C (or Z) direction it is periodic in the system, which is also the direction of electron transport. Geometry optimization computations of the thiophene-pyridine (T-P) bridge component with protonated terminal sulfur atoms on both sides of the molecule was accomplished using Gaussian '09 with a 6-31g(d',p') basis set and a B3LYP functional.[11] [14] One of the gold electrode surfaces was constructed by cleaving the bulk crystal and the second electrode was constructed by copying the first electrode. The geometry optimized T-P bridge was then placed on the surface of the gold electrode and connected to the electrodes through terminal sulfur atoms to form the bulk configuration. Before converting into the final device geometry, the constructed bulk configuration was optimized applying a single-zeta polarized basis set for the gold atoms and a double zeta basis set for all the other atoms. Optimization of bulk configuration was performed by using ATK-DFT with a Perdew-Zunger local density approximation (LDA-PZ) exchange correlation function. Optimization of the connection point between the T-P bridge component and the gold electrode through sulfur atoms was allowed by setting other parts of the molecule and the gold electrode as rigid in this bulk configuration. After the optimization of the bulk configuration, it was

converted into the final device configuration for the following calculations. For all the transport calculations a 5 × 5 × 51 K-point sampling has been used in x, y, and z directions, respectively. The fixed boundary condition (Dirichlet) was used in the z-direction, which is also the direction of transport. The boundary conditions in the x- and y-directions were disabled to make them not change, but still the default parameterization is periodic for both directions. The NEGF formalism was used to calculate the non-equilibrium electron density of the central region of the device.

Transmission probabilities and the conductance are related by the Landauer-Buttiker formula, where g = I/V.[15] This relationship is used to calculate the voltage dependent current, I(V), over the molecular junction. Integration of the transmission function, T (*E, V*), results in the voltage dependent current according to equation (2.1).

$$I(V) = \frac{e}{h}\sum_{\sigma}\int T_{\sigma}(E)\left[f\frac{(E-\mu_R)}{K_B T_R} - f\frac{(E-\mu_L)}{K_B T_L}\right]dE \qquad (2.31)$$

In the above equation, e = charge of the electron, h = Planck's constant, eV_{bias} = bias window that is equivalent to $\mu_R - \mu_L$ ($V_{bias} = V_L - V_R$), $T\sigma(E)$ = transmission coefficient of the spin component, and σ describes the junction at an energy E and at a given bias voltage V_{bias}. The expression in the brackets of equation (2.1) represents the Fermi-Dirac functions and right and left electrodes with respective to the chemical potentials μ_R and μ_L. Calculations on all the electron transport properties were performed by using the ATK software package with the virtual nano-lab associated analysis modules. The MPSH technique has been used to understand and analyze the orbitals involved in the resonant peaks in the transmission function. Molecular orbitals of the isolated T-P bridge have been

compared with the transmission eigenstates, which allows us to understand how the transmission peaks are changed with the application of an applied bias across the electrodes.[10]

2.2.3 Results and Discussions

In this study, donor and acceptor units of the T-P bridge molecule are partially decoupled by the dihedral angle between the thiophene and pyridine planes, which are connected by a σ-bond. The dihedral angle is measured to be 22° from the Gaussian computed optimized geometry. We have previously evaluated σ contribution to be $\sim$ 13 times weaker than the π-contribution with respect to the electronic coupling matrix element (H_{DA}). This quantity squared is proportional to the conductance (g), and taking this relationship in consideration there will be ~200 fold decrease in the electron transport mediated by the σ-bond compared to the π-bond.[16] Thus the σ-bonds are effective in decoupling the donor-acceptor fragment and could create the necessary tunnelling barriers between D and A, but the σ-bond also lowers the flow of current in both forward and reverse bias directions. This is the biggest limiting factor in developing an efficient rectifier compared to the semiconductor counterparts.

2.2.4 Molecular Design and Structure

The biradical complexes used in our study were synthesized by the Shultz research group at North Carolina State University.[17] [18] [19] [20] [21] [22] [16] [23] [24] [25] Bond line drawing structures, along with X-ray structures, are presented in Figure 2.2, which clearly shows torsion angles of 15°, 26° and 36° for the SQ-T, T-P and P-NN respectively in SQ-

T-P-NN complex, and similar corresponding torsion angles of 16°, 12° and 11° are found for the SQ-P-T-NN complex.

2.2.5 Exchange Couplings and Rectification Ratios

SQ and NN are both S = ½ spin bearing units, so the magnitude of electronic coupling ($H_{SQ\text{-}B\text{-}NN}$) can be measured by using high resolution spectroscopic techniques to measure the magnetic exchange interactions of the radical spins.[20 21 26 27 28 29] This magnetic exchange coupling measurement can be performed using field and temperature dependent spectroscopy techniques such as electron paramagnetic resonance, electronic absorption, and magnetic susceptibility. The exchange splitting, or singlet−triplet gap, is defined here as $2J_{SQ\text{-}B\text{-}NN}$ in the Heisenberg exchange Hamiltonian given in equation (2.2),

$$H_{SQ-B-NN} = -2J_{SQ-B-NN}\hat{S}_1 \cdot \hat{S}_2 \qquad (2.32)$$

Where $\hat{S}_i$ = Spin operators for the S = ½ radical spins.

The magnetic exchange coupling has been measured using magnetic susceptibility techniques. The susceptibility data has been plotted as $\chi_{para} \cdot T$ products vs temperature as shown in Figure 2.3, top plot for SQ-P-T-NN and bottom plot for SQ-T-P-NN.

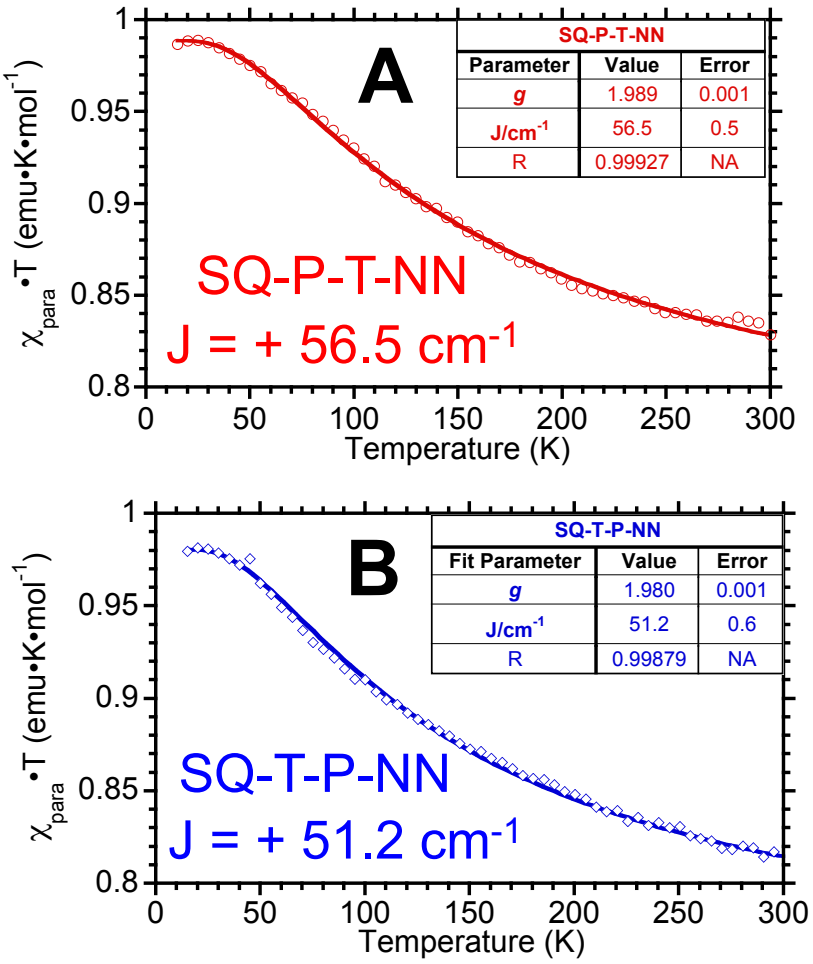

Figure 2.3: Magnetic susceptibility data for the complexes SQ-P-T-NN (Top, A) and SQ-T-P-NN (Bottom, B) recorded at variable temperature (This data was recorded and processed at North Carolina State University by David Shultz's research group (Figure has adapted from reference 6)

Fitting of the dimer exchange equations to the data allows one to get the magnetic exchange coupling values of $J_{SQ\text{-}TP\text{-}NN}$ = +51.2 cm^{-1} and $J_{SQ\text{-}PT\text{-}NN}$ = +56.5 cm^{-1}. These are related to the conductance and the electronic coupling matrix element via equation (2.3).

$$\sqrt{J_{SQ-B-NN}} \propto H_{SQ-B-NN} = \frac{H_{Sq-BHB-NN}}{\Delta}\left(\frac{H_{BB}}{\Delta}\right) \cong c \bullet \sqrt{g} \qquad (2.33)$$

Here, Δ is the SQ $\rightarrow$ B-A charge transfer energy, and $J_{\text{SQ-B-NN}}$ is the biradical magnetic exchange coupling. The magnetic exchange coupling (J) is proportional to the conductance (g) according to the equation (2.3), where c is a proportionality constant. In terms of the molecular rectifier design principles, it is very important to clearly correlate the magnetic exchange, $J_{\text{SQ-NN}}$ to the electronic couplings $H_{\text{SQ-NN}}$, $H_{\text{SQ-B}}$ and $H_{\text{B-NN}}$ respectively, as described by equation (2.3), which is based on the theories advanced by Anderson.[30] [31] [32] Equation (2.3) makes a clear connection between the computed conductance and the observed electronic coupling matrix element and magnetic exchange coupling in SQ-T-P-NN and SQ-P-T-NN complexes. The relative magnitudes of the electronic couplings $H_{\text{SQ-B}}$ and $H_{\text{B-NN}}$, and the SQ $\longrightarrow$ B-NN charge transfer energy, describe the strength of connectivity of an asymmetrical SQ and NN π-system with the asymmetrical bridge component. The value of H_{BB} describes the degree of coupling between the π- systems of the unsymmetric bridge fragment.[33]

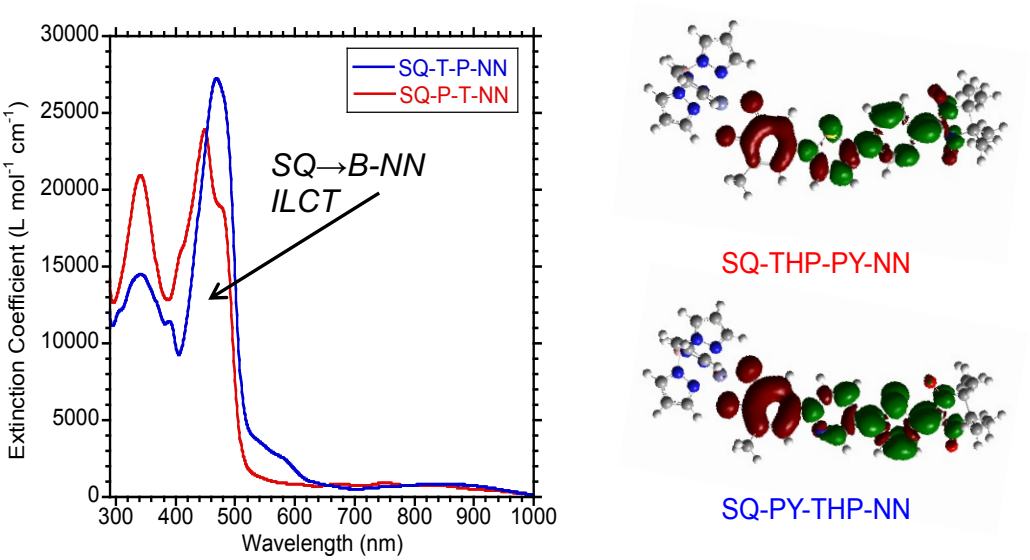

Figure 2.4: Room temperature electron absorption of SQ-T-P-NN and SQ-P-T-NN. The low energy intense band for both isomeric complex is showing the charge transfer is from SQ to B-NN LUMO (left) and time dependent DFT calculated EDDMs generated from the output file of a TD-DFT calculation indicating the nature of the charge transfer. The green color depicts a gain of electron density and red color a loss of electron density (right) in the charge transfer transition (This data was recorded and processed at North Carolina State University by David Shultz's research group and the figure is adapted from reference 6).

Electronic absorption spectra for the two isomers are shown in Figure 2.4. The band assignments of the spectra were performed with the help of TD-DFT computations, and the results where then compared to the prior SQ-B-NN complexes. The bands at ~840 nm and ~540 nm is from the SQ and NN radicals. The intense band at ~475 nm is the intra-ligand charge transfer band (ILCT), which possess dominant SQ(SOMO) ⟶ B-NN(LUMO) character with a minor contribution from the B-NN(HOMO) ⟶ SQ(SOMO) one electron promotion in Figure 2.4. The ILCT transition is important since the observed ground state ferromagnetic exchange is attributed to configurational mixing of excited states into the ground state. The configurational mixing has been successfully evaluated by the valence bond configurational interaction (VBCI) model as has been used with other similar SQ-B-NN heterospin biradical complexes.[20 21] The ILCT energy is used to evaluate

the approximate value of Δ in equation (2.3), which represents the intrinsic molecular bias between SQ and NN.[34] [22] The difference in energy between the most intense charge transfer band of SQ-P-T-NN and SQ-T-P-NN is ~900cm^{-1}, so in our study we have considered $\Delta_{SQ\text{-}T\text{-}P\text{-}NN} \cong \Delta_{SQ\text{-}P\text{-}T\text{-}NN}$. So, with $\Delta_{SQ\text{-}T\text{-}P\text{-}NN} \cong \Delta_{SQ\text{-}P\text{-}T\text{-}NN} \equiv \Delta$ and the J-values for the two isomers, equation (2.4) relates the magnetic exchange couplings to the conductance. We can restate the equation (2.3) as,

$$\frac{J_{SQ-TP-NN}}{J_{SQ-PT-NN}} = \frac{51.2cm^{-1}}{56.5cm^{-1}} = \frac{g_{TP}}{g_{PT}} = 0.91 \equiv RR \qquad (2.34)$$

Equation (2.4) can be modified to evaluate the conformational effects of a molecule with appropriate $\cos\varphi$ values of the dihedral angle that were determined from X-ray crystallography. The bond torsions directly control the degree by which the π-orbitals of the adjacent neighbor fragments decouple by torsional rotation. The unsymmetrical orbital alignment of the bridge fragment with biased electrode equivalents is affected by the torsional rotations. The rectification ratio and the magnetic exchange coupling can be varied by changing the torsional angles between the adjacent neighbor bridge units according to equation (2.5).

$$\sqrt{J_{SQBNN}} \propto H_{SQBNN} = \frac{\cos\phi SQB\, H_{SQB} \bullet \cos\phi BNN\, H_{BNN}}{\Delta} \times \left(\frac{\cos\phi BB\, H_{BB}}{\Delta}\right) \cong c\sqrt{g} \quad (2.35)$$

This study has shown that $H_{\text{SQ-B-NN}}$ (~$\sqrt{J_{\text{SQ-B-NN}}}$ as depicted in equation 2.3) varies as a product of the cosines of the SQ-B and B-NN torsion angles.[35] The product of these cosines is 0.70 for SQ-T-P-NN and 0.93 for SQ-P-T-NN. When we substitute these cosine values into equation (2.5), we get equations (2.6) and (2.7), and further taking the square of these results equation (2.8).

$$\sqrt{J_{SQBNN}} \propto H_{SQBNN} = 0.70\frac{H_{SQTP} \bullet H_{TPNN}}{\Delta} \times \left(\frac{H_{TP}}{\Delta}\right) \cong \sqrt[c]{g_{TP}} \quad (2.36)$$

$$\sqrt{J_{SQBNN}} \propto H_{SQBNN} = 0.93\frac{H_{SQTP} \bullet H_{TPNN}}{\Delta} \times \left(\frac{H_{TP}}{\Delta}\right) \cong \sqrt[c]{g_{PT}} \quad (2.37)$$

$$\frac{J^0_{SQTPNN}}{J^0_{SQPTNN}} = \frac{J_{SQTPNN}}{J_{SQPTNN}} \times \frac{0.93^2}{0.70^2} = \frac{\frac{51.2cm^{-1}}{0.49}}{\frac{56.5cm^{-1}}{0.86}} = \frac{104cm^{-1}}{66cm^{-1}} = \frac{g^0_{TP}}{g^0_{PT}} = 1.58 = RR^0 \quad (2.38)$$

When the bridge molecule is planar and the individual magnetic exchange coupling values, and the SQ ⟶ B-NN charge transfer energies (Δ), are equal the predicted intrinsic RR for the planar T-P geometry is 1.58 times greater than that of the non-planar P-T isomer. This value shows the reversal of the preferred direction of conductance compared to the experimental RR of 0.91. The rotational pre-factors of 0.70 and 0.93 in equations (2.6) and (2.7) suggest that the intrinsic coupling is higher in case of planar SQ-T-P-N

compared to SQ-P-T-NN, in agreement with their respective exchange coupling values of ~104 cm^{-1} and 66 cm^{-1}.

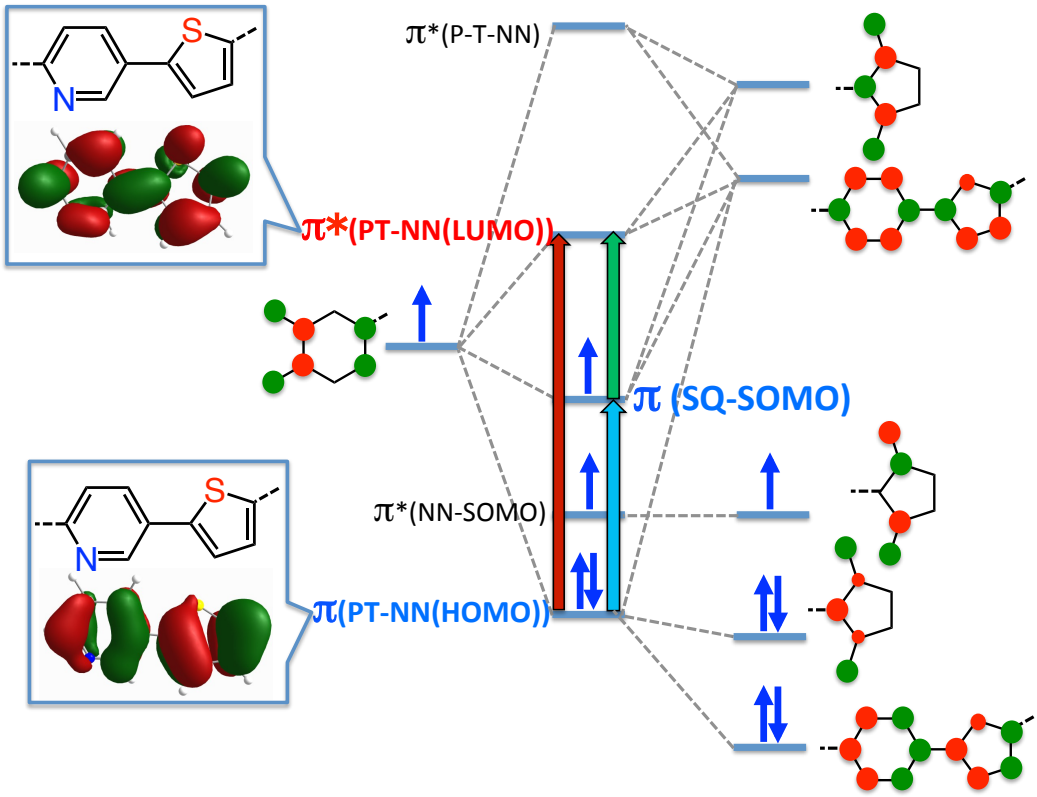

Figure 2.5: DFT computed T-P HOMO and NNHOMO wave functions that mix with frontier NN orbitals (Left), VBCI model for SQ-P-T-NN illustrating the bridge HOMO and LUMO mirror plane like symmetry (Right). Red, green, and blue arrows indicate dominant one-electron contribution to the ILCT band. The blue and red transitions probe dominant CT contribution to magnetic super-exchange pathways.

2.2.6 Mechanism of Rectification in T-P Bridges

The VBCI model can explain relationships between magnetic exchange coupling and ILCT transitions by looking the orbital topology of the HOMO and LUMO of the T-P bridge. This has added further explanation to the observed relatively low RRs despite the T-P bridge fragment possessing strong donor and acceptor character. Both the HOMO and

LUMO are involved in the energy and intensity of the charge transfer transition, magnetic exchange couplings, and electron transport. They are very symmetric as shown in Figure 2.*5* and this indicates the magnitude of T-P bridge torsion angle is not large enough to effectively reduce the π-coupling between the Py and Thp components of the bridge. Thus, an essential component of unimolecular rectification as proposed by Van Dyke and Ratner in 2015 has not been satisfied by the target molecule to break the symmetry between donor and acceptor considering the torsion angle as a decoupling unit.[7] The donor-acceptor component of the bridge can be decoupled more effectively when the torsion angle between the pyridine and thiophene planes is 90° (Figure 2.6). This simultaneously eliminates π-coupling between the donor and acceptor component with a significant reduction in the conductance. This has been studied quantitatively with a series of [SQ-$(Me)_n$Ph-NN] complexes.[16] Our study shows that to increase rectification without marked reduction in conduction, one must design a molecule in which the rotational angle between donor and acceptor fragment to be just enough to localize the HOMO and LUMO on the donor and acceptor, respectively.

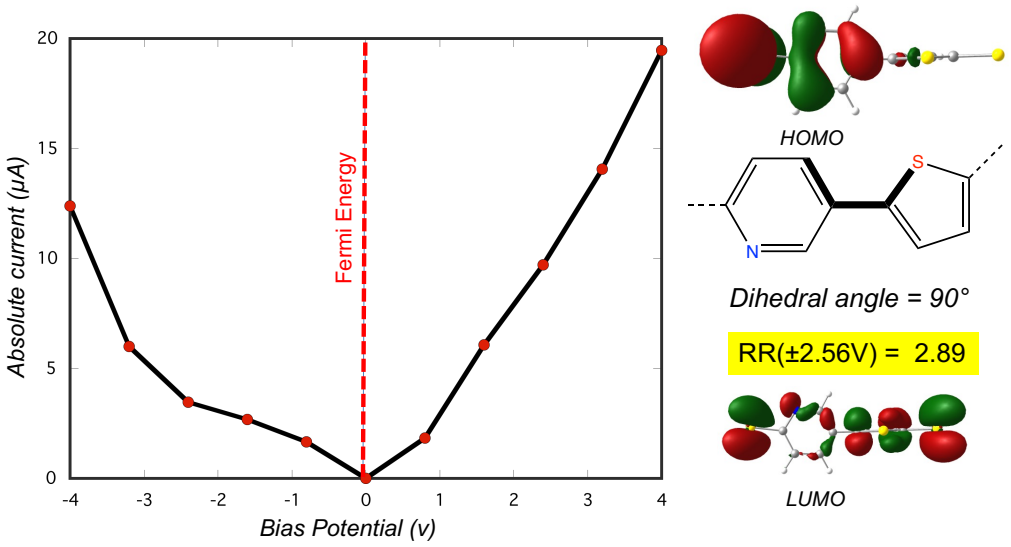

Figure 2.6: Calculated I-V curve at +/- 4 eV applied bias (left). DFT calculated wave function of 90° torsion angles of T-P bridge component (right) along with bond line drawing of 90° rotated pyridine-thiophene ring.

2.2.7 Computational Assessment of the Molecular Electron Transport Through T-P

We have used a computational approach to understand the molecular electron transport properties of the T-P bridge fragment in both bias directions by using Au-bridge-Au device construct. The primary purpose of doing transport calculations with a T-P bridge molecular fragment is to directly compare the results of a transport calculation with the experimentally determined $J_{SQ\text{-}T\text{-}P\text{-}NN}$ and $J_{SQ\text{-}P\text{-}T\text{-}NN}$, and the electronic and geometric structure. As we have shown before, the bridge mediated magnetic exchange couplings are related to the conductance through the electronic coupling matrix element.[32]

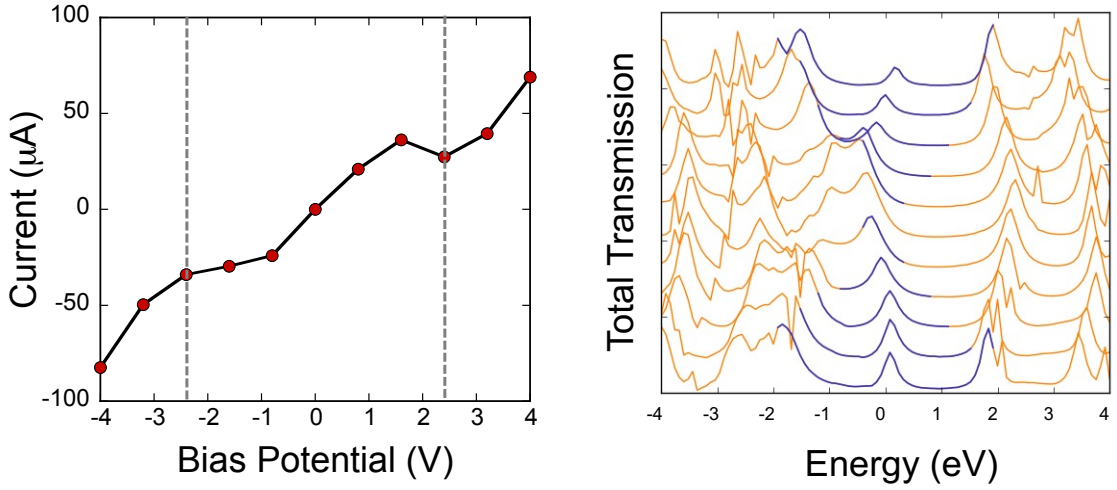

Figure 2.7: Results of transport calculation on T-P bridge molecule under forward and reverse bias direction. I-V curve calculated at ±4 eV applied bias. Vertical dashed lines indicate the intrinsic bias of SQ-PT-NN and SQ-TP-NN (Charge transfer energy) (left). The rectification ratio has been calculated at ± 2.56 V which is the intrinsic bias energy of charge transfer energy. Bias-dependent transmission spectrum. Bias window has been shown in blue color in transmission spectrum. Transmission spectra correspond with -4 V at the bottom and +4 V at the top of the plot (right).

The results of the ATK transport calculation on the $Au_{(L)}$-S-T-P-S-$Au_{(R)}$ arrangement with the bond torsion value of 20°, which is the average value of the T-P rotational angle determined from the X-ray crystallographic measurements, is shown in Figure 2.7. We observed an RR = 1.58 from magnetic exchange couplings that is compared to the computed value of 1.24, which is also small at ±2.56 V bias point. The chosen bias point is in line with ILCT energy of the SQ(SOMO) ⟶ B-NN(LUMO) transition shown in Figure 2.4. A lower RR is expected from the very small $\phi_{T\text{-}P}$ torsion angle and the highly delocalized HOMO and LUMO wave functions. We can see a very good agreement between the magnetic exchange coupling determined and computed RRs for the unsymmetrical T-P-bridge molecule connected with gold electrodes in this device construct.

This study further illustrates the advantage of using an unsymmetrical bridge component to relate the results of a transport calculation and experimentally observed magnetic exchange coupling constants. This is with consideration of the contact geometry of the bridge with gold electrodes and with the SQ and NN spin bearing organic radicals as metallic electrode analogs. Thus, we can directly compare the RR at fixed bias potential with ratio of magnetic exchange and proportionality constants *c* in equation (2.3).

2.2.8 Analysis of the Transport Calculation Results

Further insight into the system can be achieved by understanding the electronic origins of the transmission, in the context of a tight-binding model.[36] [37] Based on this approximation the transmission function, $T\ (E, V)$, can be expressed as equation (2.9).

$$T(E,V) = \frac{4\pi^2\gamma_L^2(V)DOS_L(E,V)\gamma_R^2(V)DOS_R(E,V)}{[E-E(V)]^2 + \pi^2[\gamma_L^2(V)DOS_L(E,V) + \gamma_R^2(V)DOS_{LR}(E,V)]^2} \qquad (2.39)$$

Here, $DOS_{LR}\ (V)$ = Electron density of states, and $E(\mathrm{V})$ = molecule energy levels affected by the Stark effect under an applied bias. The parameters DOS ($_{L,\ R,),}$ $\gamma_L(\mathrm{V})$, $\gamma_R(\mathrm{V})$, and $E(\mathrm{V})$ all contribute to the current through the transmission function and are bias dependent. In our device configuration, we have Au as the L and R electrodes and sulfur atoms connecting the electrodes. Thus, the dominant contribution of the transmission function in both bias directions is determined by the bias dependent energy levels of the bridge, which has allowed us to study the intrinsic components of unimolecular rectification. In Figure 2.7, the transmission plot on the right displays the computed transmission as a function of bias voltage. At low applied bias voltage only one transmission peak appears

in the bias window. As the applied bias is increased, we see the more intense peak enter the bias window in the negative bias direction, while the small peak gradually goes out of the bias window as we increase the applied bias in positive direction. Hence, we observe more current flowing in (-V) bias direction than the (+V) bias direction. We have analyzed this further by evaluating the molecular projected self-consistent Hamiltonian (MPSH) states that are associated with the transmission peak of interest. The MPSH states are defined as the molecular orbital wavefunctions of S-T-P-S bonded to the Au electrodes.

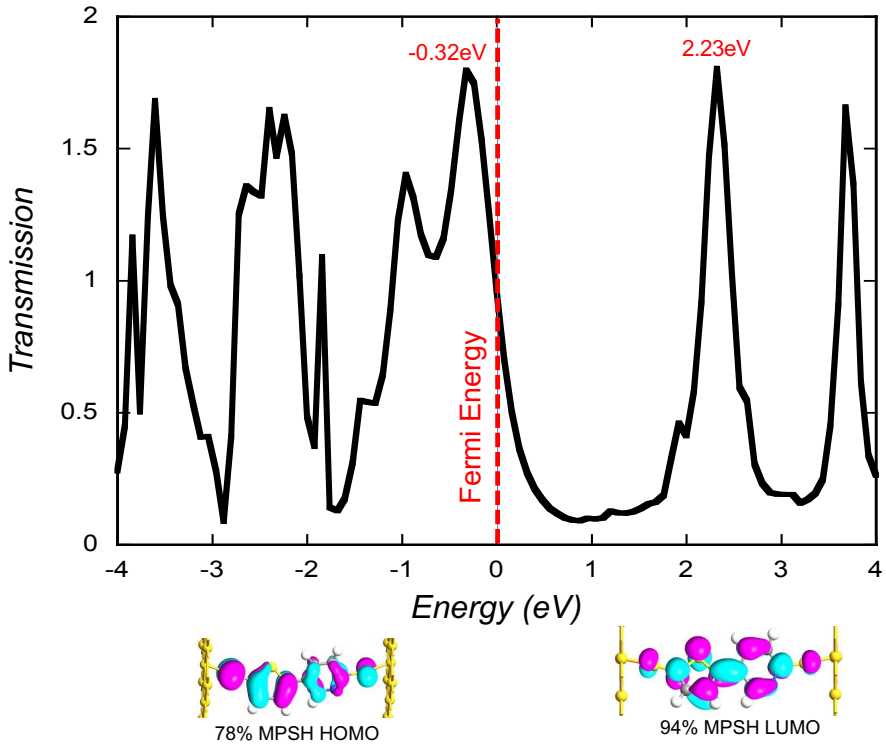

Figure 2.8: Zero bias transmission spectrum calculated as a function of energy in eV and transmission probability. Dotted line shows the Fermi Energy of electrodes.

The MPSH state that contributes to the −0.32 eV transmission peak in Figure 2.8 is 78% HOMO in character. The MPSH HOMO is nearly identical to the T-P molecular

HOMO shown in Figure 2.5. When the applied potential is lower than −1.5 V another peak clearly enters the bias window, which is also dominantly MPSH HOMO in nature. Once the bias potential is increased to 1.5 V, we observe a new transmission peak in the bias window in the transmission plot shown in Figure 2.7. The transmission at 2.23 eV in the zero bias transmission spectrum is comprised predominantly of the MPSH LUMO (98%), mirroring the bridge LUMO of the isolated bridge fragment. We can conclude that both the T-P HOMO and LUMO have contributed to the conductance in Figure 2.5. The MPSH HOMO contributes when the applied potential is low, which is due to the pinning effect of HOMOs to the electrode Fermi level.[8 38 39]

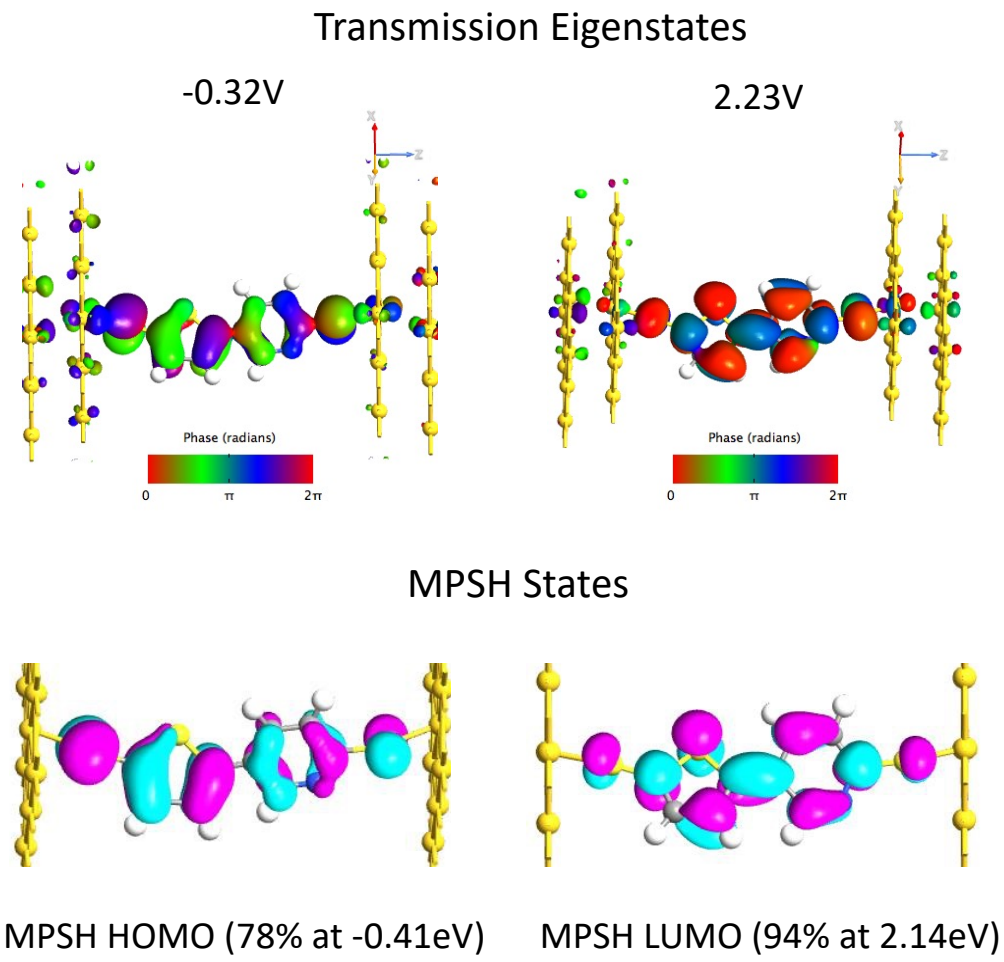

Figure 2.9: Zero bias calculated transmission eigenstates on at −0.23 eV and 2.23 eV(top). Molecular projected self-consistent Hamiltonian (MPSH) states indicating the effects of the molecular orbitals under the influence of their interaction with the electrode surfaces.

From our transport calculation results, the HOMO and LUMO of the T−P bridge are the orbitals primarily responsible for the observed transmission peak, and this sheds light on the rectification mechanism. These are also the same orbitals that contribute to the ground state magnetic exchange coupling in the system. The thiol group is most effective when connected to the gold electrode, presumably by increasing the degree of coupling of the molecular eigenstate with the electrode. This is due the fact that the molecular orbital with a large sulfur wavefunction contribution in the bias window

dominates the conductance. In the case of the SQ-B-NN complex, the bridgehead carbons of the SQ and NN radical units are the S analogs in the transport calculation.

It is very compelling that the T-P LUMO MPSH state enters the bias window at the potential that is roughly equal to the ILCT energy of SQ(SOMO) ⟶ NN(LUMO) transition. The T-P HOMO plays a role in conductance at low applied potential, but it has a very low contribution to magnetic exchange coupling since only 14% of the HOMO is involved in the ILCT as evaluated from our TD-DFT calculations. When the MPSH HOMO is pinned to the electrode Fermi level in the device configuration, the importance of a highly delocalized MPSH HOMO on conduction is higher. In the case of the T-P LUMO pinned to the Fermi level of the electrode in the device that contributes to the conductance at low bias, there is a difference in orbital contributions when using molecular contact analogs. In the case of SQ-T-P-NN and SQ-P-T-NN constitutional isomers, this favors the B-NN(LUMO) which is due to a different type of interaction of the bridge orbitals with the SQ(SOMO) and NN(LUMO). Normally, the use of other molecular contact analogs with different reduction potentials and different orbital topologies will further modulate the electronic coupling through the molecular bridge. In the future, this has the potential to make use of molecular electrodes with improved contact to further improve the RR and the conductance properties of unimolecular bridge constructs.[40]

2.2.9 Conclusion

The biradical approach we have studied can be used to evaluate the rectification ratios of any bridge fragment at many conformations as observed by X-ray crystal structures of molecular systems and can provide very important information regarding

electronic structure contributions to conductance by using high resolution spectroscopic techniques. The RR we observed from magnetic exchange coupling is close to 1 and the same is expected from the transport calculation, where a nearly planar geometry is observed due to the small torsion angle. Because of the almost planar geometry, the HOMO and LUMO orbital wavefunction primarily involved in conductance and the magnetic exchange coupling are very symmetric and delocalized in nature. Increasing the intrabridge bond torsion should significantly increase the RR, but we observed the reversed intrinsic RR through T-P bridge fragment. The RR is still relatively small with a reduction in the conductance by a factor of two. More importantly, our study connects conductance values (from transport calculations) and magnetic exchange couplings (from magnetic data) to an electronic coupling matrix element. We can extend this work to further understand the true origin of the rectification and conductance in SQ-B-NN systems by choosing different bridge fragments with various donor and acceptor components.

2.3 Transferrable Property Relationships Between Magnetic Exchange Coupling and Molecular Conductance.

(This study has been adapted from the paper published in Chemical Science in 2020: Kirk, M. L.; Dangi, R.; Habel-Rodriguez, D.; Yang, J.; Shultz, D. A.; Zhang, J. Transferrable Property Relationships between Magnetic Exchange Coupling and Molecular Conductance. *Chem. Sci.* **2020**, 10.1039. D0SC04350H. https://doi.org/10.1039/D0SC04350H)

2.3.1 Introduction

It is crucial to understand, and therefore eventually be able to control, molecular electron transport and understand the mechanisms of transport. Our approach does this through computations using a single molecule attached to metallic electrodes. The level of understanding must be at the atomic scale, which makes strides toward the goal of miniaturization of molecular electronic devices.[41] Studies of electron transport mechanisms usually take advantage of the combination of experimental and computational probes of conductance using the Metal-Bridge-Metal construct.[16 42 43 44 45 46 47 48 49 50 51 41] Experimental methodology is often used to determine the conductance (g_{mb}) in order to evaluate inherent variations in molecule-electrode binding geometries. This can be accomplished by the mechanically controlled break junction technique. This technique utilizes a scanning tunneling microscope, in which taking thousands of individual conductance measurements is necessary to assemble a complete and representative data set. This experimental method generates a distribution of conductance values, and the most probable conductance value can therefore be determined.[35] In this field, direct comparison of theoretical results and experimental observables proves difficult, since the true geometry of the M-B-M junction and the molecular junction are unknown. Thus, the current research on these molecular electronics systems is still advancing, with the goal of successfully correlating the single-molecule conductance with experimental observables, such as electron transfer rate constants ($k_{D\rightarrow A}$) [42 52 53 50 54] and magnetic exchange couplings.[10 55 22 18 21] The purpose of pursuing this type of research is to achieve deeper insights into the nature of the orbitals involved in electron transfer pathways. The correlation between theoretical results,

physical observables, and the discovery of relationships between transferable properties should have great impact on the development of functional molecular design principles for molecular electronics and spintronics.

The relationship between various transferable properties was first explained by Nitzan.[32] He derived the relation between g_{mb} and $k_{\mathrm{D}\rightarrow\mathrm{A}}$ by considering the bridge molecule, and that the conductance can be related to the square of the D-A electronic coupling matrix element, $H_{\mathrm{D}\rightarrow\mathrm{A}}^2$ ($H_{\mathrm{D}\rightarrow\mathrm{A}} = |H_{DB}H_{BA}|^2|G_B(E)|^2$) for electron transfer equations (2.10) through (2.13).[32]

$$g_{mb} \approx \frac{8e^2}{\pi^2 T_D^{(l)} T_A^{(R)} FCWDS} K_{D\rightarrow A} \tag{2.40}$$

$$g_{mb} = \frac{e^2}{\pi h} \Gamma_{LB}\Gamma_{RB}\left|\overline{G_B}\right|^2 \tag{2.41}$$

$$K_{D\rightarrow A} = \frac{2\pi}{h}[H_{DB}H_{BA}]^2[G_B(E)]^2\mathrm{FCWDS} \tag{2.42}$$

$$G_B = \frac{H_{BB}^{n-1}}{\Delta\varepsilon^n} \tag{2.43}$$

In the above equations, H_{ij} = pairwise couplings matrix elements that connect D, B, and A, T = broadening functions that represent the coupling between the molecule and electrodes, $\Delta\varepsilon$ = tunneling energy gap, G_{B} = bridge Green's function with the overbar indicating G_{B} may differ for electron transfer (or magnetic exchange) compared to conductance and, n = number of bridge units. With these transferrable property

relationships defined, it indicates that any physical observable that is a function of the square of the electronic coupling matrix element can be related to g_{mb} according to equation (2.14). This establishes the relationship between these parameters, and the distance decay constants (β_i) for conductance and magnetic exchange as shown in equation (2.15).

$$J_{D\to A} \propto H_{D\to A}^2 \propto K_{D\to A} \propto g_{mb} \tag{2.44}$$

$$K_{D\to A} \propto g_{mb} \propto J_{D\to A} \propto \exp\left(-\beta_i \times \mathrm{nL}\right) \tag{2.45}$$

In equation (2.15), nL defines the distance spanned by the bridge component. From the previous work done in this field, the correlation between $K_{D\to A}$, g_{mb} and $J_{D\to A}$ are supported by both experimental and theoretical work.[50 55 56 57 58 58 59 60 61 62 56] The work performed by Beratan and Waldeck shows there is a non-linear relationship between $K_{D\to A}$ and g_{mb} on the basis of Nitzan's work. Beratan and Waldeck studied alkane and peptide nucleic acid oligomer bridges and found that they are related by a power law function.[44 53] Waldeck and Beratan's work shows that the Green's function (G_B) is different for both electron transfer and conductance. When the decay constant β is the same for the electron transfer and the conductance, then the linear relationship between $K_{D\to A}$ and g_{mb} will occur.[44 53]

According to the equation (2.14); magnetic exchange interaction ($J_{D\to A}$) is proportional to square of the electronic coupling element ($H_{D\to A}^2$).[30 63 64 65 19 20]

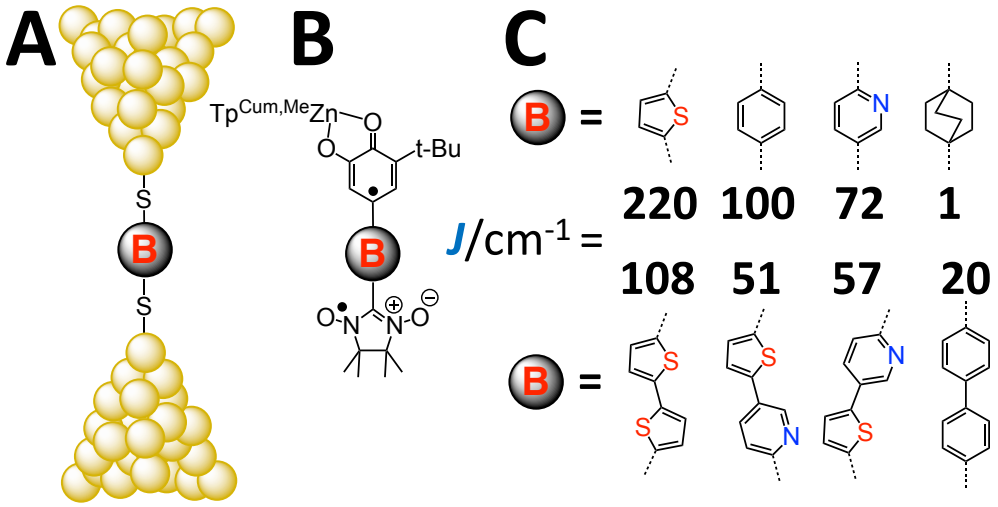

Figure 2.10: (A) Metal-Bridge-Metal junctions corresponding to biradical complexes (B). (C) Bridges common to M-B-M junctions and Donor-Bridge-Acceptor complexes (B). Ferromagnetic exchange parameters $J_{D\rightarrow A}$ are showing along with corresponding bridge fragment. BCO = Bicyclo[2,2,2] octane, Ph = Para-phenylene, Th = 2,5-thiophene, Py = pyridine, Py-Th = 2-pyridyl-5'-thiophene, ph_2 = Para-biphenylene, and Th_2 = 2,55-bithiophene.

Our research group, in collaboration with the Shultz group at NC State University, has introduced experimental designs to show the correlation of $J_{D\rightarrow A}$ between the donor and acceptor radical units SQ (S= ½) and NN (S= ½). These molecular systems have SQ and NN connected by different bridge molecules (Figure 2.10, B and C) and we use the conductance values, g_{mb}, that were evaluated from the previous theoretical work.[10 55 55 21 18 20 19 66 34 23] In this study, variable-temperature magnetic susceptibility measurements were performed in the solid state, where the molecular geometry had already been determined by X-ray crystallography. Magnetic susceptibility data is then used to determine $J_{D\rightarrow A}$ values, which has the benefit of being used from a single conformation to evaluate the exchange couplings. Furthermore, these measurements are not affected by structural and solvent bath induced inhomogeneities. This is often overlooked when

experimental measurements of conductance in a contact geometry and solution electron transfer rate measurements are carried out.

In the field of molecular electronics, there exist many challenges to completely understand the relationship between the orbital contributions for $J_{D\rightarrow A}$ and electron transport channels that facilitate conductance. Some of these are listed below:

1. There are variations in the connections of molecular fragments covalently attached to the bridge units,
2. Identifying the molecular surfactant groups,
3. Variations in surface contact,
4. Variations in the choice of electrode material and surface morphology affecting the conductance and exchange couplings,
5. Inhomogeneities in molecular structure.

Hermann and coworkers, in their recent work,[50] postulated the transferability of geometric and electronic structure contributions of the bridge moiety to $K_{D\rightarrow A}$, g_{mb} and $J_{D\rightarrow A}$ in Figure 2.***10***. Here, we also have worked to address the challenges associated with relating the transferrable properties of conductance and exchange by considering donor-bridge-acceptor biradical complexes. Then, these results are used to determine the distance decay constants(β_g) for conductance with the help of the results we have on the distance dependent decay constant (β_J) of $J_{D\rightarrow A}$ based on our prior work.[55] We have shown that the ground state bridge wavefunction involved in the conductance and the exchange are different. This was established with the help of resonance structures and valence bond terms. It has been helpful to understand the relationship between $J_{D\rightarrow A}$ and g_{mb} without structural inhomogeneities and decoherence effects.

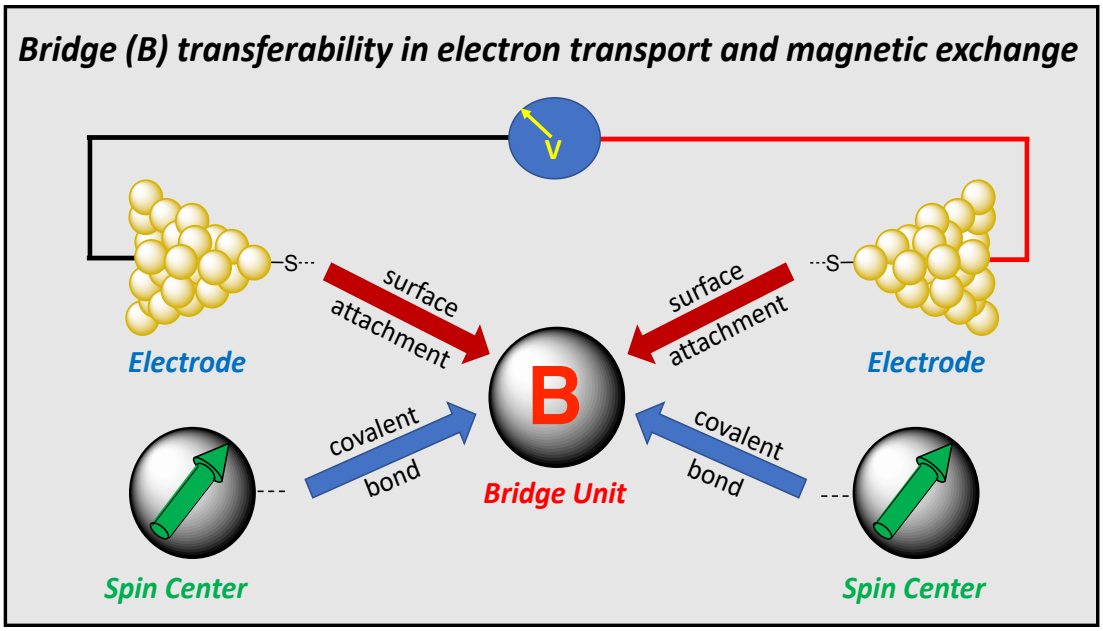

Figure 2.11: Diagram illustrating the bridge-mediated electronic coupling is related to conductance and magnetic exchange coupling.

2.3.2 Molecular Electronic Structure Calculations

The electronic structure calculations for the bridge component presented on Figure 2.***10*** (C) has been done using the Gaussian 09W software.[14] Input files were prepared using the molecular builder function in GaussView. The level of theory for all calculations used a B3LYP hybrid exchange-correlation functional and a 6-31g (d',p') split valence basis set with polarizability functions applied for all atoms. Wavefunctions were generated from the fully geometry optimized ground states.

2.3.3 Transport calculations

Details have been explained in section 2.2.2. Transmission probabilities and the conductance are related by the Landauer-Buttiker formula, g(g = I/V).[15] This relationship is used to calculate the voltage dependent current, I(V), over the molecular junction.

Integration of the transmission function, $T\,(E, V)$ results in the voltage dependent current according to equation (2.16).

$$\sum_{\sigma} \int T_{\sigma}\,(E) \left[f \frac{(E-\mu_R)}{K_B T_R} - f \frac{(E-\mu_L)}{K_B T_L} \right] dE \qquad (2.46)$$

Calculations on the conductance were performed by using the ATK software package with virtual nano-lab associated analysis modules. The MPSH technique has been used to understand and analyze the orbitals involved in the resonant peaks in the transmission function and their contribution on the conductance.

2.3.4 Results and Discussions

2.3.4.1 Exchange Coupling in SQ-bridge-NN Complexes

Magnetic exchange coupling constants, $J_{D\rightarrow A}$, have been determined by using magnetic susceptibility measurements for the complexes with monomeric bridges SQ-BCO-NN, SQ-Ph-NN, SQ-Th-NN,[55 21 16 67] and dimeric bridged complexes SQ-Py-Th-NN[10], SQ-Ph_2-NN[55] and SQ-Th_2-NN.[55] The exchange Hamiltonian for the dimers is given in equation (2.17) and this has been used to analyze the data which includes the magnetic susceptibility data for the new pyridyl-bridged complex (SQ-Py-NN), with $J_{D\rightarrow A}$ = +72cm^{-1}.

$$\mathcal{H}_{ex} = -2J_{D\rightarrow A} S_{SQ} S_{NN} \qquad (2.47)$$

We can see large variations of the exchange ranging from $J_{D\rightarrow A}$ = +1 cm^{-1} for a σ-mediated bridge in SQ-BCO-NN to $J_{D\rightarrow A}$ = +220 cm^{-1} for π-mediated superexchange in SQ-Th-NN, where the two radical spins are ferromagnetically coupled.[21 63 19]

2.3.4.2 Exchange Coupling within the Context of a Valence Bond Configuration Interaction (VBCI) Model

Based on the geometric structures of the SQ-Bridge-NN complexes, they fall into two categories,

1. Monomeric molecular bridge
2. Dimeric molecular bridge

A combination of magnetic susceptibility, spectroscopy and theoretical calculation have been employed to understand and explain the electronic origins of π-mediated exchange in SQ-Ph-NN and σ-mediated exchange in SQ-BCO-NN.[18 21 16 34 67 17] The VBCI model has been used to understand π-mediated exchange coupling, which explains the mechanism of admixing of specific excited state configurations with the ground configuration to affect the magnitude of exchange coupling.[18 21 19 20]

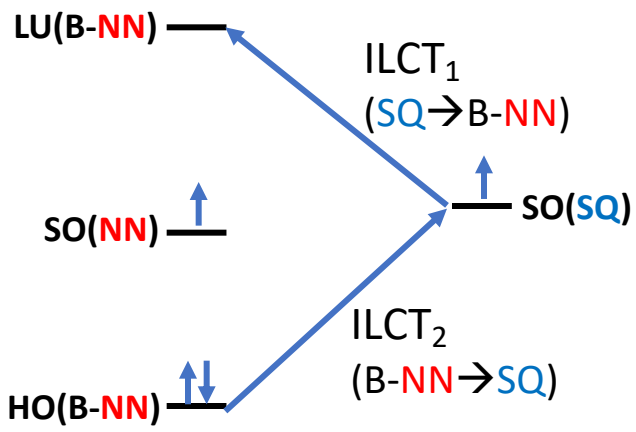

$$\psi_{CT}^{\pm} = a\varphi_{SQ\rightarrow B-NN} \pm b\varphi_{B-NN\rightarrow SQ}$$

Figure 2.12: Diagram showing the one electron transitions which contribute to the magnetic exchange coupling, NN-Bridge (HOMO) ⟶ SQ(SOMO) and SQ(SOMO) ⟶ NN-Bridge (LUMO) in SQ-Bridge-NN biradicals.

The NN(SOMO), SQ(SOMO), NN-Bridge (HOMO), and NN-Bridge (LUMO) in are the orbitals considered as the starting active space to generate the ground and excited state configurations. These orbitals are involved in the magnetic exchange couplings for the conjugated SQ-Bridge-NN systems. Previously published work has shown the

involvement of the B-NN(LUMO) in most important in the determination of exchange coupling.[18 55 21 63 20 34]

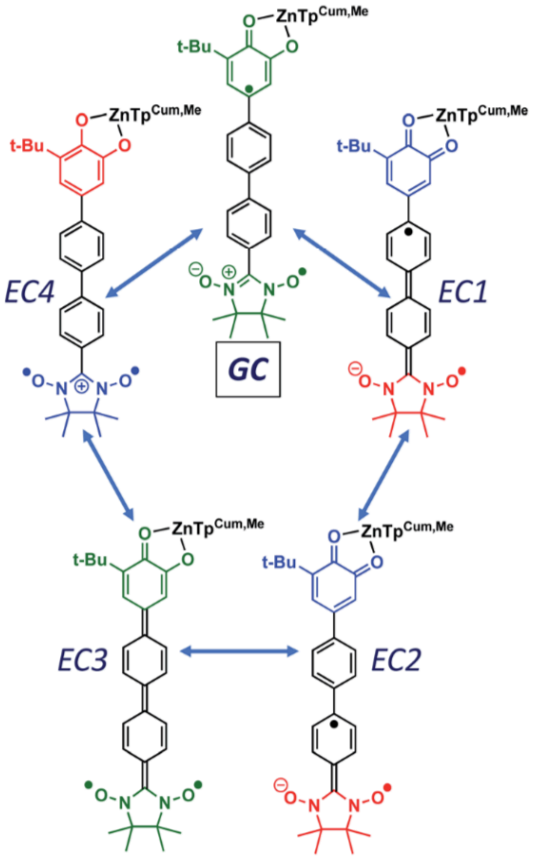

Figure 2.13: Resonance structures illustrating enhanced H_{BB}, H_{DB}, H_{BA} couplings in D-B-A biradicals (SQ-Ph-Ph-NN).

In Figure 2.13, the ground state configuration of SQ-Ph_2-NN is represented by GC and the excited state configurations resulting from the ILCT between SQ(SOMO) ⟶ NN-Bridge (LUMO) are also given. The other two excited state configurations, EC3 and EC4, are generated due to the one electron promotion from NN-Bridge (HOMO) ⟶ SQ(SOMO) as shown in the resonance structures. The analogous zwitterionic biradical resonance structures for M-B-M couplings ($H_{BB}, \Gamma_{LB}, \Gamma_{RB}$) are higher in energy, so their contributions to conductance is less in comparison. All SQ ⟶ B-NN ligands have a net (-1) charge.

Different color-coding separates donor and acceptor based on their oxidation state in Figure 2.*13* (green = 9 π-electron SQ^{1-}/7 π-electron NN; red = 10 π-electron $catecholate^{2-}$ /8 π-electron NN^{1-}; blue = 8 π-electron $quinone^{0}$/6 π-electron NN^{1+}).

In the case of conjugated SQ-Bridge-NN systems, the excited state configuration EC1 and EC2 are the dominant contributors compared to the excited state configurations EC3 and EC4 in determining the ground state ferromagnetic exchange coupling of the SQ-Ph-NN biradical complex.[55] [18] [21] [68] [19] [34] The contributions of the excited state configurations of ILCT on the magnetic exchange is varied with the nature of the bridge molecular fragment. If we have a relatively more electron rich molecular bridge like thiophene, it increases the energy of the bridge HOMO and LUMO, and the magnetic exchange is primarily contributed to by the one electron promotion from NN-Bridge (HOMO)⟶ SQ(SOMO). In the case of Ph-NN with attenuated exchange coupling, it has been observed that with increased torsional rotation between the Phenyl and NN planes, there is a reduced intensity of the ILCT band compared to more planar conformations.[67] We have observed the disappearance of the ILCT band in case of the SQ-BCO-NN complex, where exchange is mediated through a σ-only bond, and this complex displays very weak exchange coupling.[16] [18] Thus, the contribution of the bridge HOMO and LUMO wavefunctions on the magnitude of exchange coupling has provided further insight to understand the orbital contributions between the transferable properties (magnetic exchange coupling, conductance, rate of electron transfer) and electronic coupling in the biradical systems shown in Figure 2.11.

2.3.4.3 Magnetic Exchange and Conductance

Conductance through the bridges shown in Figure 2.***10*** (C) has been evaluated by the computations for the Au_n-S-Bridge-S-Au_n construct and the conductance g_{mb} is compared with the $J_{D\rightarrow A}$ values obtained from experiment. In the transport calculations, bridge molecules are connected to the voltage-biased Au electrodes through thiol anchoring groups as shown in Figure 2.14. The bridges we have used are those shown in Figure 2.10 (C) with the additional sulfur atoms attached on both sides of the bridge. These bridge molecules were optimized with attached proton on it and deprotonated before imported in the Virtual Nano-Lab (VNL) software program to construct the device configuration.

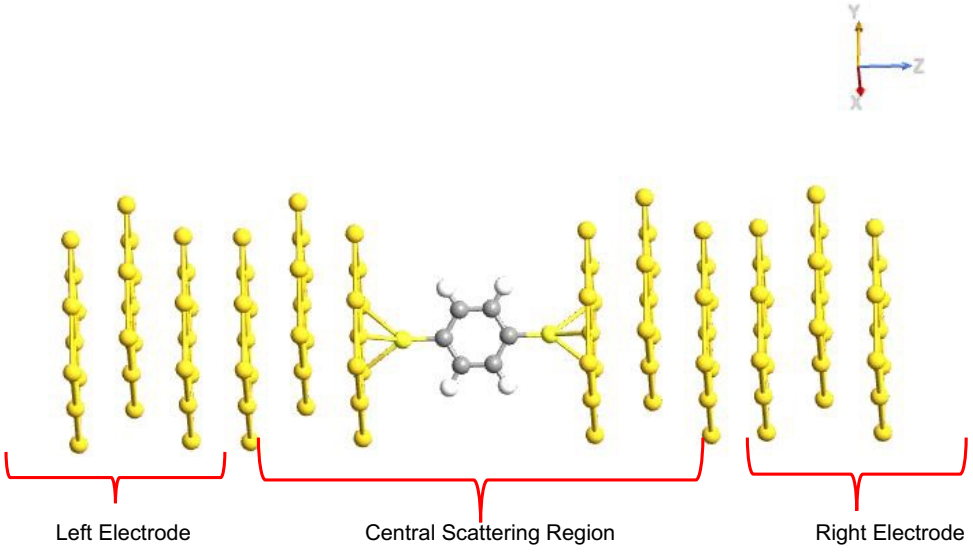

Figure 2.14: Device Configuration of the Au-S-phenylene-S-Au construct used for further transport calculation. Left electrode, central scattering region (includes central molecule and some of the gold electrodes in both sides of the electrodes) and right electrodes are labelled to understand the terms used in the results analysis. The central molecule is symmetric on both sides of the electrodes, so it behaves as a molecular wire.

These transport calculations in Au-B-Au device configurations are performed at the SCF level and the computational results are explained in terms of the Landauer-Buttiker formula as shown in equation (2.16). There is significant difference between the contributing orbitals in conductance and the magnetic exchange couplings, where conductance is dominantly contributed to by the bridge HOMOs, and magnetic exchange is primarily based on the bridge LUMO contributions. From the calculation we can see that the MPSH (Molecular projected self-consisted Hamiltonian) HOMO state is the dominant contributor, since it is in the bias window (light pink highlighted area) where $\Delta E_{\text{Gap}} = V_{\text{bias}}$. The LUMO MPSH state is higher in energy, so it remains out of the bias window under applied bias, consequently it doesn't contribute to the transmission function or g_{mb}.

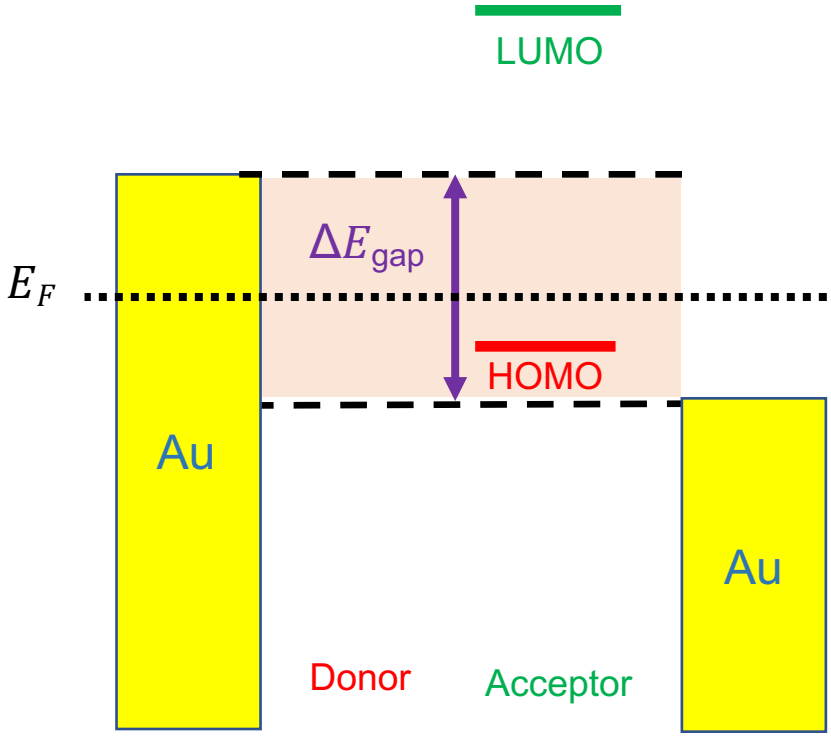

Figure 2.15 : Illustration of HOMO contribution in the conductance mechanism. The bias Au(yellow) electrodes are filled to the chemical potential of the electrodes. The variable bias window is highlighted in light pink color where $\Delta E_{Gap} = V_{bias}$.

The contribution of orbitals on the conductance is detailed in

Figure 2.16, which is the zero bias transmission function vs energy plot for the Au-Th-Au construct. The transmission peak at -0.46 eV is dominantly in the bias window when we increase the applied bias voltage to 2 V, so it is the major contributing peak for g_{mb}. This peak is comprised of 70% MPSH HOMO as shown in

Figure 2.16, and this is determined from the projection calculation. This is primarily comprised of the thiophene bridge molecular HOMO. This tells us that the molecular HOMO is effectively pinned to the electrode.[8 69 39] It is very close to the Fermi level of Au-Th-Au in

Figure 2.16. From the observation of the MPSH state we have plotted from the transport calculation, and the bridge molecular orbitals (covalently connected to the spin bearing units SQ and NN via bridgehead carbon atom, (

Figure 2.16) we concluded that the sulfur p-orbital contribution is responsible for the differences in the magnetic exchange coupling and the conductance through the same bridge fragment.

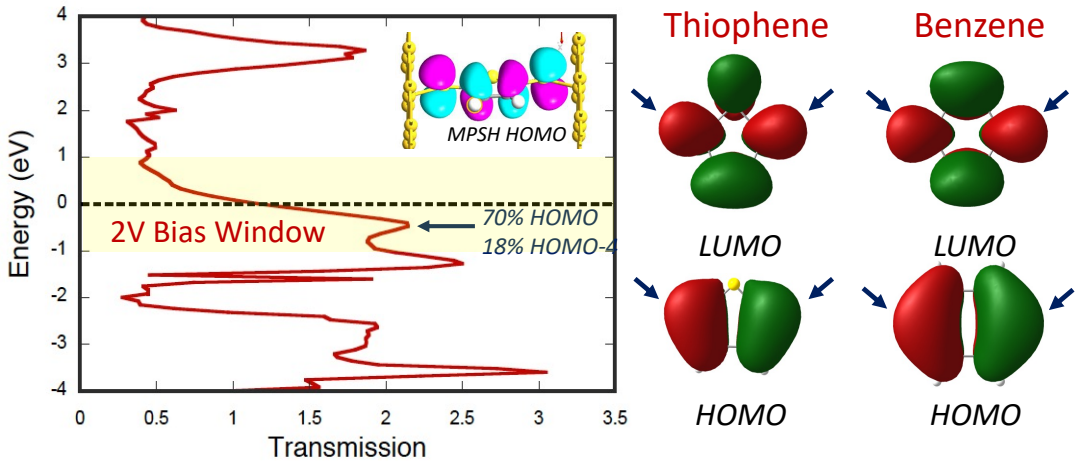

Figure 2.16: Transmission function calculated at zero bias of [M-Ph-M] with calculated percentage contribution of individual PMSH states for these transmission channel (left). Yellow region is defined as bias window of 2V at applied bias of ±2 V. Frontier molecular orbital (HOMOs and LUMOs) generated from optimized geometry of ground electronic states for thiophene and benzene ring respectively middle and right most. Arrows are pointing the connecting points of bridge fragments to the gold electrodes in conductance calculation in electrode molecule electrode constructs.

Orbital coefficient contributions to the conductance has been studied by Beratan,[70] and Yoshizawa and co-workers[71 72] by relating to the zero[th] order Green's function for the bridge $[G_B^0(E_F)\sim\overline{G_B})]$ to the molecular orbital coefficients of the bridge orbitals, Fermi energy, and the individual molecular orbital energy levels as shown in equation (2.18) below.

$$G_B^0(E_F) = \sum_K \frac{C_{rk} C_{sk}^*}{E_F - \varepsilon_K \pm i\eta} \tag{2.48}$$

Here, the C_{rk} and C_{sk}^* = molecular coefficients for the sulfur atoms added on the left and right side of the bridge molecule. The connectivity of the sulfur atom is the same as the carbon atom of the bridge molecule connected to the SQ-donor and NN-acceptor moieties in SQ-B-NN biradical complexes. As explained before with reference to Figure 2.16, the sulfur p-orbital contribution on the MPSH state is of great significance in conductance. The sulfur p-orbital allows the proper delocalization of the bridge wavefunction in the scattering region.[72] To understand the orbital contribution to conductance, we have considered the HOMO-only orbital and we rewrite the conductance as in equation 2.19.

$$G_B^0(E_F) = \sum_K \frac{C_{rHOMO} C_{sHOMO}^*}{E_F - \varepsilon_{HOMO} \pm i\eta} \tag{2.49}$$

Equation (2.19) aligns with our predictions on the importance of the sulfur atom in conductance, since the HOMO is the dominant wavefunction in conductance, and the bridge LUMO is the dominant contributor to the magnetic exchange couplings.

The computed value of conductance and the experimentally observed magnetic exchange coupling values for both monomeric and dimeric bridge fragments are fit with power law expression given by following equation (2.20),

$$g_{mb} = a \bullet (c * J^0_{D\rightarrow A})^{\gamma} \quad (2.50)$$

Here, $J^0_{D\rightarrow A}$ is the magnetic exchange parameter for SQ-NN without a bridge fragment (+550 cm^{-1}).[18 20] Based on the best fitting of the data to the power law expression, we obtain values of a = 2012 and γ = 0.675. Observing (Figure 2.17), one can clearly see that there is no linear relationship between magnetic exchange and conductance. Instead, there is a different functional relationship. Another noticeable variation is that monomeric and dimeric bridge units have not fallen on the same curve. The fit to the data has indicated a scale invariance, which relates $J_{D\rightarrow A}$ and g_{mb} (c = 1 for monomeric and c = 0.28 for dimeric bridges). Thus, magnetic exchange and conductance data sets for the monomeric and dimeric bridges are correlated by a proportionate scaling factor of the exchange interaction ($J_{D\rightarrow A}$) and they don't normally follow the proportionality relation as explained by this expression, $J_{D\rightarrow A} \propto H_{D\rightarrow A}{}^2 \propto g_{mb}$ across a series of monomeric and dimeric bridge units.

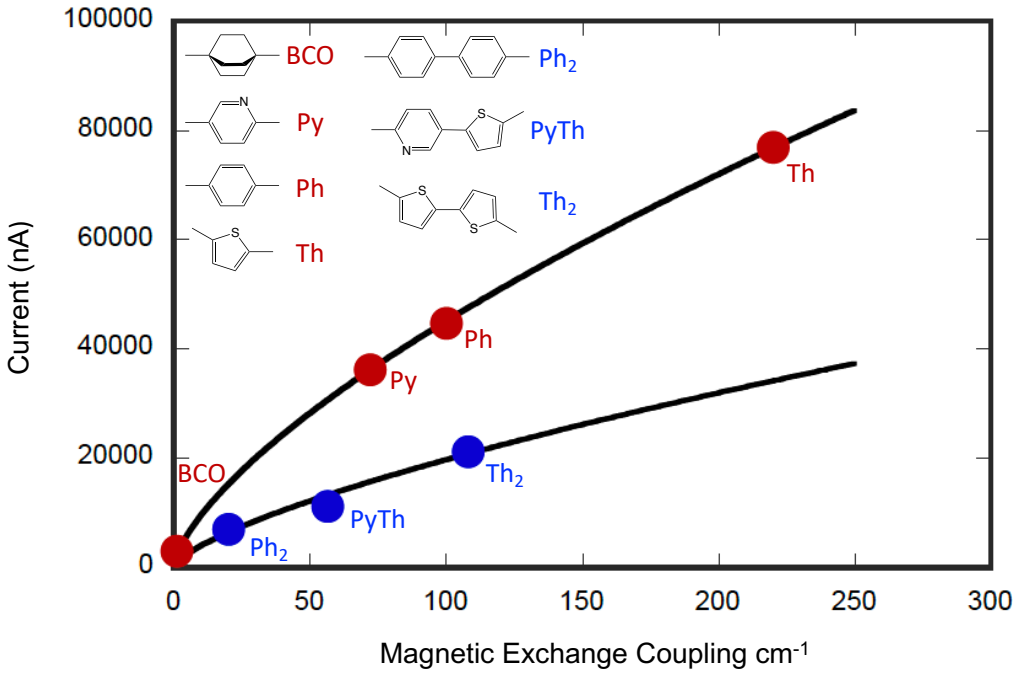

Figure 2.17: Computed current vs experimentally measured exchange coupling of the monomeric (red sphere) and dimeric (blue sphere). The data have been fitted to separate empirical power law functions with similar exponents. Best fit in the plot are shown in black solid lines. Conductance calculation was performed by applying the bias voltage of 2 V which approximates the intra-ligand charge transfer energy in SQ-Bridge-NN complexes.

The computed value of current (nA) as a function of magnetic exchange coupling for thiophene and phenylene bridges (both monomeric and dimeric) have been plotted and fit according to equation (2.21) in Figure 2.18.

$$g_{mb} = \left[g_{L=0} \bullet (J^{0}_{D\to A})^{-\beta_g/\beta_J}\right] \bullet (J_{D\to A})^{\beta_g/\beta_J} \qquad (2.51)$$

It is necessary to fit equation 2.21 to the data in order to completely understand the distance decay constant for conductance (β_g) and the exchange coupling (β_J). After fitting equation (2.21) to the data, g_{mb} and $J_{\mathrm{D}\to\mathrm{A}}$, β_g/β_J = 1.15 for the phenylene bridge series and β_g/β_J = 1.58 for the thiophene bridge series were determined. A non-linear

relationship between the heterogeneous electron transfer rate constant (k_{ET}) and the conductance (g) was also observed by Beratan and Waldeck[73] [53] but there is a key difference between their work and what we have observed. Their study has shown β_g/β_{ET} < 1 for the series of alkanethiol and peptide nucleic acid oligomer bridges, concluding that the decay of the electron transfer is more rapid with increasing the distance compared to the conductance. From the power law function fit of the equations to our data, our observation is that the conductance is decaying faster than the magnetic exchange coupling ($\beta_g/\beta_J > 1$), which is an opposite correlation to their findings.

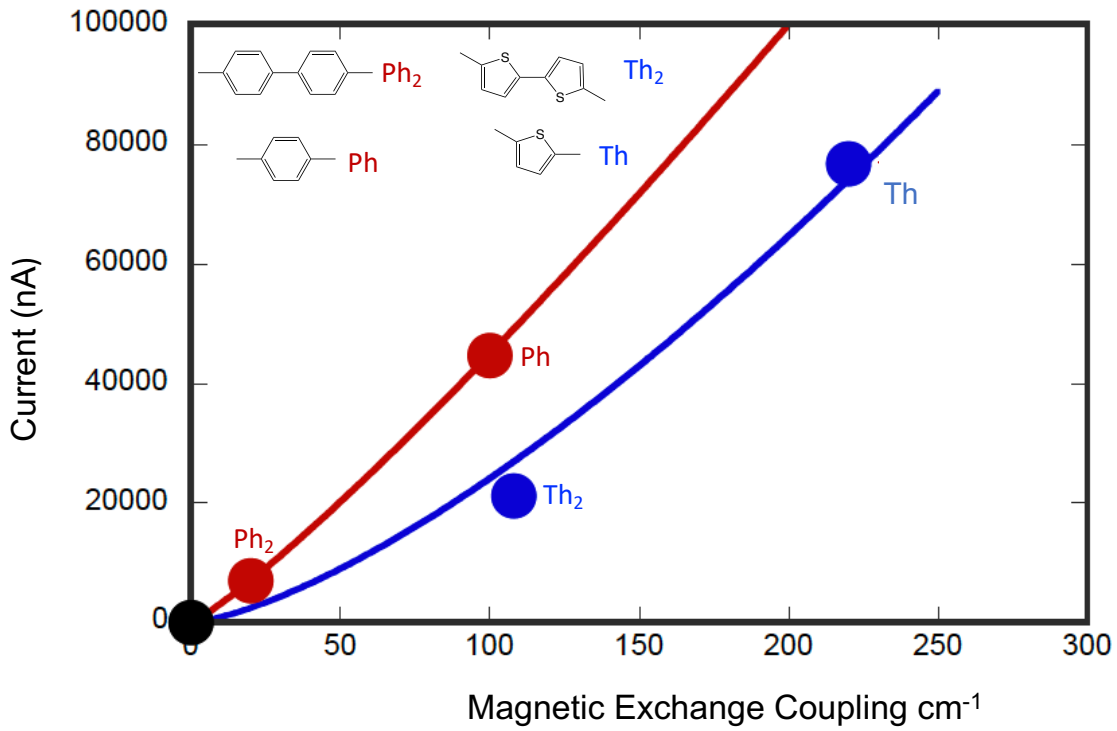

Figure 2.18: Computed value of current (nA) calculated at +2V applied bias voltage and exchange coupling (cm^{-1}) for the phenylene bridges (red circles) and thiophene (blue circles). The fit to the equation has shown by the red(phenylene) and blue(thiophene) lines. The conductance has calculated by using Landauer-Buttiker formalism which relates transmission to the probabilities of conductance (g_{mb} = I/V).

The observed differences in the correlation between conductance and exchange coupling in cases of thiophene and phenylene bridges must be explained based on the equation 2.22.

$$\beta_i = \frac{2}{L}\ln\left(\frac{\Delta\varepsilon}{H_{BB,i}}\right) \tag{2.52}$$

In the above equation, β_i = exponential decay constants, $\Delta\varepsilon$ = tunneling energy gap, H_{BB} = bridge-bridge electronic coupling and L = length of the bridge unit. Equation 2.22 describes the relationship between the exponential decay constants to the inherent differences in the tunneling energy gaps, bridge-bridge electronic coupling and the length of the bridge units.[74 75] $\Delta\varepsilon$ is the energy required to remove one electron from the donor (anode) to the bridge LUMO or promotion of a hole from the acceptor (cathode) to the bridge HOMO. The distance between donor and acceptor (or electrodes) is given by R_{DA} ($R_{DA} = R_0 + nL$). So, having a large value of H_{BB} and small $\Delta\varepsilon$ results in lower β-values that promote the long range magnetic super exchange coupling and conductance.

$$\Delta E_{eff} = \left(\frac{\hbar^2}{8m_e}\right)\beta^2 = \left(0.952\ eV\ \text{Å}^2\right)\beta^2 \tag{2.53}$$

An additional observation was the deviation of the ratio between the decay constants of conductance and the electron transfer (β_g/β_{ET}) from unity as noted in the Beratan and Waldeck work. They explained this deviation as being due to the differences in the following three things: charge transfer energy barrier in the D-B-A constructs, electron transport in Au-B-Au configurations, and the bath-induced decoherences on the

bridge molecule and bridge-bridge electronic coupling (H_{BB})[73 53]. The differences in the effective barrier heights for conductance values and the electron transfer rate constants are derived from the dissimilarity between the work function of the metal in the Au-B-Au device and donor-acceptor redox potential in D-B-A complexes.[73 53] By considering the decay constant for conductance and electron transfer which are acquired by the different values of $\Delta\varepsilon$. $\Delta\varepsilon$ and H_{BB} are highly correlated to each other, so it is hard to evaluate their contributions on $E\Delta_{eff}$ separately.[76]

In our D-B-A systems, as we performed the experimental measurements in the solid state and the computational calculations were performed with a known geometry. Thus, the decoherence effects to deviate the β_g/β_J from linearity is negligible on the conductance and exchange coupling correlation. We should certainly consider H_{BB} and $\Delta\varepsilon$. $\Delta\varepsilon$, in our D-B-A complexes has been approximated as the ILCT energy. Based on experimental data using room temperature electron absorption spectroscopy, the ILCT transition energy increases with increasing the number of bridge units in SQ-Ph-NN to SQ-Ph_2-NN. In the case of SQ-Th-NN to SQ-Th_2-NN we observed the opposite trend.[55] The observed differences are not only limited to the distance decay constant (β_J) for exchange coupling in SQ-$(Ph)_n$-NN and SQ-$(Th)_n$-NN complexes, since we also see the differences in the $E\Delta_{eff}$ for the conductance and the magnetic exchange coupling.

Table 2.6: Experimentally observed and calculated values of decay constants, barrier heights, tunneling energy gaps and bridge coupling ratios comparison.

Compound/device	Parameter	Value
Au-Ph_n-Au	β_g ΔE_{eff} $\Delta\varepsilon_g/H_{BB,g}$	0.45 $Å^{-1}$ 1555 cm^{-1} 2.63 (>$\Delta\varepsilon_J/H_{BB,J}$)
SQ-Ph_n-NN[17]	β_J ΔE_{eff} $\Delta\varepsilon_J/H_{BB,J}$	0.39 $Å^{-1}$ 1168 cm^{-1} 2.31

Au-Th$_n$-Au	β_g ΔE_{eff} $\Delta\varepsilon_g/H_{\text{BB},g}$	0.35 Å^{-1} 941 cm^{-1} 1.79 (>$\Delta\varepsilon_J/H_{\text{BB,J}}$)
SQ-Th$_n$-NN[17]	β_{J} ΔE_{eff} $\Delta\varepsilon_{\text{J}}/H_{\text{BB,J}}$	0.22 Å^{-1} 372 cm^{-1} 1.53

{Data was calculated using the distance (R_0) from the X-ray crystal structures of SQ-(bridge)$_n$-NN with a single bond distance included = 4.30 Å (Ph) and 3.87 Å (Th). Exchange coupling values are taken from the previously published work. The calculated values are consistent with $H_{\text{BB, J}} > H_{\text{BB, }g}$ and/or $\Delta\varepsilon_g > \Delta\varepsilon_{\text{J}}$}

Our previous work has used magnetic exchange coupling values to calculate ΔE_{eff} for SQ-bridge-NN systems.[55] It was found that the ΔE_{eff} = 1172 cm^{-1} for Ph and 373 cm^{-1} for Thp bridges. We have calculated the conductance barrier heights ΔE_{eff} = 1555 cm^{-1} and 941 cm^{-1} for phenylene and thiophene by using the known value of β_g/β_{J} ratios. The result has shown the decrease in the ΔE_{eff} of magnetic exchange coupling value compared to the conductance for same bridge molecules, a reduction of ~25% for phenylenes and ~60% for the thiophenes.

The β_{J} values are determined from magnetic susceptibility experiments as β_{J} = 0.39 Å^{-1} for phenylene series and β_{J} = 0.22 Å^{-1} for thiophene series and are being used to calculate the distance decay constant for the conductance through the same bridge fragments as in Table 2.1. The value for the distance decay constant for conductance for para-phenylene bridges (β_g = 0.45 Å^{-1}) is in significantly good agreement with the value evaluated by using atomic force microscopy on oligo (para-phenylene)-monothiols suspended between the metals[59]. Similarly, the decay constant for conductance through

thiophene (β_g = 0.35 Å^{-1}) is also in very good agreement with the conductance studies performed on thiophene bridges with one, two, three or five units (β_g = 0.29 Å^{-1}).[73]

2.3.4.4 Magnetic Exchange and Conductance: Resonance Structures

Distance decay constants (β_i) and effective barrier heights ΔE_{eff} are correlated to H_{BB} and the nature of the bridge frontier orbitals that mediates exchange coupling and conductance and ultimately these factors affect the magnitude of the distance decay constants. It has been assumed that H_{BB} in electron transfer/transport and magnetic exchange are analogous. Resonance structures are a useful tool to understand the electronic contributions to the distance decay constants, which explains the excited state configurations that mix with the ground state configuration within a valence bond description.[67 77 78 79 80] Figure 2.*19* exhibits the resonance structure of the SQ-Ph_2-NN complex, which explains the charge and spin density distribution of the ground state configuration (GC) and excited state configurations (ECs). Quinoidal resonance structures in (EC1) and (EC3) provide enhanced bridge-bridge coupling (H_{BB}) because of increased $\pi - \pi$ interactions between two phenyl rings. Resonance structure contributions from all excited states (EC1-EC4) contribute to increased magnetic exchange coupling in SQ-Bridge-NN biradicals. This sums the combinations of B-B, D-B and B-A electronic couplings. The orbital contributions when the bridge fragments are connected to the electrodes ($|\overline{G_B}|, \Gamma_{LB,}\, \Gamma_{RB}$) are different. This difference has been associated with the difficulty of drawing the resonance structure of S-Ph-Ph-S electrode linkage, which is possible only for high energy zwitterionic and biradical resonance structures. Resonance Raman spectroscopy has been recorded for the SQ-Ph-Ph-NN

biradical complex. It has shown that the low energy ILCT energy state at ~24 000 cm^{-1} admixes with the ground state configuration.[21 67] Once we optically pump the SQ-Bridge-NN biradical complex into ILCT state, we observed phenylene quinoidal stretching vibrations that decrease in intensity with increased SQ-Bridge and Bridge-NN bond torsions. This indicates the effect of increased electronic coupling.[67] In the case of the SQ-Ph-Ph-NN complex, there is a large resonance enhancement of the 1600 cm^{-1} quinoidal stretch after pumping into the SQ ⟶ Ph-NN ILCT band (Figure 2.19). An electron density difference map (EDDM) has shown the nature of electron transfer from red donor to the blue acceptor region of the complex. The contribution from quinoidal structures in SQ-Ph_2-NN is comparable to that of SQ-Ph-NN biradical complex studied previously[21 34], thus indicating the quinoidal structure contribution on the ground state wavefunction.

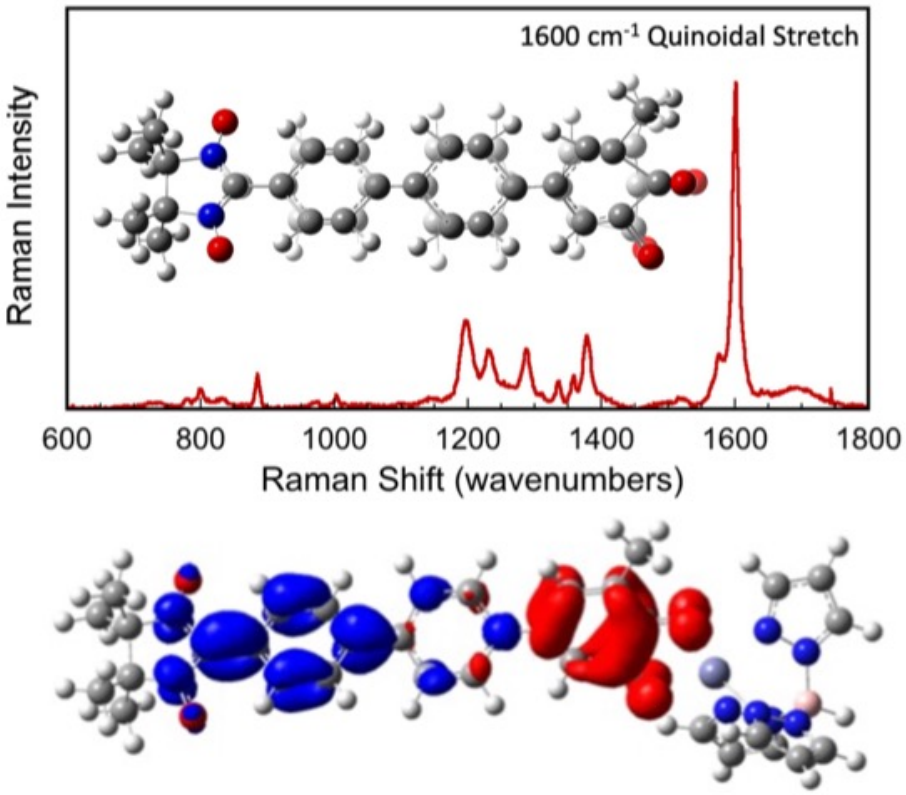

Figure 2.19: Resonance Raman enhancement pattern of SQ-Ph_2-NN biradical di-bridge collected in solid sample (top) and electron difference density map (EDDM) generated from the optimized geometry and performing TD-DFT calculation (bottom). Blue colored portion of the complex is depicting orbital accepting the electron density and the red color is indicating the portion of the molecule losing the electron density.

2.3.5 Conclusion

Our work here has explicitly explained the relationship between the experimentally determined magnetic exchange and the conductance calculated by using the same bridge fragments. The nonlinear ($\beta_g/\beta_J \neq 1$) functional relationship between magnetic exchange coupling and conductance has been developed. The plots of $J_{D\to A}\, vs. g_{mb}$ for monomeric and dimeric bridges lie on different curves due to the scale invariance among the different bridges. The distance decay constants have been calculated as $\beta_g/\beta_J = 1.15$ for the

phenylene series and $\beta_g/\beta_J = 1.58$ for thiophene series. These values are in good agreement with the recently reported value in literature for oligophenylene and oligothiophene.[73] [81]. The distance decay ratio of conductance and magnetic exchange coupling has been utilized to calculate the conductance barrier tunneling heights for oligo-phenylene ($\Delta_{\mathrm{eff}} = 1555\ \mathrm{cm}^{-1}$) and for oligothiophene ($\Delta_{\mathrm{eff}} = 941\ \mathrm{cm}^{-1}$) that span electrodes in a transport geometry. This effectively translates to a reduced effective barrier height (Δ_{eff}) of ~25% in magnetic exchange coupling for phenylenes and ~60% for thiophenes, compared to the conductance value with same bridge fragments. More noticeable nonlinearity in thiophene plot of $J_{D\to A}\ vs.\ g_{mb}$ compared to phenylene series is explained by the calculated value of tunneling gaps and bridge-bridge electronic coupling from experimental data. There is another indication from resonance Raman spectroscopy data that bridge-bridge electronic coupling may be increased by quinoidal resonance structure contributions in SQ-Bridge-NN biradicals compared to Au-B-Au constructs for conductance calculation. We have explained that a greater contribution is expected from ECs for biphenylene bridge than bithiophene bridge in Au_n-S-Bridge-S-Au_n constructs. Enhancement of resonance a Raman peak for the bridge quinoidal stretching mode indicates the major bridge distortion corresponds to higher bridge-bridge electronic coupling. The magnitude of the bridge distortion is proportional to the SQ ⟶ B-NN charge transfer that contributes to the measured magnetic exchange coupling value in SQ-Bridge-NN biradicals. Based on valence bond and resonance perspectives, the contribution of respective EC resonance structures precisely depicts the distribution of spin and charge of low lying ILCT excited states in SQ-Bridge-NN. In Au-Bridge-Au construct, the corresponding quinoidal bridge containing excited states lie at very high

energy. Aromaticity has been reported to have an effect on reducing the conductance in single molecule junctions.[73] Quinoidal resonance structures shown in Figure 2.*19* results in reducing the aromaticity of the bridge fragments, contributing more to its magnetic exchange value compared to conductance. Consequently, this results in $\gamma \neq 1$ and $\beta_g/\beta_J > 1$ for the molecular bridge fragments we have used in this study.

2.4 Transition Metal as a Decoupling Unit: A Study on Donor-Acceptor Pt(II) Complexes as Single Molecule Rectifier.

2.4.1 Introduction

Among the transition metal complexes, square planar complexes of Pt(II) are among the earliest studied complexes for their luminescence properties.[82] Square-planar complexes of Pt(II) coordinated by two different unsaturated ligands; dichalcogenolenes as donor ligand (easily oxidizable) and diamine as acceptor ligand (easily reduceable) are being focused on by researchers because of their spectroscopically rich photophysical properties and their significant photoluminescent features. They have potential applications in light energy conversion schemes, nonlinear optics[25] and in light driven information devices.[83] [84] [85] [86] [87] [88] [89] [87] [90] The importance of Pt(II) complexes have been associated with the flexible d^8 configuration, and the presence of low energy ligand-to-ligand charge transfer transitions.[25]

Another facet of ongoing research on transition metal complexes is their potential use in molecular electronics.[91] [92] [93] Transition metals have been studied for their use with organic compounds in molecular electronics by different research groups. First row transition metals Ni and Cu have been reported to break the symmetry of Ru based

molecules, and it is useful to understand the functional relationship between transition metals in molecular rectifier designs [$Ru_2Ni/Cu(dpa)_4(NCS)_2$].[94] Weng and co-workers have shown that breaking the symmetry physically is not enough to have a high RR, as concluded by a lower calculated RR from an asymmetric molecular bridge.[94] Encapsulation of Pt(II) metal by the ligand prevents unnecessary reactions with the surrounding atmosphere in the molecular metal clusters. This was designed to explore by break-junction experimental techniques.[93] Matsuura used a computational approach by using non-equilibrium Green's function (NEFG) with density functional theory (DFT) to explore the rectification and transport property of Fe-Fe and Fe-Ni bi-metallocene systems.[92] The idea of using two different metals in bi-metallocenes in Matsuura's work is to achieve asymmetry in the system. As expected, the IV curve is asymmetric in the case of the Fe-Ni system, suggesting that it could function as a rectifier.[92] The most recent studies have used transition metals (Fe, Co, Cr, Mn, Cu) in combination to create a self-assembled monolayer (SAM) to get better RRs.[95] Transport properties and the rectification mechanism of Group VIII transition metals have been studied in porphyrazine-metal di-nuclear complexes (Ru-Ru, Ru-Fe and Ru-Os) by using a computational approach with a simplified NEGF-DFT technique.[96] In the above study, the purpose of using three different metals in a molecular rectifier system is to create the asymmetry between the right and left part of the molecule to get an asymmetric I-V curve for these bimetallic systems. The calculated RR difference reported by Barone and co-workers is small (~1.2) in these systems.[96] Based on the literature reviews, a common approach of using transition metals in the single molecular rectifiers is taken by many researchers to break the π- conjugation between two coupled units.

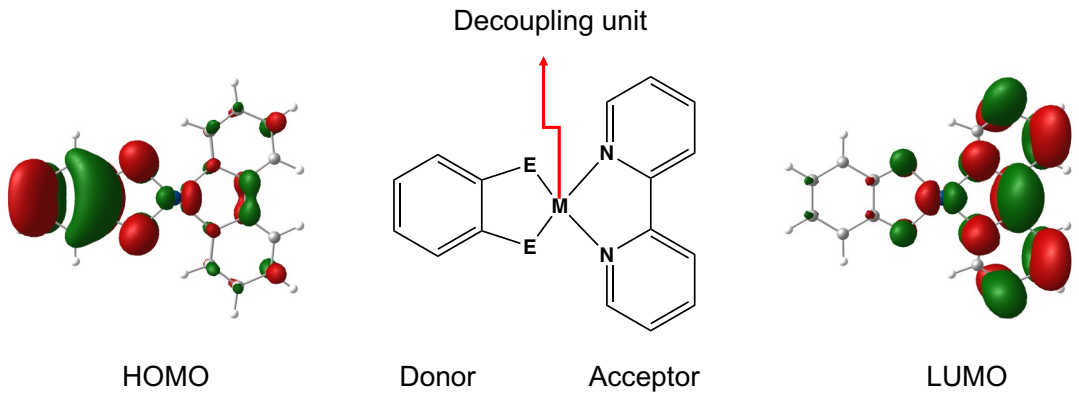

Figure 2.20: Bond line drawings of dichalcogenolenes Pt(II) Diimine complex (Centre), wavefunctions of Highest Occupied Molecular Orbital (HOMO; left) and Lowest Unoccupied Molecular Orbitals (LUMO; right).

We have studied the single molecule rectifying properties of the Group X transition metals (Ni, Pd, Pt) complexes with catecholate as the donor component, and a diimine as the acceptor component. The purpose of choosing these transition metal complexes is based on the electronic structure calculation results which are shown in Figure 2.***20***, where the frontier orbital wavefunctions are decidedly localized on the donor and acceptor portions of the molecule. Thus, these transition metals could function as a decoupler between donor and acceptor fragments, and must contribute to rectification to some extent .[8] Baranger and coworkers have studied this using a computational method to explore yet another important role of transition metals. Along with creating the asymmetry in the single molecule diode, the transition metal can lower the HOMO-LUMO gap of the molecule as the d-orbital has a higher energy level than the π-orbital of organic donor and acceptor components.[97] The D-M-A molecule is covalently connected to the gold electrodes, and the molecular energy level of the organometallic molecule should stay close to the chemical potential of the electrodes.[97] This results in the small energy difference between the Fermi level of the electrodes and the conducting frontier molecular

orbitals. In this type of system, the transport channels stay out of the bias window (the chemical potential difference of the electrodes under bias)[97] with reverse bias and enters the bias window with forward bias potential. This event is occurring with a low applied voltage is one of the most important features for a good candidate for an efficient molecular rectifier.[36] It is hypothesized that the transition metal complexes shown in Figure 2.*21*, which are used in this study, should be excellent candidates for a single molecule diode. This hypothesis has been tested by performing transport calculations using the Atomistic Tool Kit software.

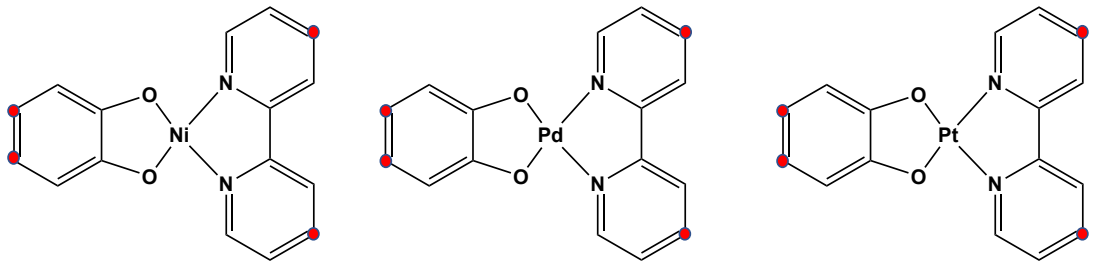

Figure 2.21: Transition metal complexes we considered to study their rectifier properties. Cat-Ni-bpy (left), Cat-Pd-bpy (middle) and Cat-Pt-bpy (right). The points indicated by red circles indicating the position of covalently bonded sulfur atoms before geometry optimization.

2.4.2. Experimental Method

The general method explained in section 2.2.2 for the transport calculation has also been followed here. Particularly for this study, the input file was generated using Gaussian '09[14] and optimized with a 6-31g(d',p') basis set and the B3LYP functional.[98] The geometry of the molecule was generated by adding two sulfur atoms on each side (donor and acceptor ligand) of the molecule Cat-M-bpy with hydrogens attached to it. Then, the molecules are subsequently deprotonated from the optimized geometry and

imported into the Virtual Nano-Lab program to construct a device configuration by covalently connecting sulfur atoms with the semi-infinite gold atoms[92] for further calculation of transport properties.[99] [16] During optimization of the bulk configuration, the central molecule was kept rigid along with both electrodes, allowing optimization of the connection between sulfur atoms and the connecting gold atom bonds. As outlined previously, the same method was employed for calculation of transport properties by using Quantum ATK. The IV curve is calculated at ±2 V applied bias, along with the total transmission spectrum under bias at different bias values. The molecular orbital origin of the resonant peaks within the bias window in the transmission spectrum has been explored by calculating the molecular projected self-consistent Hamiltonian (MPSH) states and comparing them with the eigen channels for corresponding resonant transmission functions.[8] [100]

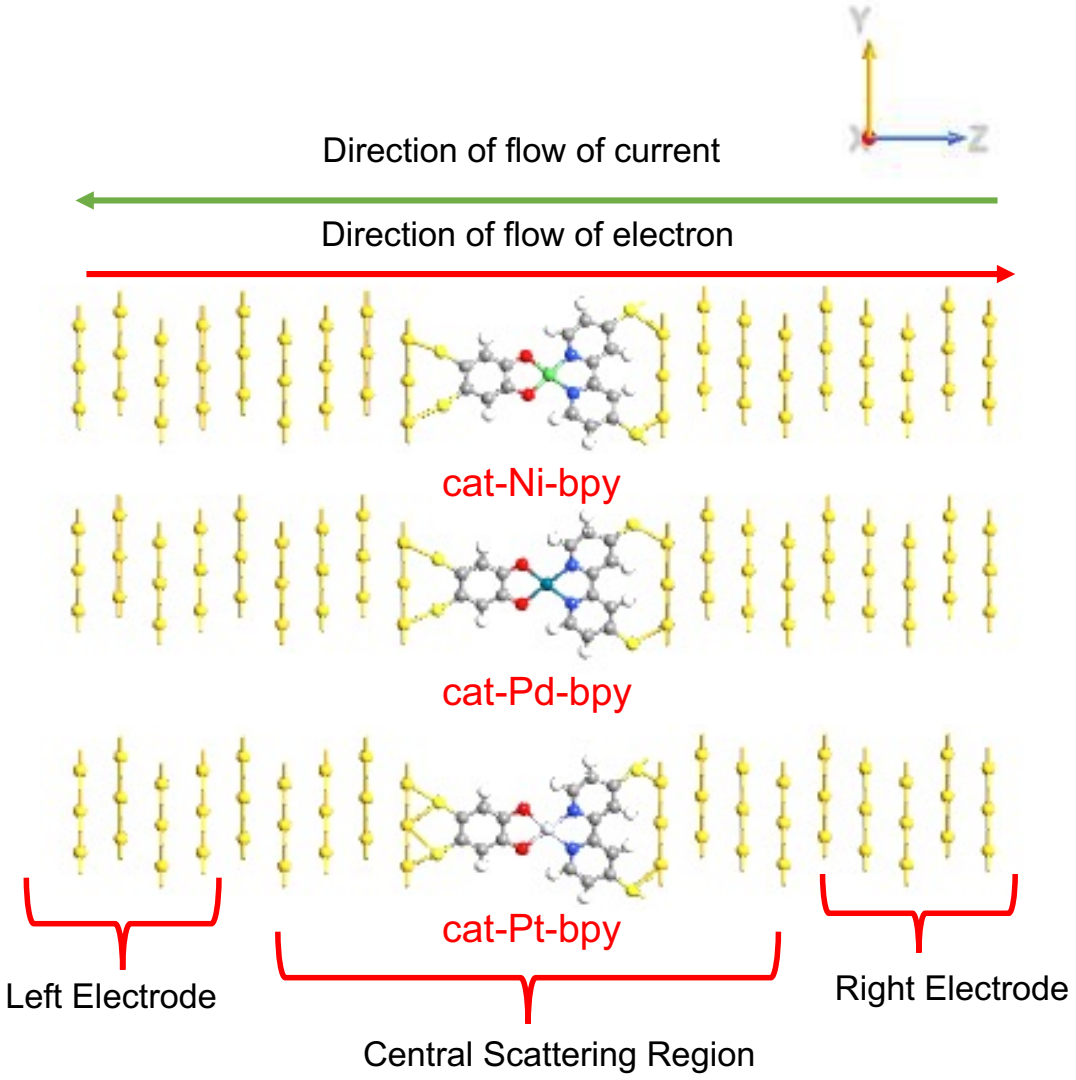

Figure 2.22: Device Configuration converted from the optimized bulk configuration of Cat-Ni-bpy(top), Cat-Pd-bpy(middle) and Cat-Pt-bpy(bottom). The left electrode, right electrode, and central scattering (includes the central molecule and few electrodes of the device as screening) has labelled as designed by the software in the device configuration. The red arrow at the top of the picture shows the preferential direction of electron flow, that is going from donor to the acceptor. The green arrow shows the preferential direction of current in this device configuration.

2.4.3. Results and Discussion

2.4.3.1 IV Curve Analysis and Rectification Ratios

Transport properties are calculated for Au-S-Molecule-S-Au constructs as shown in Figure 2.*22*. The efficiency of electron transport is defined as the conductance (g) which is proportional to the transmission probability of the electrons from left electrode to right electrode[101] based on the Landauer formula in equation 2.16. Figure 2.*23* has shown the calculated current (I) as a function of applied bias voltage (V). The IV curve is obtained by integrating the $T\ (E, V)$, which includes the series of transmission at each bias point and calculates the conductance by integrating the area under the transmission peak within the bias window.[102] The value of current in the negative bias direction is definitively greater than the positive bias direction for all three metal complexes, thus all the molecules exhibit a rectifying property. Cat-Pt-bpy and Cat-Ni-bpy possess a similar amount of current in the positive bias as observed in the IV-curve of Figure 2.*23* (55 μA and 53 μA respectively). So, the preferential direction of conductance is in the negatively biased direction for these complexes. The IV curve is highly symmetric up to the ±0.4 V applied bias which can be explained by the transmission spectrum at that applied bias in both directions as demonstrated in Figure 2.29. No significant transmission peak is found in the transmission spectrum of all three complexes at ±0.4 V. Between −0.4 V and -2.0 V, the current increases smoothly for Ni and Pt complexes, but not for the Cat-Pd-bpy complex (details are explained in later sections). In the reverse bias direction, the current passing through Cat-Pt-bpy and Cat-Pd-bpy are close in value to each other (6 μA and 8 μA respectively). Overall, the IV-curves share similar features in forward and reverse bias directions except for Cat-Pd-bpy. The value of the current has been attenuated after -1.6 V applied bias point as the intensity of the transmission function decreases in Cat-Pd-bpy. The RRs obtained from the IV curve at ±2 V are 3.3, 6.1 and 7.6 respectively for Cat-Ni-

bpy, Cat-Pd-bpy and Cat-Pt-bpy. These values are considered to be relatively higher for the synthetic single molecule rectifier design (a reported value of RR higher than 10 is rare).[8] Inspecting of the IV curve in Figure 2.*23*, the amount of current that has been passed in the negatively biased direction is greater than the positive direction. This is the result of the right electrode having a higher chemical potential than the left electrode. In other words, the preferred direction of current flow is from right electrode to the left electrode. The preferential direction of electron movement is opposite to the current flow, that is from left electrode (catecholate) to right electrode (bipyridine).[10 13] This is in good agreement with the LLCT direction from catecholate HOMO (donor ligand) to bipyridine LUMO (acceptor ligand) in these Cat-M-bpy donor-acceptor complexes (Figure 2.*22*).[25] This is a characteristic feature of an IV curve, and the amount of current passing through each molecule has been interrogated in detail based on further calculated transport properties in these device configuration constructs (Figure 2.*22*). As seen in Figure 2.*24*, both Pt and Pd complexes show the highest RR at ±2 V bias. We have observed a different pattern of rectification for the Ni complex, which has the highest RR at ±1.2 V applied bias (Figure 2.*24* and Table 2.2). In this study, we have explored in detail the mechanism[97] of the observed rectification ratios at different bias points, based on the further analysis of the transport calculations: transmission spectrum, transmission eigen channel, molecular projected self-consistent Hamiltonian (MPSH) state and device density of states (DOS) for each system.[97]

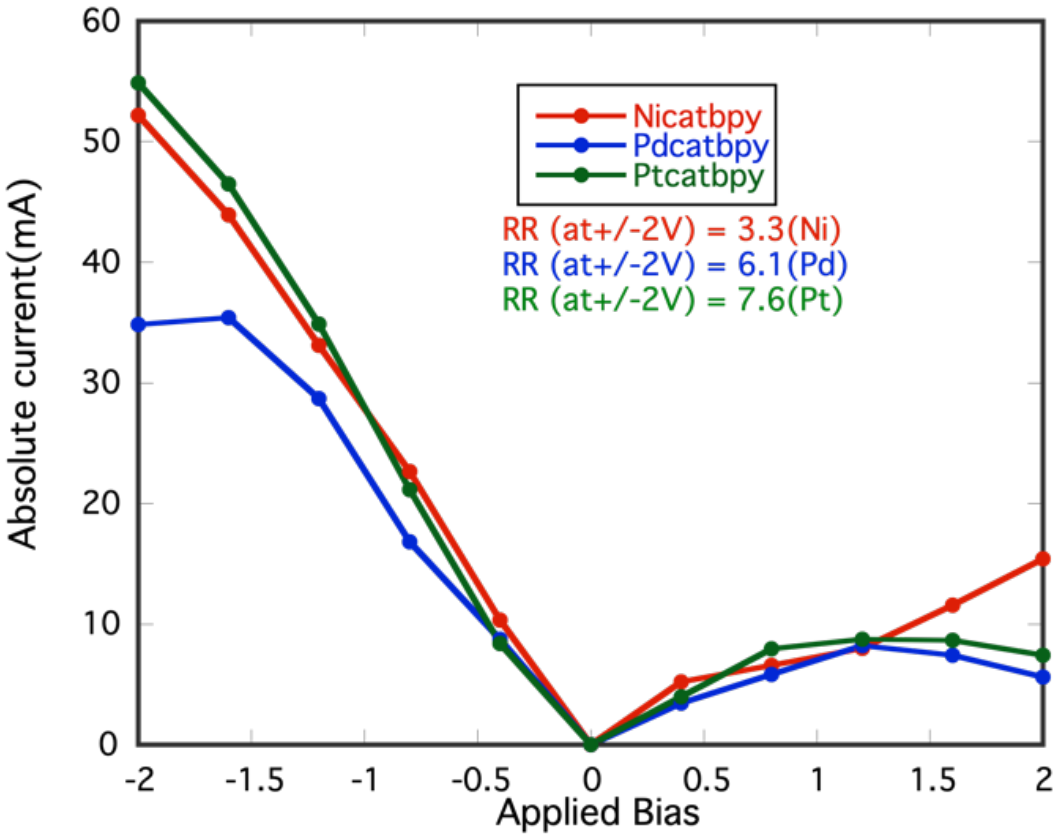

Figure 2.23: IV-curve obtained by integrating T (E, V) with absolute current calculated under an applied bias voltage of ±2 V. Cat-Ni-bpy (red), Cat-Pd-bpy(blue) and Cat-Pt-bpy (green). In set: calculated rectification ratios.

The amount of current passing through the molecule at ±0.4 V applied bias can be understood by analyzing the total transmission spectrum of all three complexes Figure 2.***26***. In all three spectra, there are no noticeable transmission peaks in the bias window (blue colored area in the spectrum).[36] In all cases, there is equal amount of current has passed in both bias directions. This argument is supported by the RR vs applied bias plot in Figure 2.*24* and the values shown in Table 2.2. The RRs at ±0.4 V for all three metal complexes are ~2.[99]

Table 2.7: Table showing the calculated rectification ratios at different applied bias voltage which have been used to calculate the transmission spectrum and the corresponding current at each bias voltage in both forward and reverse bias direction. Cat-Ni-bpy has clearly exhibited highest rectification ratio at ±1.2 V (highlighted in blue) and Cat-Pd-bpy and Cat-Pt-bpy have their maximum rectification ratios at ±2 V bias (the numbers are highlighted in red).

Applied Bias	(cat)Ni(bpy)	(cat)Pd(bpy)	(cat)Pt(bpy)
0 V	0	0	0
±0.4 V	2.1	2.4	2.1
±0.8 V	3.4	2.8	2.6
±1.2 V	4.1	3.5	3.9
±1.6 V	3.7	4.7	5.3
±2 V	3.3	6.2	7.4

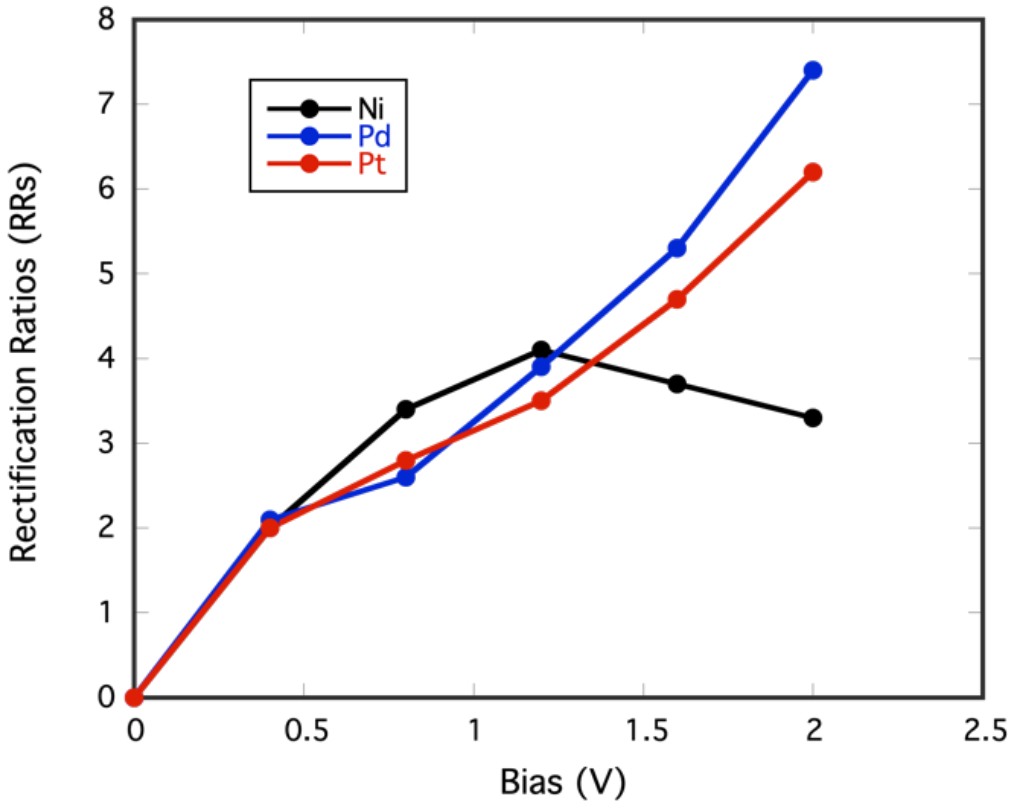

Figure 2.24: Plot of calculated rectification ratios vs applied vias. Cat-Ni-bpy (black line and circle) has clearly exhibited highest rectification ratio at ±1.2 V and Cat-Pd-bpy (blue line and circle) and Cat-Pt-bpy (red line and circle) has their maximum rectification ratios at ±2 V bias.

2.4.3.2 Analysis of Transmission Spectrum

The transmission spectrum presents the transmission probability (T) with the energy of the electrodes. It depends on three voltage dependent parameters as shown by equation (2.9).[46] The transmission probability is proportional to the conductance according to the Landauer formula:[101]

$$G = \frac{2e^2}{h}T$$

Here, $\boldsymbol{e}$ is electron charge, T is total transmission probability, and *h* is Planck's constant. Thus, the conducting capacity of a single molecule connected to the metallic electrodes is achieved by integrating the transmission function within the transmission window.[103] The total current passing through the molecule under applied bias is obtained by using the Landauer-Buttiker theory combined with a Green's function formalism for steady state electron transport as expressed in equation (2.24),

$$I(V) = \frac{2e}{h}\int_{\mu_L}^{\mu_R} T(E,V)dE \qquad (2.54)$$

Here, E is energy, $\boldsymbol{e}$ is the unit of charge, $\mu_{L/R}$ is the electrochemical potential of electrodes under applied bias of V. $T\ (E,V)$ is the transmission function.[104]

Analysis of transmission spectra calculated at equilibrium condition and under different biases demonstrates qualitative, but nonetheless very significant insight into transport properties and RRs.[105] We have studied the calculated transmission spectra of the transition metal complexes of Ni, Pd and Pt under 0 to ±2 V bias to explore the rectification mechanism of conjugate metal complexes decoupled by transition metals.

An overlay of the transmission probability as a function of electron energy at equilibrium is shown in **Error! Reference source not found.**. Two complexes (Pd and P t) share similar features in both positive and negative bias directions.[39]

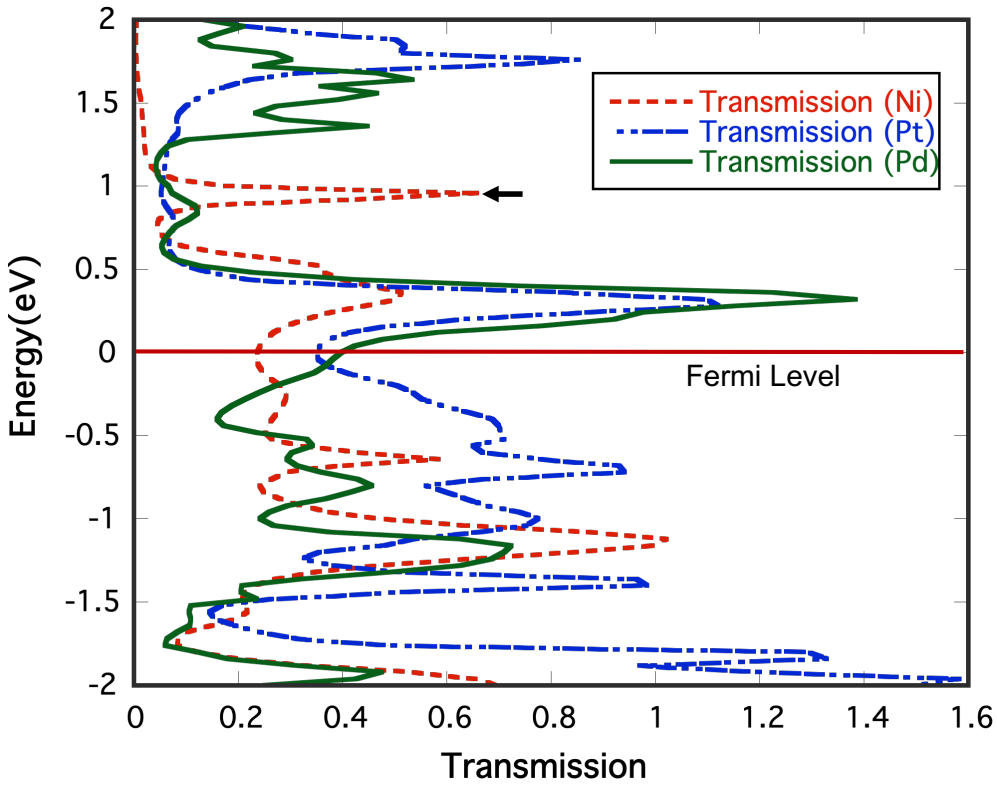

Figure 2.25: Overlay of transmission function at equilibrium for Cat-Ni-bpy (red dot line), Cat-Pd-bpy (green solid line) and Cat-Pt-bpy (blue dot and dash line). Small black arrow is indicating the transmission peak at ~+0.95 eV for all three complexes. Fermi level has indicated by the solid red line.

One common feature shared by all three complexes is the presence of one sharp transmission peak close in energy (~ +0.3 eV) above the electrode Fermi level (Fermi level defined as the energetic halfway point between HOMO and LUMO levels) in all three metal complexes. The dominant contribution to this peak is the MPSH LUMO. Clearly, they are different in the transmission probability value 1.4, 1.15, and 0.5 for Pd, Pt, and

Ni, respectively. The Ni complex shows a reduced but broadened transmission probability peak at this energy, as compared to the Pd and Pt complexes. This is attributed to the delocalized state contributing to that transmission function in the Cat-Ni-bpy system.

Despite being intense in nature with higher transmission probability, they are inconsequential in the current passing through the molecule when bias applied. This is exhibited by the total transmission spectrum in Figure 2.26, an increase of external bias in the positive direction results the moving of these transmission peaks away from the bias window with a diminishing peak intensity from 0 to +2 V bias potential**Error! R eference source not found.**.[104] [106] Thus, these are out of the integration limit for the purpose of calculating current through the complexes. The peaks are contributed to by the molecular LUMOs, which are significantly narrower than the transmission function on the right side of the Fermi level in Figure 2.25. This explains the weak coupling nature of the molecular LUMOs with the electrode in these systems.[107] The nature of the LUMO-contributed transmission peaks is also elaborated further by the transmission spectrum calculated separately at 0 V, +1.2 V and +2 V external bias as seen in Figure 2.28.[46] The dotted arrows indicate the direction of movement of the transmission peaks from the Fermi level.

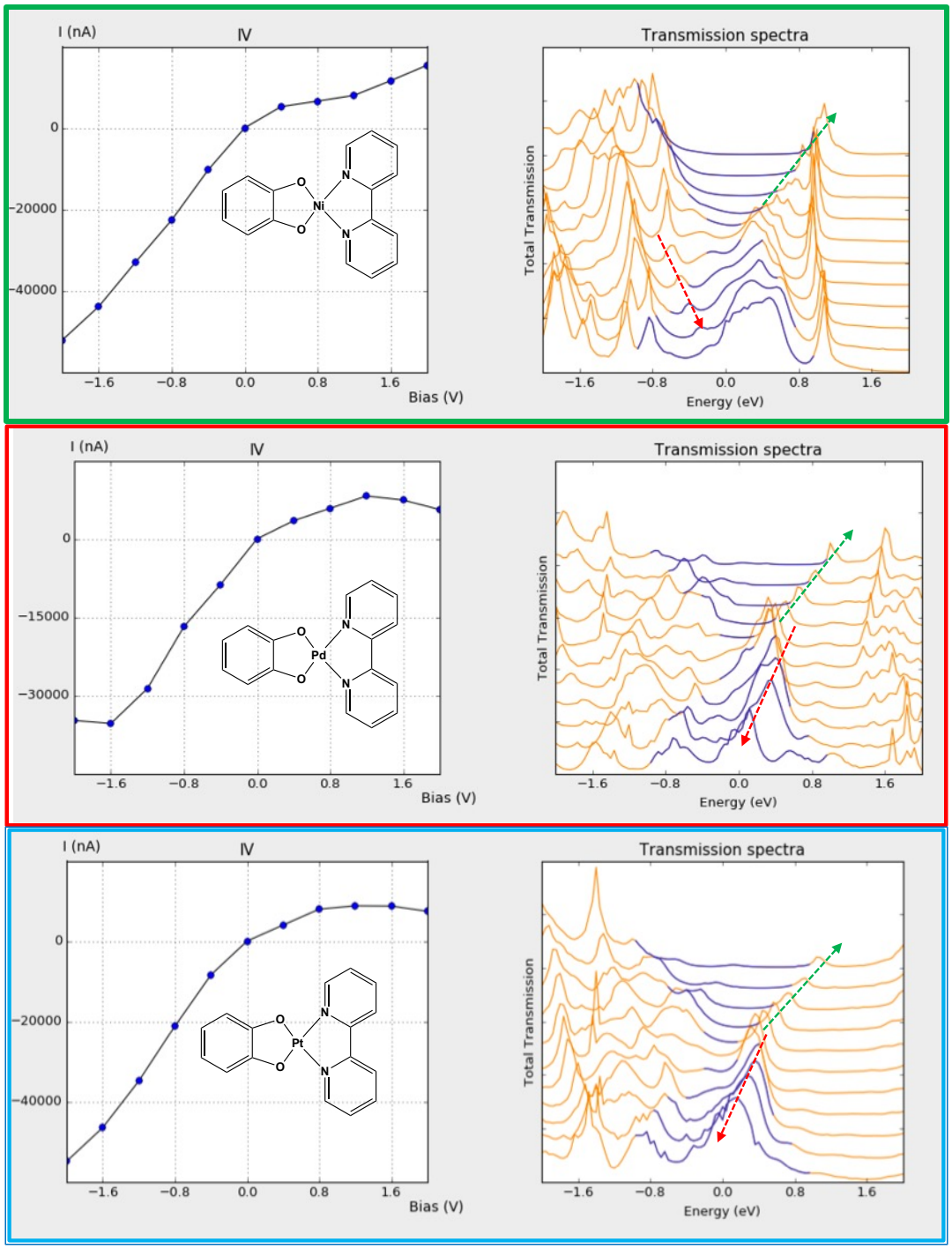

Figure 2.26: Total transmission function calculated ± 2 V applied bias. Current has expressed in nA units. Cat-Ni-bpy; top, Cat-Pd-bpy; middle, and Cat-Pt-bpy; bottom. Dotted green arrow in each case is indicating the increased positive biased voltage and red dotted arrow is for the increasing negative bias voltage. The transmission spectrum is calculated under 0 V, ±0.4 V, ±0.8 V, ±1.2 V, ±1.6 V and ±2 V. Blue area in the total transmission spectrum is bias window, which is defined as the chemical potential

difference between electrodes under an applied bias which opens symmetrically on both sides of the Fermi level.

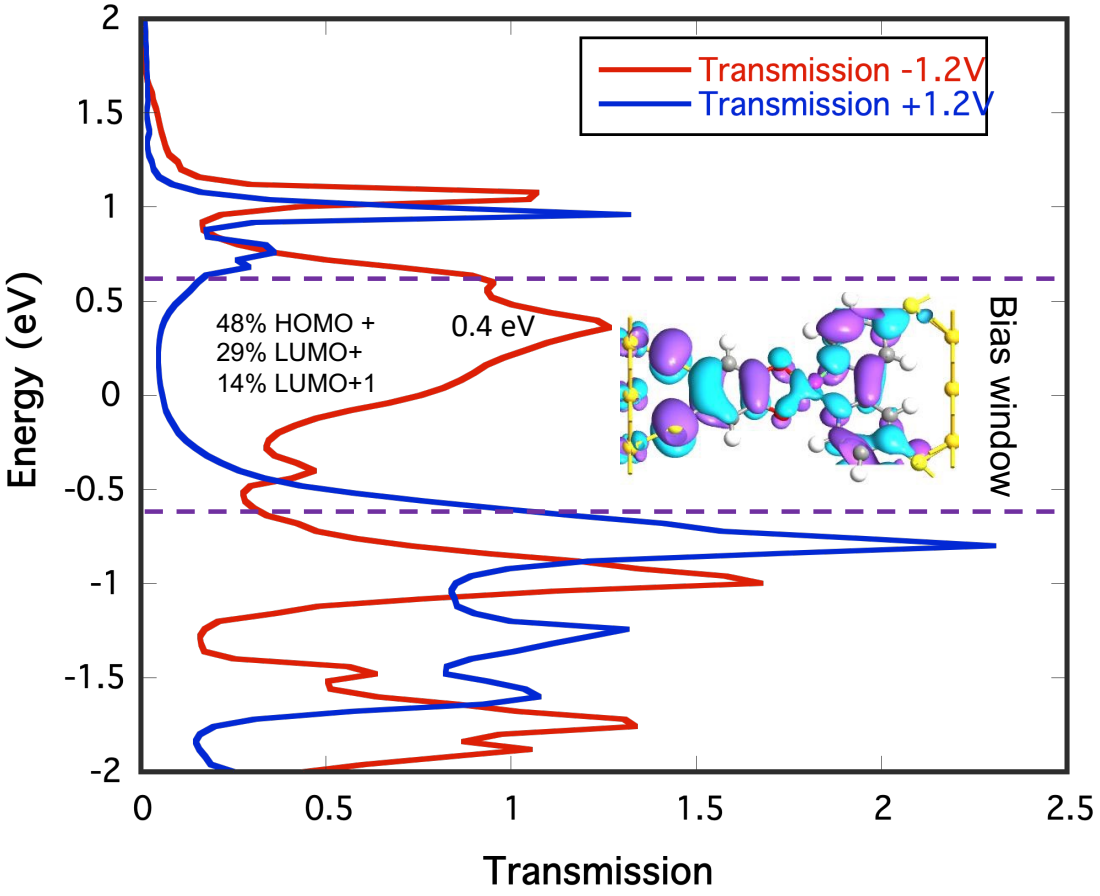

Figure 2.27: Overlay of transmission function calculated at ±1.2 V applied bias. Red spectrum is calculated at +1.2 V and blue spectrum is calculated at -1.2 V reverse and forward bias respectively. In set: contribution percentage of molecular projected self-consistent Hamiltonian (MPSH) state calculated from the projection calculation from the transmission eigen channel at +0.4 eV and the iso-surface plot of the transmission eigen channel at +0.4 eV broad transmission function responsible for the current passing channel at -1.2 V an applied bias. Bias window is defined by the purple-colored dash lines. It has bias window of 1.2 V.

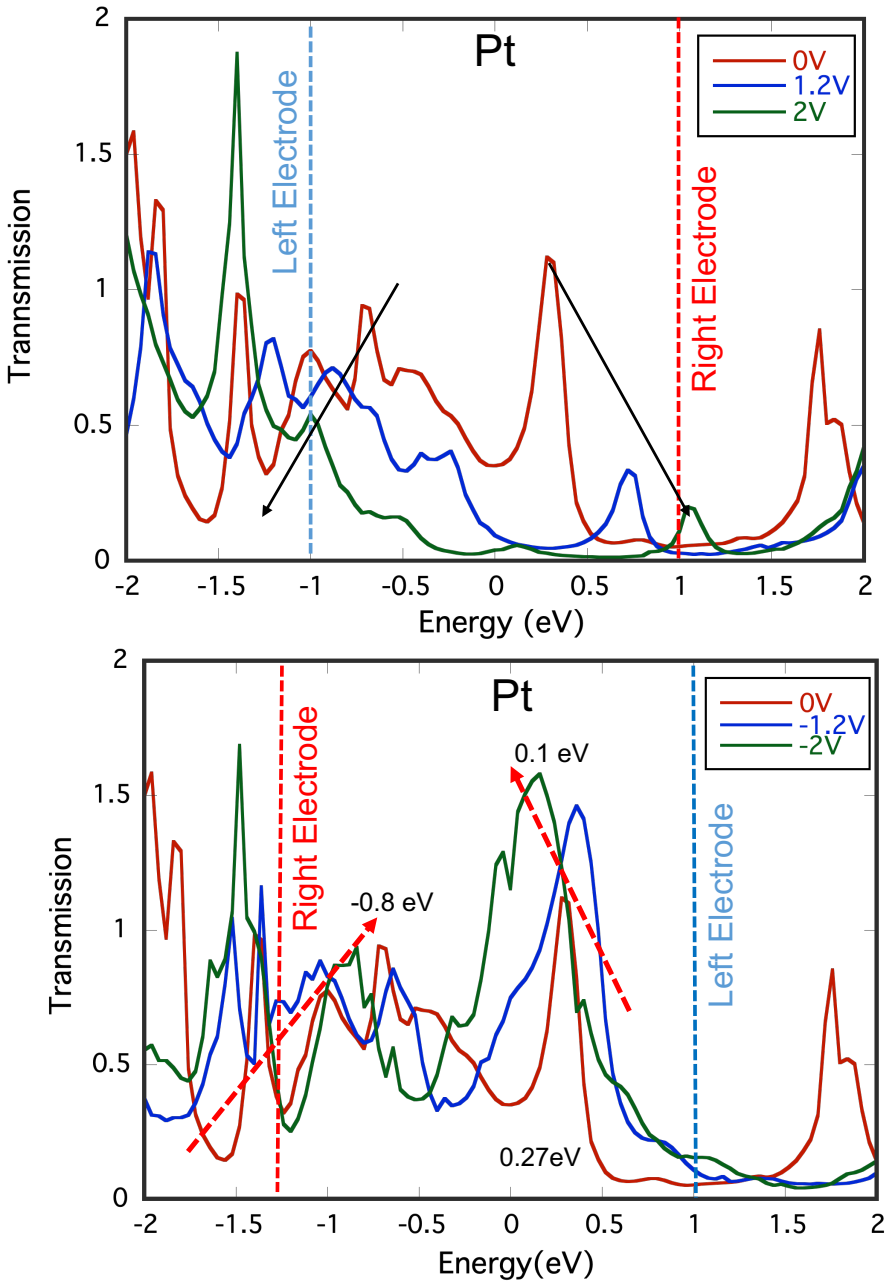

Figure 2.28: Overlay of transmission function calculated at 0 (red solid line), ±1.2 V (blue solid line), ±2 V (green solid line). Direction of arrow is indicating the transmission peak going out of the bias window; top and entering to the bias window; bottom.

On the negative energy side of the Fermi level (Figure 2.25), transmission peaks are associated with filled orbitals. These peaks enter the bias window with increasing intensity by combining with other less intense peaks, as shown in Figure 2.26. This indicates

increased hybridization of the HOMO energy level under an applied bias in the forward direction. The HOMOs are more strongly coupled with the electrode relative to the LUMOs in this system.[108] Further breaking down the individual complex features from the transmission function calculated at equilibrium (Figure 2.*23*), the increased amount of current passing through the Ni complex at reverse bias direction compared with Pd and Pt metal complexes

Higher RR at low bias is displayed by the Ni complex. As indicated in Figure 2.24, this is due to the major contribution by the transmission peak at −0.25 eV at −1.2 V. This argument has been further investigated by calculating the transmission spectrum at 1.2 V on forward and reverse bias directions as presented in Figure 2.27. A broad transmission channel at +0.4 eV under forward bias direction is the major conducting channel through the molecule[106] at -1.2 V. The projection calculation indicates the participation of 48% of MPSH HOMO, 29% of MPSH LUMO and 14% MPSH LUMO+1 (Figure 2.***27***) in this conducting channel. The broadening of the transmission eigen channel in (in set of) Figure 2.27[109] at 0.4 eV on the forward bias transmission spectrum at -1.2 V (red solid line), is because of the delocalization of the wavefunction across the molecule by inclusion of the metal electrode. There is increased hybridization with the metal electrodes as indicated by the projection calculation, which is a mixture of both HOMO and LUMO states. Both the donor and acceptor part of the molecule participate within this channel.[46] The MPSH LUMO is pinned with the left electrode under forward bias, and pinned with the right electrode under reverse bias. When the bias is reversed, the transmission probability is significantly reduced within the bias window (indicated by blue solid line in Figure 2.***27***. There is no significant transmission function within the

integration limits to promote the current.[106] Thus, we observed a RR of 4.3 in the case of Cat-Ni-bpy at ±1.2 V, which is the maximum RR for this complex.

The transmission channel within the integration area of the -2 V transmission spectrum (Figure 2.***26***) for all three complexes is due to the contribution from the various molecular states as shown by the projection calculation; it is contributed by the MPSH HOMO, LUMO and the LUMO+1 states after the molecule binds to the electrodes as displayed in

Table 2.3 Table 2.4.[110]

As depicted in (Figure 2.23 and Figure 2.24), the maximum RR is achieved at ±2 V for the other two complexes considered in this study. We have observed broadening of the resonant transmission function in the center of the transmission window. The integration of the transmission channel under the broad resonant transmission function results in the maximum amount of current passing through the molecules (Cat-Pd-bpy and Cat-Pt-bpy) at -2 V bias (red solid line), which is defined as the forward bias in this study as seen in Figure 2.29. In the reverse bias direction (blue solid line), there is a disappearance of a noticeable transmission function indicating the decrease of conductivity at +2 V bias. This results in the RR maximum at ±2 V for Cat-Pd-bpy and Cat-Pt-bpy complexes. Relatively, higher current in the reverse bias direction for the Cat-Ni-bpy complex is due to the entry of an intense transmission peak located close to the chemical potential of left electrode in equilibrium transmission spectrum. Furthermore, because of an increased amount of conductance in the reverse bias direction compared to the Pt and Pd complexes, it doesn't have its maximum RR at ±2 V. This can be seen in Figure 2.24 where the maximum RR value is at ±1.2 V (Table 2.2).

The decreased amount of current for Cat-Pd-bpy from -1.6 V to -2 V is because of a splitting of the broad band into small sharp bands, which decreases the integration area under the peak and consequently the current (Figure 2.23).[96] The sharp peaks within the transmission window indicates weak coupling of the molecule with the left and right electrodes at −2 V. Peak broadening under −1.2 V within bias window is because of hybridization of HOMO orbitals with the left electrode (Figure 2.29).

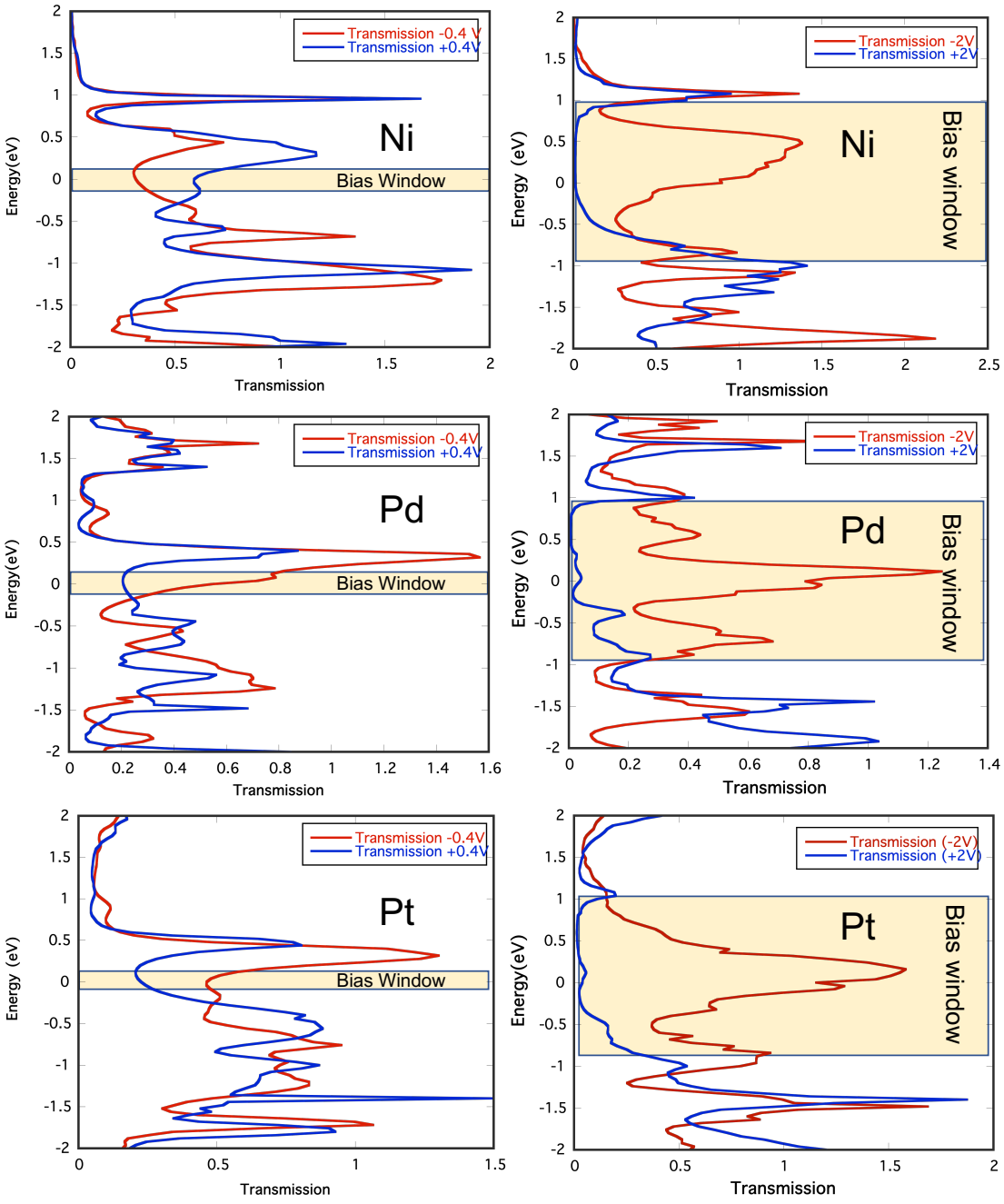

Figure 2.29: Transmission function calculated at ±0.4 V; left and ±2 V; right for bipyridine, catecholate complex of Nickel, Palladium, and Platinum top to bottom respectively. Data is depicting the negligible difference in small, applied bias and significant difference is observed when applied bias is increased to ±2 V.

2.4.3.3 Analysis of Transmission Eigen Channel and Molecular Projected Self-Consistent Hamiltonian (MPSH) State

Transmission eigen channels are the conduction channels decomposed from the transmission spectrum.[106] They are extended up to the scattering region. These are very useful to analyze the transport properties through the molecular bridge connected between two electrodes. Transmission eigen channels are the outcome of diagonalization of the transmission or scattering[100] matrix $\Gamma_L(E)G_C^R(E)\Gamma_R(E)G_C^A(E)$. [106] [109] [111] After the diagonalization, the total transmission function can be expressed as in equation (2.25),

$$T(E) = Tr[\Gamma_L(E)G_C^R(E)\Gamma_R(E)G_C^A(E)] = \sum_m T_m(E) \qquad (2.55)$$

where T_m represents the transmission eigenvalues. The transmission eigen channel constitutes the defined scattering states, which has the transmission probability between 0 and 1.[109] Transmission eigen states include the entire scattering region from the left electrode to the right electrode.[111] There are various transmission eigen channels with different transmission probabilities within the energy range of our calculation. [111]

It is very important to understand the electronic structure of the molecule after it is connected to the gold electrodes to explicitly understand the transport properties. Thus, we have used the MPSH approach to characterize the electronic structure at the junctions.[38] The MPSH analysis includes the diagonalization of the Hamiltonian of the scattering region[11] where the LCAO basis set is restricted to the atoms of the central

molecule including the anchoring sulfur atoms. Thus, MPSH states are the eigen states of the molecule within the electrodes which do not include the self-energy of the electrodes. Results of the MPSH state analysis contains important information about the alignment of the molecular states relative to the Fermi level of the electrodes in terms of energy. We can also extract information from the spatial distribution of the associated MPSH states for conducting channels. In general, the energy of the MPSH states coincide with the position of transmission peaks.[111] This may not always be the case, due to shifting of the MPSH state from the conducting channel by the real part of the self-energy, which depends on the surface Green's function of the junctions and the electrodes.[105] Their location is crucial to explain the nature and intensity of the transmission spectrum. This is related to the delocalization of the MPSH state to have great transmissive channel contrast to the localized MPSH states, which have less probability to generate the conducting channels. This ultimately provides a conclusive explanation for the mechanism of rectification.[38]

In this study, we have analyzed the calculated resonant transmission eigen channel with the maximum transmission coefficient and other relevant transmission functions that have a possibility to enter the integration area under applied bias. Associated MPSH states of the transmission channel possessing reasonable transmission probability have also been analyzed to help explain the calculated transport properties.

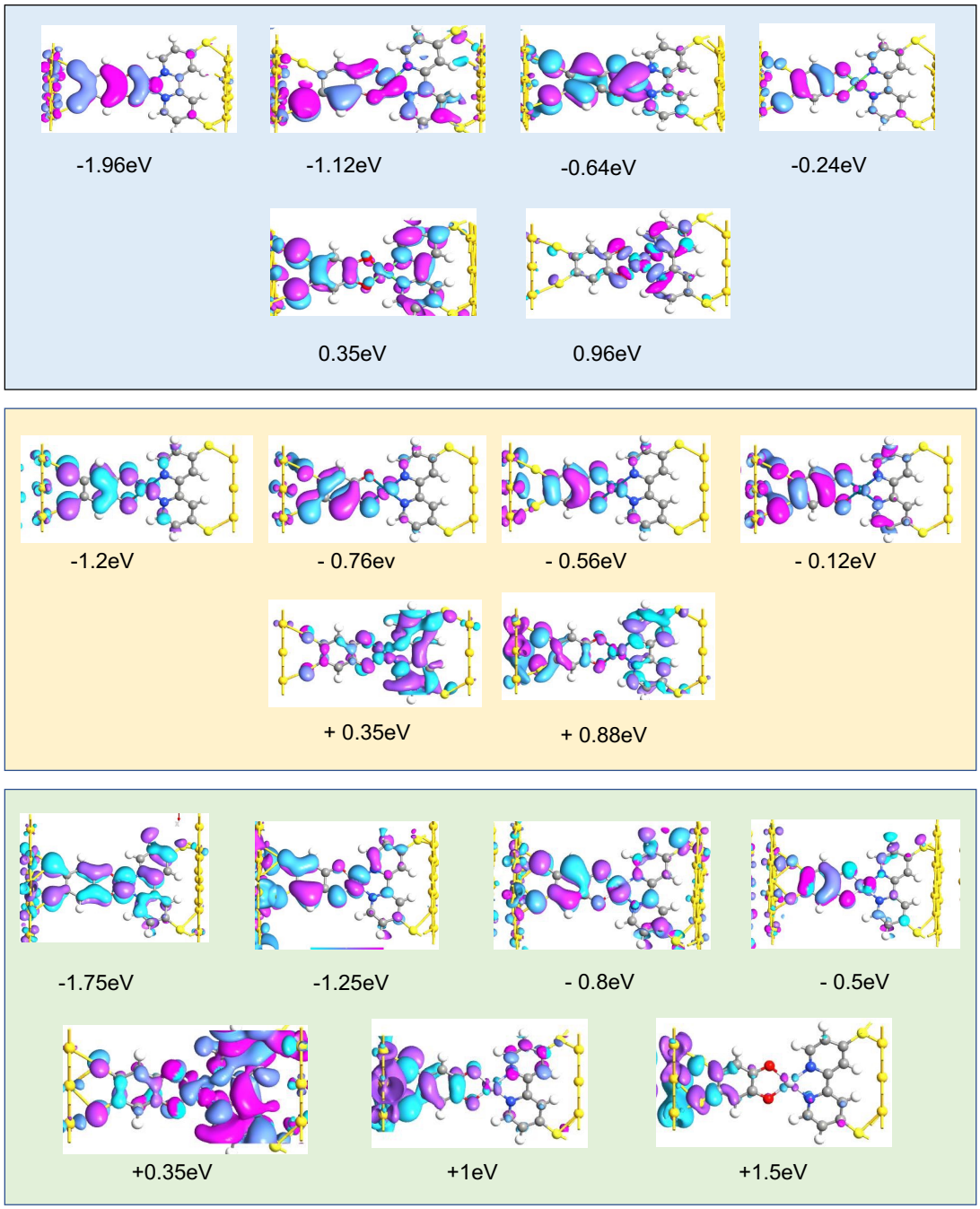

Figure 2.30: Iso-surface (isovalue =0.029) plot of transmission eigen channel calculated from the transmission spectrum at equilibrium with corresponding energy. Top on the bluish background is Cat-Ni-bpy, middle on light yellow background in for Cat-Pd-bpy and the bottom on the light green background is for Cat-Pt-bpy transition metal complexes. Transmission eigen channels are the combination of more than one eigen states. They indicate the type of the MPSH state used in transport and relative hybridization of the molecule with the metallic electrodes.

Transmission eigen channels have been calculated at equilibrium for all three metal complexes for the important transmission function as displayed in (Figure 2.30). The transmission function at +0.35 eV (Figure 2.25) in the transmission spectrum calculated at zero bias, has the eigen channel plotted with an isovalue 0.029 (being a comparative study, the isovalue is kept the same for all plots). The transmission eigen channel plotted at maximum intensity of the transmission peak exhibited by all three metal complexes at zero bias transmission shows the localization of wavefunction mostly on the bipyridine portion of the molecule than on the catecholate portion (Figure 2.30). The sharp nature of the transmission function indicates the reduced hybridization of these channels with the gold electrodes, supported by the reduced spatial distribution of connecting sulfur p-orbital wavefunctions (Figure 2.30).[38] A projection calculation was performed to evaluate the contribution of individual MPSH states to these transmission eigen channels. This shows that the transmission eigen channel at +0.35 eV is constituted by the mixing of the majority of LUMO and LUMO+1, and ~15% of HOMO-1. This explains the small amplitude of the wavefunction over the donor portion of the central molecule.[105] The eigen channel at +0.35 eV for the Ni complexes is very delocalized over both the donor and the acceptor part of the molecule, including the metal, which results in a broader peak compared to the Pt and Pd complexes.[38]

There is a unique transmission peak at +0.96 eV for the Ni complex in the zero bias transmission spectrum (Figure 2.25). It is sharp, which reflects diminished hybridization with the electrodes and its localized nature as shown in Figure 2.30. This conduction channel is mostly comprised of the MPSH LUMO+2 (88%) as shown in

Table 2.3 and Figure 2.31. The spatial distribution of the wavefunction shows the metal centered channel with a small degree of acceptor character as shown in Figure 2.30 (displayed in a light blue background). The transmission peaks associated with these eigen channels stay unaffected under applied bias. Even though it is a unique peak in the Ni transmission spectrum, it doesn't play a role in the rectification mechanism of the Cat-Ni-bpy complex at low bias since it moves smoothly out of the bias window in both conducting and insulating polarities. The zero bias transmission spectrum of Pt and Pd have a diminished peak in close proximity to the aforementioned peak at ~+0.84 eV. Suppression of these transmission peaks are because of reduced amplitudes of contributing molecular states on both sides of the electrodes.[112]

The broadened transmission function at +0.34 eV is primarily comprised of 29% HOMO and 50% LUMO+1 character as seen in

Table 2.3. The transmission function lies close in energy to the LUMO+1 as shown in both Figure 2.30 and

Table 2.3 (top). The broadness of the transmission function is explained by the larger amplitudes of MPSH states on the connecting sulfur atoms. This achieves maximal hybridization and the delocalized transmission eigenstate over the entire molecule, since the eigen channel is the combination of two orbitals.[113] There is a small misalignment between the transmission eigen channel and the MPSH state. This occurs because of coupling of molecule with the electrodes.[110] The transmission eigen state associated with the transmission function at −0.24 eV below the Fermi level is primarily due to catecholate donor based orbitals Figure 2.30 (displayed in blue background). The conduction channel close to the Fermi level at -0.24 eV energy is dominated by the MPSH HOMO (88%) and

another sharp conduction channel at -0.64 eV as shown in Figure 2.25 is constituted by the mixing of the MPSH HOMO (55%) and the HOMO-1 (37%) (

Table 2.3; top). There is another localized channel, corresponding to the sharp resonance peak at -1.96 eV as seen in Figure 2.25 and Figure 2.30. The eigen channel located at -0.64 eV originates from the nearly equal contribution of the HOMO-1 and HOMO-2 as shown in

Table 2.3. The sharpness of its nature is due to localization of the wavefunction only on the donor part of the molecule, with negligible metal character.

Similarly, the transmission eigen channel at +0.32 eV for the Pd complex is based on 83% MPSH LUMO (+0.35 eV) as shown in

Table 2.3, Figure 2.30 and Figure 2.31. This channel is aligned with the energy of dominant eigen state. The broad transmission eigen state (−0.12 eV) is comprised of 90% of MPSH HOMO. These types of eigen channels represent a dominant contribution from a single molecular state.[11] The other two reduced intensity peaks around −0.56 eV and −0.76 eV are comprised of the HOMO (73%) and the HOMO-4 (20%), and latter one is a mixture of the HOMO-1 (50%) and HOMO-4 (20%), respectively. Transmission eigen channels contributed to by the MPSH HOMO and molecular HOMO orbitals share similar features among all three metal complexes. Eigen channels just below the Fermi level are predominantly the MPSH HOMOs. These are localized mostly on the donor part of the molecule as shown by the projection calculation on those specific resonance peaks.

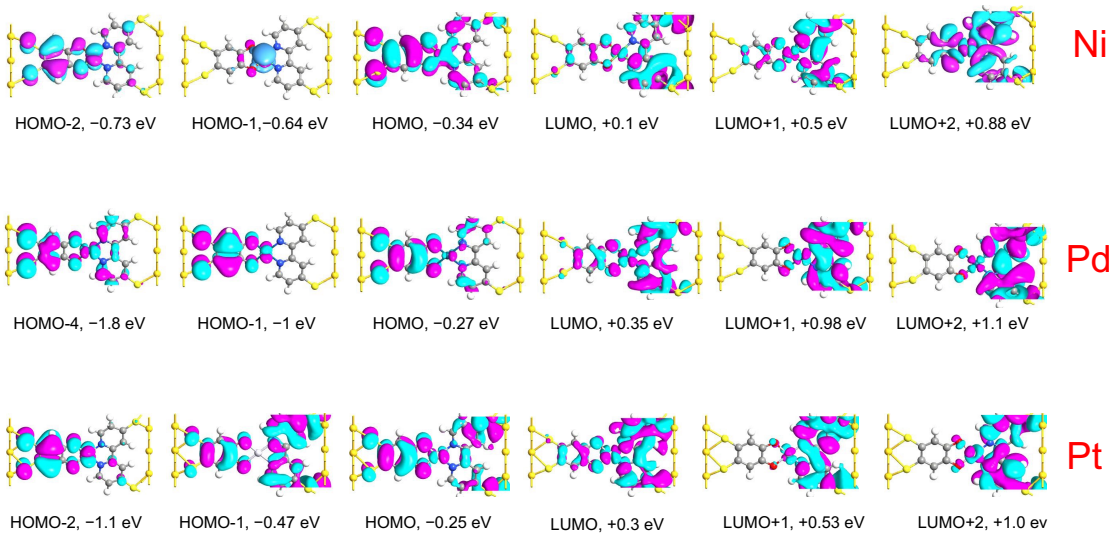

Figure 2.31: Molecular projected self-consistent Hamiltonian (MPSH) states calculated at equilibrium condition for Nickel, Palladium, and platinum complexes of catecholate donor and bipyridine as acceptor (iso-value 0.027 has kept constant for comparison purpose)

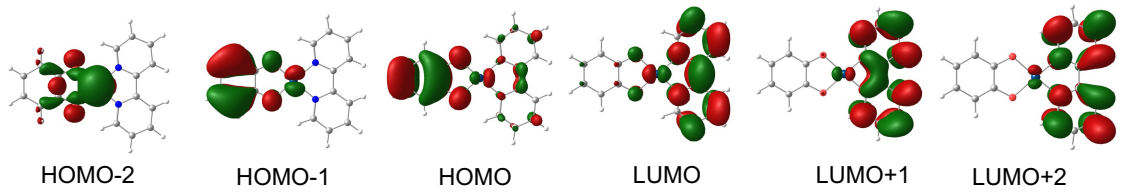

Figure 2.32: Frontier Molecular orbitals wavefunction of bpy-Pt-Cat complex generated from fully optimized geometry and plotted by Chem-Craft.

In the case of the bpy-Pt-Cat complex, the transmission eigen channel at +0.35 eV is dominated by contributions from the HOMO-1, LUMO and LUMO+1 MPSH states. This eigen channel is very delocalized over the molecule so it will result in a greater amount of current flow if it enters into the bias window. The energy of the eigen channel is aligned with the MPSH LUMO. The localized transmission eigen channels toward the left electrode (1 eV and 1.5 eV) indicates the vanishing of the transmission function at these energies.[38] There is one broad and one sharp transmission function present below the

Fermi level of the zero bias transmission spectrum of Pt (at −0.5 eV and −0.8 eV). The broadness of 0.5 eV transmission function is once again due to the delocalization of the wavefunction over the molecule and increased hybridization of the HOMO and HOMO-1 with electrodes. The sharp resonant peak at −0.8 eV is because of a 51% contribution to the transmission eigen channel from the polarized MPSH state HOMO-2, as shown in Figure 2.31. These peaks are located in the vicinity of the Fermi level, so they have a higher probability of impacting the overall conductance under bias.

Table 2.8: Contribution from individual molecular projected self-consistent Hamiltonian (MPSH) state molecular orbital, perturbed by the metallic electrodes connected to it to the specific transmission peak at zero bias transmission spectrum cat-Ni-bpy; top, Cat-Pd-bpy; middle, and Cat-Pt-bpy; bottom. The dashed lines represent the calculated percentage contribution less than 5 for that specific energy peak.

Eigen state (Ni)	−0.64 eV	−0.24 eV	+0.35 eV	+0.96 eV
LUMO+2	–	–	–	88%
LUMO+1	–	–	50%	–
LUMO	–	–	–	–
HOMO	–	88%	29%	–
HOMO-1	55%	–	15%	–
HOMO-2	37%	–	–	–

Eigen states (Pd)	−1.2eV	−0.76eV	−0.56eV	−0.12	+0.32eV	+0.88eV
LUMO+1		–	–	–	10%	42%
LUMO		–	–	–	83%	6%
HOMO		23%	73%	90%	–	18%
HOMO-1		50%		–	–	–
HOMO-2		–	–	–	–	–
HOMO-4	80%	20%	20%	–	–	–

Eigen state (Pt)	−0.8eV	−0.5eV	+0.35eV
LUMO+1	−	−	26%
LUMO	−	−	47%
HOMO	13%	29%	−
HOMO-1	−	60%	15%
HOMO-2	51%	−	−

2.4.3.4 Correlation Between Transmission Eigen States and MPSH States at Finite Bias.

In our study, projection of self-consistent Hamiltonian (Hc) on to the metal complex orbitals has been used. Those eigen states and MPSH states at equilibrium position and under an applied biased have been presented in Figure 2.31 and Figure 2.33. These computations have been performed to analyze their contribution on conductivity at zero and applied bias conditions.[110] A transmission spectrum alone is not enough to explain the conductance under applied bias. Thus, the transmission eigen channel and the MPSH states have been calculated and analyzed under bias. The transmission eigen channel and the MPSH state change their occupancy, nature of the wavefunction, and the energy under finite bias, as we have optimized the device configuration at every bias point.[112] The bias has been applied up to ±2 V. The transmission spectrum and the corresponding value of current is calculated at ten different points: ±0.4 V, ±0.8 V, ±1.2 V ±1.6 V and ±2 V. It is clearly visible that both the MPSH HOMOs and LUMOs have contributed to the eigen channel in conducting polarity, thus contributing to the current and creating a very delocalized transmission eigen channel as viewed in Figure 2.***34***. The greater observed

RR value at low bias for the Ni complex compared to Pt and Pd is due to the LUMO state entering the bias window earlier, resulting in a broad resonant peak at −1.2 V. This is because of the smaller HOMO-LUMO gap for this complex as shown in Table 2.5.[110] The eigen channel representing a large transmission value at +0.4 eV for the Ni complex under forward bias of −1.2 V, corresponds to the MPSH states HOMO, LUMO and LUMO+1 as shown in Table 2.4. The transmission channel at + 0.1 eV and +0.13 eV for both the Pd and Pt complexes under +2 V show a larger amplitude only on the left side of the scattering region as demonstrated in Figure 2.***34***. As a result, there is a diminished amount of current passing at reverse bias.[111] This describes the rectifying behavior of the Ni complex at the ±1.2 V bias point. The transmission eigen states are systematically changed from being delocalized over the entire channel to localized on the left side of electrode from +1.2 V to -1.2 V applied bias in the Ni complex as shown in Figure 2.***34***.[111] In general, for all three complexes, suppression of the transmission peaks in reverse bias is due to the localization of a conducting molecular eigen state.[112] The amplitude of the wavefunction on the connecting sulfur atoms is larger on the eigen channel calculated for the forward bias direction at the bias that has the maximum RR value. The corresponding eigen channels calculated at the same energy in the positive bias direction for all three complexes have a transmission eigen channel localized only on the donor part of the molecule as demonstrated in Figure 2.***34***. Thus, the probability of transmission has been significantly reduced in the positive biased direction at higher bias values.[110]

The transport properties at ±1.2 V and ±2 V external bias has further been analyzed by calculating the MPSH states under finite bias as seen in Table 2.4 and Figure 2.33. The geometry optimization has been performed for each bias point to have the

MPSH states under biased conditions. The contribution of MPSH states at finite bias on the transmission function is exhibited in Table 2.4. The major transmission peak inside the integration area is primarily from the MPSH LUMO states for the Pt complex. The spatial distribution of the MPSH LUMO state is delocalized over the entire molecule, which transforms into the broadened transmission functions. This symmetric spatial distribution of the molecular state is the origin of rectification, as the integrated area of the broad transmission peak results in a higher value of calculated current at −2 V applied bias for Pt.[114] The calculated current has diminished in the case of the Pd complex compared to the Ni and Pt complexes at a forward bias of 2 V. The current has decreased from –1.6 V to −2 V by a small quantity. The decreased conductivity of the Pd complex at −2 V compared to the Ni and Pt complexes is due to the very localized molecular MPSH HOMO and metal centered MPSH HOMO-2 orbitals presented in Table 2.4 and Figure 2.***34***, which create a narrower transmission channel.[115] This will be described below in section 2.4.3.6 when considering the device density of states. The molecular states associated with the most prominent peak also has a larger amplitude on the connecting sulfur atoms that causes a higher degree of hybridization with the electrodes.[38] The MPSH states under bias do not directly correspond to the frontier orbital of the isolated molecule, as it is not a pure LUMO state under bias as shown in Figure 2.32 and Figure 2.33. In the opposite bias direction, the calculated eigen channel and contributing MPSH state LUMO is localized on the catecholate part of the molecule. The amount of current through these molecular states is negligible compared to the negative bias direction.[38] This also explains the rectification mechanism of the complexes in our study. At positive bias, the HOMO-LUMO peaks get separated and they gradually go out of the bias window

as depicted in Figure 2.26.[116] Figure 2.34 has clearly shown the evolution of the major conducting channel on increasing applied bias in forward and reverse polarity.

Table 2.9: Contribution from individual molecular projected self-consistent Hamiltonian (MPSH) state, molecular orbital perturbed by the metallic electrodes connected to it to the specific transmission peak at -1.2 V biased transmission spectrum Cat-Ni-bpy (top), and -2 V for Cat-Pd-bpy (middle) and Cat-Pt-bpy (bottom). The empty entries indicate the calculated percentage contribution less than 5 for that specific energy peak.

Eigen state (Ni)	−1.0eV	−0.4eV	+0.08eV	+0.4eV	+0.6eV	+1.08eV
LUMO+2	–	–	–	–	–	77%
LUMO+1	–	–	–	14%	80%	–
LUMO	–	–	65%	48%	–	–
HOMO	–	–	24%	27%	8%	–
HOMO-1	–	80%	–	–	–	–
HOMO-3	64%	–	–	–	–	–

Eigen state (Pd)	− 0.68eV	−0.08eV	+ 0.12eV	+ 0.56eV	+ 1.0eV
LUMO+2	–	–	–	40%	83%
LUMO+1	–	–	13%	34%	–
LUMO	–	57%	74%	6%	–
HOMO	9%	12%	–	–	–
HOMO-2	87%	–	–	–	–

Eigen state (Pt)	−0.92eV	−0.84eV	−0.04eV	+ 0.25eV
LUMO+1	–	–	–	75%
LUMO	–	–	30%	–
HOMO	6%	9%	68%	15%
HOMO-3	70%	65%	–	–

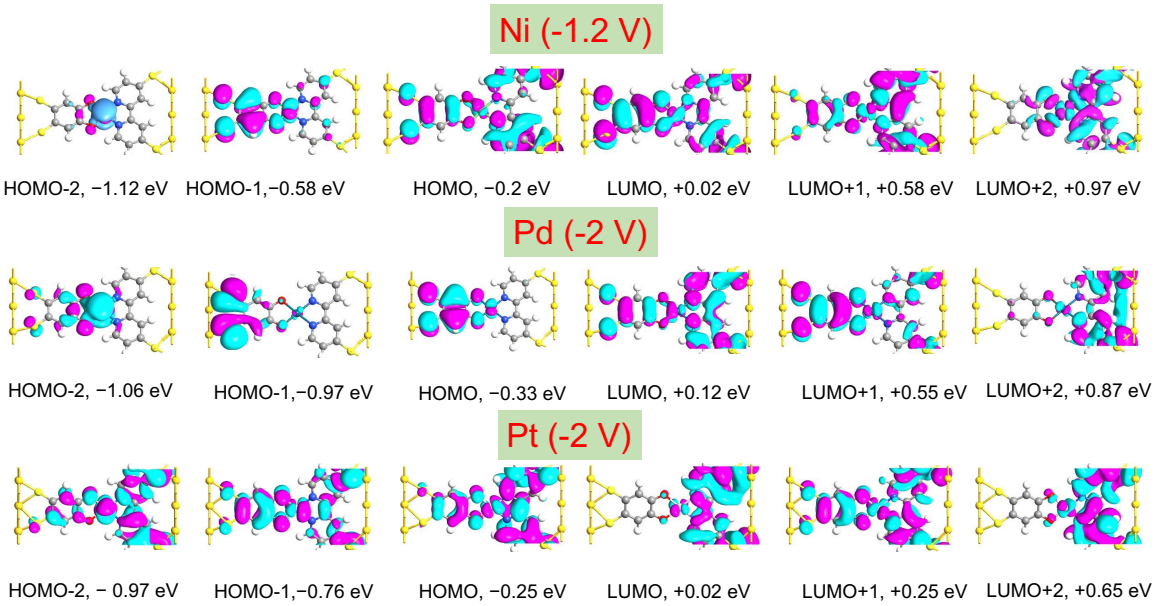

Figure 2.33: Molecular projected self-consistent Hamiltonian (MPSH) eigen state at −1.2 V; top of Ni and −2 V of Pd; middle and −2 V of Pt; bottom. Plotted with a same iso value of 0.27.

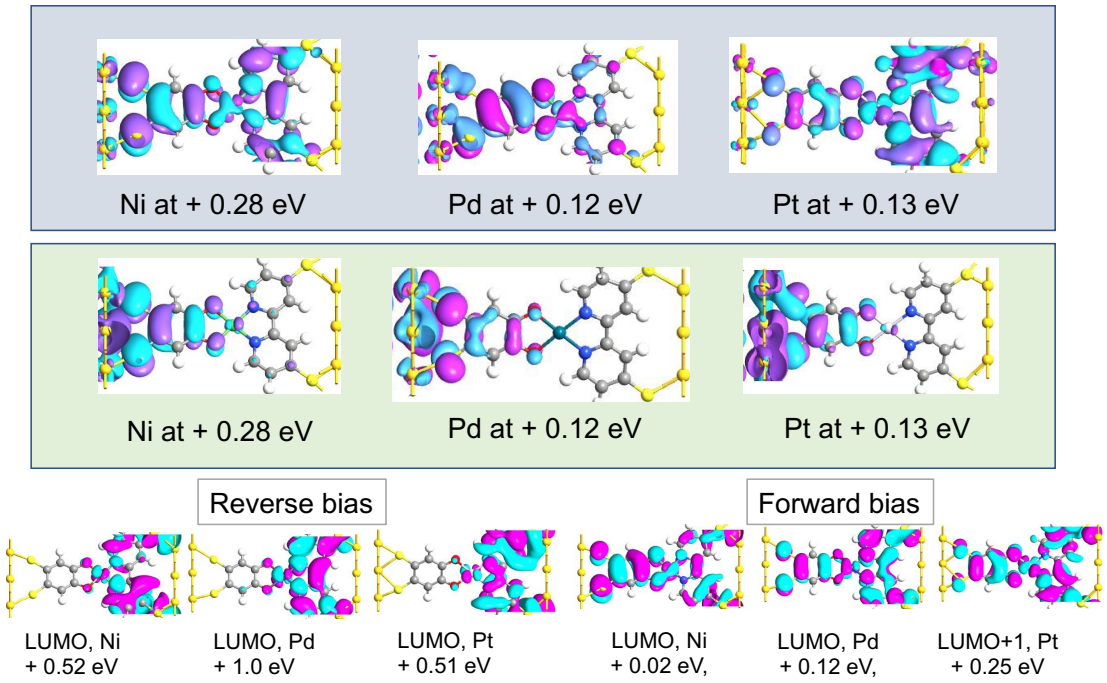

Figure 2.34: Transmission eigen channel calculated at the bias point of maximum rectification ratio. Value for iso-surface (0.29) has kept same for all of them for comparison purpose. it corresponds to the 1.2 V for Ni, 2 V for Pd and 2 V for the Pt complexes at top. The most prominent resonant transmission function within the bias window has chosen to calculate the eigen channel. The delocalized nature of these eigen channel describes the highest amount of current passing through them at respective bias in forward direction. Middle: transmission channel calculated at the same energy above the Fermi level for reverse bias of 1.2 V for nickel and 2 V for platinum and palladium complexes. These are localized eigen channels so allows very little current in reverse bias direction. At bottom, the molecular eigenstate MPSH LUMO are exhibited at forward and reverse bias.

2.4.3.5 Evolution of HOMO-LUMO Gap

We have considered charge transfer (CT) complexes of Ni, Pd and Pt complexed with catecholate donors and bipyridine acceptor ligands. Based on our literature review, the HOMO-LUMO gap (HLG) is directly related to the photophysical properties of these types of CT complexes.[25] As a rectifier it is equally important, since this determines the energy of molecular states relative to the Fermi level, which in turn determines the transport properties through the molecule. An earlier study by Van Dyck and coworkers

has demonstrated that the compression of the HLG occurs by the electrode-molecule contact when the coupling between the donor and acceptor component is weak, since the HOMO and LUMO follows the respective electrodes independently. They have also shown that the HLG is bias dependent, and it behaves differently with conducting and insulating polarity.[116] In our study, the HLG shows a different nature for Ni, Pd, and Pt complexes as displayed in Table 2.5. At equilibrium conditions, the HLG for Ni in the device configuration is compressed (0.7 eV to 0.4 eV) when compared with DFT calculated value of the isolated molecule. This is suggesting poor overlap with the donor and acceptor fragments, resulting in a weakly coupled system compared to Pd and Pt. The HLG for Pd and Pt widens from ~0.2 eV in isolated molecule to ~0.6 eV when they are connected to the electrodes. This observation suggests better overlap of their orbitals with donor-acceptor fragments as a consequence of the strong coupling with electrodes.[38] The opposite holds true for the RRs, as the Pd and Pt atoms are better decoupling units since they are larger in size.

When a positive bias is applied, the HLG has increased continuously for all three complexes (Figure 2.35). The LUMOs are localized on the right electrodes and HOMOs are localized on the left electrode, thus showing poor conductivity along the insulating polarity.[117] In the negative bias direction, the energy of the LUMOs move away from Fermi level with their respective electrodes, as shown in Figure 2.35 and Table 2.5. The HLG decreases to its minimum at −1.2 V for Ni and at −2 V for the Pd and Pt complexes. These are the bias points where the maximum RR has been calculated for the complexes in our study. Upon increasing the negative bias from −0.4 V to −2 V, the narrowing of the HLG is significant except for some irregularity in the Pd complex as the applied bias localizes

the LUMOs on the right electrode and HOMOs on the left electrode.[115] The increased HLG for the Ni complex results since both the HOMO and LUMO stay away from the Fermi level of both electrodes after an external bias of −1.2 V, again indicating the intrinsic weak coupling nature of this complex with the electrodes under bias.[38]

The consequence of narrowing of the HLG brings the conducting frontier orbitals very close to the Fermi level, which translates into a good conducting channel as it enters the transmission window. The calculated maximum RR is clearly associated with the bias point where the HLG is at a minimum. This provides an explanation of the rectification mechanism from another perspective.[116] [11] [97]

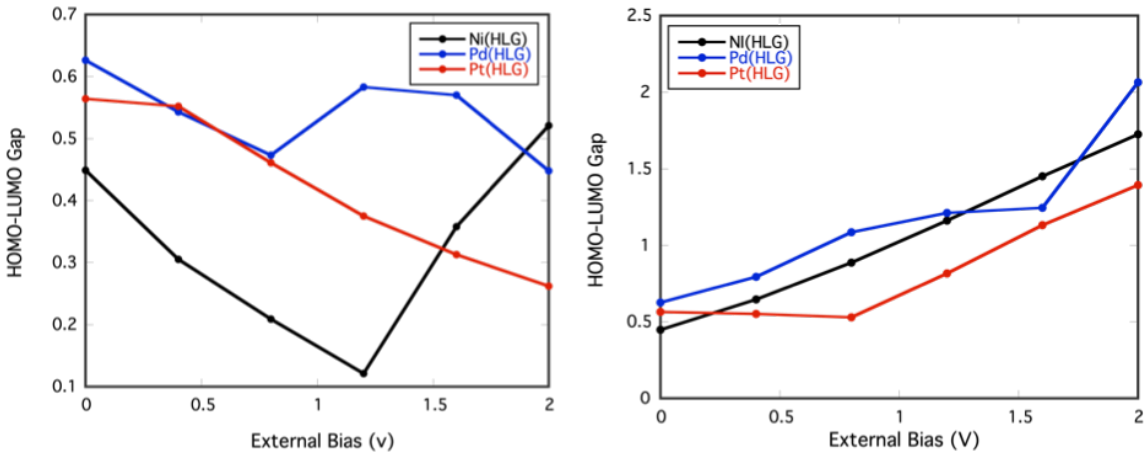

Figure 2.35: Calculated HOMO-LUMO gap under positive and negative bias.

Table 2.10: Calculated HOMO-LUMO gap under 0V to ±2V. Top; Cat-Ni-bpy, middle; Cat-Pd-bpy and bottom; Cat-Pt-bpy.

bias (Ni)	H(eV)	L(eV)	HLG (eV)	bias (Ni)	H(eV)	L(eV)	HLG (eV)
0 V	−0.347	+0.102	0.449	0	−0.347	+0.102	0.449
+0.4 V	−0.427	+0.218	0.647	−0.4 V	−0.276	+0.029	0.305
+0.8 V	−0.521	+0.366	0.887	−0.8 V	−0.206	+0.003	0.209
+1.2 V	−0.645	+0.516	1.161	−1.2 V	−0.199	+0.022	0.121
+1.6 V	−0.773	+0.678	1.451	−1.6 V	−0.267	+0.091	0.358
+2 V	−0.881	+0.884	1.725	−2 V	−0.397	+0.124	0.521

bias (Pd)	H(eV)	L(eV)	HLG (eV)	bias(Pd)	H(eV)	L(eV)	HLG(eV)
0 V	−0.271	+0.355	0.626	0	−0.271	+0.355	0.626
+0.4 V	−0.365	+0.429	0.794	−0.4 V	−0.181	+0.362	0.543
+0.8 V	−0.517	+0.569	1.086	−0.8 V	−0.069	+0.404	0.473
+1.2 V	−0.610	+0.602	1.212	−1.2 V	−0.595	+0.048	0.643
+1.6 V	−0.476	+0.769	1.245	−1.6 V	−0.468	+0.102	0.570
+2 V	−0.975	+1.090	2.065	−2 V	−0.366	+0.122	0.458

bias(Pt)	H(eV)	L(eV)	HLG(eV)	bias(Pt)	H(eV)	L(eV)	HLG(eV)
0 V	−0.259	+0.305	0.564	0	−0.259	+0.305	0.564
+0.4 V	−0.266	+0.254	0.520	−0.4 V	−0.166	+0.386	0.552
+0.8 V	−0.378	+0.493	0.871	−0.8 V	−0.203	+0.258	0.461
+1.2 V	−0.697	+0.119	0.816	−1.2 V	−0.157	+0.218	0.375
+1.6 V	−0.820	+0.311	1.131	−1.6 V	−0.151	+0.162	0.313
+2 V	−0.893	+0.501	1.394	−2 V	−0.237	+0.025	0.262

2.4.3.6 Projected Device Density of States (PDDOS)

The PDDOS has been calculated by breaking down the whole complex into three parts: the central metal atom, the donor, and acceptor, both with sulfur atoms. They are calculated at the central molecule with boundary conditions (we did not include the bulk electrodes) and the 5, 5 k-point sampling is set up in the X-Y plane. The magnitudes of the DOS peaks depend on the energy and the k-point sampling. A small change in energy makes a great difference on the DOS amplitudes.[118]

The PDDOS at equilibrium for the whole molecule is superimposed with the transmission spectrum of the complexes Figure 2.***38***. As molecular states, they change with the applied external bias[110] since the external bias shifts the chemical potential of the Fermi level.[119] When an external bias of −1.2 V is applied to the Ni complex, the PDDOS of the bipyridine has the same features as the transmission spectrum at the same bias as shown in Figure 2.***38***. When the bias is reversed, all the major states contributing to the transmission probability are out of the bias window. It is concluded that the MPSH states that correspond to the conducting channel are also the same as the contributing molecular states.[111]

In the case of Pd and Pt, at −2 V bias the PDDOS of bipyridine is superimposed with the transmission spectrum calculated at the same bias. This is shown in Figure 2.***38***. This also supports our arguments that the conducting channel is mainly comprised of acceptor-based molecular states. In the insulating polarity, the bipyridine fragments have exhibited a sharp peak within the transmission window, but the catecholate fragment does not have a projected density of states within the integration area. The discontinuity of the density of states from the catecholate fragments results in the probability of transmission

being very low in the reverse bias direction. Based on our previous discussion, a delocalized pathway over the molecule is required to have a flow of electrons between the electrodes. The transmission eigen channel calculated at the corresponding peak position of PDDOS in the +2 V bias transmission spectrum are only catecholate based wavefunctions, as shown in Figure 2.37. This is also supported by the projected local density of states heat map generated for the Pt complex. A representative map depicted in Figure 2.***36***. Thus, the calculated current at positive bias is lower compared to the current at negative voltage.

The most common striking feature exhibited by all three PDDOS plots in both bias directions is that the central metal fragment has none of its density of states in the transmission spectrum of both conducting and insulating polarity. Those results suggest that the metal atom has weak or very little participation in the transmission of electrons through the molecule. It is therefore behaving efficiently as a decoupler in the complex allowing the molecule to act as the intrinsic rectifier, as we have hypothesized.[97]

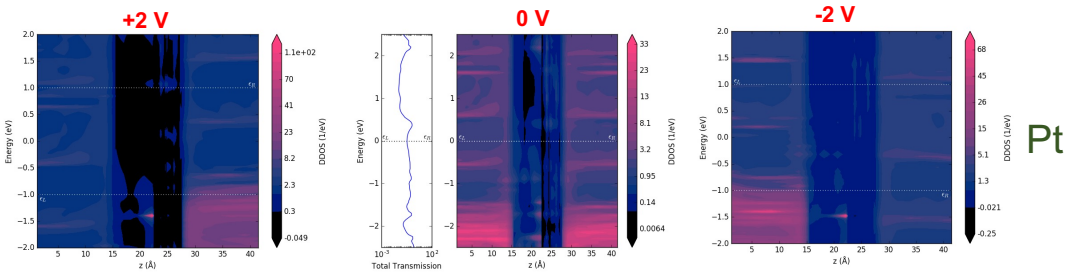

Figure 2.36: Heat map depicting the projected local density of states for platinum complex calculated at +2 V bias; left, 0 bias; middle and −2 V bias; right. The weight scale has shown on the right side of the plot. The pattern of the projected local density of states clearly shows that more density of states is present on the −2 V map compared to the +2 V map.

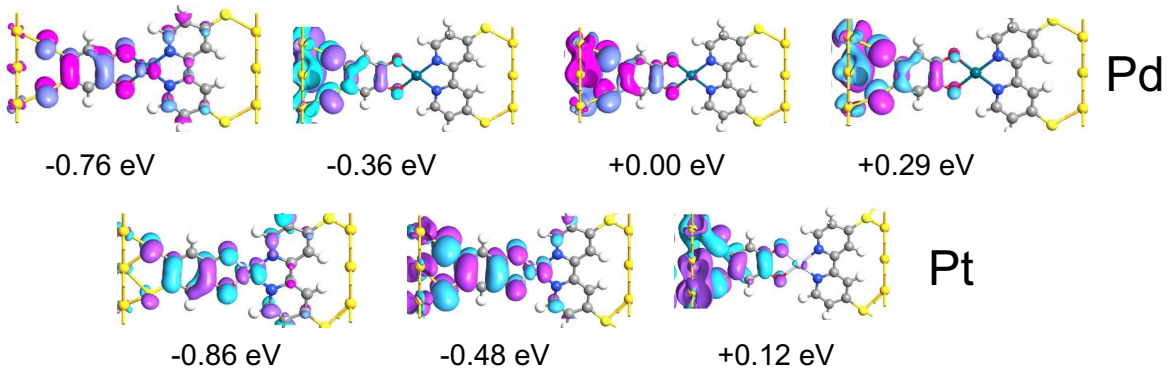

Figure 2.37: Transmission eigen states calculated at the energy corresponding to the peaks position of PDDOS in positive bias plot of palladium; top and platinum (Pt); bottom.

2.4.4 Conclusion

This rectification mechanism has been fully rationalized by using the calculated transmission spectra at equilibrium conditions and at finite external bias. Supporting arguments were made by calculating the MPSH states, eigen channels, HLG analysis and the PDDOS, all at equilibrium and under bias. The preferential direction of current flow is from the right to the left electrode. The opposite holds for the electron flow: electrons flow from donor (catecholate) to the acceptor (bipyridine) fragments of complex, as expected in the charge transfer transition.

Rectification at low bias has been observed for the Ni complex. It is correlated with the lowest HLG at ±1.2 V, localization, and delocalization of the conducting channel at +1.2 V and −1.2 V respectively. Pd and Pt both have a maximum RR at ±2 V. The rectification is primarily from the LUMOs entering, and going out of, the transmission window in opposite bias polarities. This is also supported by the symmetrical distributions of eigen states and transmission eigen states at negative bias.

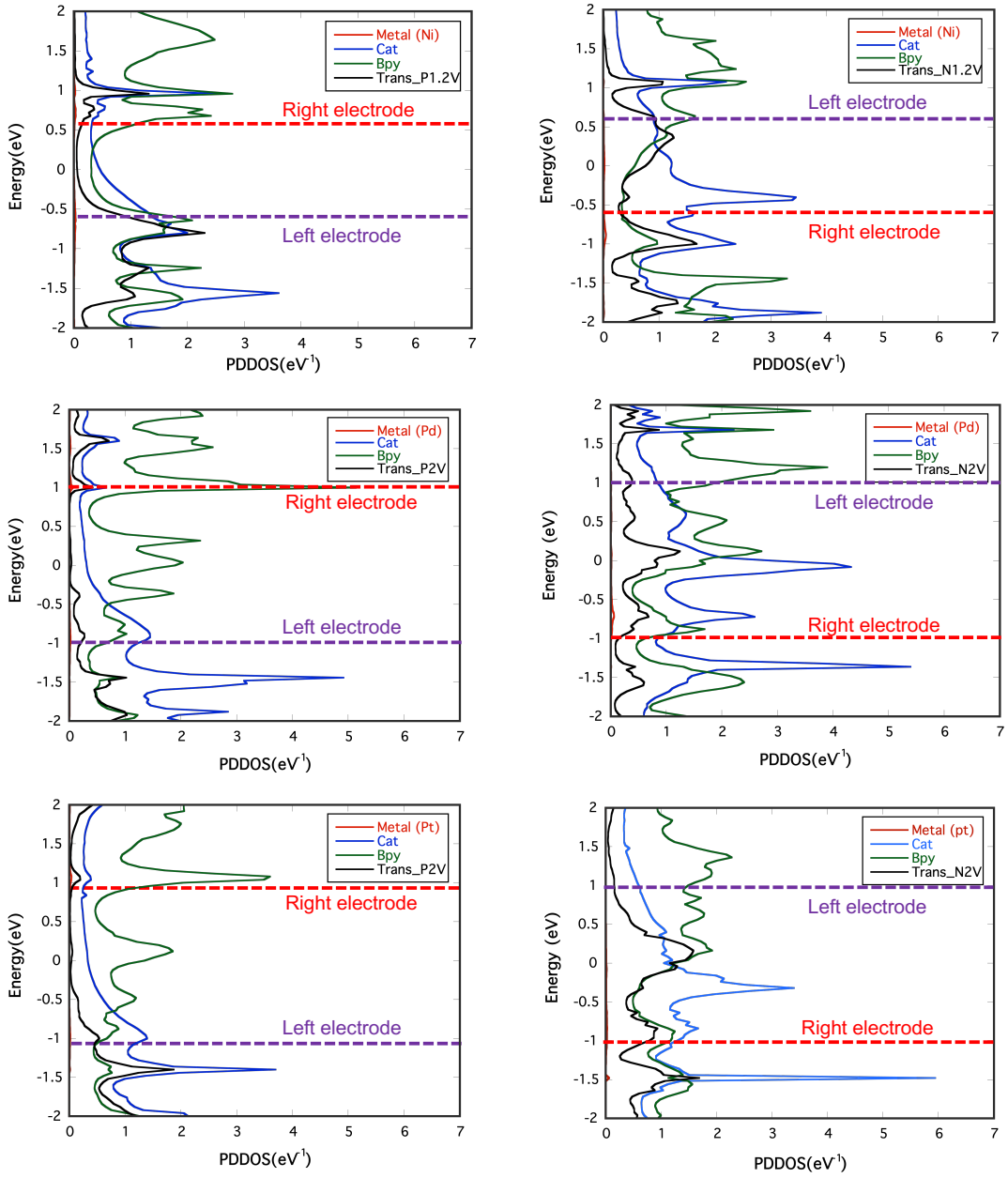

Figure 2.38: Overlay of transmission function forward and reverse bias with individual contribution from the metal, catecholate, bipyridine on PDDOS at forward and reverse bias for platinum, palladium, and nickel respectively.

As we hypothesized in this study, the transition metal has functioned as an effective decoupler of the donor and acceptor π-fragment. The RR is relatively higher in relation to the other currently studied synthetic rectifier molecules. The overall

performance as rectifier is best through the Pt complex, followed by Pd. The Ni complex exhibited the smallest RR.

Looking forward, our group has been able to synthesize these complexes, with plans to compare experimental observations with these calculated results. The molar extinction coefficients of the LLCT should agree with the conductance pattern through these complexes. Thus, it has opened new research interests in the field of single molecule rectifier design for a new range of molecules which can be synthesized in the laboratory.

2.5 References

(1) Ratner, M. A. Introducing Molecular Electronics. *Mater. Today* **2002**, *5* (2), 20–27.

(2) Aviram, A.; Ratner, M. A. Molecular Rectifiers. *Chem. Phys. Lett.* **1974**, *29* (2), 277–283. https://doi.org/10.1016/0009-2614(74)85031-1.

(3) Andrews, D. Q.; Solomon, G. C.; Van Duyne, R. P.; Ratner, M. A. Single Molecule Electronics: Increasing Dynamic Range and Switching Speed Using Cross-Conjugated Species. *J. Am. Chem. Soc.* **2008**, *130* (51), 17309–17319. https://doi.org/10.1021/ja804399q.

(4) Ratner, M. A Brief History of Molecular Electronics. *Nat. Nanotechnol.* **2013**, *8* (6), 378–381. https://doi.org/10.1038/nnano.2013.110.

(5) Davis, W. B.; Ratner, M. A.; Wasielewski, M. R. Dependence of Electron Transfer Dynamics in Wire-like Bridge Molecules on Donor–Bridge Energetics and Electronic Interactions. *Chem. Phys.* **2002**, *281* (2), 333–346.

(6) Lörtscher, E. Wiring Molecules into Circuits. *Nat. Nanotechnol.* **2013**, *8* (6), 381–384. https://doi.org/10.1038/nnano.2013.105.

(7) Van Dyck, C.; Ratner, M. A. Molecular Rectifiers: A New Design Based on Asymmetric Anchoring Moieties. *Nano Lett.* **2015**, *15* (3), 1577–1584. https://doi.org/10.1021/nl504091v.

(8) Van Dyck, C.; Ratner, M. A. Molecular Rectifiers: A New Design Based on Asymmetric Anchoring Moieties. *Nano Lett.* **2015**, *15* (3), 1577–1584. https://doi.org/10.1021/nl504091v.

(9) Xu, B.; Xiao, X.; Tao, N. J. Measurements of Single-Molecule Electromechanical Properties. *J. Am. Chem. Soc.* **2003**, *125* (52), 16164–16165. https://doi.org/10.1021/ja038949j.

(10) Kirk, M. L.; Shultz, D. A.; Zhang, J.; Dangi, R.; Ingersol, L.; Yang, J.; Finney, N. S.; Sommer, R. D.; Wojtas, L. Heterospin Biradicals Provide Insight into Molecular Conductance and Rectification. *Chem. Sci.* **2017**, *8* (8), 5408–5415. https://doi.org/10.1039/c7sc00073a.

(11) Brandbyge, M.; Mozos, J.-L.; Ordejón, P.; Taylor, J.; Stokbro, K. Density-Functional Method for Nonequilibrium Electron Transport. *Phys. Rev. B* **2002**, *65* (16), 165401. https://doi.org/10.1103/PhysRevB.65.165401.

(12) Soler, J. M.; Artacho, E.; Gale, J. D.; García, A.; Junquera, J.; Ordejón, P.; Sánchez-Portal, D. The SIESTA Method for *Ab Initio* Order- *N* Materials Simulation. *J. Phys. Condens. Matter* **2002**, *14* (11), 2745–2779. https://doi.org/10.1088/0953-8984/14/11/302.

(13) Atomistix ToolKit 2016.0 Version 16.0, QuantumWise A/S, Http://Www.Quantumwise.Com.

(14) Gaussian 09, R. C. G., Inc., Pittsburgh, PA, 2009.

(15) Büttiker, M.; Imry, Y.; Landauer, R.; Pinhas, S. Generalized Many-Channel Conductance Formula with Application to Small Rings. *Phys. Rev. B* **1985**, *31* (10), 6207–6215. https://doi.org/10.1103/PhysRevB.31.6207.

(16) Stasiw, D. E.; Zhang, J.; Wang, G.; Dangi, R.; Stein, B. W.; Shultz, D. A.; Kirk, M. L.; Wojtas, L.; Sommer, R. D. Determining the Conformational Landscape of σ and π Coupling Using *Para* -Phenylene and "Aviram–Ratner" Bridges. *J. Am. Chem. Soc.* **2015**, *137* (29), 9222–9225. https://doi.org/10.1021/jacs.5b04629.

(17) Depperman, E. C.; Bodnar, S. H.; Vostrikova, K. E.; Shultz, D. A.; Kirk, M. L. Spin Robustness of a New Hybrid Inorganic- Organic High-Spin Molecule. *J. Am. Chem. Soc.* **2001**, *123* (13), 3133–3134.

(18) Kirk, M. L.; Shultz, D. A. Transition Metal Complexes of Donor–Acceptor Biradicals. *Coord. Chem. Rev.* **2013**, *257* (1), 218–233. https://doi.org/10.1016/j.ccr.2012.07.007.

(19) Kirk, M. L.; Shultz, D. A.; Depperman, E. C. Beyond the Active-Electron Approximation: Origin of Ferromagnetic Exchange in Donor–Acceptor Heterospin Biradicals. *Polyhedron* **2005**, *24* (16–17), 2880–2884. https://doi.org/10.1016/j.poly.2005.08.010.

(20) Kirk, M. L.; Shultz, D. A.; Depperman, E. C.; Brannen, C. L. Donor−Acceptor Biradicals as Ground State Analogues of Photoinduced Charge Separated States. *J. Am. Chem. Soc.* **2007**, *129* (7), 1937–1943. https://doi.org/10.1021/ja065384t.

(21) Kirk, M. L.; Shultz, D. A.; Depperman, E. C.; Habel-Rodriguez, D.; Schmidt, R. D. Spectroscopic Studies of Bridge Contributions to Electronic Coupling in a Donor-Bridge-Acceptor Biradical System. *J. Am. Chem. Soc.* **2012**, *134* (18), 7812–7819. https://doi.org/10.1021/ja300233a.

(22) Kirk, M. L.; Shultz, D. A.; Stasiw, D. E.; Habel-Rodriguez, D.; Stein, B.; Boyle, P. D. Electronic and Exchange Coupling in a Cross-Conjugated D–B–A Biradical: Mechanistic Implications for Quantum Interference Effects. *J. Am. Chem. Soc.* **2013**, *135* (39), 14713–14725. https://doi.org/10.1021/ja405354x.

(23) Shultz, D. A.; Vostrikova, K. E.; Bodnar, S. H.; Koo, H.-J.; Whangbo, M.-H.; Kirk, M. L.; Depperman, E. C.; Kampf, J. W. Trends in Metal−Biradical Exchange Interaction for First-Row M ^{II} (Nitronylnitroxide-Semiquinone) Complexes. *J. Am. Chem. Soc.* **2003**, *125* (6), 1607–1617. https://doi.org/10.1021/ja020715x.

(24) Kirk, M. L.; Shultz, D. A.; Schmidt, R. D.; Habel-Rodriguez, D.; Lee, H.; Lee, J. Ferromagnetic Nanoscale Electron Correlation Promoted by Organic Spin-Dependent Delocalization. *J. Am. Chem. Soc.* **2009**, *131* (51), 18304–18313. https://doi.org/10.1021/ja904648r.

(25) Yang, J.; Kersi, D. K.; Giles, L. J.; Stein, B. W.; Feng, C.; Tichnell, C. R.; Shultz, D. A.; Kirk, M. L. Ligand Control of Donor–Acceptor Excited-State Lifetimes. *Inorg. Chem.* **2014**, *53* (10), 4791–4793. https://doi.org/10.1021/ic500217y.

(26) Blondin, G.; Girerd, J. J. Interplay of Electron Exchange and Electron Transfer in Metal Polynuclear Complexes in Proteins or Chemical Models. *Chem. Rev.* **1990**, *90* (8), 1359–1376. https://doi.org/10.1021/cr00106a001.

(27) Herrmann, C.; Elmisz, J. Electronic Communication through Molecular Bridges. *Chem. Commun.* **2013**, *49* (89), 10456. https://doi.org/10.1039/c3cc45125a.

(28) Brunold, T. C.; Gamelin, D. R.; Solomon, E. I. Excited-State Exchange Coupling in Bent Mn(III)−O−Mn(III) Complexes: Dominance of the π/σ Superexchange Pathway and Its Possible Contributions to the Reactivities of Binuclear Metalloproteins. *J. Am. Chem. Soc.* **2000**, *122* (35), 8511–8523. https://doi.org/10.1021/ja000264l.

(29) Bertrand, P. Electron Transfer between Biological Molecules Coupled by an Exchange Interaction. *Chem. Phys. Lett.* **1985**, *113* (1), 104–107. https://doi.org/10.1016/0009-2614(85)85019-3.

(30) Anderson, P. W. Antiferromagnetism. Theory of Superexchange Interaction. *Phys. Rev.* **1950**, *79* (2), 350.

(31) De Silva, A. P.; Gunaratne, H. N.; Gunnlaugsson, T.; Huxley, A. J.; McCoy, C. P.; Rademacher, J. T.; Rice, T. E. Signaling Recognition Events with Fluorescent Sensors and Switches. *Chem. Rev.* **1997**, *97* (5), 1515–1566.

(32) Nitzan, A. A Relationship between Electron-Transfer Rates and Molecular Conduction †. *J. Phys. Chem. A* **2001**, *105* (12), 2677–2679. https://doi.org/10.1021/jp003884h.

(33) McConnell, H. M. Intramolecular Charge Transfer in Aromatic Free Radicals. *J. Chem. Phys.* **1961**, *35* (2), 508–515. https://doi.org/10.1063/1.1731961.

(34) Kirk, M. L.; Shultz, D. A.; Habel-Rodriguez, D.; Schmidt, R. D.; Sullivan, U. Hyperfine Interaction, Spin Polarization, and Spin Delocalization as Probes of

Donor−Bridge−Acceptor Interactions in Exchange-Coupled Biradicals †. *J. Phys. Chem. B* **2010**, *114* (45), 14712–14716. https://doi.org/10.1021/jp102955j.

(35) Venkataraman, L.; Klare, J. E.; Tam, I. W.; Nuckolls, C.; Hybertsen, M. S.; Steigerwald, M. L. Single-Molecule Circuits with Well-Defined Molecular Conductance. *Nano Lett* **2006**, *6* (3), 5.

(36) Capozzi, B.; Xia, J.; Adak, O.; Dell, E. J.; Liu, Z.-F.; Taylor, J. C.; Neaton, J. B.; Campos, L. M.; Venkataraman, L. Single-Molecule Diodes with High Rectification Ratios through Environmental Control. *Nat. Nanotechnol.* **2015**, *10* (6), 522–527. https://doi.org/10.1038/nnano.2015.97.

(37) J.C. Cuevas, E. Scheer. *Molecular Electronics: An Intriduction to Theory and Experiment, World Scientific Publishing Co. Pte. Ltd., Hackensack, NJ. 2010*.

(38) Van Dyck, C.; Geskin, V.; Kronemeijer, A. J.; de Leeuw, D. M.; Cornil, J. Impact of Derivatization on Electron Transmission through Dithienylethene-Based Photoswitches in Molecular Junctions. *Phys. Chem. Chem. Phys.* **2013**, *15* (12), 4392. https://doi.org/10.1039/c3cp44132f.

(39) Van Dyck, C.; Geskin, V.; Cornil, J. Fermi Level Pinning and Orbital Polarization Effects in Molecular Junctions: The Role of Metal Induced Gap States. *Adv. Funct. Mater.* **2014**, *24* (39), 6154–6165. https://doi.org/10.1002/adfm.201400809.

(40) Scodeggio, M. Toward Resolving the Mystery of Galaxy Formation. 2.

(41) Latha Venkataraman. Seeing Is Believing. **2008**, *3*, 187–188.

(42) Tsuji, Y.; Movassagh, R.; Datta, S.; Hoffmann, R. Exponential Attenuation of Through-Bond Transmission in a Polyene: Theory and Potential Realizations. *ACS Nano* **2015**, *9* (11), 11109–11120. https://doi.org/10.1021/acsnano.5b04615.

(43) Xia, J.; Capozzi, B.; Wei, S.; Strange, M.; Batra, A.; Moreno, J. R.; Amir, R. J.; Amir, E.; Solomon, G. C.; Venkataraman, L.; Campos, L. M. Breakdown of Interference Rules in Azulene, a Nonalternant Hydrocarbon. *Nano Lett.* **2014**, *14* (5), 2941–2945. https://doi.org/10.1021/nl5010702.

(44) Venkatramani, R.; Wierzbinski, E.; Waldeck, D. H.; Beratan, D. N. Breaking the Simple Proportionality between Molecular Conductances and Charge Transfer Rates. *Faraday Discuss* **2014**, *174*, 57–78. https://doi.org/10.1039/C4FD00106K.

(45) Fung, E.-D.; Gelbwaser, D.; Taylor, J.; Low, J.; Xia, J.; Davydenko, I.; Campos, L. M.; Marder, S.; Peskin, U.; Venkataraman, L. Breaking Down Resonance: Nonlinear Transport and the Breakdown of Coherent Tunneling Models in Single Molecule Junctions. *Nano Lett.* **2019**, *19* (4), 2555–2561. https://doi.org/10.1021/acs.nanolett.9b00316.

(46) Ding, W.; Koepf, M.; Koenigsmann, C.; Batra, A.; Venkataraman, L.; Negre, C. F. A.; Brudvig, G. W.; Crabtree, R. H.; Schmuttenmaer, C. A.; Batista, V. S. Computational Design of Intrinsic Molecular Rectifiers Based on Asymmetric Functionalization of *N* -Phenylbenzamide. *J. Chem. Theory Comput.* **2015**, *11* (12), 5888–5896. https://doi.org/10.1021/acs.jctc.5b00823.

(47) Darancet, P.; Widawsky, J. R.; Choi, H. J.; Venkataraman, L.; Neaton, J. B. Quantitative Current–Voltage Characteristics in Molecular Junctions from First Principles. *Nano Lett.* **2012**, *12* (12), 6250–6254. https://doi.org/10.1021/nl3033137.

(48) Aradhya, S. V.; Meisner, J. S.; Krikorian, M.; Ahn, S.; Parameswaran, R.; Steigerwald, M. L.; Nuckolls, C.; Venkataraman, L. Dissecting Contact Mechanics from Quantum

Interference in Single-Molecule Junctions of Stilbene Derivatives. *Nano Lett.* **2012**, *12* (3), 1643–1647. https://doi.org/10.1021/nl2045815.

(49) Park, Y. S.; Widawsky, J. R.; Kamenetska, M.; Steigerwald, M. L.; Hybertsen, M. S.; Nuckolls, C.; Venkataraman, L. Frustrated Rotations in Single-Molecule Junctions. *J. Am. Chem. Soc.* **2009**, *131* (31), 10820–10821. https://doi.org/10.1021/ja903731m.

(50) Herrmann, C. Electronic Communication as a Transferable Property of Molecular Bridges? *J. Phys. Chem. A* **2019**, *123* (47), 10205–10223. https://doi.org/10.1021/acs.jpca.9b05618.

(51) Kamenetska, M.; Quek, S. Y.; Whalley, A. C.; Steigerwald, M. L.; Choi, H. J.; Louie, S. G.; Nuckolls, C.; Hybertsen, M. S.; Neaton, J. B.; Venkataraman, L. Conductance and Geometry of Pyridine-Linked Single-Molecule Junctions. *J. Am. Chem. Soc.* **2010**, *132* (19), 6817–6821. https://doi.org/10.1021/ja1015348.

(52) Venkatramani, R.; Wierzbinski, E.; Waldeck, D. H.; Beratan, D. N. Breaking the Simple Proportionality between Molecular Conductances and Charge Transfer Rates. *Faraday Discuss* **2014**, *174*, 57–78. https://doi.org/10.1039/C4FD00106K.

(53) Wierzbinski, E.; Venkatramani, R.; Davis, K. L.; Bezer, S.; Kong, J.; Xing, Y.; Borguet, E.; Achim, C.; Beratan, D. N.; Waldeck, D. H. The Single-Molecule Conductance and Electrochemical Electron-Transfer Rate Are Related by a Power Law. *ACS Nano* **2013**, *7* (6), 5391–5401. https://doi.org/10.1021/nn401321k.

(54) Joachim, C.; Ratner, M. A. Molecular Electronics: Some Views on Transport Junctions and Beyond. *Proc. Natl. Acad. Sci.* **2005**, *102* (25), 8801–8808. https://doi.org/10.1073/pnas.0500075102.

(55) Kirk, M. L.; Shultz, D. A.; Stasiw, D. E.; Lewis, G. F.; Wang, G.; Brannen, C. L.; Sommer, R. D.; Boyle, P. D. Superexchange Contributions to Distance Dependence of Electron Transfer/Transport: Exchange and Electronic Coupling in Oligo(*Para* -Phenylene)- and Oligo(2,5-Thiophene)-Bridged Donor–Bridge–Acceptor Biradical Complexes. *J. Am. Chem. Soc.* **2013**, *135* (45), 17144–17154. https://doi.org/10.1021/ja4081887.

(56) Ricks, A. B.; Solomon, G. C.; Colvin, M. T.; Scott, A. M.; Chen, K.; Ratner, M. A.; Wasielewski, M. R. Controlling Electron Transfer in Donor−Bridge−Acceptor Molecules Using Cross-Conjugated Bridges. *J. Am. Chem. Soc.* **2010**, *132* (43), 15427–15434. https://doi.org/10.1021/ja107420a.

(57) Tsuji, Y.; Hoffmann, R.; Strange, M.; Solomon, G. C. Close Relation between Quantum Interference in Molecular Conductance and Diradical Existence. *Proc. Natl. Acad. Sci.* **2016**, *113* (4), E413–E419. https://doi.org/10.1073/pnas.1518206113.

(58) Nishizawa, S.; Hasegawa, J.; Matsuda, K. Theoretical Investigation of the β Value of the π-Conjugated Molecular Wires by Evaluating Exchange Interaction between Organic Radicals. *J. Phys. Chem. C* **2013**, *117* (49), 26280–26286. https://doi.org/10.1021/jp407452p.

(59) Nishizawa, S.; Hasegawa, J.; Matsuda, K. Theoretical Investigation of the β Value of the π-Conjugated Molecular Wires by Evaluating Exchange Interaction between Organic Radicals. *J. Phys. Chem. C* **2013**, *117* (49), 26280–26286. https://doi.org/10.1021/jp407452p.

(60) Herrmann, C.; Elmisz, J. Electronic Communication through Molecular Bridges. *Chem. Commun.* **2013**, *49* (89), 10456. https://doi.org/10.1039/c3cc45125a.

(61) Proppe, J.; Herrmann, C. Communication through Molecular Bridges: Different Bridge Orbital Trends Result in Common Property Trends. *J. Comput. Chem.* **2015**, *36* (4), 201–209. https://doi.org/10.1002/jcc.23781.

(62) Weiss, E. A.; Ahrens, M. J.; Sinks, L. E.; Gusev, A. V.; Ratner, M. A.; Wasielewski, M. R. Making a Molecular Wire: Charge and Spin Transport through *p Ara* -Phenylene Oligomers. *J. Am. Chem. Soc.* **2004**, *126* (17), 5577–5584. https://doi.org/10.1021/ja0398215.

(63) Kirk, M. L.; Shultz, D. A.; Depperman, E. C.; Brannen, C. L. Donor−Acceptor Biradicals as Ground State Analogues of Photoinduced Charge Separated States. *J. Am. Chem. Soc.* **2007**, *129* (7), 1937–1943. https://doi.org/10.1021/ja065384t.

(64) Kramers, H. A. L'interaction Entre Les Atomes Magnétogènes Dans Un Cristal Paramagnétique. *Physica* **1934**, *1* (1), 182–192. https://doi.org/10.1016/S0031-8914(34)90023-9.

(65) Hay, P. J.; Thibeault, J. C.; Hoffmann, R. Orbital Interactions in Metal Dimer Complexes. *J. Am. Chem. Soc.* **1975**, *97* (17), 4884–4899. https://doi.org/10.1021/ja00850a018.

(66) Steenbock, T.; Shultz, D. A.; Kirk, M. L.; Herrmann, C. Influence of Radical Bridges on Electron Spin Coupling. *J. Phys. Chem. A* **2017**, *121* (1), 216–225. https://doi.org/10.1021/acs.jpca.6b07270.

(67) Shultz, D. A.; Kirk, M. L.; Zhang, J.; Stasiw, D. E.; Wang, G.; Yang, J.; Habel-Rodriguez, D.; Stein, B. W.; Sommer, R. D. Spectroscopic Signatures of

Resonance Inhibition Reveal Differences in Donor–Bridge and Bridge–Acceptor Couplings. *J Am Chem Soc* **2020**, 9.

(68) Kirk, M. L.; Shultz, D. A.; Depperman, E. C.; Brannen, C. L. Donor−Acceptor Biradicals as Ground State Analogues of Photoinduced Charge Separated States. *J. Am. Chem. Soc.* **2007**, *129* (7), 1937–1943. https://doi.org/10.1021/ja065384t.

(69) Nguyen, Q. van; Martin, P.; Frath, D.; Della Rocca, M. L.; Lafolet, F.; Barraud, C.; Lafarge, P.; Mukundan, V.; James, D.; McCreery, R. L.; Lacroix, J.-C. Control of Rectification in Molecular Junctions: Contact Effects and Molecular Signature. *J. Am. Chem. Soc.* **2017**, *139* (34), 11913–11922. https://doi.org/10.1021/jacs.7b05732.

(70) Priyadarshy, S.; Skourtis, S. S.; Risser, S. M.; Beratan, D. N. Bridge-mediated Electronic Interactions: Differences between Hamiltonian and Green Function Partitioning in a Non-orthogonal Basis. *J. Chem. Phys.* **1996**, *104* (23), 9473–9481. https://doi.org/10.1063/1.471690.

(71) Yoshizawa, K.; Tada, T.; Staykov, A. Orbital Views of the Electron Transport in Molecular Devices. *J. Am. Chem. Soc.* **2008**, *130* (29), 9406–9413. https://doi.org/10.1021/ja800638t.

(72) Tsuji, Y.; Staykov, A.; Yoshizawa, K. Orbital Views of Molecular Conductance Perturbed by Anchor Units. *J. Am. Chem. Soc.* **2011**, *133* (15), 5955–5965. https://doi.org/10.1021/ja111021e.

(73) Capozzi, B.; Dell, E. J.; Berkelbach, T. C.; Reichman, D. R.; Venkataraman, L.; Campos, L. M. Length-Dependent Conductance of Oligothiophenes. *J. Am. Chem. Soc.* **2014**, *136* (29), 10486–10492. https://doi.org/10.1021/ja505277z.

(74) Gray, H. B.; Winkler, J. R. Long-Range Electron Transfer. *Proc. Natl. Acad. Sci. U. S. A.* **2005**, *102* (10), 3534–3539.

(75) Durola, F.; Sauvage, J.-P.; Wenger, O. S. Sterically Non-Hindering Endocyclic Ligands of the Bi-Isoquinoline Family. *Chem Commun* **2006**, No. 2, 171–173. https://doi.org/10.1039/B513222C.

(76) Wenger, O. S. Photoinduced Electron and Energy Transfer in Phenylene Oligomers. *Chem. Soc. Rev.* **2011**, *40* (7), 3538. https://doi.org/10.1039/c1cs15044h.

(77) Pauling, L.; Wheland, G. W. The Nature of the Chemical Bond. V. The Quantum-Mechanical Calculation of the Resonance Energy of Benzene and Naphthalene and the Hydrocarbon Free Radicals. 14.

(78) Wheland, G. W.; Pauling, L. A Quantum Mechanical Discussion of Orientation of Substituents in Aromatic Molecules. *J. Am. Chem. Soc.* **1935**, *57* (11), 2086–2095. https://doi.org/10.1021/ja01314a017.

(79) L. Pauling, The Nature of the Chemical Bond, Cornell University Press, Ithaca, NY, 3rd Edn, 1960.

(80) F. Weinhold and C. R. Landis, Valency and Bonding: A Natural Bond Orbital Donor–Acceptor Perspective, Cambridge University Press, Cambridge, UK; New York, 2005.

(81) Beebe, J. M.; Engelkes, V. B.; Miller, L. L.; Frisbie, C. D. Contact Resistance in Metal−Molecule−Metal Junctions Based on Aliphatic SAMs: Effects of Surface Linker and Metal Work Function. *J. Am. Chem. Soc.* **2002**, *124* (38), 11268–11269. https://doi.org/10.1021/ja0268332.

(82) ZULETA, J. A.; BURBERRY, M. S.; EISENBERG, R. Elsevier Science Publishers BV, Amsterdam-Printed in The Netherlands. *Coord. Chem. Rev.* **1990**, *97*, 47–64.

(83) Cummings, S. D.; Eisenberg, R. Tuning the Excited-State Properties of Platinum (II) Diimine Dithiolate Complexes. *J. Am. Chem. Soc.* **1996**, *118* (8), 1949–1960.

(84) Hissler, M.; McGarrah, J. E.; Connick, W. B.; Geiger, D. K.; Cummings, S. D.; Eisenberg, R. Platinum Diimine Complexes: Towards a Molecular Photochemical Device. *Coord. Chem. Rev.* **2000**, *208* (1), 115–137.

(85) Krishna, M. M. G. Excited-State Kinetics of the Hydrophobic Probe Nile Red in Membranes and Micelles. *J. Phys. Chem. A* **1999**, *103* (19), 3589–3595. https://doi.org/10.1021/jp984620m.

(86) Paw, W.; Cummings, S. D.; Mansour, M. A.; Connick, W. B.; Geiger, D. K.; Eisenberg, R. Luminescent Platinum Complexes: Tuning and Using the Excited State. *Coord. Chem. Rev.* **1998**, *171*, 125–150.

(87) Zuleta, J. A.; Burberry, M. S.; Eisenberg, R. Platinum(II) Diimine Dithiolates. New Solution Luminescent Complexes. *Coord. Chem. Rev.* **1990**, *97*, 47–64. https://doi.org/10.1016/0010-8545(90)80079-9.

(88) Zuleta, J. A.; Bevilacqua, J. M.; Proserpio, D. M.; Harvey, P. D.; Eisenberg, R. Spectroscopic and Theoretical Studies on the Excited State in Diimine Dithiolate Complexes of Platinum(II). *Inorg. Chem.* **1992**, *31* (12), 2396–2404. https://doi.org/10.1021/ic00038a019.

(89) Zuleta, J. A.; Chesta, C. A.; Eisenberg, R. Square-Planar Complexes of Platinum(II) That Luminesce in Fluid Solution. *J. Am. Chem. Soc.* **1989**, *111* (24), 8916–8917. https://doi.org/10.1021/ja00206a023.

(90) Adams, C. J.; Fey, N.; Parfitt, M.; Pope, S. J. A.; Weinstein, J. A. Synthesis, Structures and Properties of a New Series of Platinum–Diimine–Dithiolate Complexes. *Dalton Trans.* **2007**, No. 39, 4446. https://doi.org/10.1039/b709252k.

(91) Hao, H.; Zheng, X.; Dai, Z.; Zeng, Z. Gate-Induced Switching in Single-Molecule Magnet Mn ^{III} Cu ^{II}. *J. Appl. Phys.* **2011**, *110* (2), 023702. https://doi.org/10.1063/1.3610448.

(92) Matsuura, Y. Current Rectification in Nickelocenylferrocene Sandwiched between Two Gold Electrodes. *J. Chem. Phys.* **2013**, *138* (1), 014311. https://doi.org/10.1063/1.4773404.

(93) Zotti, L. A.; Leary, E.; Soriano, M.; Cuevas, J. C.; Palacios, J. J. A Molecular Platinum Cluster Junction: A Single-Molecule Switch. *J. Am. Chem. Soc.* **2013**, *135* (6), 2052–2055. https://doi.org/10.1021/ja3100116.

(94) Weng, T.; DeBrincat, D.; Arcisauskaite, V.; McGrady, J. E. In Search of Structure–Function Relationships in Transition-Metal Based Rectifiers. *Inorg Chem Front* **2014**, *1* (6), 468–477. https://doi.org/10.1039/C4QI00038B.

(95) Park, J.; Belding, L.; Yuan, L.; Mousavi, M. P. S.; Root, S. E.; Yoon, H. J.; Whitesides, G. M. Rectification in Molecular Tunneling Junctions Based on Alkanethiolates with Bipyridine–Metal Complexes. *J. Am. Chem. Soc.* **2021**, *143* (4), 2156–2163. https://doi.org/10.1021/jacs.0c12641.

(96) Barone, V.; Cacelli, I.; Ferretti, A.; Visciarelli, M. Transport Properties of Binuclear Metal Complexes of the VIII Group Using a Simplified NEGF-DFT Approach. *Phys. Chem. Chem. Phys.* **2013**, *15* (27), 11409. https://doi.org/10.1039/c3cp50974e.

(97) Liu, R.; Ke, S.-H.; Yang, W.; Baranger, H. U. Organometallic Molecular Rectification. *J Chem Phys* 6.

(98) Lee, C.; Yang, W.; Parr, R. G. Development of the Colle-Salvetti Correlation-Energy Formula into a Functional of the Electron Density. *Phys. Rev. B* **1988**, *37* (2), 785–789. https://doi.org/10.1103/PhysRevB.37.785.

(99) Kirk, M. L.; Dangi, R.; Habel-Rodriguez, D.; Yang, J.; Shultz, D. A.; Zhang, J. Transferrable Property Relationships between Magnetic Exchange Coupling and Molecular Conductance. *Chem. Sci.* **2020**, 10.1039.D0SC04350H. https://doi.org/10.1039/D0SC04350H.

(100) Taylor, J.; Guo, H.; Wang, J. *Ab Initio* Modeling of Quantum Transport Properties of Molecular Electronic Devices. *Phys. Rev. B* **2001**, *63* (24), 245407. https://doi.org/10.1103/PhysRevB.63.245407.

(101) Chen, F.; Tao, N. J. Electron Transport in Single Molecules: From Benzene to Graphene. *Acc. Chem. Res.* **2009**, *42* (3), 429–438. https://doi.org/10.1021/ar800199a.

(102) Batra, A.; Darancet, P.; Chen, Q.; Meisner, J. S.; Widawsky, J. R.; Neaton, J. B.; Nuckolls, C.; Venkataraman, L. Tuning Rectification in Single-Molecular Diodes. *Nano Lett.* **2013**, *13* (12), 6233–6237. https://doi.org/10.1021/nl403698m.

(103) Ding, W.; Koepf, M.; Koenigsmann, C.; Batra, A.; Venkataraman, L.; Negre, C. F. A.; Brudvig, G. W.; Crabtree, R. H.; Schmuttenmaer, C. A.; Batista, V. S. Computational Design of Intrinsic Molecular Rectifiers Based on Asymmetric Functionalization of *N* -Phenylbenzamide. *J. Chem. Theory Comput.* **2015**, *11* (12), 5888–5896. https://doi.org/10.1021/acs.jctc.5b00823.

(104) Barone, V.; Cacelli, I.; Ferretti, A.; Visciarelli, M. Transport Properties of Binuclear Metal Complexes of the VIII Group Using a Simplified NEGF-DFT Approach. *Phys. Chem. Chem. Phys.* **2013**, *15* (27), 11409. https://doi.org/10.1039/c3cp50974e.

(105) Tsuji, Y.; Staykov, A.; Yoshizawa, K. Molecular Rectifier Based on π–π Stacked Charge Transfer Complex. *J. Phys. Chem. C* **2012**, *116* (3), 2575–2580. https://doi.org/10.1021/jp209547a.

(106) Kondo, M.; Tada, T.; Yoshizawa, K. A Theoretical Measurement of the Quantum Transport through an Optical Molecular Switch. *Chem. Phys. Lett.* **2005**, *412* (1–3), 55–59. https://doi.org/10.1016/j.cplett.2005.05.126.

(107) Zhuang, M.; Ernzerhof, M. Reversibility and Transport Properties of Dithienylethene Photoswitches. *J. Chem. Phys.* **2009**, *130* (11), 114704. https://doi.org/10.1063/1.3086078.

(108) Zhuang, M.; Ernzerhof, M. Mechanism of a Molecular Electronic Photoswitch. *Phys. Rev. B* **2005**, *72* (7), 073104. https://doi.org/10.1103/PhysRevB.72.073104.

(109) Paulsson, M.; Brandbyge, M. Transmission Eigenchannels from Nonequilibrium Green's Functions. *Phys. Rev. B* **2007**, *76* (11), 115117. https://doi.org/10.1103/PhysRevB.76.115117.

(110) Stokbro, K.; Taylor, J.; Brandbyge, M. Do Aviram−Ratner Diodes Rectify? *J. Am. Chem. Soc.* **2003**, *125* (13), 3674–3675. https://doi.org/10.1021/ja028229x.

(111) Huang, B.; Zhang, F.; Yang, Y.; Zhang, Z. Length-Dependent Electronic Transport Properties of the ZnO Nanorod. *Micromachines* **2018**, *10* (1), 26. https://doi.org/10.3390/mi10010026.

(112) Odell, A.; Delin, A.; Johansson, B.; Rungger, I.; Sanvito, S. Investigation of the Conducting Properties of a Photoswitching Dithienylethene Molecule. *ACS Nano* **2010**, *4* (5), 2635–2642. https://doi.org/10.1021/nn100217r.

(113) Tsuji, Y.; Staykov, A.; Yoshizawa, K. Orbital View Concept Applied on Photoswitching Systems. *Thin Solid Films* **2009**, *518* (2), 444–447. https://doi.org/10.1016/j.tsf.2009.07.037.

(114) Pan, J. B.; Zhang, Z. H.; Ding, K. H.; Deng, X. Q.; Guo, C. Current Rectification Induced by Asymmetrical Electrode Materials in a Molecular Device. *Appl. Phys. Lett.* **2011**, *98* (9), 092102. https://doi.org/10.1063/1.3556278.

(115) Staykov, A.; Nozaki, D.; Yoshizawa, K. Photoswitching of Conductivity through a Diarylperfluorocyclopentene Nanowire. *J. Phys. Chem. C* **2007**, *111* (8), 3517–3521. https://doi.org/10.1021/jp067612b.

(116) Chang, W.; Congreve, D. N.; Hontz, E.; Bahlke, M. E.; McMahon, D. P.; Reineke, S.; Wu, T. C.; Bulović, V.; Van Voorhis, T.; Baldo, M. A. Spin-Dependent Charge Transfer State Design Rules in Organic Photovoltaics. *Nat. Commun.* **2015**, *6*, 6415. https://doi.org/10.1038/ncomms7415.

(117) Staykov, A.; Nozaki, D.; Yoshizawa, K. Photoswitching of Conductivity through a Diarylperfluorocyclopentene Nanowire. *J. Phys. Chem. C* **2007**, *111* (8), 3517–3521. https://doi.org/10.1021/jp067612b.

(118) Quantum ATK Manual, Https://Docs.Quantumatk.Com/Manual/Manual.Html.

(119) QuantumWise Tutorials; Https://Docs.Quantumatk.Com/Tutorials/Tutorials.Html.

Chapter 3

Vibronic Spin-orbit Coupling Contributions to Spin Forbidden Non-Radiative Decay Pathways

3.1 Introduction

Square planar complexes of the transition metal complexes were studied earlier for their photoluminescence properties in the solid state and at low temperature in a rigid frozen glass state. At the beginning, observation of their luminescence properties were limited only in the solid state.[1] Only a few studies were reported on the synthesis and study of photophysical properties of these complexes prior to Zuleta and co-workers in 1990[1]. They published observations on the luminescence properties of fluid solutions of Pt complexes with various diimines (bpy, phen, and alkyl or aryl substituted derivatives of them) and dithiolene chelating ligands. Their study was extended to include solvatochromism effects for both electronic absorption spectroscopy and emission spectroscopy, and later thermochromism was investigated as well. Vogler and Kunkely in 1981 studied ligand to ligand charge transfer transitions in a (2,2'-bipyridine)(3,4-toluenedithiolato)Pt(II) complex[2]. Following this, Vogler and co-workers in 1984 reported solvatochromism studies in complexes with diimine and dithiolate ligands.[3] Matsubayashi et al., in 1984 and 1988, had published their work on related platinum (II) complexes that also contained diimine and dithiolate ligands. Studies of charge transfer complexes of Pt(II) coordinated with both diimine (easily reduceable) and dithiolate (easily oxidizable) ligands have been continuously investigated since then.[4] These molecules are the earliest among the transition metal complexes studied for their photoluminescent

properties.[1] The research interest in the Pt(II) complexes has been increased due to its flexible d^8 configuration, as well as having unique electronic properties. Most notably, its ligand-to-ligand charge transfer transition in the visible region possesses a relatively long lived excited state, making it ideal for fundamental research.[5] [6] The field of inorganic photochemistry has been dominated by the study of platinum dithiolate complex excited state processes.[7] They are spectroscopically rich with unusual photophysical properties. Applications of these complexes include solar energy conversion, photoluminescent probes, light driven information devices, nonlinear optics, and artificial photosynthetic receptors.[8] [4] [9] Over the years, research work on these complexes has been constantly growing, focusing on the synthesis of highly stable complexes by modifying the donor and acceptor ligands. This may allow for more control of the excited states processes.[7] Among others, Eisenberg and Cummings have pioneered the systematic study of tuning the excited state properties of diimine-Pt(II)-dithiolate complexes by applying ligand variations on a related series of platinum complexes.[6] The research work done by our group is focused on understanding the mechanism of relaxation from the excited state to ground state by these diimine-Pt-dichalcogenolenes complexes. This is accomplished by systematically changing the donor atoms, as this enhances the anisotropic covalency and rotates the metal d-orbitals toward the softer coordinating atom(s). As a consequence of the asymmetry, the enhanced spin orbit coupling (SOC) mediated higher rates of inter-system crossing (ISC), which was previously unexplained, despite the decades of research on related complexes. In our previous work, we observed a dramatic reduction of excited state lifetimes compared to symmetric donor atoms coordinated to Pt as shown in Figure 3.*10*.[9] [5] The consequence of anisotropic covalency on relaxation is in the in-plane

distortion, which resembles the dynamic in-plane b_2 antisymmetric S-Pt-S vibrations, where the Pt d-orbital rotates towards the softer ligand. Thus, statistically inducing the vibronic spin-orbit coupling (vSOC) mechanism to facilitate enhanced ISC to relax from the lowest triplet (T_1) to the singlet ground state (S_0) for the parent (bdt)Pt(bpy) complex[9] as shown in Figure 3.*10*.

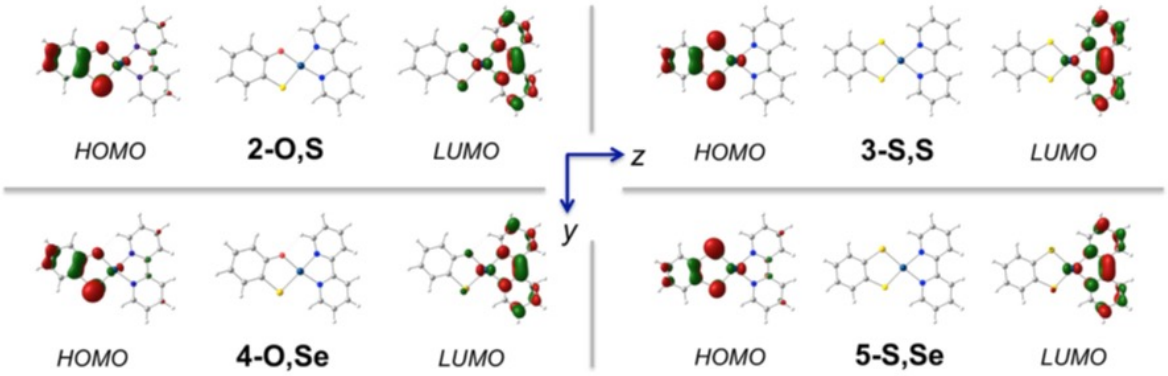

Figure 3.10: DFT calculated molecular wavefunction map of (bpy)Pt(O, S), (bpy)Pt(S,S), (bpy)Pt(O,Se) and (bpy)Pt(S,Se) respectively. Platinum d-orbital has notably rotated toward the more covalent dichogenolenes in the mixed dichalcogenes complexes.

Following the absorption of electromagnetic radiation by the chromophore, higher electronic excited states are populated. Photons are then emitted during the relaxation processes, defined as fluorescence and/or phosphorescence. These are two important processes after interaction of light with matter.[10] In the case of the Pt complexes with diimine and dithiolate ligands, photoluminescence occurs in the visible and near IR region. The de-excitation accompanied by the phosphorescence process is spin forbidden (T_1 to S_0) in this system.[9] ISC is the mechanism for decay from the excited state to the ground state, which bears a different spin multiplicity. The ISC is a spin forbidden process which is overcome by SOC.[5] In some complexes, molecular symmetry eliminates the first order,

out of state SOC, slowing ISC to allow relaxation to the state of different multiplicity. In this case, the importance of the Hertzberg-Teller vSOC theory appears on depopulating the T_1 state in the systems which are also forbidden by symmetry.[11 12]

A more specific explanation on the importance of SOC can be discussed by using a Jablonski Diagram, such as the one depicted below in Figure 3.*11*. After photoexcitation of the closed shell singlet electronic state of the (diimine)Pt(II)(dithiolate) chromophore, the higher excited singlet states (S_n) are populated. Usually, the higher singlet excited state depopulation occurs by fast internal conversion ($10^{-11} - 10^{-9}$ s) from higher singlet excited (S_n, n≥ 2) to the lowest excited singlet state. It is a relatively faster process than ISC ($10^{-10} - 10^{-8}$ s). The de-excitation from the lowest singlet excited state occurs by three types of radiative and/or non-radiative intramolecular mechanisms: fluorescence (radiative de-excitation process between the state of same multiplicity $S_1 \longrightarrow S_0$), internal conversion (IC) (non-radiative de-excitation process from $S_1 \longrightarrow S_0$) and ISC (can be radiative or non-radiative) to the excited triplet states (T_n).[13] When the molecule goes into the triplet manifold by spin-orbit mediated ISC, it quickly relaxes back to the lowest triplet state by IC. Once the molecule goes into T_1 by ISC, then the excited state depopulation process must occur by ISC, mediated by SOC. If the process is forbidden by the symmetry (such as that in rigorous C_{2v} symmetry of the 2,2'-bipyridine and 1,2-benzene dithiol complexes)[5], then the molecule must relax the C_{2v} symmetry via the dynamic molecular vibrations. These dynamic molecular vibrations allow the SOC to facilitate ISC, then the process of ground state repopulation can occur as shown in Figure 3.*11*.[9 11 12 14] The SOC induced by the dynamic molecular vibration is termed as vSOC and the mechanism of relaxation is reliant on molecular vibrations. Evidence of the vSOC mechanism to relax

excited electronic state to the ground state has been studied on (S,S)Pt(bpy) complexes as shown in Figure 3.*10*, since they have rigorous C_{2v} symmetry. The transition from T_1 to S_0 is both spin and symmetry forbidden for this complex. Complete active space self-consistent field (CASSCF) calculated SOC matrix elements between T_1 and S_0 states is zero, as expected. Thus, the only route of de-excitation is through vSOC to allow ISC. The observed excited state decay lifetime for this process is 620 ns.[5] In the case of chromophores that are distorted statically and the distortion is similar to the normal vibrational modes of the parent complex, a vSOC-like mechanism is induced to relax the excited state population quicker. These types of complexes must exhibit shorter lifetimes compared to the parent complex. The study done by our research group has reported observed shorter lifetimes for the distorted molecules along S-Pt-S anti-symmetric stretch by changing the donor atoms within chalcogens series (O, S); (S, Se); and (O, Se) as depicted in Figure 3.10. The expression for the vSOC is given by equation 3.1:

$$\frac{\partial}{\partial Q}\langle {}^1_1A|\mathcal{H}_{SO}|{}^3_1A\rangle \neq 0 \text{ for } \Gamma_Q = a_2, b_1, b_2 \qquad (3.1)$$

where H_{SO} is the spin-orbit operator, and Γ_Q is the irreducible representation of the C_{2v} symmetry normal modes responsible for promoting vSOC.[12] The vSOC Herzberg-Teller coupling[15] term is similar to the mechanism to overcome Laporte forbiddenness of ligand field transitions in centrosymmetric transition metal complexes through vibronic couplings.

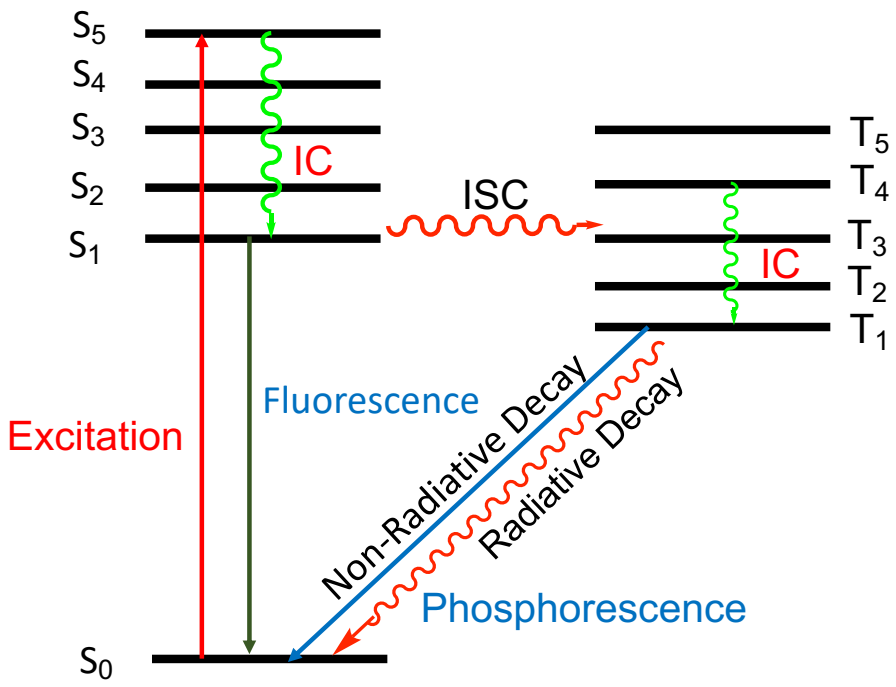

Figure 3.11: Jablonski diagram showing the excited state photo-processes after absorption of electromagnetic radiation by the molecule. IC is non-radiative transition between the states of same spin multiplicity, ISC is non-radiative transition between the states of different multiplicity, fluorescence and phosphorescence are radiative de-excitation processes.

Understanding of molecular excited state processes is important for controlling them, and for their potential use in molecular photonics and electronics fields. To gain insight into atomic and vibronic level control of excited state lifetimes, our group has initiated the study of excited state lifetimes of such molecules which are distorted along two coordinates (y and z). Here we have synthesized and studied the new diimine platinum (II) dichalcogenolenes. In this study, we aim to understand structure property correlations to gain insight into vSOC promoted ISC to repopulate the ground electronic state of the molecule via radiative and non-radiative decay pathways. One of the most recent works in the field has proposed the idea of reverse intersystem crossing (rISC) to control thermally activated delayed fluorescence.[16] The approach we have used to study

the vibrational mode that depopulates the molecule from T_1 is by synthetically introducing asymmetry to the molecule along three different axes of rotation. This study will have broad reaching impacts on nearly all fields of chemical research and to advance technology in the development process of molecule based solar energy conversion devices, photochemical processes, optoelectronics, solar energy conversions, photo-driven molecular motors, and photonics.

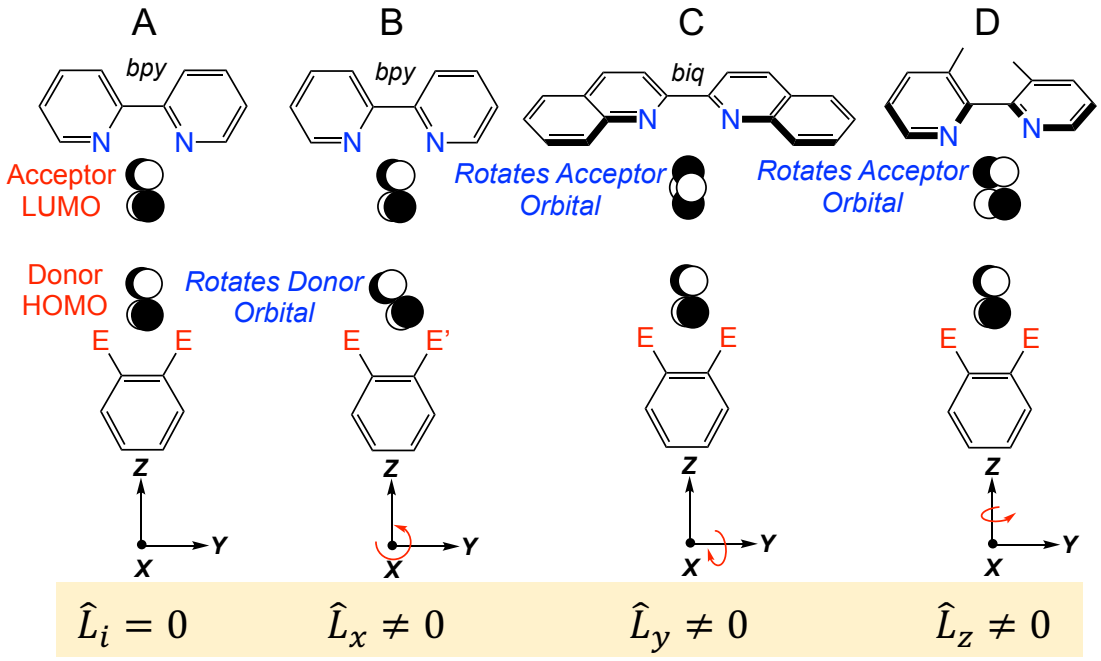

Figure 3.12: Metal d-orbital rotation by introducing the static distortions along three vibrational rotational axes to lower the symmetry. The distortion along x -axis is achieved by introducing the asymmetric covalency in on donor atom from (S,S) to (O,S), the distortion along y-axis has achieved by the replacing bi-pyridine to biquinoline and along z-axis has done by replacing bipyridine ligand with 2,2-methyl bipyridine ligand.

To test our proposed hypothesis, four complexes are needed: one of them is the parent complex (S,S)Pt(bpy) and other three are statically distorted along each respective cartesian coordinate of the parent complex as shown in Figure 3.12. We have adapted spectroscopic data from published work by our group for the parent compound

(S,S)Pt(bpy) and one of the symmetry lowered complexes, (bipyridine)Pt(mercaptothiol), also commonly known as (O,S))Pt(bpy). The other two complexes are presented in Figure 3.*12* using biquinoline and dimethyl bipyridine acceptor ligands complexed with Pt(II).

3.2 Synthesis, Characterization and Spectroscopy of (2,2'-biquinoline)Pt (II)(1,2-benzenedithiol) Complex, (biq)Pt(bdt).

3.2.1 Background

The use of the 2,2'-biquinoline ligand to synthesize a photoluminescent ruthenium complex was reported in the early 1980s by Belser.[17] Its steric effect on absorption and emission properties have been studied in detail by Barigelletti and co-workers in 1983.[18] [19] They synthesized the ruthenium complexes $Ru(biq)_3^{2+}$, $Ru(bpy)_2(biq)^{2+}$ and $Ru(biq)_3^{2+}$by using bipyridine and biq ligands. They reported a red shift of the charge transfer band with reduced intensity, due to a low lying π-acceptor orbital. They also reported a long Ru-N bond length due to a steric effect by the (biq) ligands. This resulted in the lowered intensity of the charge transfer band, which represents the smaller metal-ligand orbital overlap. They have also exhibited a decreased field strength of the steric biq ligand.[18] This inspired the study of photophysical properties with various solvents by the Belser and Juris group in 1985.[20] Study of transition metal photophysical properties continues to this day, to explore the steric features of the biq compared to other commonly used diimine ligands such as bipyridine and phenanthroline. Based on the reported literature, the biq ligand exhibits steric effects that sufficiently distort (diimine)Pt(dichalcogenolene) molecules to lower the symmetry from C_{2v} to C_s, inducing a static vSOC effect that mimics the normal vibrational modes of parent complex. Thus,

relaxation of these complex in our study is expected to be faster than in the parent complex. Here, we have used a combination of electronic absorption, transient spectroscopies, and group theoretical arguments to understand the remarkable dependence of excited state lifetimes as a function of these static distortions and anisotropic covalency.

3.2.2 Synthesis and Characterization

Synthesis of (biq)Pt(bdt) is carried out by using a modified procedure from previously reported syntheses.[5 9] At first, $(DMSO)_2PtCl_2$ was synthesized following the literature method.[21] 300 mg (72 mmol, 1eq.) of Potassium tetra-chloroplatinate (II) (K_2PtCl_4) is reacted with 3 ml (1.5 mmol, 2.2 eq) of dimethyl sulfoxide in 20 ml of distilled water for 2 hours at room temperature. The light-yellow complex was filtered and washed with methanol, water, hexane and finally with diethyl ether. The product was dried under vacuum, then the pale-yellow micro-crystalline product was collected with 94% yield. The structure was confirmed by NMR spectroscopy. The product was reacted with the biq ligand without further purification.

Synthesis of $biqPtCl_2$ was performed by following a modified procedure reported in the literature.[22 23 24] A mixture of 300 mg (0.71 mmol) of biq ligand and one equivalent (0.182 mg) of $(DMSO)_2PtCl_2$ was dissolved in acetone and refluxed for 30h at 50°C. The color of the solution turned brick red within 24h. The solvent was partially removed, and the left-over reaction mixture was precipitated by adding pentane. The precipitate was filtered, then washed with pentane and diethyl ether. NMR of crude $biqPtCl_2$ showed a significant amount of unreacted biq ligand in the product. Thus, unreacted biq ligand was

removed by recrystallizing in DMF and diethyl ether. The structure of biqPtCl$_2$ was characterized by NMR. The chemical shift (δ) of proton NMR ($CDCl_3$, 300 MHz, 298 K) data collected in deuterated DMSO (four signals were observed because of symmetric nature of ligand 12 protons); 7.98 ppm (m, 4H, pyridine and additional benzene ring), 7.46 ppm (m, 4H, pyridine), 7.22 ppm (m, 2H, pyridine and benzene ring), 6.98 ppm (m, 2H, pyridine and benzene ring).

Synthesis of (biq)Pt(bdt) was carried out by following the reported procedure in literature.[5] 100 mg (1eq, 0.19 mmol) of biq$_2$PtCl$_2$ was dissolved in dry degassed dichloromethane. 17.0 mg (1.3 eq) of 1,2 benzene dithiol was dissolved in dry degassed methanol and 16.0 mg (3eq, 0.247 mmol) KOH was dissolved in dry degassed methanol. 1,2 benzene dithiol was deprotonated and mixed in the stirring solution of biqPtCl$_2$. The solution turned a bluish green color immediately. The solution was left to stir for 1h at room temperature. Solvent was then removed partially, and the precipitate was filtered. The residue was purified by running a column in CH_2Cl_2 with 2% methanol as eluant. The bluish amorphous solid complex is obtained as pure compound with 68% yield corresponding to the quantity of biqPtCl$_2$ used.

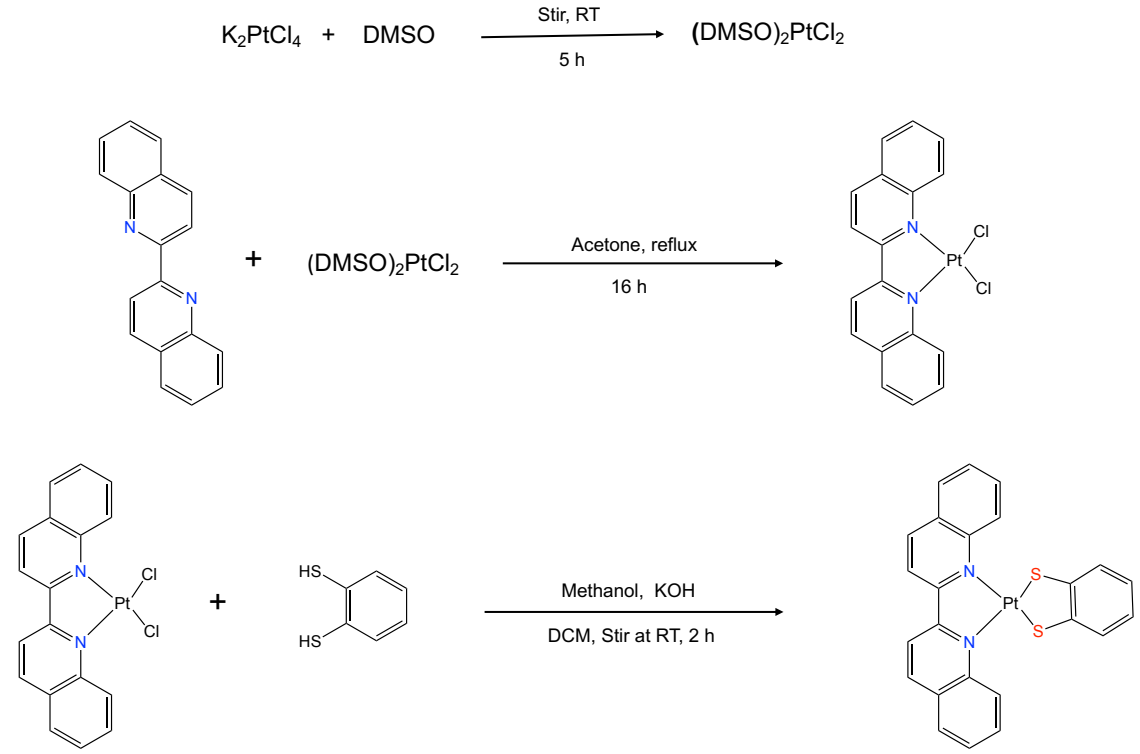

Figure 3.13: Synthetic scheme of (bdt)Pt(biq) complex. Top; synthesis of $(DMSO)_2PtCl_2$, middle; synthesis of $biqPtCl_2$ and bottom; synthesis of (bdt)Pt(biq) final complex by stirring the mixture of reactants in room temperature for 1 h.

Characterization of the final complex was performed by MS, NMR, and elemental analysis. High-resolution electrospray ionization (ESI) mass spectrometry (m/z): calculated for $[C_{24}H_{16}N_2PtCl_2]$; 591.04, observed $(M+Na)^+$ 614.03. Observed Platinum isotope pattern is also in good agreement with the calculated isotope pattern. ^1H NMR data collected by dissolving in deuterated dichloromethane (300 MHz, 298K) shows eight proton signals due to their symmetric structure by the presence of a mirror plane. The chemical shifts for the protons: 9.1 ppm (d, 2H pyridine coordinated to platinum), 9.04 ppm (d, 2H, pyridine ring), 8.9 ppm (d, 2H), 8.28 ppm (d, 2H), 8.14 ppm (m, 2H), 7.9 ppm (m, 2H) 7.22 ppm (m, 2H, aromatic protons from 1,2 benzene dithiol), 6.68 ppm (m, 2H, aromatic protons from 1,2 benzene dithiol). The third method of characterization used

was elemental analysis which is in good agreement with the calculated composition. This was done by adding 0.5 mole of CH_2Cl_2 as co-crystalized solvent molecule for $[C_{24}H_{16}N_2PtCl_2]$: C, 48.42; H, 2.98; N, 4.61; observed percentage of C, 48.04; H, 2.62; N, 4.52.

3.2.3 Electronic Structure and Spin-Orbit Coupling Matrix Element Calculation

Spin restricted geometry optimization computations for a gas phase molecule of (bdt)Pt(biq) and the parent complex (bdt)Pt(bpy), and further electronic structure calculations, were performed at density functional (DFT) level of theory using the Gaussian '09 version C.01 software package.[25] The calculations were performed with the B3LYP[26] exchange correlation functional usnig the def2-tzvp basis set,[27] and the basis sets were generated from the EMSL basis set exchange website for all atoms except for Pt.[28 29] An effective core potential was applied for Platinum.[30] Time dependent DFT (TD-DFT) methods were used to analyze the singlet and triplet excited states, as applied in Gaussian 09 software package.[31 32 33 34 35 36] Frontier molecular orbitals were generated from the optimized ground state computations.

The CASSCF computational method was employed to calculate the reduced SOC matrix element between lowest triplet state (T_1) and the electronic ground state (S_0) by using the Orca 4.0 software program.[37 38] All-electron basis sets were used to construct the 4-electron-in-3-orbital (HOMO-1, HOMO and LUMO) active space. Input files for these calculations were generated from the optimized geometries by using the same basis set

and functional. Previously optimized molecular orbitals were used as the input orbitals for the calculation of SOC matrix element.

S K-edge XAS computations were conducted using ORCA (version 3.0.3)[37] on optimized geometries by using def2-tzvp basis set generated from EMSL website and B3LYP functional. This is the basis set and functional also used for the optimization of geometry along with zero-order regular approximation (ZORA).

3.2.4 Experimental Details

Electronic absorption spectroscopy was collected on a Hitachi U-4100 UV-vis-NIR double beam spectrophotometer, capable of scanning a wavelength between 180 nm to 3200 nm. The spectrometer uses a double-beam configuration at 2.0 nm resolution. Baseline was performed by using the solvent dichloromethane and background data was collected to correct for the residual absorption from the solvent which is automatically subtracted from the sample spectrum by the Hitachi Grams software. The sample was loaded into a micro-volume quartz cuvette. Dry degassed dichloromethane (DCM) was used to collect the absorption spectrum. All the data were recorded at room temperature.

Transient absorption spectra were collected using an Edinburgh LP920 laser flash photolysis spectrometer with the following set up: the excitation source was Q-switched Continuum Surelite I-10 ND: YAG laser a 5 ns pulse width operating 10 Hz. The excitation pulse was passed through a Continuum Surelite OPO system to generate excitation wavelengths in the 400-710 nm range. The pulsed laser source (5mJ/pulse) was tuned to the maximum absorption wavelength of the sample and focused onto a quartz fluorescence sample cuvette (Starna Cell Inc. path length: 5 mm).[5] Detection of the signal

was performed by using a DH720 ICCD camera mounted on a TMS300 symmetrical Czerny-Turner triple grating monochromator. For the measurement of the kinetic data, a Xe lamp was used as a light source and the data was collected at ns – ms time scales. To detect the kinetic traces, a red sensitive Hamamatsu R928 photomultiplier was used covering 185-870 nm region. Signals obtained from the PMT were recorded on a Tektronix TDS3012C digital storage oscilloscope. The sample was prepared in dry dichloromethane and sample solution was degassed by purging nitrogen gas for half an hour just before data collection.

The emission spectrum and lifetime data were collected by using an Edinburgh FLS 980, a computer controlled modular spectrofluorometer which has capacity to count single photon sensitivity from UV to near IR spectral range (200 nm − 1700 nm). The spectra of (bdt)Pt(biq) wer collected in a solution of dry DCM. The solution was degassed by purging with nitrogen for 20 minutes prior to the experiment. The absorption of solution was kept less than 0.3 to avoid self-absorption. The sample holder has the hexagonal box with two chambers. For the emission photon count, the FLS980 has a high-gain photomultiplier (PMT) detector with high sensitivity. To analyze whether the sample degraded during excitation process or not, we recorded electronic absorption spectra before and after collecting photoluminescence data.

Lifetime data were obtained by plotting the phosphorescence decay vs time and the following equation was fit to the data.

$$Fit = A + B_1 e^{\left(-\frac{t}{t_1}\right)} + B_2 e^{\left(-\frac{t}{t_2}\right)} + B_1 e^{\left(-\frac{t}{\tau_3}\right)} + B_1 e^{\left(-\frac{t}{t_4}\right)} \qquad (3.2)$$

Here, A is the calculated numerical value that accounts for a constant detector background, B is a pre-exponential factor, τ is the calculated lifetime, and the quality of the data fitting is given b χ^2. A value of χ^2 close to unity indicates a good fit. Having a relatively short lifetime $(< 50\mu s)$, as suggested by the user guide from Edinburgh Instruments, a calculation of instrument response function was performed. Both a re-convolution and tail fitting were performed, which provides decay analyses, lifetimes, pre-exponential factors and numerical values for the background level, as well as other derived parameters.[39]

A sample for resonance Raman analysis was prepared inside the glove box as a solid-state matrix, consisting of finely ground NaCl/Na_2SO_4 in 10:1 ratio by weight. The powder form of sample was ground together with the powder matrix until it was uniform. The finely ground solid sample was loaded into a quartz capillary tube, and the tube was flame-sealed immediately upon removing it from the glove box. The resonance Raman data was collected by exciting the molecule using available laser line energies. From a Coherent Innova Ar^+ laser source, the following wavelengths were used: 458 nm, 488 nm, 514 nm; and the Coherent Innova Kr^+ laser source provided lines at 407 nm, 568 nm, and 614 nm. These lines are on resonance with an LL'CT absorption band, thus the enhancement of Raman modes as a function of energy of excitation can be observed on the spectrum collected at each energy of excitation. This indicates that the LL'CT transition is coupled with specific excited state distortions as a consequence of electron density redistribution.[40] There is possibility of thermal degradation of sample during excitation, thus, the laser power at the sample was kept to 40 and 100 mW.[41]

The S K-edge X-ray absorption spectra of (bdt)Pt(biq) was collected at Stanford Synchrotron Radiation Light source under standard ring conditions. These include 3 GV and ~500 mA on the unfocused 20-pole 2 T wiggler side-station 4-3, equipped with a liquid N_2 cooled Si (111) double-crystal monochromator for energy selection. The sample was collected in the solid, ground powder form on Kapton tape, and the signal was collected at 90° to the incident beam to avoid fluorescence self-absorption. The beam line was optimized at 2740 eV. To calibrate the monochromator, $Na_2S_2O_3.5H_2O$ was used with maximum pre-edge feature at 2470.02 eV. S K-edge spectra was collected in the energy range of 2420-2740 eV using an unfocused beam in a He-purged fly path at room temperature, using a passivated Implanted Planar Silicon (PIPS) fluorescence detector (CANBERRA). ATHENA, which is a part of the Demeter software package version 0.9.24[11] was used to calibrate the energy, for background correction, data averaging, and normalization. The pre-edge features were fit using ATHENA and pseudo-Voigt functions, and one arctangent step line function for the rising edge. Integration of the pseudo-Voigt functions were performed to define the integrated area of each peak. All parameters of the pseudo-Voigt peaks were allowed to float.

3.2.5 Results and Discussion

Room temperature EAS data is shown in Figure 3.14. An observed spectral feature at 13,300 cm^{-1} is assigned as the one electron promotion from donor to acceptor, which is referred to as the ligand to ligand charge transfer (LLCT) transition.[5 9] Based on the TD-DFT calculation, the low energy intense peak at 13 300 cm^{-1} has been assigned as the dominant transition from the benzene dithiol donor HOMO to the biq LUMO. The

energy of LLCT has been red shifted by ~ 5000 cm^{-1} compared to the parent complex. This can be explained due to the low lying π-acceptor orbital, resulting in increased π delocalization throughout the system in the biq ligand. These types of complexes are easier to reduce, but difficult to oxidize.[20] Similarly, the molar extinction coefficient is reduced from 7725 $L•mol^{-1}•cm^{-1}$ to 5000 $L•mol^{-1}•cm^{-1}$, which is due to the decreased metal-ligand orbital overlap. This is correlated with the steric hinderance introduced by the biq ligand. It has an out-of-plane distorted structure compared to the parent molecule. This observation is also corroborated by the information obtained from the electronic structure calculation[18] as shown in Figure 3.***16***.

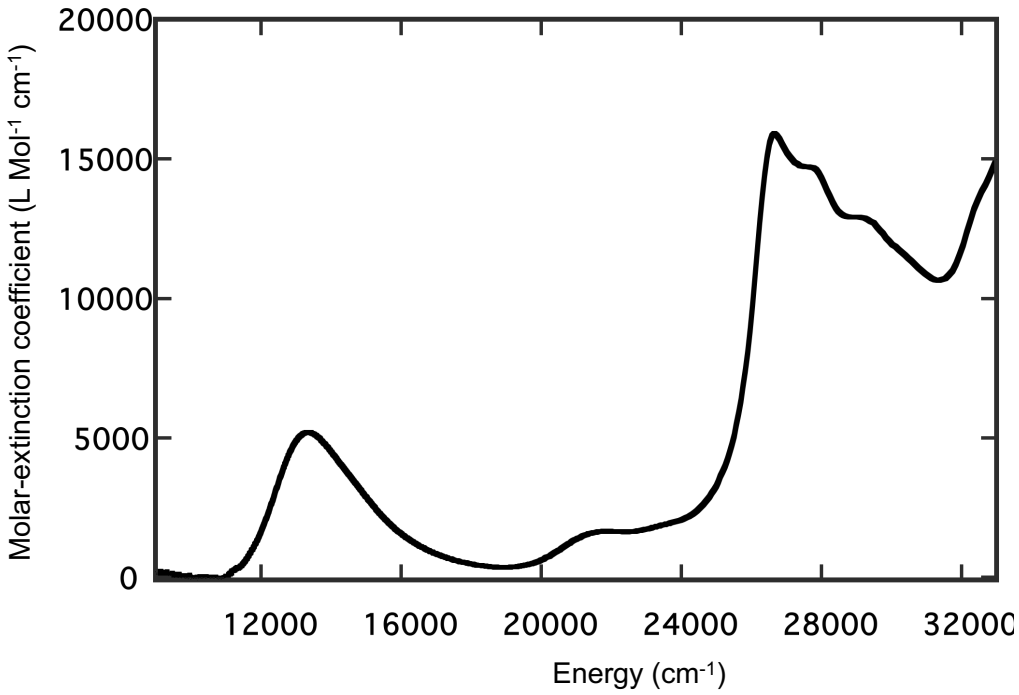

Figure 3.14: Room temperature electronic absorption spectrum of (bdt)Pt(biq) complex as solution in dry degassed methylene dichloride. It is depicting the ligand-to-ligand charge transfer transition at 13300cm^{-1} associated with the molar extinction coefficient value of 5000 $Lmol^{-1}cm^{-1}$. The charge transfer energy has been red shifted from the value of parent complex (bdt)Pt(bpy)

Resonance Raman spectroscopic data (details of this method of data collection and vibrational modes assignment has been explained in experimental section 3.1.4.2) proves the LL'CT transition involves the bdt HOMO and the biq based LUMO orbitals. The excitation profile was generated by exciting the molecule at 407 nm, 458 nm, 467 nm, 488 nm, 514 nm, and 568 nm to observe the enhancement of different vibrational modes within the energy range of the LL'CT transition band.

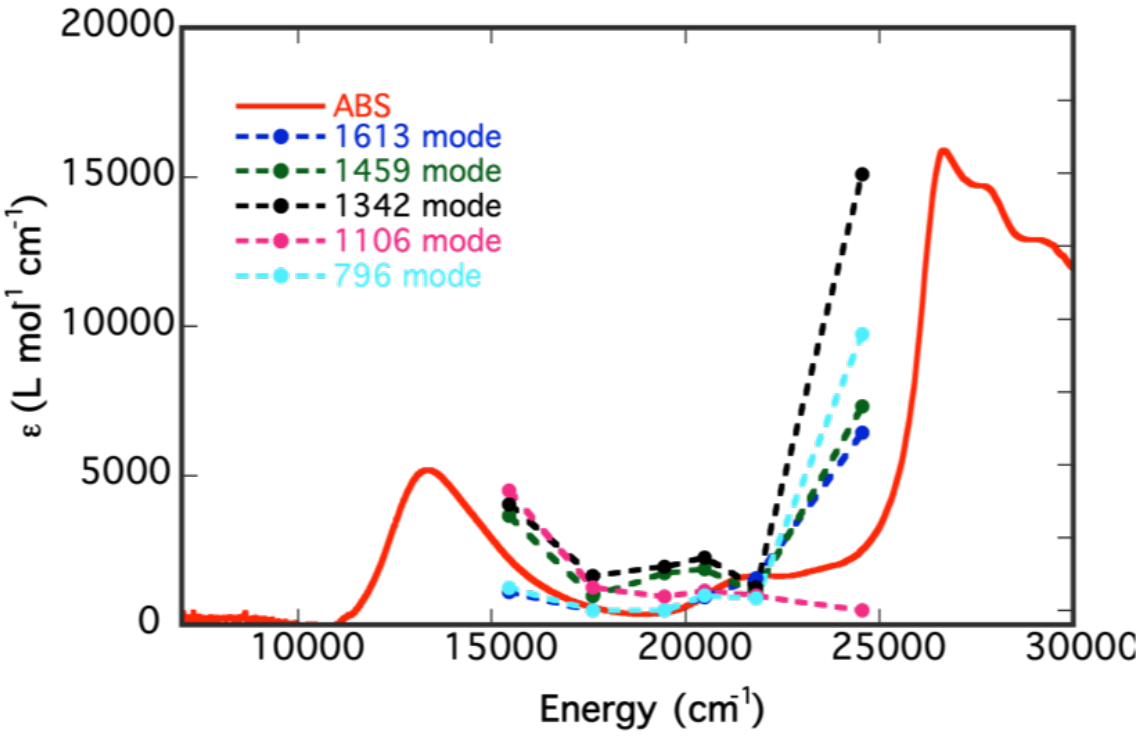

Figure 3.15: Resonance Raman profile of (bdt)Pt(biq) by exciting the molecule at 407 nm, 458 nm, 488 nm, 514 nm, 568 nm, 647 nm wavelengths and the enhancement modes are shown with different color codes; 1613 cm^{-1} mode in blue, 1459 cm^{-1} mode in green, 1342 cm^{-1} mode in black.

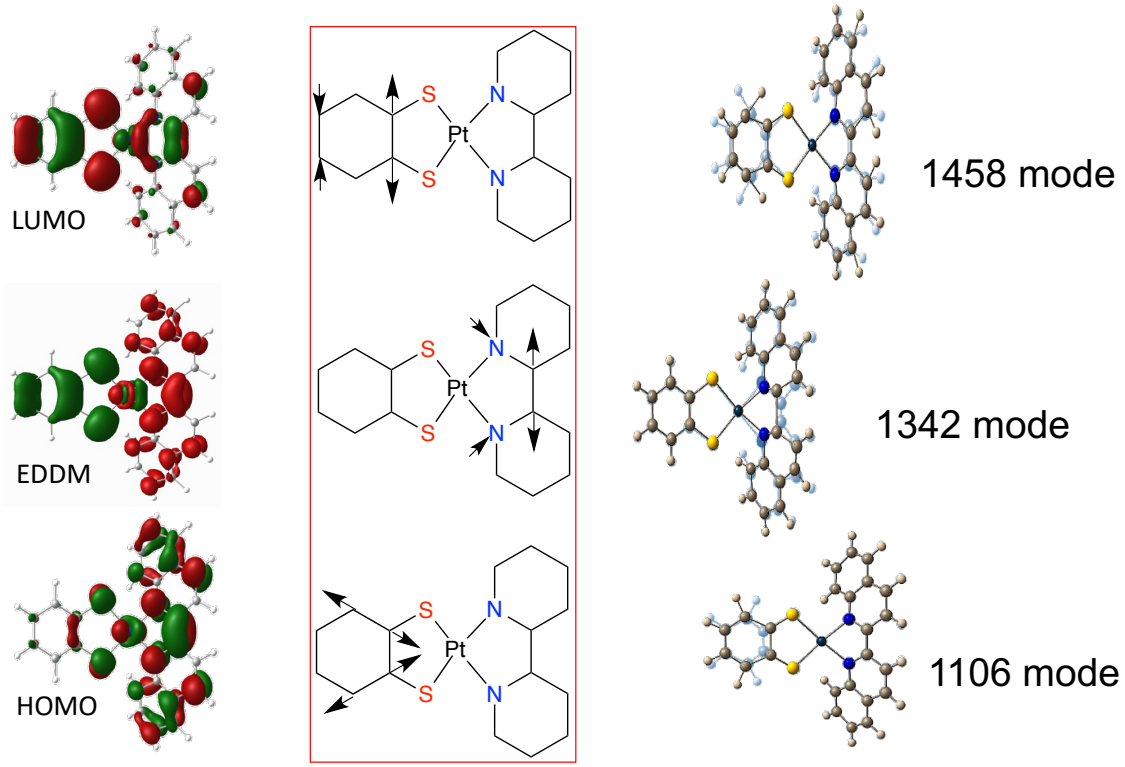

Figure 3.16: The assignment of vibrational modes contributing the LL'CT band on the resonance Raman profile plot. Left hand side; Homo, EDDM and LUMO of (bdt)Pt(biq) are from bottom to top. The bond line drawing and arrows pointing the normal vibrational mode; middle.

The resonance Raman enhancement pattern shown in the profile plot as shown in Figure 3.***15*** supports the band assignment for the low energy charge transfer as the LL'CT band. Following the one electron promotion from the HOMO to the LUMO, the electron density is shifted from the dithiolene to the diimine. This results in large, excited state distortions relative to the ground state. The profile reveals the excited state distortions along the bdt donor and biq acceptor fragments. Based on the vibrational calculation of (bdt)Pt(biq), the 1458 cm^{-1} and 1106 cm^{-1} stretches are assigned as the symmetric dithiolene C=C bond stretches, and 1342 cm^{-1} is the biq ring stretch, as shown in Figure 3.16. The electron density difference map (EDDM) obtained from the TD-DFT calculation

also supports the nature of the charge transfer transition in the (bdt)Pt(biq) complex as shown in Figure 3.***16***.

The collected emission spectrum is presented in Figure 3.17. The excitation wavelength (λ_{exc}) was 750 nm, and the observed emission (λ_{emisn}) was 980 nm. The calculated stokes shift value is 3096 cm^{-1}. The Stokes shift value is less than the Stokes shift of the parent complex. The molecule has exhibited a weak emission feature. The molecule relaxes from the low-lying triplet state LUMO to the ground electronic state HOMO.

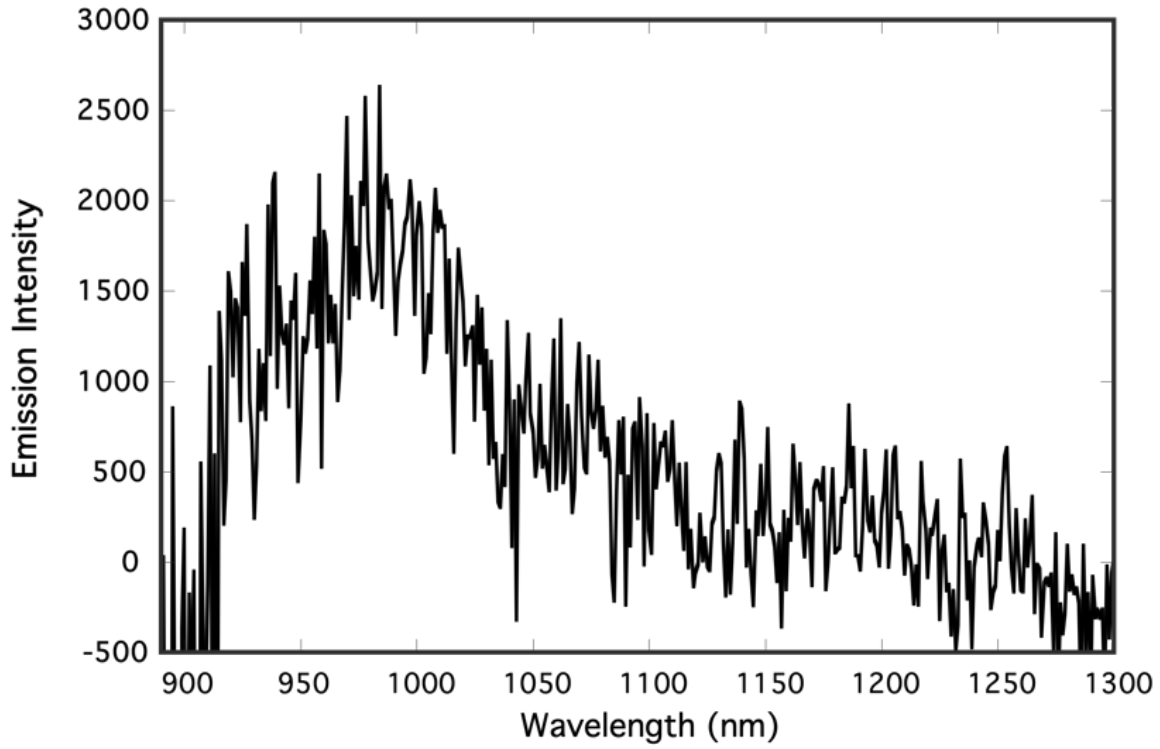

Figure 3.17: Room temperature emission spectrum of (bdt)Pt(biq) collected in solution of dry degassed dichloromethane (CH_2Cl_2). The emission maximum wavelength is observed at 980 nm.

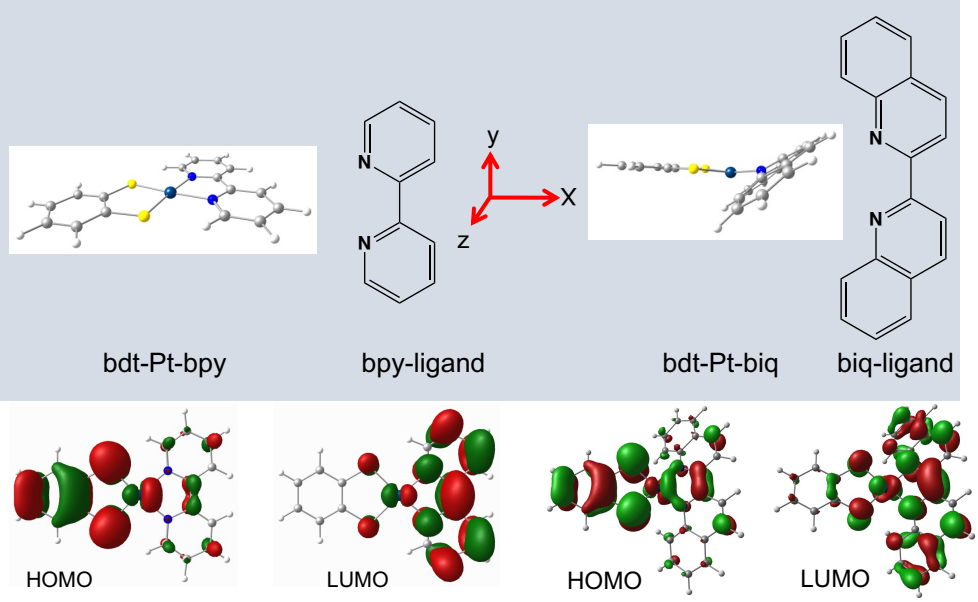

Figure 3.18: Optimized geometry is demonstrating the (bdt)Pt(biq) has out of plane distorted structure compared to the parent complex (bdt)Pt(bpy). Steric hinderance is exhibited by the biq ligand. Molecular axis is defined in the center. Bottom left: HOMO LUMO of parent complex, and right HOMO and LUMO of (bdt)Pt(biq). It is clearly demonstrating the metal orbital rotation on (bdt)Pt(biq) complex.

Transient absorption and transient absorption kinetics data were collected using LP920 and LP920-K spectrometers, respectively. These instruments apply the laser flash photolysis principle. Room temperature transition absorption (TA) difference data was collected in degassed DCM, applying 450 nm excitation wavelength (Figure 3.***19***). The gate width was set up to 5 ns and centered at 600 nm. A broad absorption band from 400 – 600 nm is observed, and the ground state depletion peak is observed at 760 nm which is correlated to the LL'CT in electronic absorption spectrum. Relatively weak positive absorption peak feature is present at 850 nm.

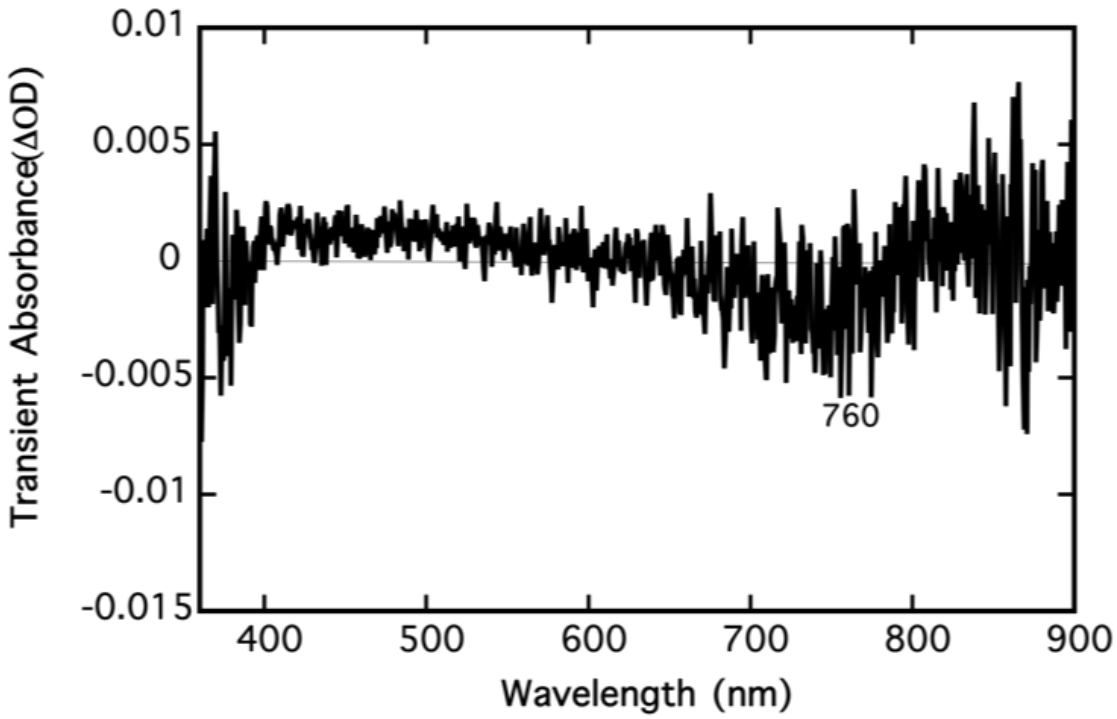

Figure 3.19: Transient absorbance (TA) difference data collected at room temperature in the degassed solution of dichloromethane following 450 nm wavelength. The gate width 5 ns centered at 600 nm.

Kinetic absorption trace was obtained with the sample in dry, degassed DCM (Figure 3.20). λ_{exc} was 450 nm, and the absorption kinetic trace was collected at 525 nm. The lifetime was measured to be 24 ns. The lifetime value was decreased by more than three orders of magnitude compared to the parent (bdt)Pt(bpy) complex (614±10 ns).[9] As outlined in previous sections, the relaxation from the T_1 state to the S_0 ground occurs by ISC, and is allowed by the SOC. Since ISC is a spin forbidden process, it is a relatively slower process compared to IC. The rate of ISC (k_{NR}) from the T1 to S_0 is expressed by the following equation:

$$K_{NR} \propto \sum_i \frac{\langle \varphi_{S_0} | \hat{L}_i | \varphi_{T_1} \rangle^2}{\left(E_{T_1} - E_{S_0}\right)^2} \qquad (3.3)$$

Equation 3.3 can be reduced, as shown below in case of the (bdt)Pt(biq), when the sum over all indices (x, y, and z) limited to only one direction (along y),

$$K_{NR} \propto \frac{\langle \varphi_{S_0} | \widehat{L_y} | \varphi_{T_1} \rangle^2}{\Delta E^2} \tag{3.4}$$

Thus, K_{NR} is related to the square of the SOC matrix element that connects T_1 to S_0 and the energy gap between the T_1 and S_0 states as seen in equation 3.4. The latter term is also explained by the energy gap law[42], K_{NR} is inversely proportional to the energy gap between T_n and S_n states[43]. From the electronic absorption data, the energy gap between HOMO and LUMO orbitals of (bdt)Pt(biq) compared to (bdt)Pt(bpy) complex has been reduced by ~5000 cm^{-1}. Thus, we should also consider the energy gap while comparing the lifetime data between two complexes. The calculated lifetime difference is predicted to be two times shorter than that of the parent complex based on the energy gap law. However, we have observed more than ~20-fold reduction in lifetime compared to the parent complex. We conclude that the observed lifetime must more than an energy gap dependance.

The SOC matrix element that connects the T_1 to S_0 is zero, $\langle T_1 | L_y | S_0 \rangle = 0$, for the (bdt)Pt(bpy) complex. Additionally, there is an absence of spin-orbit matrix element that connects T_1 and $^3A_1$, or S_0 and $^1A_1$ states. This originates from the numerator term of equation 3.4, as there is no $\hat{L}_i$ operator that transforms as $\boldsymbol{a}1$ in the C_{2v} point group. Therefore, the excited state population decay must occur through a distortion of C_{2v} symmetry by a molecular vibration that momentarily gives non-zero value to the SOC

matrix element.[5] Hence, the non-radiative decay rate of the excited state depopulation is slower. The dramatic reduction in lifetime of (bdt)Pt(biq) is due to the static, out-of-plane distortion that mirrors the out-of-plane b_1 symmetry bending vibrations along N-Pt-S bonds in the parent complex. Furthermore. we can conclude that the dynamic distortion along the b_1 vibrational coordinate contributes to a vSOC mechanism that facilitates $T_1 \longrightarrow S_0$ relaxation of the parent complex as determined by equation 3.1.[9]

Replacement of the bpy ligand by the sterically hindered biq ligand introduces a distortion along the molecular y-axis, lowering the molecular symmetry to Cs. Consequently, the Pt d-orbital rotation results in $\langle \varphi_{S_0} | \widehat{L_\iota} | \varphi_{T_1} \rangle \neq 0$, with the non-zero matrix element occurring by connecting T_1 to S_0 through the mixing of the Pt d_{zx} and d_{z^2} orbitals as shown in Figure 3.*12* and Figure 3.***18***. The following expression shows the mixing of these two orbitals Pt d_{zx} and d_{z^2} that make $\langle T_1 | \hat{L}_y | S_0 \rangle \neq 0$,

$$\langle T_1 | \hat{L}_y | S_0 \rangle = 0 \, , \langle \varphi_{XZ} | \hat{L}_y | \varphi_{XZ} + \varphi_{Z^2} \rangle = \{ \langle \varphi_{XZ} | \hat{L}_y | \varphi_{XZ} \rangle = 0 \; + \langle \varphi_{XZ} | \hat{L}_y | \varphi_{Z^2} \rangle \neq 0 \}$$

This argument is supported by the CASSCF computed value of the SOC matrix element that connects the T_1 and S_0 states. The computed SOC matrix element from the optimized geometry of (bdt)Pt(biq) is 164 cm^{-1}, and dynamic vibrational modes are now operating on the statically distorted C_{2v} symmetry.

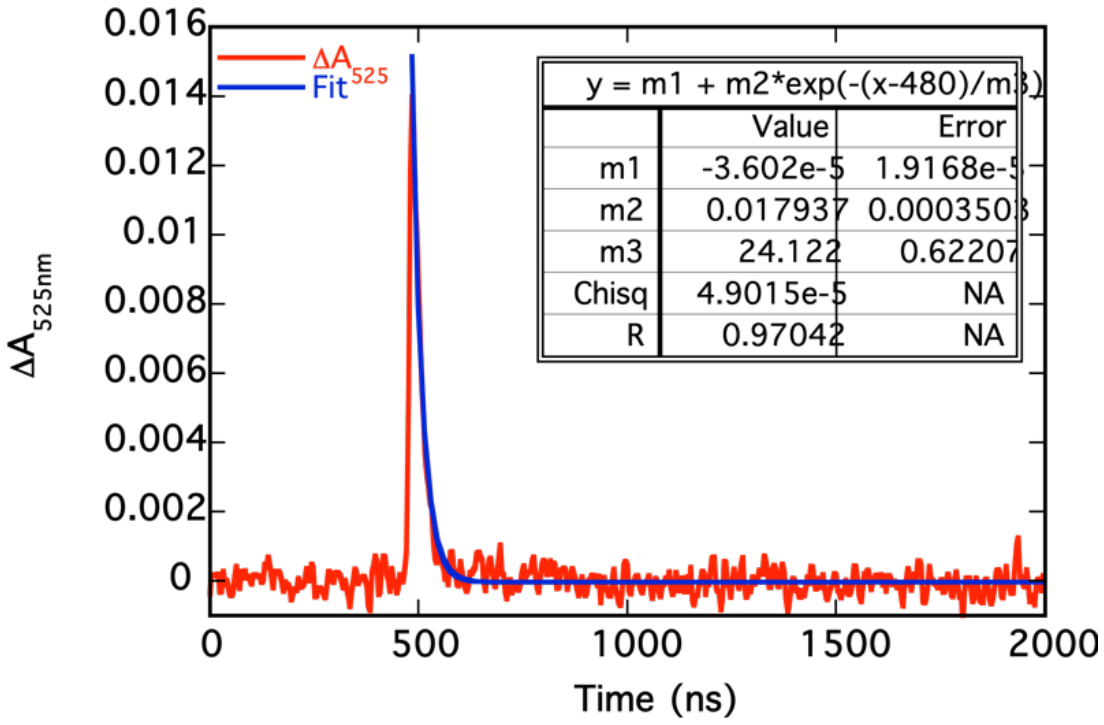

Figure 3.20: Kinetic absorption trace at 525 nm by exciting the molecule at 450 nm. The solution was prepared by using dry dichloromethane. Actual data is shown in red, and the fit is the blue color solid line. The kinetic absorption lifetime obtained was 24 ns.

X-ray absorption spectroscopy at the S K-edge is a method to quantitatively evaluate the amount of sulfur p-orbital character present in unoccupied valence molecular orbitals. The sulfur K-edge transitions are sulfur (1s) ⟶ sulfur (3p) + Pt(5d) excitations. The total sulfur 3p orbital character per hole (c_i^2) that is a major contributor of the intensity of the pre-edge peak at ~2472 eV, $(1s \rightarrow \psi_{yz}^*)$ is given by the following equation,[44 45 46]

$$D_0 = \frac{h}{3N} c_i^2 I_{s(1s\rightarrow 3p)} \qquad (3.5)$$

Here, D_0 is the integrated area under the $1s \rightarrow \psi^*_{yz}$ transition peak, h is the number of holes in the p-orbital, N is the number of absorbers, and $I_{s(1s\rightarrow 3p)}$ is the dipole integral associated to $1s \rightarrow 3p$ transition ($I_{s(1s\rightarrow 3p)} = 12$ for dichalcogenolenes)[44]. Applying all parameters and observed variables in equation 3.5, the experimentally measured value of sulfur character in (bdt)Pt(bpy) is 22.25% ($0.22 = c_i^2$ per S) that has admixed into the platinum d_{yz} orbital. The c_i^2 observed for (bdt)Pt(biq) is 22% per hole. These very close values for the sulfur p orbital coefficient indicates that the orbital rotation has less of an impact on the sulfur orbital overlap with the Pt d-orbital. Another transition is from $1s \longrightarrow \varphi^*_{LUMO,}$ which has a value of 3.5%. This is markedly increased when compared to the similar transition in the parent complex, which has 1.4% sulfur character in this LUMO.[9] [44] This increased value of sulfur character in the second transition peak that sulfur mixing is more in the LUMO of (bdt)Pt(biq), and is induced by the bending along the y-coordinate and the lowering of the overall symmetry. Consequently, the HOMO orbital with sulfur character admixes more with the LUMO of (bdt)Pt(biq).

The structural perturbation in (bdt)Pt(biq) results in an effective molecular symmetry lowering, permitting the Pt d-orbitals to rotate relative to the bipyridine plane. These orbital rotations are important for inducing Pt d-orbital contributions to SOC, which will modify $T_1 \rightarrow S_0$ decay rates.

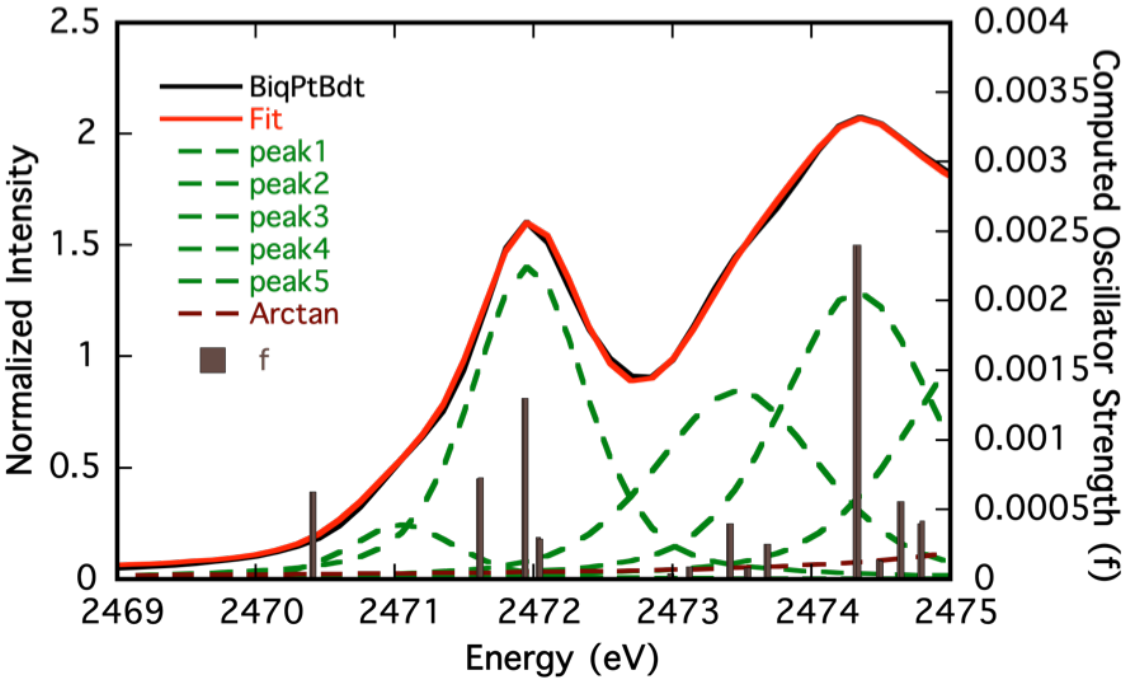

Figure 3.21: Overlay of experimental peak fitting (red solid line) gaussian resolved peak (green dotted line) and computed oscillator strength (brown sticks) of XAS S k-edge data collected in solid state sample of (bdt)Pt(biq) in the Synchrotron facility at Stanford University. Two low energy peaks have been analyzed as the transition from sulfur (1S) ⟶ 3P (sulfur) + Pt (5d) orbital and sulfur $1S \longrightarrow \varphi^*_{\text{LUMO}}$ transition.

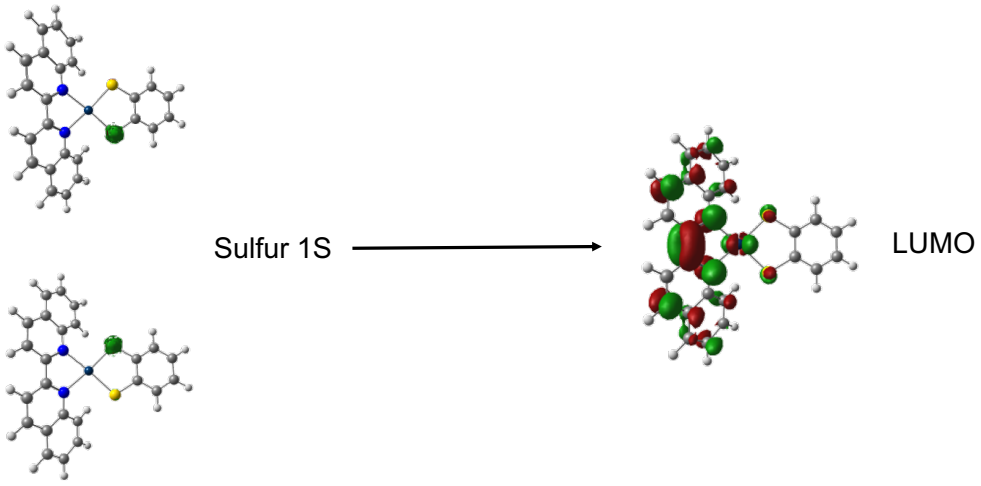

Figure 3.22: The molecular orbitals involved in first peak of the **(**bdt)Pt(biq)complex S K-edge data. The sulfur 1s orbitals are on the left side and the LUMO is on the right. The biq LUMO wavefunction has significant S character.

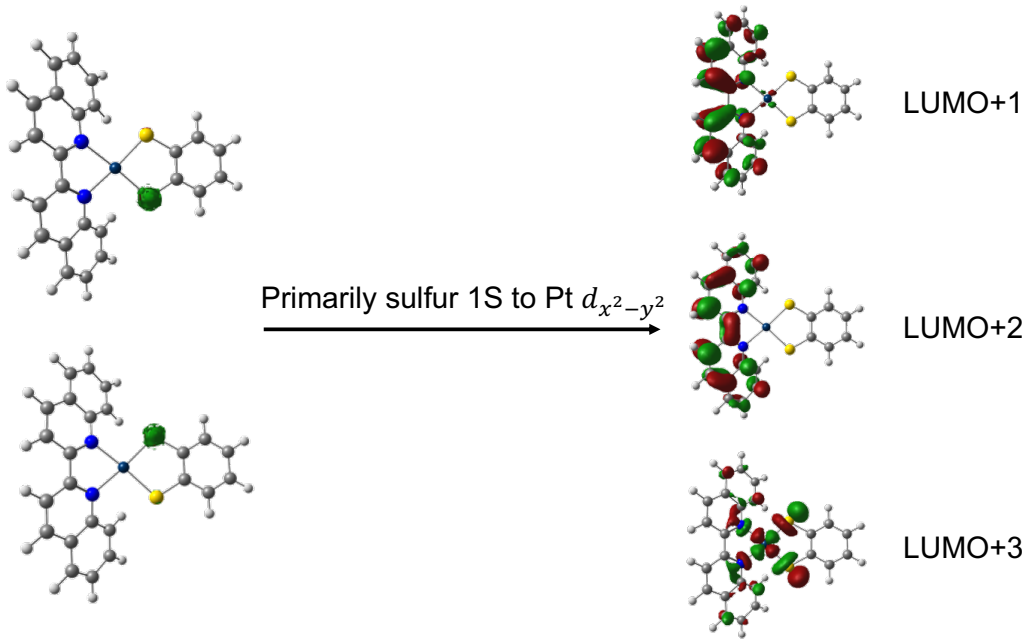

Figure 3.23: The molecular orbitals involved in the more intense second transition. Noticeably three transitions are involved but only the LUMO+3 has sulfur character in it and contributes dominantly to the intensity of second peak.

3.2.6 Conclusion

Our results, based on the electronic structure calculations and experimental observations, (electronic absorption, transient absorption, kinetic lifetime measurement, resonance Raman, XAS spectroscopy), show that low-symmetry distortions control SOC and vSOC. These distortions are the origin of enhanced $T_1 \rightarrow S_0$ ISC in these systems. $T_1 \rightarrow S_0$ lifetimes of (bdt)Pt(biq) are ~20 times shorter than those of (bdt)Pt(bpy), and this is due to a strong, static distortion induced SOC along the molecular y-coordinate. This effectively mixes Pt d_{z^2} and d_{xz} orbital character in the LUMO, leading to a non-zero SOC matrix element. Similar dynamic distortions along this coordinate contribute to $T_1 \rightarrow S_0$ relaxation in (bpy)Pt(bdt). This information can be used to evaluate vSOC contributions to the $T_1 \rightarrow S_0$ lifetimes of other (dichalcogenolene)Pt(diimine) complexes, contributing to

our understanding of important excited state processes. vSOC may play a critical role in solar energy converting devices that employ heavy atoms and contribute to enhanced ISC rates, and a more informed approach toward synthetic strategy of producing molecules with long-lived triplet excited states.

3.3 Synthesis, Characterization and Spectroscopy of (3,3'-methyl 2,2'-bipyridine)Pt(II)(1,2-benzene dithiol) Complex: (dmbpy)Pt(II)(bdt).

3.3.1 Introduction and Background

Bipyridine is considered as the most widely explored and commonly used chelating ligand in coordination chemistry[47] since its first discovery at the end of the nineteenth century.[48] Its extensive use is correlated to its robust redox stability and relative ease in derivatization to synthesize bipyridine analogs.[47] Its use has even broader reaches, because of its bidentate metal-binding nature, and a different range of properties of its analogs.[49] Here, we have synthesized a distorted diamine molecule from C_{2v} symmetry by using a bipyridine analog: 3,3'-dimethyl 2,2'-bipyridine (dmbpy). In this ligand, the methyl groups at the 3,3' positions are sterically hindered to one another when coordinated as a bidentate ligand to the metal, inducing a platinum metal d-orbital rotation. Following the coordination of the dmbpy ligand to Pt and adding the 1,2-benzene dithiol ligand, the molecule is effectively distorted along the z-direction of the molecular axis, allowing for a vSOC type mechanism analysis to occur. Once again, this completes our understanding of the vSOC mechanism with distortions along all three cartesian axes that we initiated in the previous study by synthesizing a distorted molecule along the molecular y-axis (bdt)Pt(biq) (section 3.2) and along x-axis with (OS)Pt(bpy).[9]

3.3.2. Synthesis and Characterization of the 3,3'-dimethyl 2,2'-bipyridine (dmbpy) Ligand.

Methyl substituted derivative of bipyridine (dmbpy) was synthesized by following literature procedures. This utilizes reductive homocoupling using palladium acetate as the catalyst and piperazine as an ancillary ligand.[50] Synthesis of bipyridine analogs has remained challenging because of the coordination to the transition metal catalyst with the pyridine monomer that deactivates the catalytic properties of catalyst. The use of piperazine has minimized the deactivation of catalytic properties of transition metal catalyst by temporarily coordinating with it.[50]

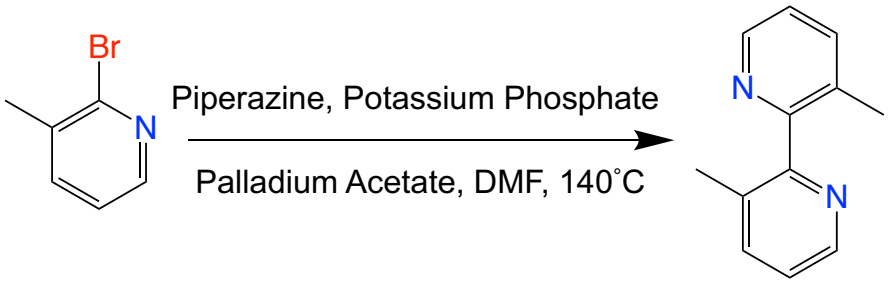

2-Bromo-3-methyl pyridine 3,3'-dimethyl, 2,2'-bipyridine

The dimethyl-bipyridine ligand was synthesized by following the reported method in the literature.[50] Mixture of 0.222 ml of 2-bromopyridine (2 mmol, 0.244 g, 1 eq), 0.0112 g of palladium acetate (0.05 mmol, 1 eq), 0.004 g of piperazine (0.1 mmol, 2 eq) and 0.848 g of potassium phosphate salt (0.4 mmol, 2 eq) was mixed with 20 ml of dry degassed dimethyl formamide (DMF). This reaction mixture was kept stirring at 140°C for 24 h under strictly anaerobic condition. After reacting, the contents were a brown colored

solution. The solution was allowed to cool, mixed with distilled water, and transferred to a separatory funnel containing ethyl acetate. Extraction was carried out three times. $MgSO_4$ was used to dry the residual solvent. A reddish, oily compound remained in the vial. Further purification by column chromatography was performed, using silica gel as the adsorbent and 1:1 (petroleum ether: ethyl acetate) as eluent. A colorless, oily compound was isolated as the pure target ligand with 63% yield relative to the amount of 2-bromopyridine used. The structure of ligand is characterized by mass spectroscopy (MS) and proton NMR techniques. High-resolution electrospray ionization (ESI) mass spectroscopy data showed a clean parent (m/z) peak: calculated for $C_{12}H_{12}N_2$: 184.01, observed (M/z) for $[M+H]^+$ 185.108. The chemical shift (δ) of proton NMR (CDCl3, 300 MHz, 298 K) data collected in deuterated chloroform (four signal were observed because of symmetric nature of ligand); δ 8.5 ppm (dd, J = 5.0, 2.4 Hz, 2H, pyridine), 7.71-7.56 ppm (m, 2H, pyridine), 7.24 ppm (dd, J = 7.6, 4.8, 2.3 Hz 2H) and 2.17 ppm (s, 6H, methyl group). The observed data are in good agreement with reported values.

3.3.3 Synthesis and characterization of (3,3'-dimethyl 2,2'-bipyridine) Pt(II) (dichloride); (dmbpy)$PtCl_2$.

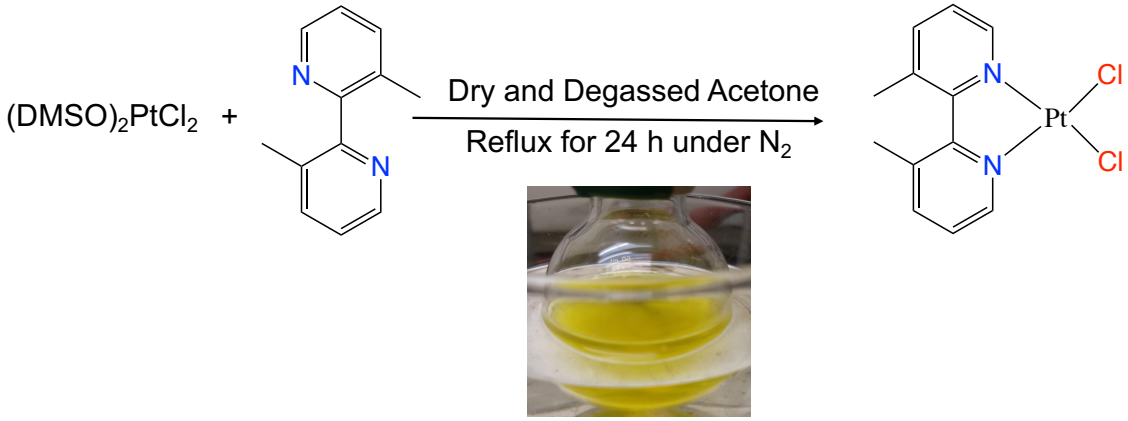

The synthesis of (dmbpy)$PtCl_2$ was performed by applying the modified methodology reported in the literature.[23] [22] $DMSO_2PtCl_2$ (0.106 g 0.25 mmol) was dissolved in dry 30 ml of acetone. Then, 0.047 g (1 eq, 0.25 mmol) of ligand was added. The reaction mixture was allowed to stir under refluxing conditions for 24 h. The initial light-yellow solution turned to a brick red. Partial removal of solution and adding pentane resulted in (dmbpy)$PtCl_2$ precipitate. Product with 74% yield respective to dmbpy ligand was isolated by filtration. The product was washed with pentane, hexane, and diethyl ether. Then, it was purified by column chromatography using silica gel as adsorbent and 100% ethyl acetate as eluent. The structure was confirmed by MS, NMR, and X-ray crystallography. Selected X-ray crystallographic data are presented in (Tables 3.1, 3.2, 3.3 and 3.4).

ESI-MS data showed a clean parent (m/z) peak: calculated for $C_{12}H_{12}Cl_2N_2Pt$: 449.00, observed (M/z) for $[M+CH_3CN]^+$ 493.04. The chemical shift (δ) of proton NMR ($CDCl_3$, 300 MHz, 298 K) data collected in deuterated chloroform (four signal were observed because of symmetric nature of ligand by mirror plane); 9.77 ppm (dd, J = 5.0,

2.4 Hz, 2H, pyridine), 7.97 ppm (m, 2H, pyridine), 7.50 ppm (dd, *J* = 7.6, 4.8, 2.3 Hz 2H, pyridine) and 2.48 ppm (s, 6H, methyl group).

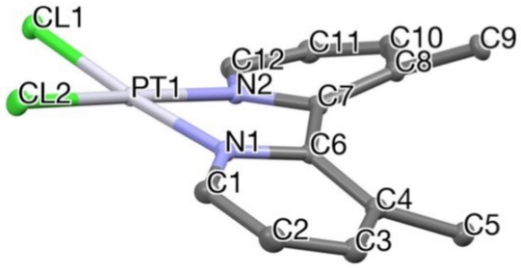

Figure 3.24: X-ray crystal structure of the (dmbpy)$PtCl_2$. Respective atoms have been depicted in the standard color indication. Numbering of the constituent atoms has done by using Mercury software.

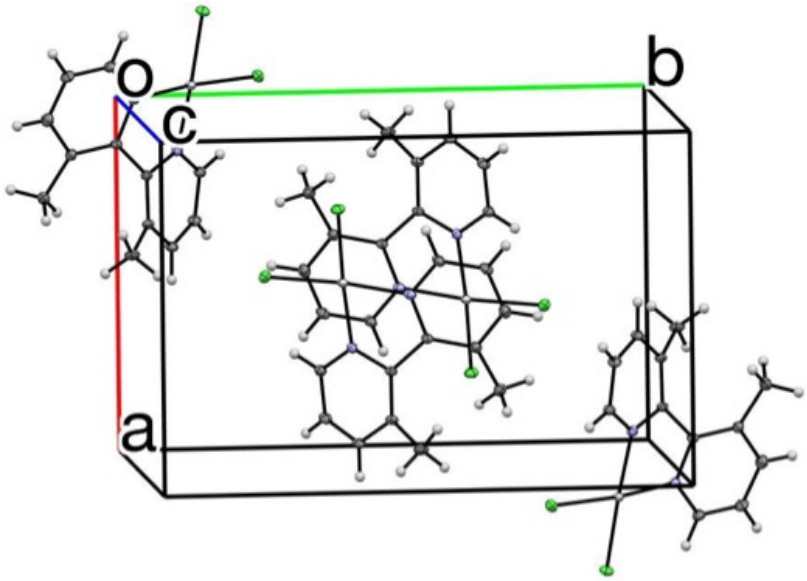

Figure 3.25: Crystal packing diagram of the (dmbpy)$PtCl_2$. Data collected at UTEP X-ray crystallography facility. The crystal was grown in dry ethyl acetate by using a slow evaporation method at room temperature.

Table 3.7: Crystal structure and refinement for (dmbpy)$PtCl_2$.

Empirical formula	$C_{12}H_{12}Cl_2N_2Pt$
Formula weight	450.23
Temperature/K	100.0
Crystal system	monoclinic

Space group	$P2_1/n$
a/Å	10.136(2)
b/Å	15.269(3)
c/Å	8.025(2)
α/°	89.97(3)
β/°	84.88(3)
γ/°	89.81(3)
Volume/Å^3	1237.1(5)
Z	4
ρ_{calc}g/cm^3	2.417
μ/mm^{-1}	11.750
F(000)	840.0
Radiation	MoKα (λ = 0.71073)
2Θ range for data collection/°	4.83 to 101.218
Index ranges	-21 ≤ h ≤ 21, -33 ≤ k ≤ 32, -9 ≤ l ≤ 16
Reflections collected	32554
Independent reflections	12884 [R_{int} = 0.0503, R_{sigma} = 0.0593]
Data/restraints/parameters	12884/0/156
Goodness-of-fit on F^2	1.002
Final R indexes [I>=2σ (I)]	R_1 = 0.0360, wR_2 = 0.0616
Final R indexes [all data]	R_1 = 0.0600, wR_2 = 0.0677
Largest diff. peak/hole / e Å^{-3}	4.62/-4.29

Table 3.8: Selected bond lengths of (dmbpy)$PtCl_2$

Atom	Atom	Length/Å	Atom	Atom	Length/Å
Pt1	Cl2	2.3030	C2	C3	1.379
Pt1	Cl1	2.3126	C11	C10	1.387
Pt1	N2	2.0154	C7	C8	1.399
Pt1	N1	2.0144	C7	C6	1.484
N2	C12	1.346	C10	C8	1.407
N2	C7	1.377	C8	C9	1.516
N1	C1	1.341	C4	C3	1.409
N1	C6	1.378	C4	C6	1.406

Table 3.9: Selected bond angles of (dmbpy)$PtCl_2$

Atom	Atom	Atom	Angle/°
Cl2	Pt1	Cl1	88.81
N2	Pt1	Cl2	175.44
N2	Pt1	Cl1	95.57
N1	Pt1	Cl2	95.63

Table 3.10: Selected torsion angles of (dmbpy)$PtCl_2$

Atom	Atom	Atom	Atom	Angle/°
N1	C6	C7	C8	151.9
N1	C6	C7	N2	29.10

3.3.4 Synthesis and Characterization of (3,3'-dimethyl 2,2'-bipyridine)Pt(II) (1,2-benzenedithiol); (dmbpy)Pt(bdt)

The synthesis of (dmbpy)Pt(bdt) was performed by following methodology reported in literature[9] [5]. 0.06 g (0.13 mmol, 1 eq) of brilliant yellow crystalline salt of platinum chloride, (dmbpy)$PtCl_2$ was dissolved in dry 20 ml of THF and degassed with a stream of nitrogen gas for thirty minutes. Then, 0.018 g (1.2 eq, 0.156 mmol) of 1,2-benzene dithiol and 0.021 g (3 eq, 0.39 mmol) KOH was dissolved separately in anhydrous methanol. The solutions were purged with nitrogen gas for 30 minutes separately. Solutions of 1,2-benzene dithiol and KOH was mixed anaerobically to deprotonate benzene dithiol. It turned into a light blue color. Deprotonated 1,2-benzene dithiol was added to the stirring solution of (dmbpy)$PtCl_2$ anaerobically. The reaction mixture turned to a purple color immediately. Then, the reaction mixture was allowed to stir for 1h at room temperature. The solution was removed partially so that all the THF

evaporates and the (bdt)Pt(dmbpy) complex precipitates in the left-over methanol solvent. The final complex was filtered, washed with an excess amount of methanol, hexane, and then diethyl ether. The product was purified by column chromatography (flash chromatography) method using silica gel as an adsorbent and 99% dichloromethane/1% methanol as eluent. The brick red final product was isolated with 59% yield relative to the amount of (dmbpy)$PtCl_2$ used. The structure and purity of the final complex was determined by using MS, NMR, and elemental analysis.

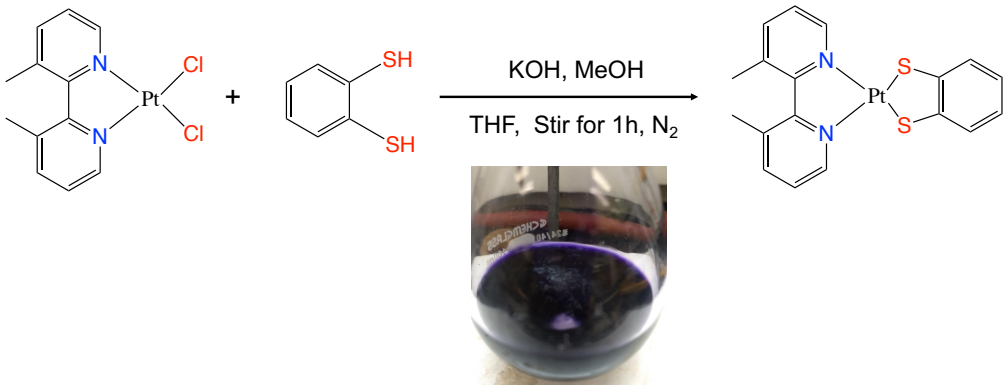

ESI-MS data collected showed a parent (m/z) peak: calculated for $C_{18}H_{16}N_2PtS_2$: 519.04, observed (M/z) for $[M]^+$ 519.038 and the dimer peak also appeared on the mass spectrum for $C_{36}H_{32}N_4Pt_2S_4$; calculated 1038.08, observed (M/z) for $[M\text{-}M]^+$, 1038.08. The platinum isotope pattern is in good agreement with both monomeric and dimeric units. The chemical shift (δ) of proton NMR ($CDCl_3$, 300 MHz, 298 K) data collected in deuterated chloroform (five signal were observed because of the symmetric nature of the complex by a mirror plane and a C_2 rotation axis); 9.36 ppm (m, 2H, pyridine), 7.89 ppm (d, J = 7.9 Hz, 2H, pyridine), 7.47 ppm (m, 4H, pyridine and benzene dithiol), 6.78 ppm (dd, J = 6.0, 3.3, Hz, 2H, benzene dithiol) and 2.45 ppm (s, 6H, methyl group). The result of elemental analysis was in good agreement with the calculated composition. The sample

was sent to Robertson Microlit laboratories in New Jersey. Sample was dried under vacuum for a week and packed under nitrogen before it shipped to eliminate the error from the solvent molecule. The calculated composition for $C_{18}H_{16}N_2PtS_2$: C, 41.61; H, 3.10; N, 5.39; and observed percentage; C, 41.70; H, 2.87; N, 5.14.

3.3.5 Experimental Details

Experimental electronic absorption, photoluminescence, lifetime measurements and spin-orbit calculations were explained in detail in section 3.2.4. X-ray crystallographic data were collected at the UTEP X-ray crystallography facility, where data on a single crystal of $C_{12}H_{12}Cl_2N_2Pt$ was collected. A suitable crystal was collected from the vial of crystal samples and placed on a Brucker APEX-II CCD diffractometer. The crystal was kept at 100.0 K during data collection using Olex2.[51] After data collection, the structure was solved with the SHELXT structure solution program using Intrinsic Phasing and refined with the SHELXL[52] refinement package using Least Squares Minimization.

3.3.6 Results and Discussions

Electronic absorption data collected at room temperature in DCM solution is shown in Figure 3.27. The energy of the LL'CT band is at 17,513 cm^{-1}. The band assignment is made with the help of TD-DFT results. The one electron promotion is primarily from the 1,2-benzenedithiol donor HOMO orbital with some Pt d_{xz} character to the acceptor LUMO as depicted below in Figure 3.17.

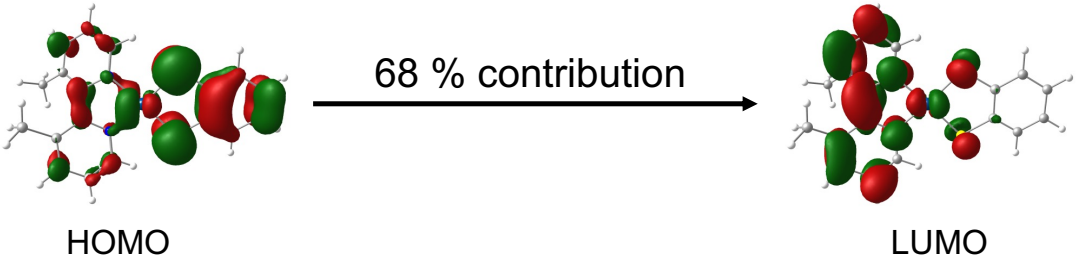

Figure 3.26: Depicting the dominant orbital involved in LL'CT process in (bdt)Pt(dmbpy). HOMO is on left and LUMO is in right, has weight percentage of 68 as obtained from TD DFT calculation.

The energy of this transition is slightly red shifted compared to the parent complex (bdt)Pt(bpy) (500 cm^{-1}). The molar extinction coefficient (MEC) is reduced relative to the parent complex (from 7,725 to 5,523 $L•M^{-1}•cm^{-1}$). The reduced orbital overlap is reflected by the MEC, as it is proportional to the orbital overlap integral. The Pt d orbital rotation due to steric hinderance of the two methyl groups, which has lowered the orbital overlap between the metal and the acceptor ligand.[5 9] MEC values were obtained by using the serial dilution method. Electronic absorption of all four solutions were collected to observe the nature of the electronic absorption spectrum with respect to concentration. The concentration as a function of absorbance is plotted to validate the observed value of the molar extinction coefficient in Figure 3.28**Error! Reference source not found.**.

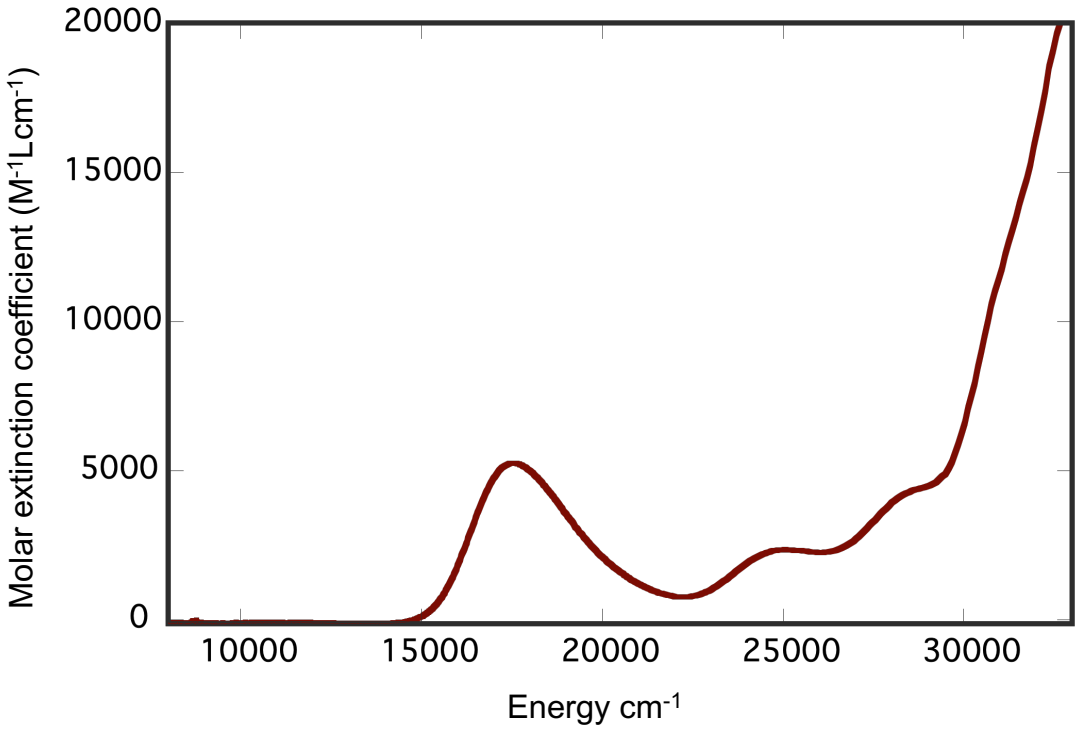

Figure 3.27: Room temperature electron absorption spectrum of (bdt)Pt(dmbpy). The x-coordinate represents the energy in wavenumbers and the y-coordinate represents the molar extinction coefficient calculated by the serial dilution method using dry degassed dichloromethane as the solvent.

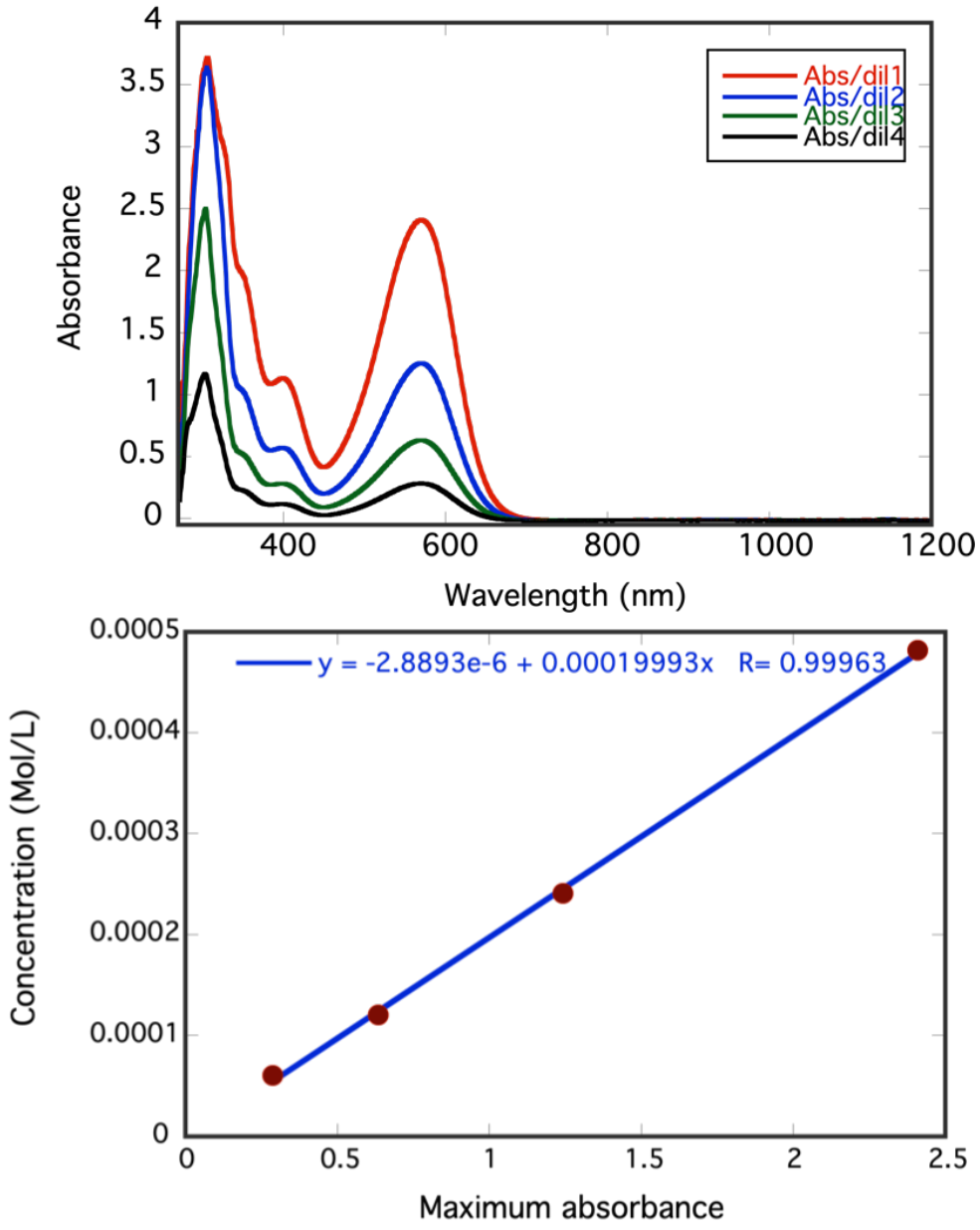

Figure 3.28: Room temperature electronic absorption spectrum collected in a degassed solution of dichloromethane at different known concentrations (top). The different concentrations of the solutions were achieved by using the serial dilution method. The plot of concentration vs absorbance (bottom).

Photoluminescence data were collected in solution at room temperature in using dry degassed THF, and this is exhibited in Figure 3.29. The absorbance of the sample was kept below 0.3 to avoid the self-absorption by sample molecule.[39] The sample was

excited at 600 nm and the observed $\lambda_{emisn} = 806\, nm$. The Stokes shift is 4260 cm $^{-1}$, which is comparable to that of the parent complex[5].

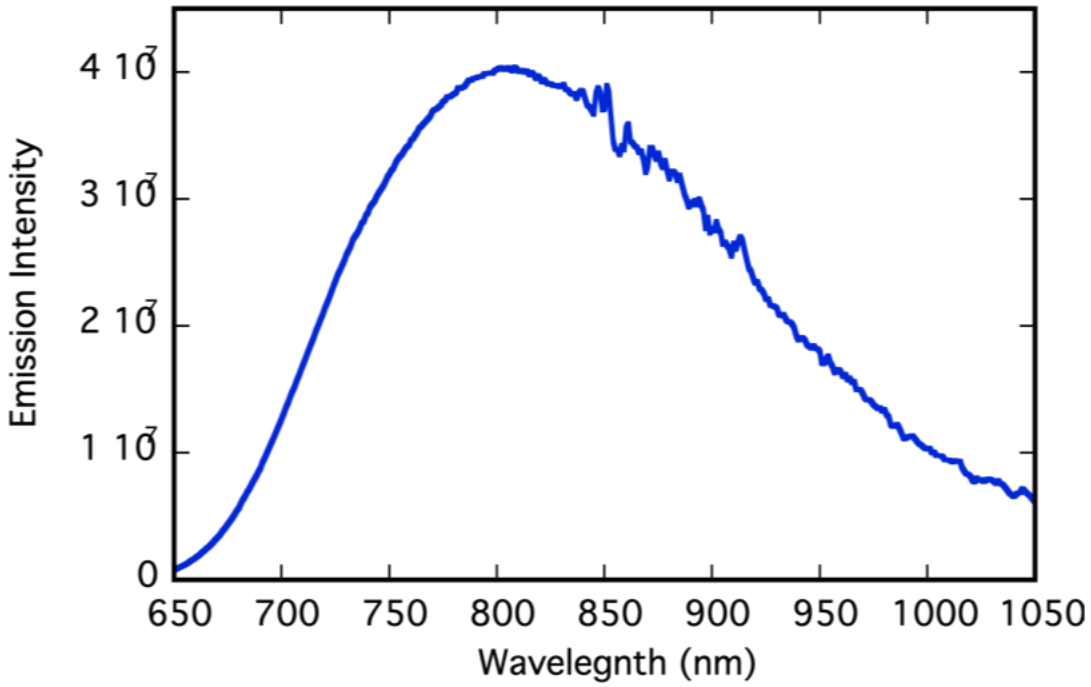

Figure 3.29: Emission spectrum collected at room temperature in dry degassed THF as solvent. The sample was purged under nitrogen for 30 minutes just before collection of the emission data. The emission maximum is at 806 nm.

Emission lifetimes were measured at room temperature in a solution of dry THF. The data and the fitting parameters are shown in Figure 3.31. The sample was purged by nitrogen gas before the experiment. The excitation source was a 450 nm diode laser and emitted photons were counted at 800 nm. The lifetime of 179 ns was obtained by fitting equation 3.2 to the data. The observed lifetime is reduced by more than 4-fold, due to the Pt d orbital rotation along the z-coordinate. These mimics the a_2 symmetry twisting vibrational mode along the plane of bipyridine in the rigorous C_{2v} point group of the parent complex. This dynamic twisting vibrational mode about the Py-Py bond induces mixing of

the Pt d_{xz} orbital character in the HOMO by rotating about z-axis, resulting in a non-zero $\langle\varphi_{T_1}|L_i|\varphi_{S_0}\rangle \neq 0$. This type of distortion turns on the vSOC mechanism to facilitate ISC and the relaxation of parent molecule to the ground state (S_0). This is achieved statically in (bdt)Pt(dmbpy) molecule. The consequence of a static distortion is observed to enhance the rate of non-radiative decay relative to parent complex, despite of having comparable ΔE^2 values. The observed difference in emission lifetime of (bdt)Pt(dmbpy) from the parent complex is due to orbital allowedness by orbital mixing as indicated below.

$$\langle T_1|\hat{L}_y|S_0\rangle = 0\,,\langle\varphi_{XZ}|\hat{L}_y|\varphi_{XZ}+\varphi_{YZ}\rangle \;=\; \{\langle\varphi_{XZ}|\hat{L}_y|\varphi_{XZ}\rangle = 0 \;+\langle\varphi_{XZ}|\hat{L}_y|\varphi_{YZ}\rangle \neq 0\,\}$$

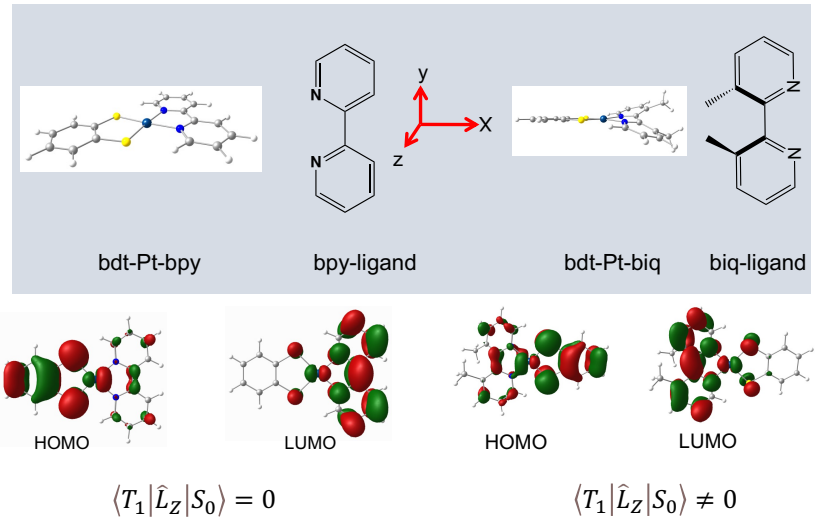

Figure 3.30: Static distortion induced orbital rotation in the (bdt)Pt(dmbpy) complex along the molecular z-coordinates resulting in a non-zero first order spin-orbit coupling matrix element.

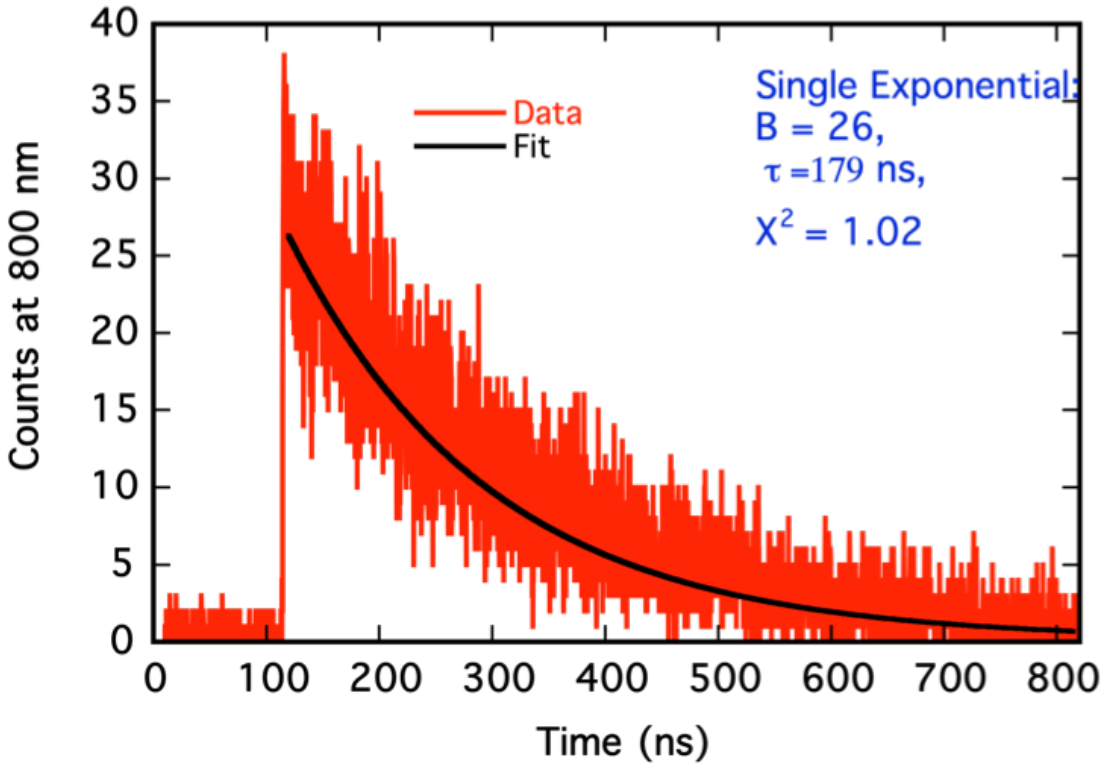

Figure 3.31: Emission lifetime data (red) at room temperature in a degassed solution of dry THF by using 450 nm diode laser as an excitation source and the emission counts were made at 800 nm. The lifetime is 179 ns with a single exponential decay. The best fit to the data is shown in blue.

Sulfur K edge XAS data shown in Figure 3.32. There are distinctly different features than were observed in the parent complex. The lower energy shoulder peak is more intense and has 8.5% sulfur character compared to that of the parent complex (1.4%). This indicates more mixing of the LUMO and HOMO in the complex. The addition of two methyl groups at the 3,3 positions of bipyridine has distorted the bipyridine rings out of plane. Thus, the symmetry of the complex has been lowered from C_{2v}, allowing more orbital mixing. The orbitals displayed in Figure 3.33 contribute to the first weak peak in the XAS data. This increased amount of sulfur character in the LUMO is complemented by the computed SOC matrix element value. These are 294 cm^{-1} for (bdt)Pt(dmbpy), 0

cm^{-1} for the parent, and 164 cm^{-1} for the less distorted (bdt)Pt(biq) complex, which has been presented in table 3.5. The second transition observed at the next lowest energy (defined as the pre-edge peak in S Kedge spectrum) is associated with the transfer of an electron from a sulfur 1s orbital to the four acceptor LUMOs of the complex as shown in Figure 3.34. The sulfur character was determined to be 35.16%, which is the highest of all the other systems we have studied, and this is presented in Table 3.5.

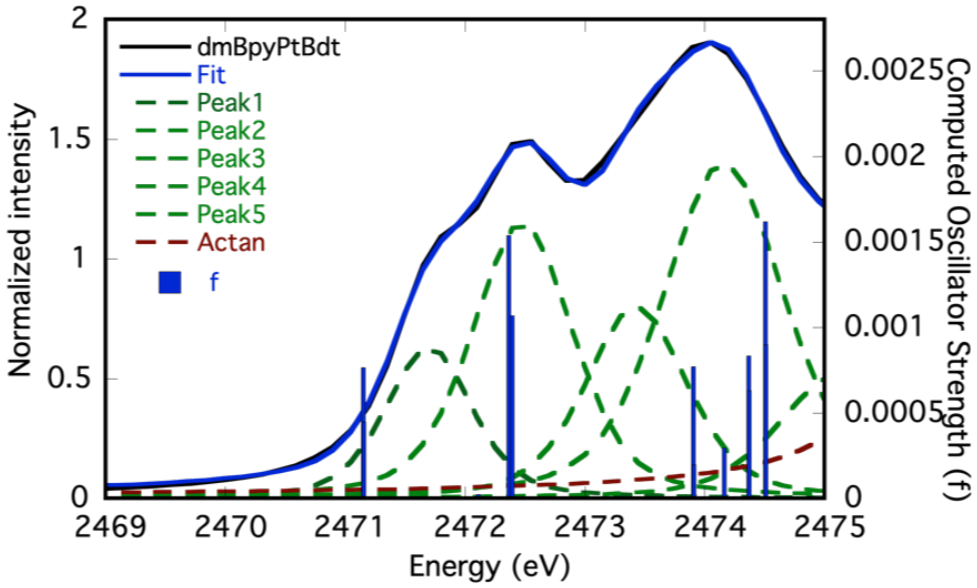

Figure 3.32: Overlay of experimental peak fitting (blue solid line) Gaussian resolved peaks (green dotted line) and computed oscillator strengths (blue sticks) of XAS S K-edge data collected using a solid sample of (bdt)Pt(bmbpy). Data were collected at SSRL. Two low energy peaks have been analyzed as the transition from sulfur (1S) ⟶ 3p (sulfur) + Pt (5d) (second peak) and sulfur 1s ⟶ φ^*_{LUMO} transition (first peak).

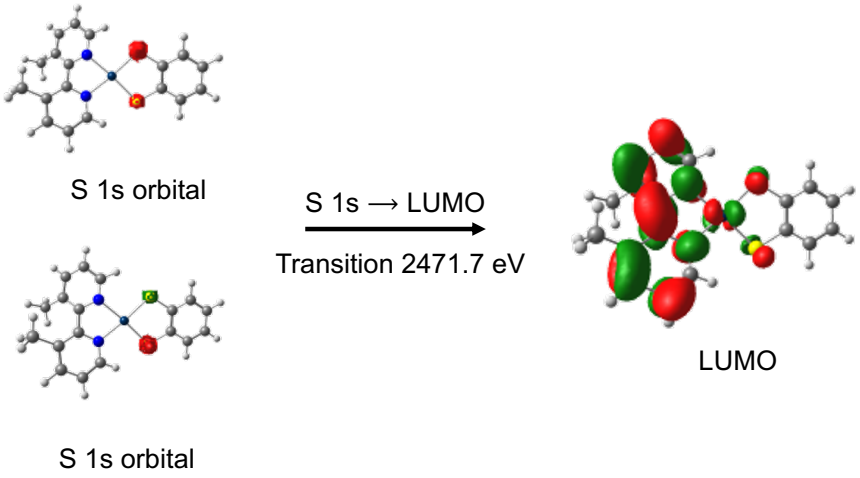

Figure 3.33: Computed orbitals of 1s sulfur and LUMO of the complex (bdt)Pt(dmbpy) associated with the lower energy weak transition at 2471.7 eV.

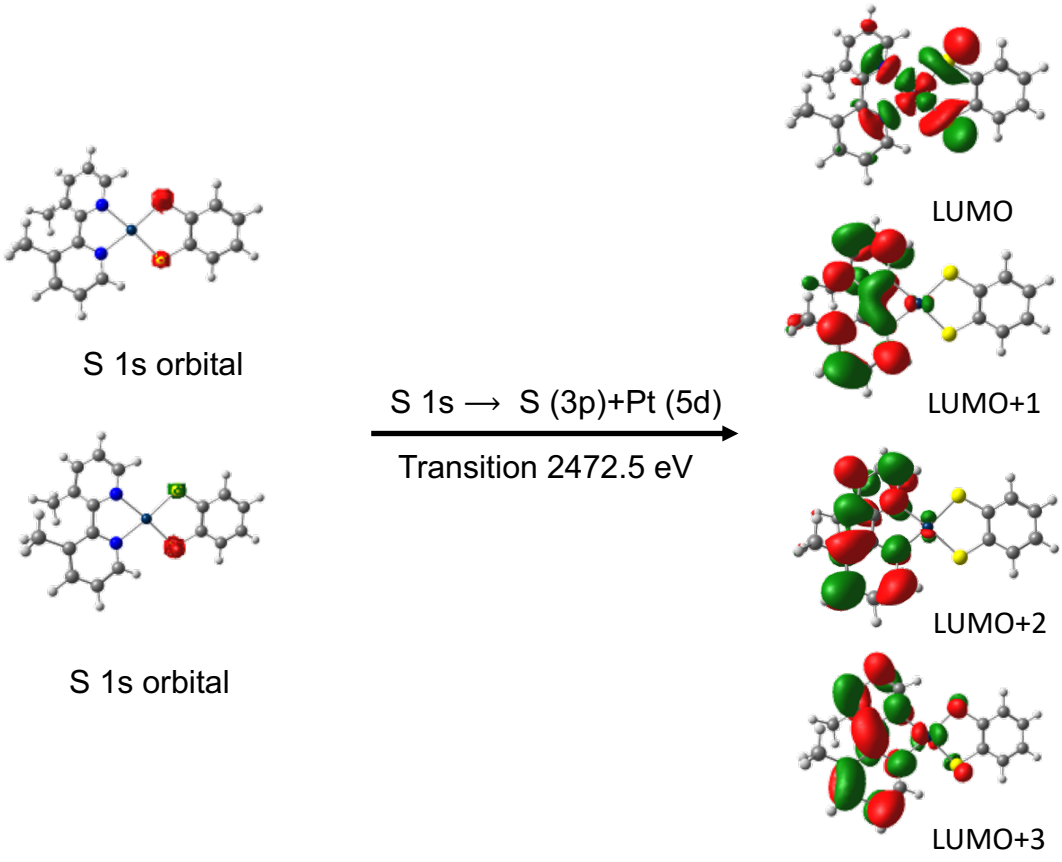

Figure 3.34: the acceptor orbitals responsible for pre-edge peak observed in 2472 eV of the XAS S Kedge spectrum of (bdt)Pt(dmbpy) complex. All acceptor orbitals have sulfur character thus have been included in the S contribution calculation area under that peak.

3.3.7 Conclusion

The study of static distortion induced enhanced first order SOC along three coordinates has been done by synthesizing molecules with distorted geometries along the molecular x, y, and z coordinates individually, with respect to the parent molecule (bdt)Pt(bpy). The SOC matrix element that connects the lowest triplet (T_1) to the ground electronic state (S_0) was calculated for all four complexes by using the CASSCF method implemented in the ORCA program. The values obtained were 0 cm^{-1}, 64 cm^{-1}, 164 cm^{-1}, and 294 cm^{-1} [9] as seen in Table 3.5. These increased values of $\langle \varphi_{T_1} | L_i | \varphi_{S_0} \rangle$ for (O,S)Pt(bpy), (S,S)Pt(biq) and (S,S)Pt(dmbpy) compared to 0 cm^{-1} for the parent complex is due to the Pt d-orbital rotation along x, y, and z coordinates respectively, and inducing non-zero first order SOC. These static orbital rotations have contributed to overcome the orbital forbidden nature of transitions between the T_1 and S_0 states in rigorous C_{2v} geometry. Short, excited state lifetimes (faster ground state recovery rate) for the non-radiative decay mechanism have also been observed with values in Table 3.5 and Figure 3.***35***. These static distortions are sufficiently similar to the dynamic vibrational normal modes having b_1 and b_2 symmetry (out of plane $N-Pt-O$ bending, $S-Pt-S$ anti-symmetric stretch along $x-$ and $y-$ coordinate respectively) and a_2 symmetry (twisting of $N-Pt-O$ along z-coordinate)[9] in the parent (bdt)Pt(bpy) complex. These vibrations are responsible for faster depopulation of T_1 and the repopulation of S_0 by inducing vSOC, and overcoming orbital forbiddenness of the ISC process.[5] We have noticed that all three distortions have a significant contribution to the non-radiative decay mechanism. Another finding from this study involves determining the dynamic vibration that has the greatest effect on excited state decay. It was found that the normal vibrational mode for the $S-$

$Pt - S$ anti-symmetric stretch (along x-coordinates that is a_2 symmetry) is likely to be the most effective vibrational mode to allow ISC to repopulate the ground state of the parent molecule. [9] Despite the trend of the SOC matrix elements, there is one exception to the lifetime trend. The distortion of the plane of the bipyridine ring twist is the largest as determined by the computed value of the SOC matrix element. Compared with the bending and stretching vibrational normal modes, the twisting mode is less effective in depopulating the excited state of the parent complex as shown in Table 3.5. Based on the spectroscopic observations and electronic structure calculation results, our synthesized series of (E,E)Pt(N,N) (E = O, S) complexes have helped us to correlate $T_1 \longrightarrow S_0$ decay rates with strategic molecular distortions statically along all three principal cartesian axis directions. These results are crucial to our understanding of excited state lifetimes for other chromophores, allowing us to synthetically design donor-acceptor molecules of platinum having desired lifetimes.

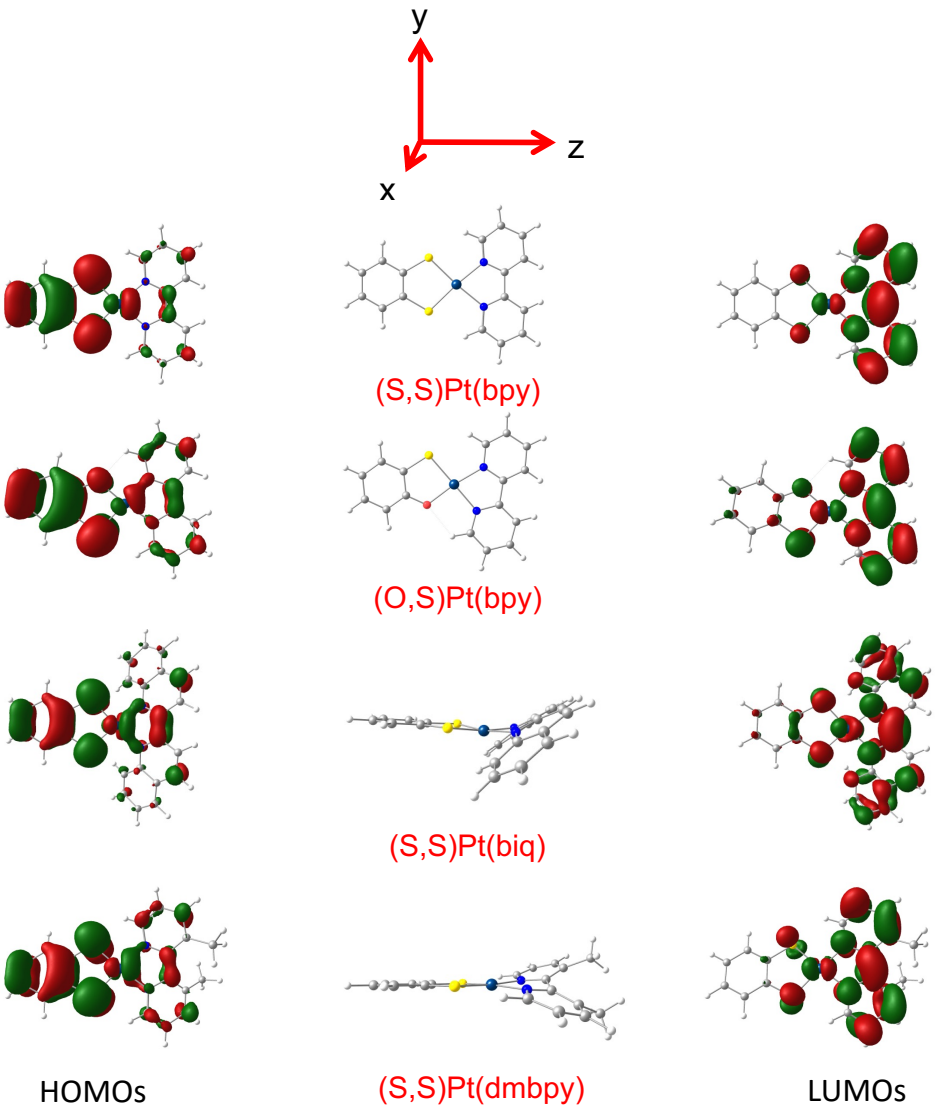

Figure 3.35: Comparison of frontier molecular orbital (HOMOs on left and LUMOs on right, DFT optimized geometry at the center) of (S,S)Pt(bpy) (parent complex), (O,S)Pt(bpy) (complex having static distortion along x-axis), (S,S)Pt(biq) (static distortion along y-axis) and (S,S)Pt(dmbpy) (static distortion along z-axis) from top to bottom.

Table 3.11: Comparison of lifetime, CASSCF calculated spin-orbit coupling matrix element, Stokes shift value and absorption maximum in dichloromethane for (S,S)Pt(bpy), (O,S)Pt(bpy) (S,S)Pt(biq) and (S,S)Pt(dmbpy) complexes. Values of (S,S)Pt(bpy) and (bpy)Pt(O,S) are adapted from the published work by our group.[9]

Observation	(S,S)Pt(bpy)	(O,S)Pt(bpy)	(S,S)Pt(biq)	(S,S)Pt(dmbpy)
Lifetime ($\boldsymbol{t}$) ns	621 ± 10	51 ± 10	24 ± 10	179 ± 10
$\langle \boldsymbol{\varphi_{S_0}} \vert \boldsymbol{L_x} \vert \boldsymbol{\varphi_{T_1}} \rangle$ (cm^{-1})	0	64	164	294
Stokes Shift (cm^{-1})	4104	4217	3096	4260
$(\boldsymbol{\lambda_{\max, abs}})$ (cm^{-1})	18350 (545 nm)	17750 (564 nm)	13350 (761 nm)	17513 (570 nm)

3.4 Orbital Topology Control of the Ground State Recovery Pathway

3.4.1 Background

The heterocyclic, nitrogen-containing chelating ligands biq and i-biq were mentioned as early as the twentieth century by Smirnoff and Helv.[53] In 1952, Case and co-workers reported the synthesis of i-biq by using an amino-derivative of 3-bromoisoquinoline by heating it in a sealed capsule at high temperature (~200°C).[54] After the method developed to synthesize i-biq and biq ligands, the comparative studies of photophysical properties of transition metal complexes were extensively performed in order to understand the identity of the emissive state. These studies were most active in the 1980s through 1990s and were mostly related to coordinated Ru complexes with biq and i-biq ligands. In1982, Belser and Zelewsky reported the comparative study of the photophysical properties of $Ru(bpy)_3^{2+}$, $Ru(biq)_3^{2+}$ and $Ru(i\text{-biq})_3^{2+}$. Based on their study, the observed luminescence from $Ru(i\text{-biq})3^{2+}$ was ligand centered, which was not the case in $Ru(biq)_3^{2+}$ and $Ru(bpy)_3^{2+}$. The lowest excited state is ^{3}LC in case of $Ru(i\text{-biq})_3^{2+}$

and ^{3}MLCT is the lowest excited state for $Ru(biq)_3^{2+}$ and $Ru(bpy)_3^{2+}$. Their study also revealed the relative difficulty of reducing i-biq compared to biq.[55] Temperature dependent, radiationless lifetime of bpy, biq and i-biq complexed with Ru also support the lowest excited state determination as LC in the i-biq complex.[56] In 1985, two independent research groups, the Juris and co-workers and the Belser research group, synthesized similar Ru complexes also coordinated to bpy, biq and i-biq to study their comparative photophysical properties.[57] [20] As anticipated, the energy of the ^{3}MLCT transition was red shifted for the $Ru(biq)_3^{2+}$ complex compared to $Ru(bpy)_3^{2+}$. Because of extended π-conjugation, the reduction of biq is easier than bpy (the π* LUMO of biq lies in lower energy compared to the same orbital of bpy). This study was also in agreement with previously reported data. Research has been continuously pursued on these two structural isomers, biq and i-biq. The Kato group is currently studying i-biq platinum (II) complexes, considering their structure and luminescence property correlations.[58] [59] These two isomers have exhibited distinctly different photophysics when complexed with different transition metals. Biq is sterically hindered upon coordination with a metal center, whereas i-biq is not, as the benzene ring is present at a different position on the pyridine rings.[19] In our lab, we are synthesizing donor acceptor platinum (II) complexes by varying the donor and acceptor ligands to gain further insight into their excited state dynamics. We have studied the ligand control of excited state lifetimes[5] and studied vSOC effects on lifetimes (section 3.1) that allow radiationless deexcitation processes.[9] Here, in this study, we have synthesized the platinum complexes of i-biq and biq, and performed a comparative study of their photophysical properties. The results of electronic structure calculations and spectroscopic observations are summarized here.

3.4.2 Synthesis of 3,3'-iso-biquinoline (i-biq) Ligand

Synthesis of i-biq was performed by following the reported procedure for the synthesis of different bipyridine analogs[50]. All required reagents were purchased from Sigma-Aldrich and used without further purification. The reactants: 0.208 g (1 eq, 1 mmol,) of 2-bromo-3-isoquinoline, 0.0056 g (0.025 mmol) a catalytic amount of palladium acetate, 0.004 g (0.5 eq, 0.05 mmol) piperazine and 0.424 g (2 millimole, 2 eq) of potassium phosphate were dissolved in 20 ml of dry DMF. The reaction mixture was allowed to stir at 140°C, 24 h under atmosphere of N_2. The reaction mixture was allowed to cool to room temperature and transferred into a separatory funnel with distilled water. Three extractions were performed using ethyl acetate. The extracted product was dried with Na_2SO_4. The organic solvent was evaporated and the remaining contents were purified by column chromatography using silica gel as adsorbent and chloroform:hexane (10:1) as the eluent. White, needle shaped crystals of i-biq ligand was isolated with 57% yield relative to the amount of 2-bromo-3-isoquinoline used.

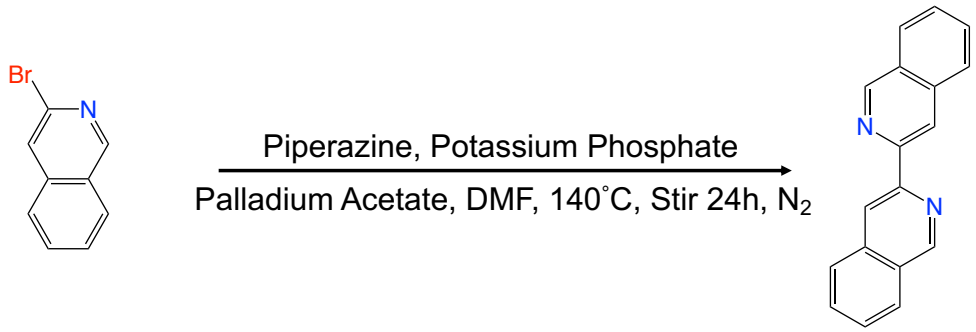

2-bromo-3-isoquinoline

3,3' iso-biquinoline

The characterization and purity of the ligand was confirmed and analyzed by MS and NMR techniques. MS data showed a single parent peak (m/z): calculated for $C_{18}H_{12}N_2$: 256.01, observed (M/z) for $[M+1]^+$ 257.108 peak. The chemical shift (δ) of the proton NMR ($CDCl_3$, 300 MHz, 298 K) data was collected in deuterated chloroform: 9.37 ppm (s, 2H, pyridine), 8.92 ppm (s, 2H, pyridine), 8.01 ppm (dd, J = 11.3, 8.2, Hz 4H, pyridine and benzene ring), 7.73 ppm (ddd, J = 8.2, 6.8, 1.3 Hz, 2H, pyridine and benzene ring), 7.62 (ddd, J = 8.1, 6.9, 1.2 Hz, 2H).

3.4.3 Synthesis of (3,3'-iso-biquinoline)Pt(II)(dichloride) (i-biq)$PtCl_2$

Synthesis of (i-biq)$PtCl_2$ was achieved by following the reported literature procedure[60] with some modifications from Rund's method.[61] 0.104 g (0.25 mmol, 1 eq) of K_2PtCl_4 was dissolved in 8 ml of distilled water. One ml of 2 M HCl was added to the stirring red orange solution of platinum salt. A suspension of 0.064 g (0.25 mmol, 1eq) i-biq from previous synthesis in acetonitrile was prepared and added to the stirring acidic solution. The reaction mixture was stirred at 70°C until the red orange solution turned to a yellow precipitate. Upon cooling, a yellow solid was deposited at the bottom of the flask. The precipitate was filtered, washed with methanol, water, diethyl ether, and purified further by recrystallization method in DMF. Yellow crystals were collected with 68% yield relative to the amount of ligand used.

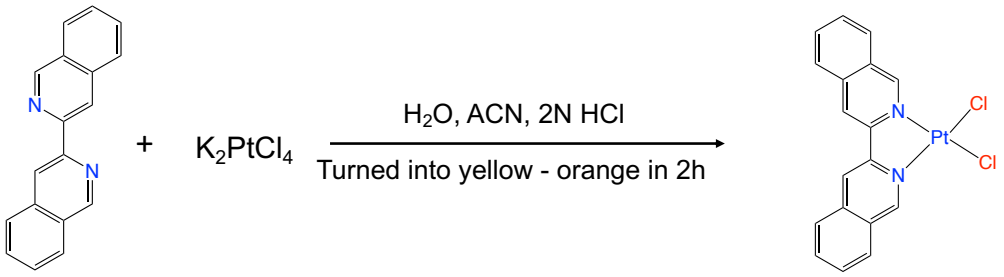

3,3' iso-Biquinolene

(i-biq)$PtCl_2$

Characterization and structural analysis were performed using MS and NMR. MS data showed a single parent peak (m/z): calculated for [$C_{18}H_{12}N_2PtCl_2$]: 521.00, observed (M/z) for parent ion and sodium adduct $[M+Na]^+$ 544.99. The chemical shift (δ) of proton NMR (DMSO d_6, 300 MHz, 298 K) data recorded in deuterated DMSO (four signals are observed because of symmetric nature of ligand accompanied by absence of any other unlabeled peak); 10.25 ppm (s, 2H, pyridine), 9.22 − 9.19 ppm (m, 2H, pyridine and benzene ring), 8.51−8.46 ppm (m, 4H, pyridine and benzene ring), 7.91 ppm (s, 2H, pyridine and benzene ring).

3.4.4. Synthesis of (3,3'-iso-biquinoline)Pt(II)(1,2-benzene dithiol) (bdt)Pt(i-biq) Complex

The final complex (bdt)Pt(i-biq) was prepared by modifying established literature procedures.[62] [63] [5] 0.260 g (0.5 mmol, 1 eq) of (i-biq)$PtCl_2$ was placed in round bottom flask, flushed with nitrogen, and dissolved in distilled THF. 0.085 g (0.6 mmol, 1.2 eq) of 1,2 benzene dithiol was dissolved in anhydrous methanol (purchased from Sigma-Aldrich) in a separate flask, and 0.086 g (1.5 mmol, 3 eq) of KOH was dissolved in anhydrous methanol. The solution of the potassium salt was transferred anaerobically into the stirring

solution of 1,2-benzene dithiol. The color of the solution turned light blue, correlating to deprotonation. To ensure complete deprotonation, the solution was stirred for 10+ minutes. The mixture was then anaerobically transferred into the stirring solution of (i-biq)$PtCl_2$. The color of the solution turned reddish immediately. The reaction mixture was stirred for 1 h at room temperature to ensure completion of reaction. Solvent was then partially removed, and the product started to precipitate in the remaining methanol. 5 ml of methanol was added to enhance precipitation. The mixture was allowed to settle for 20 minutes to complete precipitation. Separation of the solid by filtration was performed. The remainder was washed three times with an additional 50 ml of methanol, hexane, and finally with diethyl ether. The product was dried under vacuum for 48 hours. Red colored powder of (bdt)Pt(i-biq) was isolated with 61% yield relative to the amount of (i-biq)$PtCl_2$ used.

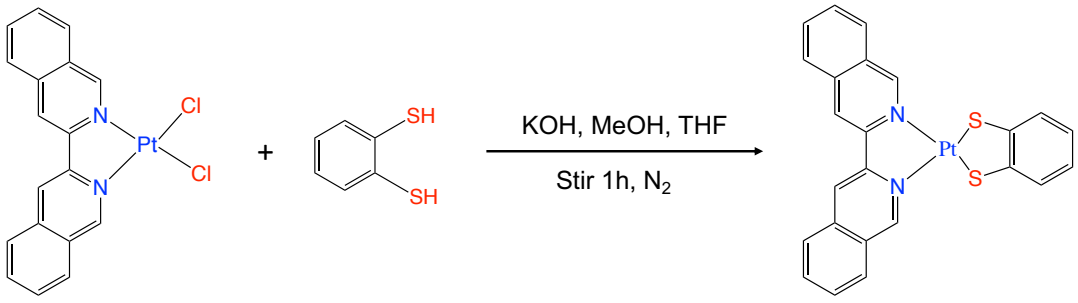

(i-biq)$PtCl_2$ 1,2 benzene dithiol (i-biq)Pt(bdt)

Characterization and structural analysis were performed by using MS, NMR and elemental analysis. The data recorded from MS has a notable peak for the parent and another peak for the dimer of the parent complex, (m/z): calculated for [$C_{24}H_{16}N_2PtS_2$]: 591.04, observed (M/z) for parent ion $[M]^+$ 591.04 peak and the dimeric peak calculated:

[$C_{28}H_{32}N_4Pt_2S_4$]: 1182.08, the observed (M/Z) is 1182.07 for $[M]^+$. NMR data was collected in deuterated chloroform ($CDCl_3$, 300 MHz, 298 K). The chemical shift (δ) of protons: 9.51 ppm [s, 2H, (i-biq) ligand], 8.59 ppm [s, 2H, (i-biq) ligand], 8.04 ppm [d, $J = 8.2$ Hz 2H, (i-biq) ligand], 7.90 ppm [t, $J = 7.5$ Hz, 2H, (i-biq) ligand] 7.72 ppm [d, $J = 8.3$, Hz, 2H, (i-biq) ligand], 7.59 ppm [t, $= 7.3$ Hz, 2H, (i-biq) ligand], 7.47ppm (dd, $= 5.9, 3.2$ Hz, 2H, 1,2 benzene dithiol) and 6.86 ppm (dd, 5.2, 3.2 Hz, 2H, 1,2 benzene dithiol).

3.4.3 Experimental Methods

Electronic structure calculations, electronic absorption spectroscopy, photoluminescence, and X-ray absorption spectroscopy were performed. Experimental details have been presented in section 3.2.4 of this chapter.

3.4.6 Results and Discussion

3.4.6.1 Electronic Absorption Spectroscopy

The absorption spectrum of (bdt)Pt(i-biq) in distilled THF at room temperature was recorded and is displayed in Figure 3.***36***. The MEC was calculated by using the serial dilution method. The lowest energy intense transition was observed at 20,225 cm^{-1}. Based on the results of TD-DFT calculations, that transition has been assigned as the donor HOMO to the LUMO+1. The energy of the lowest energy LL'CT transition is blue shifted compared to its structural isomer complex (bdt)Pt(biq), since the LUMO+1 was involved as acceptor orbital for (bdt)Pt(i-biq), the LL'CT is from HOMO to LUMO of (bdt)Pt(biq) and HOMO to LUMO+1 of (bdt)Pt(i-biq). The LUMO of (bdt)Pt(i-biq) has nodal character at the coordinating nitrogen atoms. The LUMO is shown in Figure 3.*37*.

Another band feature at 22,721 cm^{-1} is attributed to a one electron promotion from the donor HOMO to the LUMO+2, and HOMO-1 to LUMO+1 (orbitals involved can be seen in Figure 3.*37*).[7 64]

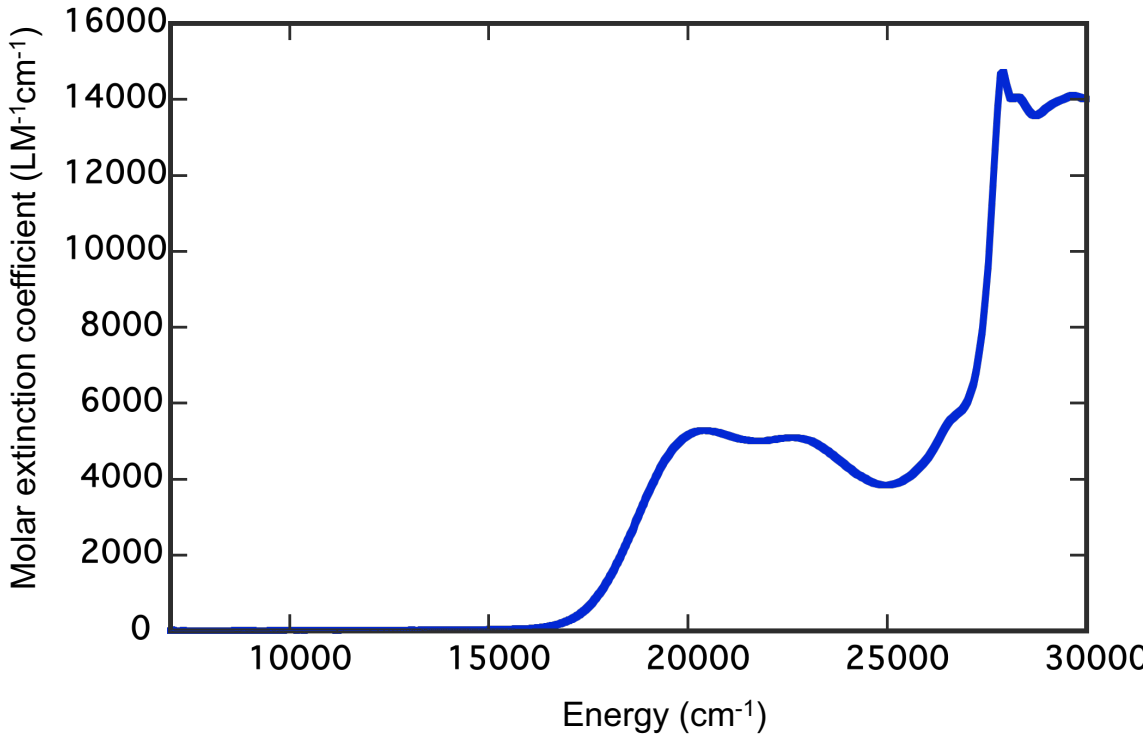

Figure 3.36: Room temperature electronic absorption spectrum of (bdt)Pt(***i***-biq) recorded using a Hitachi UV-vis-NIR spectrometer. The sample was prepared in distilled THF. The molecular extinction coefficient value is obtained by using the serial dilution method.

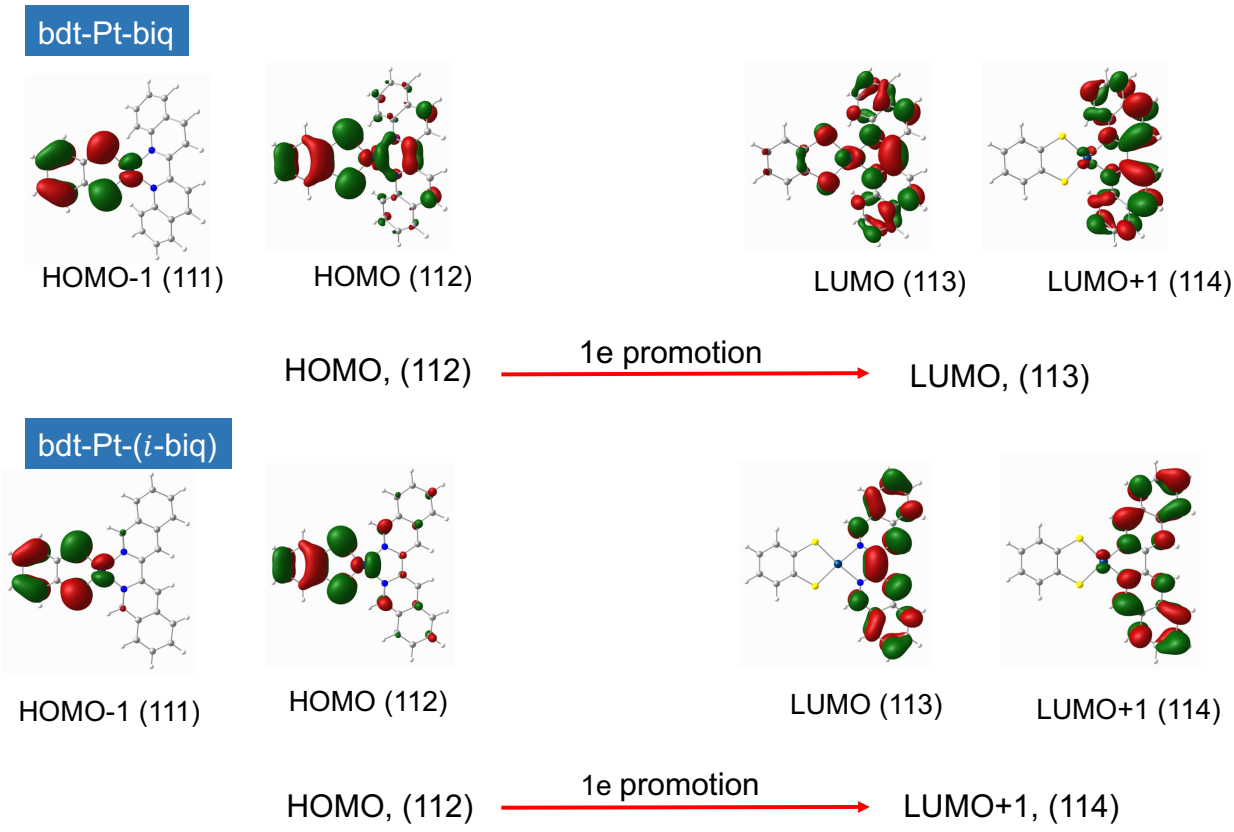

Figure 3.37: Time dependent DFT calculation results of (bdt)Pt(biq); Top and (bdt)Pt(i-biq; bottom). The LL'CT transition is associated with the one electron promotion primarily from the benzenedithiol donor HOMO to the quinoline LUMO for (bdt)Pt(biq) and for (bdt)Pt(i-biq) the transition involves a one electron promotion from HOMO to the LUMO+1 acceptor i-biq orbital

3.4.6.2 Photoluminescence and Kinetic Data

The emission spectrum recorded at room temperature has been shown in Figure 3.***38***. It was collected using an FLS 980 Fluorescence Spectrometer, and the sample was prepared in distilled DCM and purged with nitrogen before data collection. The concentration was appropriate (Absorbance = 0.45) as checked by electronic absorption prior to photoluminescence data to avoid self-absorption. The absorption and emission spectrum of the ligand was also recorded in the same solvent to exclude any possible contribution to the emission intensity from the ligand. After eliminating the possibility of a

contribution by the free ligand, we are confident that any emission intensity is originating from the pure (bdt)Pt(i-biq) complex as shown in Figure 3.***40***. Here, $\lambda_{exc} = 485$ nm and the observed λ_{emisn} = 780 nm. The data were recorded using both UV-visible and near IR detectors. The Stokes shift is 7530 cm^{-1}. This shift is large compared to its isomeric complex (3096 cm^{-1}). This is due to the involvement of higher lying orbitals in the LL'CT transition, and emission[55] must come from the lowest lying orbital (Kasha's rule). Thus, there is a large energy difference between emission and absorption maximum energies.

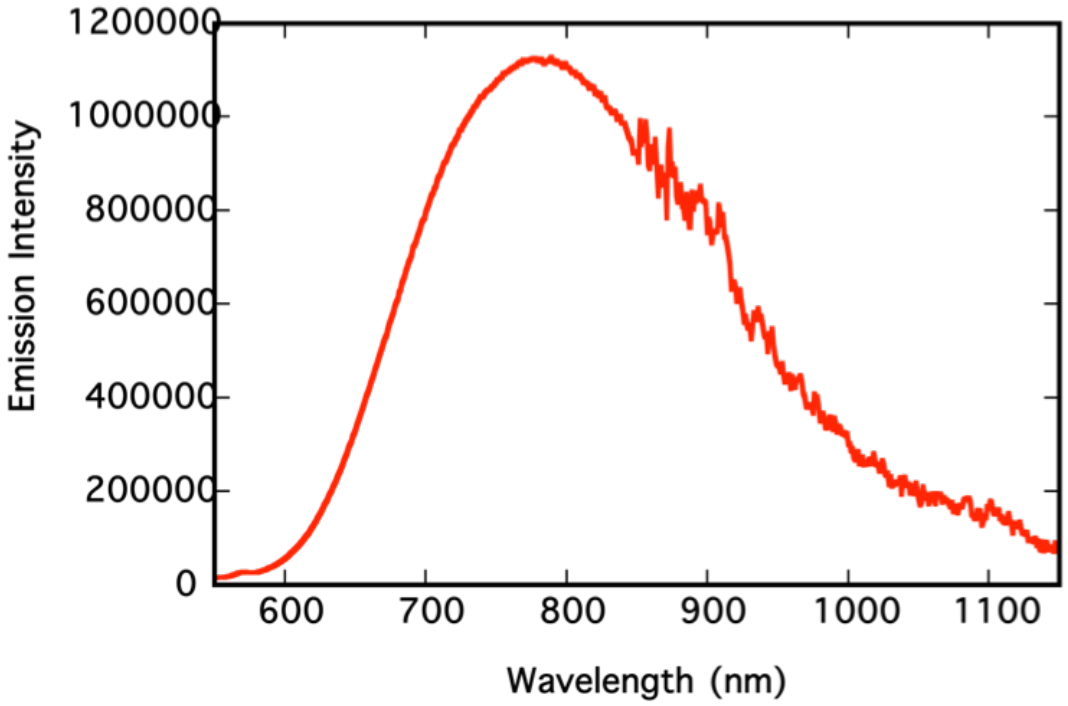

Figure 3.38: Room temperature emission spectrum recorded in DCM solution. Excitation wavelength was 485 nm with an absorption value of 0.45. Emission maximum wavelength was observed at 780 nm.

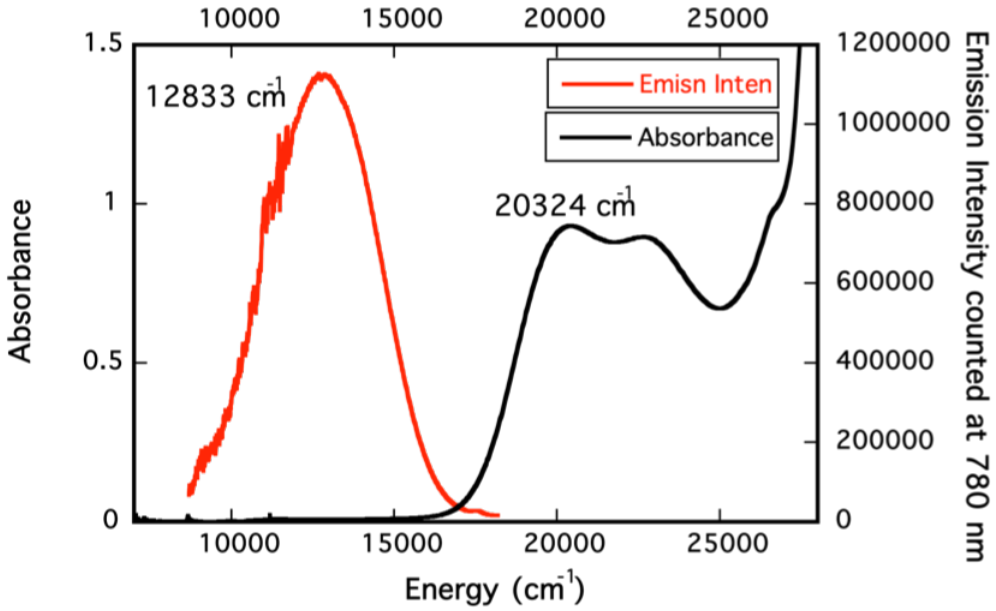

Figure 3.39: Room temperature electronic absorption (black solid line) and emission spectrum (red solid line) overlay for (bdt)Pt(***i***-biq). Data collected by using an FLS 980 fluorescence spectrometer.

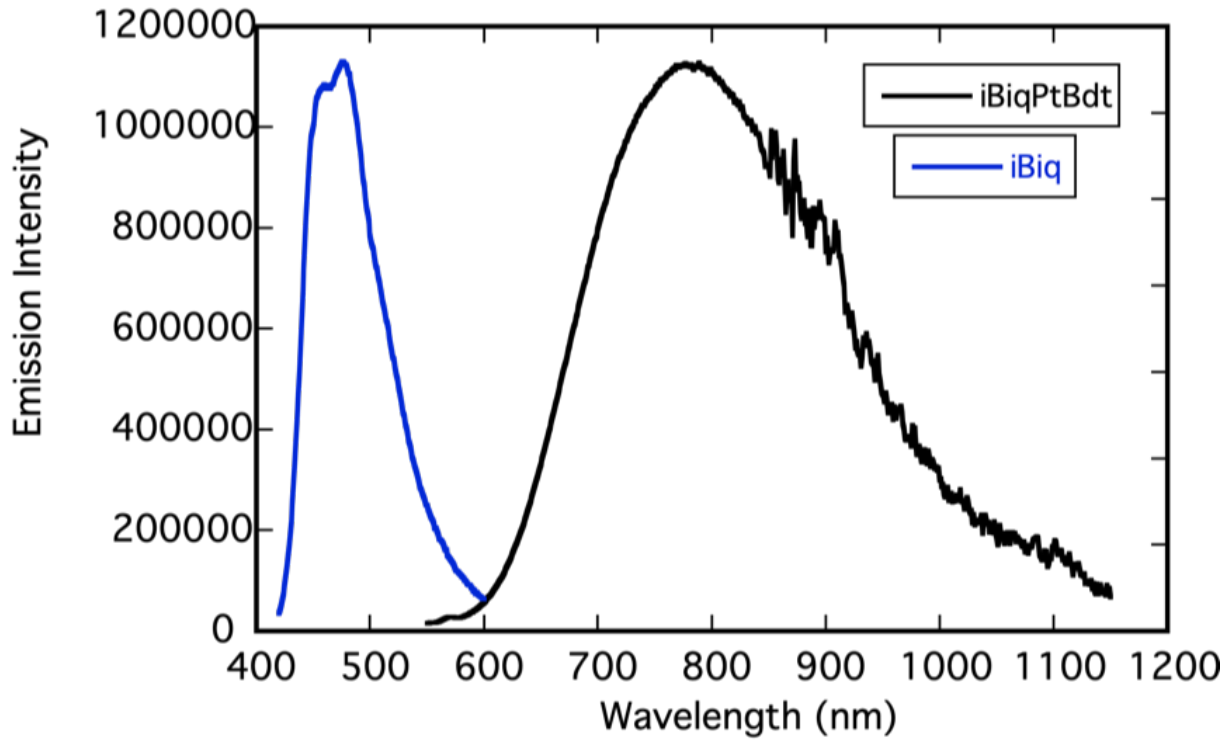

Figure 3.40: Overlay of emission data recorded by using FLS 980 fluorometer in THF of (***i***-biq) ligand (blue solid line) and (bdt)Pt(***i***-biq) complex (black solid line) excited at 400 nm and 480 nm respectively.

Room temperature lifetime kinetic data were recorded from the same sample used in the emission measurement. A 450 nm laser diode was used for the purpose of the lifetime measurement. The lifetime was measured at 780 nm (at the emission maximum). The data were fit to Equation 3.2. The mono-exponential decay lifetime was determined to be 9 ns. The lifetime of the ligand was also recorded, which was very short (less than 1 ns) and we were unable to fit instrument limitations. Thus, the emission data and recorded lifetime for the metal complex has no contribution from the free ligand. The emission lifetime is possibly from the ligand-based triplet orbital ($\pi^* \longrightarrow \pi$ relaxation).[65]

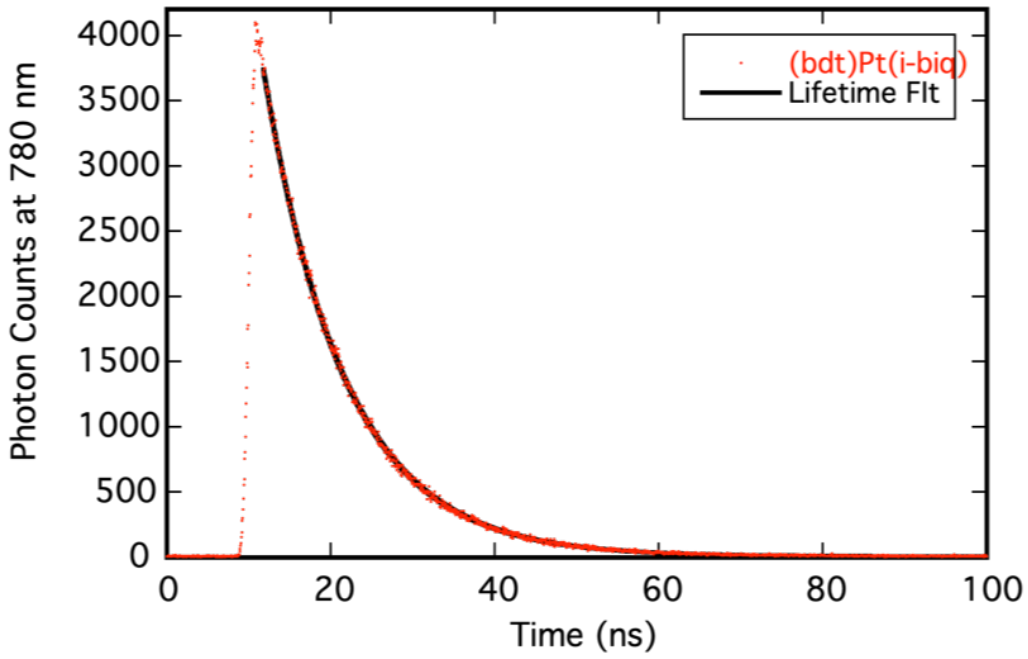

Figure 3.41: Room temperature data recorded by using FLS 980 exhibiting a mono-exponential decay excited state lifetime of 9 ns. The χ^2 value is 0.948 and the B (pre-exponential factor) value is 1006. The sample was purged with nitrogen to avoid interference from the oxygen present in the solution.

A shorter lifetime than expected can be explained by the orbital topology of the LUMO of the (bdt)Pt(i-biq) complex. In this complex, LUMO+1 orbital is involved in the depopulation process. The symmetry of both the HOMO (A1) and LUMO+1 (A1) is the same in C_{2v} point group of the (bdt)Pt(i-biq) complex.[5 9] Thus, being a spin forbidden but symmetry allowed process, the excited state depopulation occurs faster than in the (bdt)Pt(biq) complex. In (bdt)Pt(biq), the relaxation of the excited state occurs by transfer of the electron from the LUMO to the HOMO.

The nature and extent of orbital mixing differences in (bdt)Pt(biq) and (bdt)Pt(i-biq) is clearly reflected in the Orca calculated TD-DFT calculation presented in Table 3.6. Energy splitting between the singlet excited state and triplet excited state is very large

(~6,000 cm^{-1}) for the (biq)Pt(bdt) complex, and this value is significantly reduced (~600 cm^{-1}) for the (biq)Pt(i-biq) complex. A explanation of these calculated differences in energy splitting originates in their point groups and different orbital topologies. (biq)Pt(bdt) has C_s symmetry due to steric hindrance of the biq ligand with the donor ligand. The orbitals can mix in greater extent and because of that mixing we observed a larger S_1-T_1 splitting. This type of mixing is nearly impossible in the (bdt)Pt(i-biq) complex since there is no orbital overlap between the HOMO and LUMO. There is 10-fold decrease in the calculated S_1-T_1 splitting value seen below in Table 3.6. A similar trend has been observed on the S_n-T_n splitting pattern of higher excited states.

Table 3.12: Orca calculated values of singlet and triplet transition energies (cm^{-1}) for (bdt)Pt(biq) and (bdt)Pt(i-biq).

	(bdt)Pt(biq)		(bdt)Pt(i-biq)	
Excited states	Singlet (cm^{-1})	Triplet (cm^{-1})	Singlet(cm^{-1})	Triplet (cm^{-1})
1	13054	6522	10854	10250
2	13143	10898	14005	11352
3	18899	16597	14661	12909
4	20001	18649	14814	14389
5	21010	19970	17040	15320

3.4.6.3 S K-edge X-ray Absorption Spectroscopy

X-ray absorption spectroscopy at the S K-edge has been used to explain Pt-S covalency differences as a function of orbital overlap with Pt d-orbitals. Changing the donor and acceptor ligand has a dramatic effect on respective sulfur covalency in the LUMO and Pt 5d-orbital which are the origin of the first two pre-edge transitions from sulfur 1s orbital.[9] (bdt)Pt(i-biq) has extended π-conjugation compared to the parent

(bdt)Pt(bpy), and a different obital topology relative to its isomer (bdt)Pt(biq). Observed data has been analyzed by using the Orca calculated TD-DFT results. As seen in Figure 3.***43***, at 2471 eV there is a very low intensity transition, as we know intensity of this pre-edge peak is directly proportional to the sulfur orbital character in the LUMO of the complex. For (bdt)Pt(i-biq), the origin of first transition peak is from 1s ⟶ LUMO+1. Calculation and experimental observations have depicted the percentage of S character 0.92% per S atom, per molecular orbital. There is a significant reduction of the S percentage from the first transition peak as compared to (bdt)Pt(biq) (3.5%). Different behavior of the first transition is explained based on the spatial distribution of the LUMO and LUMO+1 ligand-based acceptor orbitals.[13] The LUMO of (bdt)Pt(i-biq) is nodal at the coordinating nitrogen atoms thus doesn't admix with the HOMO. This is the mechanism for acquiring sulfur character, therefore the transition from 1s to the LUMO is not observed. The LUMO+1 has a different symmetry in the C_{2v} point group from HOMO of the complex, thus mixing between these two orbitals is forbidden by symmetry. The energy of LUMO+1 for (bdt)Pt(i-biq) compared to the LUMO of (bdt)Pt(biq) is greater. This results in very little mixing between the HOMO and the LUMO+1, which is observed from the X-ray absorption pre-edge intensity being nearly invisible compared to the (bdt)Pt(biq) complex. This can be seen comparatively in the two XAS spectra in Figure 3.21 (biq) and Figure 3.43 (i-biq).

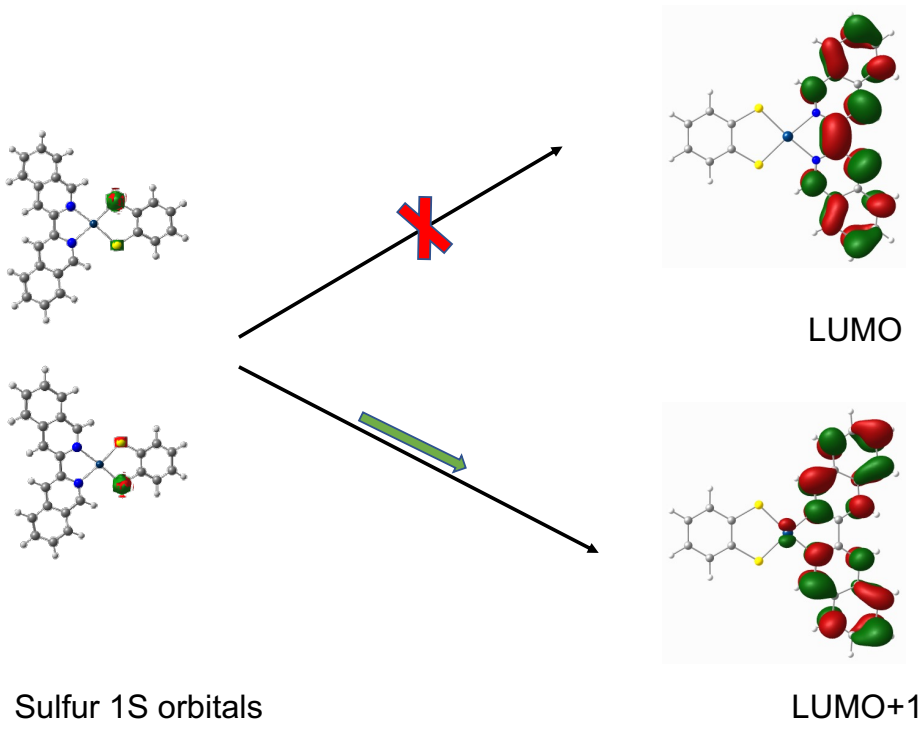

Figure 3.42: Depicting the acceptor orbital involved in first transition from sulfur 1s orbital. Left, 1s orbitals of two sulfur atoms. Right, howing the molecular LUMO (top) and LUMO+1 (bottom). A transition is not possible into LUMO orbital due to the absence of mixing with the HOMO. It is possible to promote an electron into the LUMO+1 but the admixture of the LUMO+1 and the HOMO is very little. This is clearly observed in the intensity of respective peak.

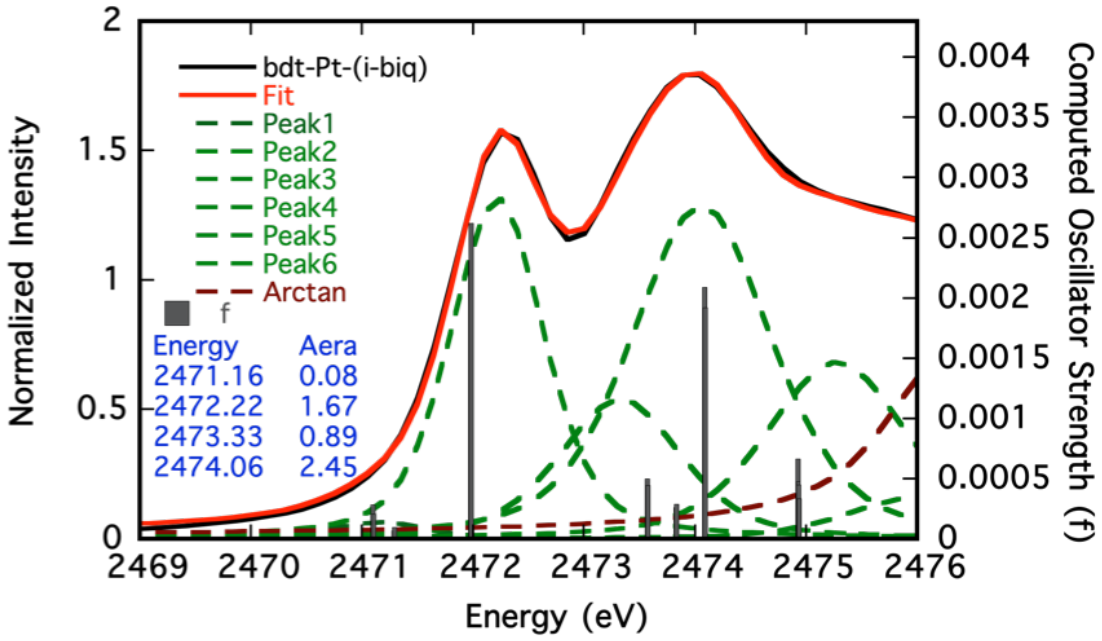

Figure 3.43: Overlay of experimental peak fitting (red solid line) Gaussian resolved peaks (green dotted lines) and computed oscillator strength (brown sticks) of XAS S K-edge data collected on a solid-state sample of (bdt)Pt(i-biq) at SSRL. Two low energy peaks have been analyzed as the transition from sulfur (1s) ⟶ 3p (sulfur) + Pt (5d) (second peak) and sulfur 1S ⟶ $\boldsymbol{\varphi}^*_{\text{LUMO}}$ transition (first peak).

The second intense transition on the S K-edge plot has been assigned as an electron promotion from the sulfur 1s orbital to sulfur 3p + Pt 5d-orbital. This is predominantly from 1s to the Pt $d_{x^2-y^2}$ orbital, since there are no other orbitals that have comparable energies to the LUMO+5 orbital and the Pt $d_{x^2-y^2}$ is the only empty metal orbital in a square planar d^8 geometry. An orbital composition analysis of the LUMO+5 for (bdt)Pt(i-biq) shows ~25% sulfur 3p orbital character. The analysis of the second intense peak (272.3 eV) has shown 17% sulfur character per sulfur atom. The decreased amount of sulfur compared to (bdt)Pt(biq) is explained by the higher energy of LUMO+5 orbital than the LUMO+3 of (bdt)Pt(biq) complex from the nature of their respective HOMOs.

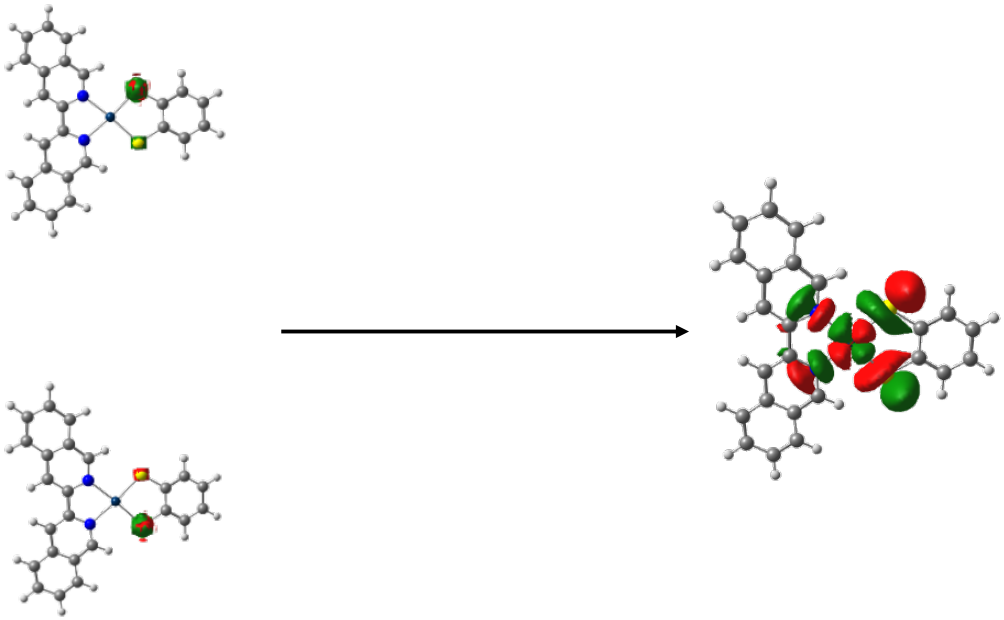

Sulfur 1S orbitals LUMO+5, Pt, $dx^2 - y^2$

Figure 3.44: (bdt)Pt(i-biq), computed orbital contributions. Molecular orbitals involved in the second intense peak at 2472.2 eV of the S K-edge plot. Sulfur 1s orbitals are shown on the left, whereas molecular LUMO+5 and Pt d_{x2-y2} orbitals are shown on the right.

3.4.7 Conclusion

The observed lifetime for (bdt)Pt(*i*-biq) is much shorter and the phosphorescence band exhibits a very large Stokes shift compared to (bdt)Pt(biq). There is an absence of an orbital pathway to effectively relax excited state (LUMO) to the ground state (HOMO). The observed higher energy of the electronic transition is due to higher lying acceptor LUMO orbitals. Thus, observed shorter life time than (bdt)Pt(biq) is due to the involvement of HOMO-1 and LUMO+1 in the relaxation process. They share the same symmetry in the C_{2V} point group. This provides a faster relaxation pathway from excited triplet state to ground electronic state being a symmetry allowed process compared.

3.5 References

1. Zuleta, J. A., Burberry, M. S. & Eisenberg, R. Platinum(II) diimine dithiolates. New solution luminescent complexes. *Coord. Chem. Rev.* **97**, 47–64 (1990).
2. Vogler, A. & Kunkely, H. Photooxidation of (2,2'-bipyridine)(3,4-toluenedithiolato)platinum(II) following ligand-to-ligand and charge-transfer excitation. *J. Am. Chem. Soc.* **103**, 1559–1560 (1981).
3. Vogler, A., Kunkely, H., Hlavatsch, J. & Merz, A. Mixed-ligand (1,2-diimine)(ethylene-1,2-dithiolate) complexes of nickel, palladium, and platinum. *Inorg. Chem.* **23**, 506–509 (1984).
4. Balzani, V. & Moggi, L. Photochemistry of coordination compounds: a glance at past, present, and future. *Coord. Chem. Rev.* **97**, 313–326 (1990).
5. Yang, J. *et al.* Ligand Control of Donor–Acceptor Excited-State Lifetimes. *Inorg. Chem.* **53**, 4791–4793 (2014).
6. Cummings, S. D. & Eisenberg, R. Tuning the Excited-State Properties of Platinum(II) Diimine Dithiolate Complexes. *J. Am. Chem. Soc.* **118**, 1949–1960 (1996).
7. Cummings, S. D. & Eisenberg, R. Tuning the excited-state properties of platinum (II) diimine dithiolate complexes. *J. Am. Chem. Soc.* **118**, 1949–1960 (1996).
8. Meyer, T. J. Chemical approaches to artificial photosynthesis. 8.
9. Yang, J. *et al.* Ground State Nuclear Magnetic Resonance Chemical Shifts Predict Charge-Separated Excited State Lifetimes. *Inorg. Chem.* (2018) doi:10.1021/acs.inorgchem.8b02087.
10. Valeur, B. Molecular Fluorescence Principles and Applications. *Mol. Fluoresc.* 399 (2001).

11. Rodriguez-Serrano, A., Rai-Constapel, V., Daza, M. C., Doerr, M. & Marian, C. M. Internal heavy atom effects in phenothiazinium dyes: enhancement of intersystem crossing via vibronic spin–orbit coupling. *Phys. Chem. Chem. Phys.* **17**, 11350–11358 (2015).
12. Tatchen, J., Gilka, N. & Marian, C. M. Intersystem crossing driven by vibronic spin–orbit coupling: a case study on psoralen. *Phys. Chem. Chem. Phys.* **9**, 5209 (2007).
13. Valeur, B. Molecular Fluorescence Principles and Applications. *Mol. Fluoresc.* 399 (2001).
14. Chakrabarti, S. K. Vibronic spin-orbit interactions in 2-naphthaldehyde and 2-naphthyl methyl ketone. *Mol. Phys.* **16**, 467–479 (1969).
15. Solomon, E. I. *Inorganic Spectroscopy, An Overview*. vol. 3 (Comm. Inorg. Chem. Sutin, N., Ed.; Gorden and Breach: New York, 1984).
16. Lyskov, I. & Marian, C. M. Climbing up the Ladder: Intermediate Triplet States Promote the Reverse Intersystem Crossing in the Efficient TADF Emitter ACRSA. *J. Phys. Chem. C* **121**, 21145–21153 (2017).
17. Peter Belser, Alex Von Zelewsky. Synthesis, spectroscopic Data and Electrochemical Behaviour of Ruthenium(II) Complexes with Bidentate Ligands. *Helv. Chim. Acta* **63**, 1675–1702 (1980).
18. Barigelletti, F., Juris, A., Balzani, V., Belser, P. & Von Zelewsky, A. Excited-state properties of complexes of the tris(diimine)ruthenium(2+) ion family. *Inorg. Chem.* **22**, 3335–3339 (1983).
19. Barigelletti, F., Juris, A., Balzani, V., Belser, P. & Von Zelewsky, A. Temperature dependence of the bis(2,2'-bipyridine)dicyanoruthenium(II) and bis(2,2'-

bipyridine)(2,2'-isobiquinoline)ruthenium(II) luminescence. *J. Phys. Chem.* **91**, 1095–1098 (1987).

20. Peter Belser, Alex Von Zelewsky, Alberto Juris, Francesco Barigelletti and Vincenzo Balzani. Excited-state properties of some new ruthenium(II) cyano-polypyridine complexes in various solvents. *Gaeeetta Chim. Ital.* **115**, (1985).
21. Atoini, Y. *et al.* Luminescence of Amphiphilic Pt ^{II} Complexes Controlled by Confinement. *Chem. – Eur. J.* **24**, 12054–12060 (2018).
22. Minghetti, G., Stoccoro, S., Cinellu, M. A., Soro, B. & Zucca, A. Activation of a C−H Bond in a Pyridine Ring. Reaction of 6-Substituted 2,2'-Bipyridines with Methyl and Phenyl Platinum(II) Derivatives: N',C(3)-"Rollover" Cyclometalation. *Organometallics* **22**, 4770–4777 (2003).
23. Shafaatian, B. & Heidari, B. Synthesis, characterization, crystal structure, solvatochromism, fluorescence and electrochemical studies of new organometallic platinum complexes, kinetic investigation of oxidative addition reaction. *J. Organomet. Chem.* **780**, 34–42 (2015).
24. Egan, T. J. *et al.* In Vitro Antimalarial Activity of a Series of Cationic 2,2'-Bipyridyl- and 1,10-Phenanthrolineplatinum(II) Benzoylthiourea Complexes. *J. Med. Chem.* **47**, 2926–2934 (2004).
25. Gaussian 09, R. C. G., Inc., Pittsburgh, PA, 2009.
26. Becke, A. D. Density-functional thermochemistry. III. The role of exact exchange. *J. Chem. Phys.* **98**, 5648–5652 (1993).

27. Weigend, F. & Ahlrichs, R. Balanced basis sets of split valence, triple zeta valence and quadruple zeta valence quality for H to Rn: Design and assessment of accuracy. *Phys. Chem. Chem. Phys.* **7**, 3297 (2005).

28. Feller, D. The role of databases in support of computational chemistry calculations. *J. Comput. Chem.* **17**, 1571–1586 (1996).

29. Schuchardt, K. L. *et al.* Basis Set Exchange: A Community Database for Computational Sciences. *J. Chem. Inf. Model.* **47**, 1045–1052 (2007).

30. Andrae, D., Häußermann, U., Dolg, M., Stoll, H. & Preuß, H. Energy-adjustedab initio pseudopotentials for the second and third row transition elements. *Theor. Chim. Acta* **77**, 123–141 (1990).

31. Bauernschmitt, R. & Ahlrichs, R. Treatment of electronic excitations within the adiabatic approximation of time dependent density functional theory. *Chem. Phys. Lett.* **256**, 454–464 (1996).

32. Stratmann, R. E., Scuseria, G. E. & Frisch, M. J. An efficient implementation of time-dependent density-functional theory for the calculation of excitation energies of large molecules. *J. Chem. Phys.* **109**, 8218–8224 (1998).

33. Casida, M. E., Jamorski, C., Casida, K. C. & Salahub, D. R. Molecular excitation energies to high-lying bound states from time-dependent density-functional response theory: Characterization and correction of the time-dependent local density approximation ionization threshold. *J. Chem. Phys.* **108**, 4439–4449 (1998).

34. Van Caillie, C. & Amos, R. D. Geometric derivatives of density functional theory excitation energies using gradient-corrected functionals. *Chem. Phys. Lett.* **317**, 159–164 (2000).

35. Furche, F. & Ahlrichs, R. Adiabatic time-dependent density functional methods for excited state properties. *J. Chem. Phys.* **117**, 7433–7447 (2002).

36. Scalmani, G. *et al.* Geometries and properties of excited states in the gas phase and in solution: Theory and application of a time-dependent density functional theory polarizable continuum model. *J. Chem. Phys.* **124**, 094107 (2006).

37. Neese, F. The ORCA program system. *WIREs Comput. Mol. Sci.* **2**, 73–78 (2012).

38. Turro, N. J., Ramamurthy, V. & Scaiano, J. J. Modern Molecular Photochemistry of Organic Molecules. *Univ. Sci. Books* (2010).

39. FLS980 Photoluminescence Spectrometer uUser Guide ISS2, Edinburgh Instrument.

40. Ferraro, J. R., Nakamoto, K. & Brown, C. W. INTRODUCTORY RAMAN SPECTROSCOPY. *Acad. Press San Diego* 4 (2003).

41. Kirk, M. L., Shultz, D. A., Depperman, E. C., Habel-Rodriguez, D. & Schmidt, R. D. Spectroscopic Studies of Bridge Contributions to Electronic Coupling in a Donor-Bridge-Acceptor Biradical System. *J. Am. Chem. Soc.* **134**, 7812–7819 (2012).

42. Wilson, J. S. *et al.* The Energy Gap Law for Triplet States in Pt-Containing Conjugated Polymers and Monomers. *J. Am. Chem. Soc.* **123**, 9412–9417 (2001).

43. Caspar, J. V., Kober, E. M., Sullivan, B. P. & Meyer, T. J. Application of the energy gap law to the decay of charge-transfer excited states. *J. Am. Chem. Soc.* **104**, 630–632 (1982).

44. Sarangi, R. *et al.* Sulfur K-Edge X-ray Absorption Spectroscopy as a Probe of Ligand−Metal Bond Covalency: Metal vs Ligand Oxidation in Copper and Nickel Dithiolene Complexes. *J. Am. Chem. Soc.* **129**, 2316–2326 (2007).

45. Szilagyi, R. K. *et al.* Description of the Ground State Wave Functions of Ni Dithiolenes Using Sulfur K-edge X-ray Absorption Spectroscopy. *J. Am. Chem. Soc.* **125**, 9158–9169 (2003).

46. Glaser, T., Hedman, B., Hodgson, K. O. & Solomon, E. I. Ligand K-Edge X-ray Absorption Spectroscopy: A Direct Probe of Ligand−Metal Covalency. *Acc. Chem. Res.* **33**, 859–868 (2000).

47. Kaes, C., Katz, A. & Hosseini, M. W. Bipyridine: The Most Widely Used Ligand. A Review of Molecules Comprising at Least Two 2,2‘-Bipyridine Units. *Chem. Rev.* **100**, 3553–3590 (2000).

48. Fritz Blau. *Uber die trocken Destillation Von pyridincarbon-sauren Salzen*. vol. 8 (1889).

49. Constable & Housecroft. The Early Years of 2,2’-Bipyridine—A Ligand in Its Own Lifetime. *Molecules* **24**, 3951 (2019).

50. Chen, M., Hu, J., Tang, X. & Zhu, Q. Piperazine as an Inexpensive and Efficient Ligand for Pd-Catalyzed Homocoupling Reactions to Synthesize Bipyridines and Their Analogues. *Curr. Org. Synth.* **16**, 173–180 (2019).

51. Dolomanov, O. V., Bourhis, L. J., Gildea, R. J., Howard, J. A. K. & Puschmann, H. *OLEX2* : a complete structure solution, refinement and analysis program. *J. Appl. Crystallogr.* **42**, 339–341 (2009).

52. Sheldrick, G. M. Crystal structure refinement with *SHELXL*. *Acta Crystallogr. Sect. C Struct. Chem.* **71**, 3–8 (2015).

53. Case, F. H. THE PREPARATION OF 1,1’- AND 3,3’-BIISOQUINOLINE [1]. *J. Org. Chem.* **17**, 471–472 (1952).

54. Case, F. H. THE PREPARATION OF 1,1'- AND 3,3'-BIISOQUINOLINE [1]. *J. Org. Chem.* **17**, 471–472 (1952).

55. Peter BELSER, Alex VON ZELEWSKY. LIGAND_CENTERED LUMINESCENCE FROM RUTHENIUM(II) COMPLEX. **89**, 101–104 (1982).

56. Barigelletti, F. & Balzani, V. LUMINESCENCE OF MIXED-LIGAND Ru(Ii) CHELATES. IS THERE ANY BONA FZDE CASE OF DUAL EMISSION? *Chem. Phys. Lett.* **104**, 5 (1984).

57. Juris, A., Barigelletti, F., Balzani, V., Belser, P. & Von Zelewsky, A. Luminescence of ruthenium(II) tris chelate complexes containing the ligands 2,2'-bipyridine and 2,2'-biisoquinoline. Behavior of the Ru(bpy)2+ and Ru(bpy)22+ emitting units. *Inorg. Chem.* **24**, 202–206 (1985).

58. Kato, M. *et al.* Crystal Structures and Luminescence Properties of Platinum(II) Complexes Containing 3,3'-Biisoquinoline. *Inorg. Chem.* **35**, 116–123 (1996).

59. Kato, M. *et al.* Luminescence Properties and Crystal Structures of Dicyano(diimine)platinum(II) Complexes Controlled by Pt···Pt and π−π Interactions. *Inorg. Chem.* **38**, 1638–1641 (1999).

60. Kato, M. *et al.* Crystal Structures and Luminescence Properties of Platinum(II) Complexes Containing 3,3'-Biisoquinoline. *Inorg. Chem.* **35**, 116–123 (1996).

61. Hodges, K. D. & Rund, J. V. Oxidative addition of halogens and pseudohalogens to dihalo(1,10-phenanthroline)platinum(II). *Inorg. Chem.* **14**, 525–528 (1975).

62. Bossi, A. *et al.* Photophysical Properties of Cyclometalated Pt(II) Complexes: Counterintuitive Blue Shift in Emission with an Expanded Ligand π System. *Inorg. Chem.* **52**, 12403–12415 (2013).

63. Niedermair, F. *et al.* Heteroleptic κ2(N,C2)-2-phenylpyridine platinum complexes: The use of bis(pyrazolyl)borates as ancillary ligands. *Inorganica Chim. Acta* **360**, 2767–2777 (2007).

64. Stiefel, E. I. & Karlin D., K. Dithiolene Chemistry: Synthesis, Properties, and Applications,. *Prog Inorg Chem* **52**, (2004).

65. Kato Masako, Sasano Kumiko, KImura Masaru, Yamauchi Seigo. Solid State Effect on the Phosphorescence Spectrum of a Tris(3,3'-biisoquinoline) ruthenium(II) Salt. *Chem. Lett.* **21**, 1887–1890 (1992).

Chapter 4

A Study on Spin Delocalization in Radical Coordinated Platinum (II) Donor-Acceptor Complexes

4.1 Introduction

Recent technological advancements are emerging into the field of molecular level, or nanoscale, devices. Chemists are more inclined than ever to synthesize and design these molecules with scalable properties to inspire future technologies. The emerging fields include spintronics (molecular spin based electronics, or spin transport electronics) and nuclear and electron spin manipulation (spin qubits)[1] [2] [3] [4] [5], as well as molecular quantum information science applications[6] [7] [8], which includes quantum sensing, quantum computing, teleportation, and cryptography.[8] The rationale for moving away from traditional inorganic semiconductors toward molecular systems in future technologies is the hope that these future classes of molecules can be synthesized in varieties of combinations. Furthermore, their properties can be tuned by synthetic modifications in a systematic way with desirable molecular characteristics, and their electronic properties and functionalities can be bridged to include conductivity and magnetism in polymers.[9] [4] Understanding how to control and manipulate single spins in multi-spin systems is the basis for molecular spintronics and quantum information science.[10] Particularly, the controlled generation and manipulation of spin entanglement is one of the key requirements in quantum information processing.[11] Spin entanglement is defined as the correlation between two spins in a system where separation of single spin feature is mostly impossible.[12] The current major challenge is increasing the spin coherence time.[13] Even though remarkable progress has been made in this field, there is still a lack of

information on some key fundamentals. For example, how can molecular spin-qubits be coupled and manipulated, what are the effects of magnetic exchange coupling on the relaxation process of photogenerated qubits, how we can develop understanding of excited state spin polarization effects, and how synthetic design principles can be used to tailor molecular spin qubits. Our study here aims to extract some of this information by synthesizing single and multiple spin bearing transition metal complexes and to study their excited state and magnetic properties by high resolution spectroscopic techniques.

4.2 Background

As mentioned earlier (section 2.1 and 3.1), square planar Pt complexes are among the most studied transition metal complexes due to their interesting photophysical and redox properties.[14] [15] [16] In particular, this includes donor-acceptor complexes where bipyridine has been used as the diimine acceptor and dichalcogenolenes as the donor moiety coordinated with Pt(II).[14] In the late 1980s, (diimine)Pt(dithiolate) complexes were the earliest systems to observe emission in room temperature fluid solutions.[16] Before then, photoluminescence was reported only in rigid media at low temperature. Pt(II) complexes of diimine and 1,1 and 1,2 dithiolates possess excited states which are unique to other related systems regarding their luminescence properties.[17] [18] All of them possess an absorption band that is highly solvatochromic in nature and occurs around 540-700 nm[18]. Recently this charge transfer band has been defined as the LLCT transition based on spectroscopy and electronic structure calculation results.[19] This transition was previously assigned as a mixed metal-ligand to ligand (MMLL'CT) type of transition.[20] [21] In general, excited state lifetimes of Pt(II) complexes coordinated with a dithiolene donor

ligand have been found to be relatively long.[22] This is due to an ISC mechanism, based on the comparatively small energy gap between singlet and triplet excited state energies. ISC is typically not observed with catecholate donors.[22] A recent study from our group has reported that the excited state lifetime in synthesized Pt(II) complexes with diimine acceptors and chalcogen donors (O, S, Se) are heavily influenced by spin-orbit and spin-vibronic effects.[19]

In recent years, the effect of organic radicals on excited state dynamics has been a very active field of research. Synthesis of molecular based magnetic materials with various modifications to probe radical effects is a major focus of current molecular material research. The role of appended organic radical(s) is reported in the process of enhanced ISC,[23] [24] and for understanding photoinduced electron transfer processes[25]. Our study here expands on earlier work, in which a stable organic radical is covalently attached to the donor or acceptor component of a Pt(II) donor-acceptor complex. Our group, in collaboration with the Shultz group at North Carolina State University, has published work that attributes the effect of an appended radical on facilitating ISC using catecholate donor ligands. This is accomplished by inducing exchange-mediated ISC, which was not previously possible in the parent complex (bpy)Pt(II)(cat), (cat = catecholate). A series of complexes have been synthesized with a persistent stable radical moiety, nitronylnitroxide(NN) or verdazyl (VD). These complexes are of the form (bpy)Pt(II)(cat-Radical).[10] In these radical elaborated systems, the localized chromophore excited singlet and triplet electronic states exchange couple with the covalently appended radical, resulting in Sing-Doublet (D_{sing}), Trip-Doublet (D_{trip}) and Quartet ($D_{quartet}$) excited states.[10] As a result of this mixing, the chromophore can access the triplet state, and an

exchange induced (enhanced) ISC, relative to the chromophore, occurs between D_{sing} to D_{trip}. Magnetic exchange coupling between the chromophore spins in the excited state has been determined by using variable temperature magnetic circular dichroism (MCD) spectroscopy. Previous work on these radical appended systems was focused on spin manipulation using the excited state exchange interaction.[10] Significant ground state spin polarization effects were also observed in those complexes, which is an important aspect of these systems to understand and use in quantum information science applications.[26] Later, studies on these radical elaborated systems was expanded to include the bridge fragment between the dichalcogenolene moiety and the radical unit in (bpy)Pt(II)(cat-bridge-NN) systems.[27] Findings from these studies include significant lifetime differences, and that lifetime control can be accomplished through the use of different bridges. This modulation is attributed to the exchange coupling mediated mixing of D_{sing} character to the lower excited state D_{trip} character.[27]

In this study, we use the verdazyl radical (VD) instead of the NN radical to further understand the excited state dynamics, photophysical properties, and magnetic properties of radical coordinated platinum donor-acceptor complexes. VD has been appended to both the donor dichalcogenolene ligand and the acceptor bipyridine ligand. The discovery of VD was reported in the early 1960s by Kuhn and Trischmann as a stable organic radical,[28] [29] and since then VD has been used to synthesize spin bearing paramagnetic molecular systems ubiquitously. The study of the magnetic properties of VD coordinated to transition metals started in the 1990s, when the first reported VD-Ru coordinated complex was synthesized by Brook et. al. in 1997.[30] Early studies were limited to VD coordination to only diamagnetic metal centers. Effects of redox properties

of isolated and functionalized VD were studied by Gilroy in 2007, and it was concluded that it could be reduced and oxidized reversibly, and that the spin distribution and ring substituents influenced the redox properties.[31] Its redox behavior and non-innocent nature was explored by McKinnon in 2010, by synthesizing coordination complexes containing VD, Ru, and the ancillary ligand acetylacetone (acac) with and without fluorine substitution. They also extended this study to investigate the nature of spin delocalization in these two complexes.[32] Later, coordination of VD to different paramagnetic metal systems was performed so that exchange coupling between these metal centers and VD could be elucidated, as reported by Hicks et. al.[33] These investigations uncovered complex exchange coupling between them due to the inherent inter- and intra-molecular interactions that are difficult to quantitatively measure.[34] [30] [35] [32] [36] This included a Ni-VD complex that showed a strong ferromagnetic interaction between the VD spin and Ni metal center, but synthesized Cu and Mn analogs showed only weak anti-ferromagnetic interactions. These findings can be explained with molecular orbital theory and symmetry arguments.[37] [38] [39] The magnetism of VD-Ru complexes was also explored in the early 2000s,[32] when VD was employed to synthesize a supramolecular complex as reported by Hicks in 2004.[40] VD is air stable, and its overall stability is comparable to the NN organic radical. As a weak base, VD is stabilized when coordinated with transition metals that are weak Lewis acids, and its coordination properties are not comparable to other organic radicals such as NN, imino-nitroxide (IN) and anion based radical semiquinone (SQ).[38] [41] NN and VD radicals have some similarities such as their similar electronic structures, similar spatial distributions of frontier orbital wavefunctions, and similar physical properties, as outlined in Figure 4.24. Here, we will explore in more detail the

excited state properties, magnetic behavior, and nature of spin delocalization of donor-acceptor Pt(II) complexes by introducing the VD radical in these systems.

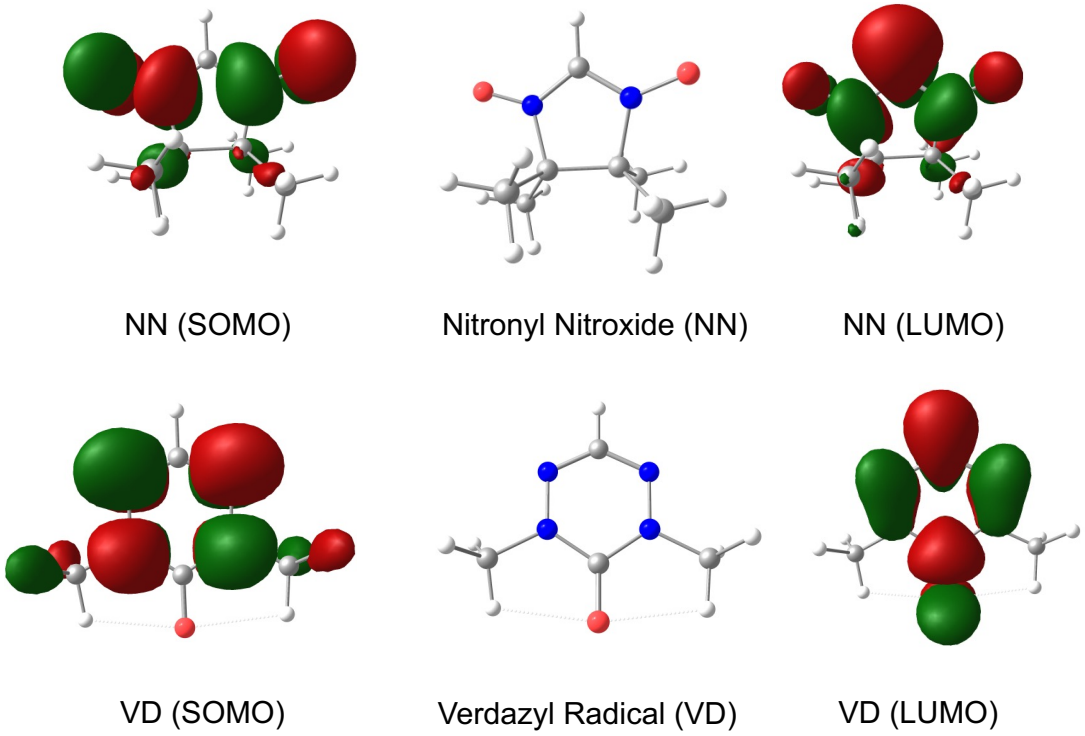

Figure 4.24: Frontier orbital SOMOs and LUMOs of NN radical (top) and verdazyl radical (VD) (bottom). Calculations were performed on the geometry optimized ground state. The frontier orbitals share a common nodal character.

4.3 Synthesis and Characterization

4.3.1. Synthesis of 1,5-diisopropyl-3-pyridin-2yl-6-Oxoverdazyl (VD) Radical

The 1,5-diisopropyl-6-oxoverdazyl radical was synthesized by following literature procedures.[42] [43] The synthetic procedure followed Scheme 1 (R = 2-pyridyl). Characterization was performed by MS analysis.

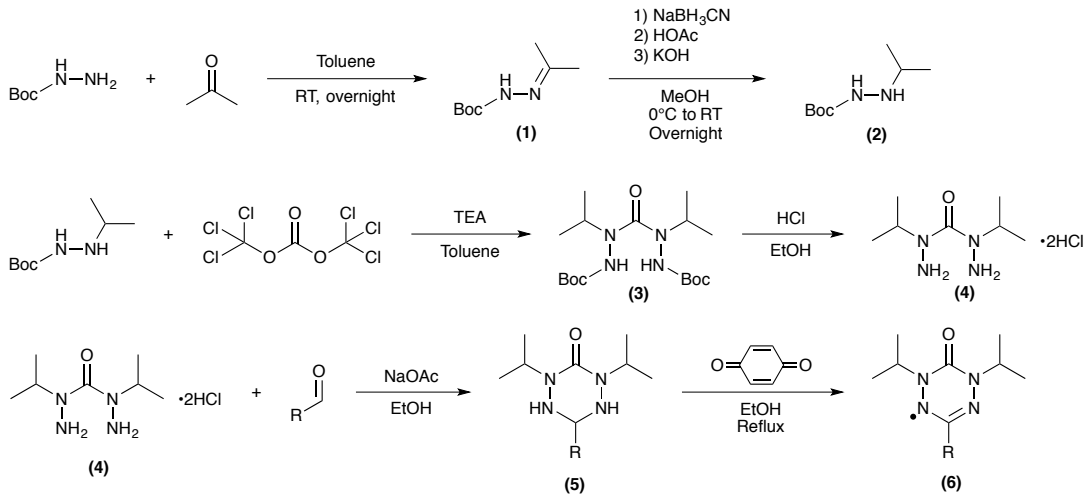

Scheme 4.1: Synthetic scheme of 1,5-diisopropyl-6-oxoverdazyl radical

The compound 2,4-diisopropyl-6-pyridin-2-yl-1,2,4,5-tetrazinan-3-one (pyridine-tetrazine) was synthesized by adding 0.247 g (1 mmol) of 2,4-diisopropylcarbonohydrazide bis-hydrochloride and 0.89 ml (1 mmol, 1 equiv.) of 2-pyridylcarboxaldehyde to 10 ml of ethanol and stirred. A solution of 0.082 g (2 mmol, 2 equiv.) anhydrous sodium acetate was dissolved in 2 ml of ethanol and was added to the stirring mixture at room temperature. This was left undisturbed for 24 h. The solution turned pale yellow. The solution was filtered, and the yellow-colored filtrate was concentrated by evaporation. Pure tetrazine was obtained by performing a recrystallization in heptane. The structure was confirmed by proton NMR, which is in good agreement with the reported data.[43] Room temperature NMR data recorded in deuterated chloroform displays the following chemical shift values associated with different protons: δ_H; 8.58 (1H, d J = 2.1), 7.79 (1H,td, J = 2.0) 7.43 (1H, td, J = 1.9); 7.35 (1H, ddd, J = 4.1), 4.73 (2H, septate, J = 2.3), 4.40 (1H, S), 1.11 (6H, D, J = 5.9), 1.09 (6H, d, J = 5.8).

The 1,5-diisopropyl-3-pyridin-2-yl-6-oxoverdazyl radical (PyVD) was obtained by oxidizing 2,4-diisopropyl-6-(pyridine-2-yl)-1,2,4,5-tetrazinan-3-one with benzoquinone. 0.228 g (1.24 mmol) of tetrazine solution in 40 ml of toluene was mixed with 0.18 g (3 mmol) of benzoquinone dissolved in 10 ml of toluene. Then, the reaction mixture was refluxed for 4 h. While refluxing, the solution turned into red. The solvent was removed, and the solid product was purified by using column chromatography with silica gel as the adsorbent and a 9:1 mixture of dichloromethane and ethyl acetate as the eluent. The dark red fraction was concentrated and crystalized in ethyl acetate to obtain crystals of pure compound with a 74% calculated yield based on the used amount of the pyridine-tetrazene precursor. The product was characterized by MS. Calculated $[M/z]^+$ for [C13H18N5O] is 260.15 g/mol representing 100% peak, observed $[M/z]^+$ is 260.15 as the major product. The product was utilized in subsequent syntheses.

4.3.2. Synthesis of 1,5-diisopropyl 6-oxoverdazyl Radical Platinum (II) catecholate; $(PyVD)PtCl_2$

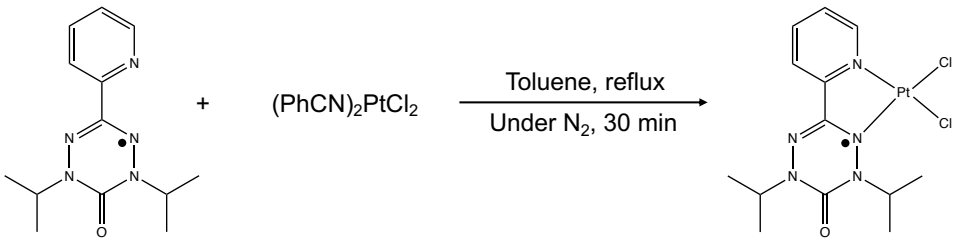

Pyridine verdazyl radical

Pyridine verdazyl platinum(II) dichloro

The preparation of (PyVD)$PtCl_2$ was accomplished by following reported literature procedures.[39] 0.037 g (0.092 mmol) of dibenzonitrile platinum dichloride, $(PhCN)_2PtCl_2$, was dissolved in 20 ml of toluene. The solution was refluxed for 20 minutes. After the solution turned light brown, 0.024 g (1 eq, 0.092 mmol) of VD solution dissolved in 5 ml of toluene was added anaerobically. The reaction mixture immediately turned a dark color, and the reaction mixture was refluxed for 30 minutes. The solution was allowed to settle down for 24 h at room temperature for the crystallization. Black needle shaped crystals of the product were isolated by filtration with 52% (0.021 g) yield after 24 h. Characterization was performed by electronic absorption spectroscopy and IR. Ft-IR (KBr)/cm^{-1}: 2975 (w), 2932 (w), 1684 (s), 1508 (w), 1442 (w), 1395 (w), 1297 (w), 1257 (w), 1220 (w), 1074 (w), 784 (m), 748 (s), 719 (w), 666 (s), 655 (w) 642 (s), 579 (s), 540 (w), 442 (w) and 426 (w), and the data are is good agreement with reported data.[39] Observed MS data showed the parent ion peak without the chlorides. Apparently, the experimental conditions of the MS resulted in elimination of the donors. Magnetic susceptibility data were recorded on a Quantum Design MPMS SQUID magnetometer and showed that the mono-radical has exhibited intermolecular antiferromagnetic exchange coupling with $2J = -12$ cm^{-1}. This further supports its purity and structure, and a detailed explanation of the magnetic data is presented in section 4.3.

4.3.3 Synthesis of (pyridine verdazyl) Pt (II) (1,2-benzenedithiol); (PyVD)Pt(bdt).

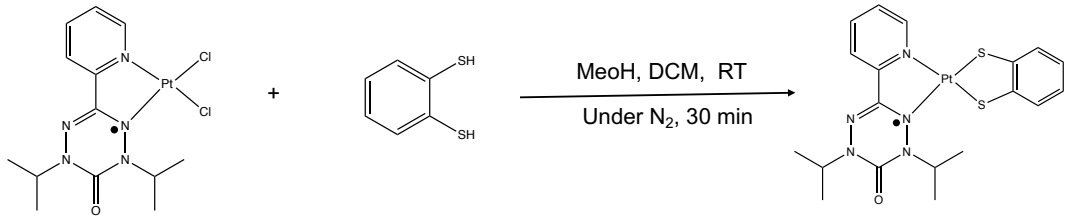

Pyridine verdazyl radical dichloro 1,2 benzene dithiol (PyVD)Pt(bdt)

The (PyVD)Pt(bdt) complex was synthesized by applying a modified procedure reported in the literature.[19] 0.020 g (0.057 mmol) (PyVD)$PtCl_2$ was dissolved in dry degassed DCM. 0.010 g (0.074 mmol, 1.3 eq) of 1,2 benzene dithiol and 0.009 g (0.171 mmol, 3 eq.) KOH was dissolved in anhydrous methanol in a separate flask. A clear solution of KOH was transferred to the 1,2-benzenedithiol solution and it immediately turned a slightly bluish color. The mixture was stirred for 1 h and transferred to the stirring brown solution of (PyVD)$PtCl_2$. The color of the solution turned purple. The reaction mixture was stirred for 1 h at room temperature. The solvent was then evaporated. Dry, degassed DCM was transferred anaerobically to the flask. The purification was carried out by multiple precipitations using ether and DCM. A dark purple amorphous from of the complex was collected and characterized by MS and elemental analysis. ESI MS data showed a clean parent peak (m/z): calculated for [$C_{19}H_{22}N_5OPtS_2$]; 595.09; observed (M/z) for $[M]^+$ 595.09 (100%). The calculated composition percentage for [$C_{19}H_{22}N_5OPtS_2$] including one mole of DCM: C, 35.30; H, 3.55; N, 10.29; and observed percentage; C,

35.74; H, 3.78; N, 10.33. The electronic absorption maximum energy was found to be 11600 cm^{-1} in acetonitrile. This energy has been shifted by ~1000 cm^{-1} compared to that of (PyVD)Pt(cat). Detailed band assignments has been presented in Table 4.1 and Figure 4.*25*. The lowest energy transition is at 11,600 cm^{-1} and involves the dominantly one electron promotion from catecholate 80% HOMO to the VD SOMO. A second band is observed at 18,000 cm^{-1}, which involves a donor HOMO-1 to VD SOMO one electron promotion and another distinct band is found at 24,600 cm^{-1} that originates from a 90% contribution of a HOMO to LUMO one electron promotion.

Further studies on the photophysical and magnetic properties of this complex have been limited due to the sensitivity of the complex. The two coordinating sulfur atoms are easily oxidized to the mono- and di-sulfur oxides as evidenced by data obtained from MS.

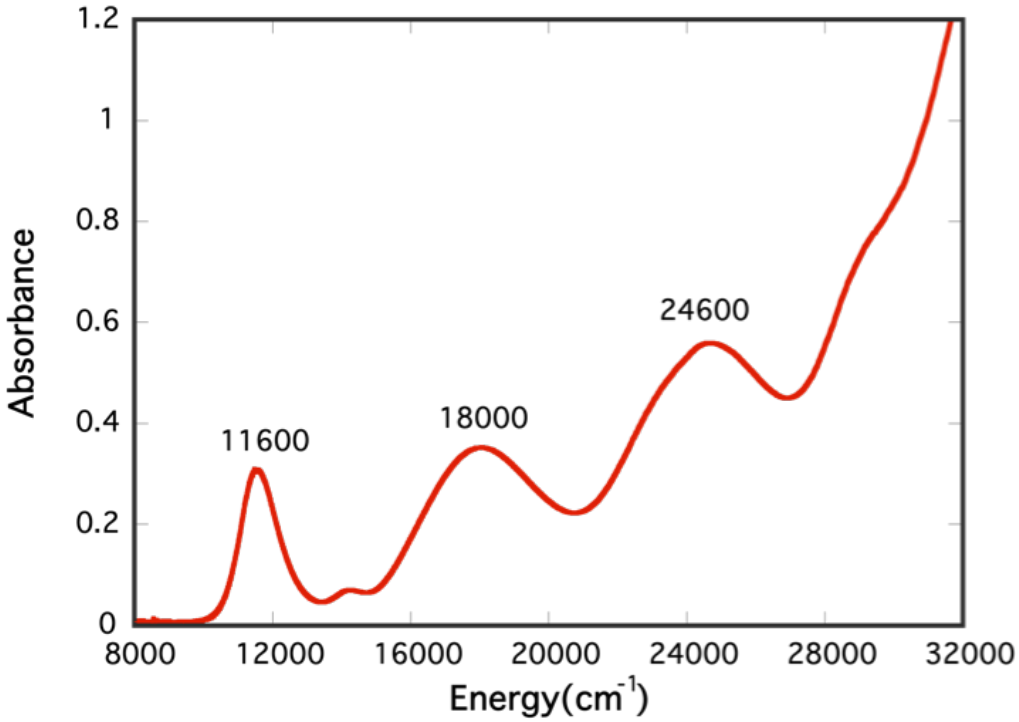

Figure 4.25. Room temperature Electronic absorption spectrum of (PyVD)Pt(bdt) expressed in absorbance vs energy on wavenumber. The sample solution was prepared in acetonitrile.

Table 4.10: Observed band assignment based on the TD-DFT calculation and electron density difference map (EDDMs) associated with selected electronic transitions (green for going and red for accepting orbitals)

Experimental Band	Energy (cm^{-1})	EDDM	Calculated oscillator strength
1.	11600	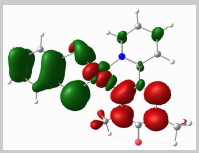	0.049 (Exc. State 1)
2.	18000	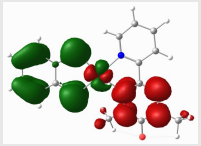	0.067 (Exc. State 2)
3.	24600	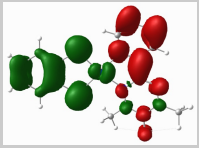	0.079 (Exc. State 3)

4.4 (Pyridine-Verdazyl) Pt(II)(Catecholate); (PyVD)Pt(Cat).

4.4.1 Synthesis and Characterization

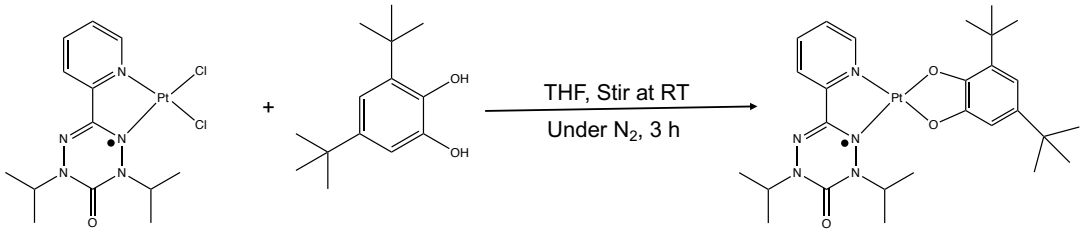

Pyridine verdazyl radical dichloro 3,4 di-tbutyl catecholate (PyVDZ)Pt(dtbCat)

The synthesis of the (PyVD)Pt(Cat) complex was performed using a modified synthetic procedure from that reported in the literature for the non-radical donor-acceptor Pt(II) complexes[19]. 0.02 g (0.038 mmol) of (PyVD)$PtCl_2$ was dissolved in dry degassed THF. A solution of 0.012 g (0.114 mmol) of potassium tert-butoxide was prepared in dry THF solvent and mixed with a solution of 3,4 di-tert-butoxide catecholate in dry THF to facilitate deprotonation. The bluish green solution of the deprotonated catecholate is slowly added to the stirring solution of (PyVD)$PtCl_2$ by canula transfer. The reaction mixture turned dark red. It was allowed to stir for 3 h. The solvent was removed by evaporation. Dark colored product was purified by column chromatography using silica gel as adsorbent and 6:4 ethyl acetate:hexane as the eluent. The second bluish fraction was collected and dried to obtain pure crystalline compound with relatively poor yield (0.003 g,12%). The low yield is associated with the decomposition of the dichloride into the PyVD ligand, due to the weak basicity of the coordinating PyVD.[29] The yield was dramatically improved to 49% by using the sodium salt of catecholate. Characterization was performed by MS, elemental analysis, and X-ray crystallography. ESI-MS data showed clean parent (m/z) peak: calculated for [$C_{27}H_{38}N_5PtO_3$] is 675.26, observed (M/z) for $[M+H]^+$ 676.26. The calculated composition percentage for [$C_{27}H_{38}N_5PtO_3$] with one mole of ethyl acetate: C, 48.75; H, 6.07; N, 9.17; and observed percentage; C, 48.97; H, 5.91; N, 8.95.

4.4.2 Experimental and Computational Methods

Electronic absorption spectroscopy and X-ray crystallography were performed for (PyVD)Pt(Cat) (details of these techniques are given in section 3.2.3 of chapter 3).

The electron paramagnetic resonance spectrum (EPR) was recorded in fluid solution. X-band EPR at room temperature was performed on an IBM-Bruker E200SRC continuous-wave spectrometer. Samples were prepared by dissolving the solid in distilled acetonitrile and a quartz X-band EPR tube was used to hold the sample. The recorded EPR spectrum was then simulated by using EasySpin[44] to determine the experimental spin Hamiltonian parameters. Line shape modeling showed an angular dependence on g and a Gaussian line shape.[45]

Magnetic susceptibility measurements were performed on a Quantum Design MPMS3 SQUID magnetometer. The instrument was calibrated by using a palladium sphere, a copper acetate salt having five waters of crystallization, $Cu(OAc)_2$, and $HgCo(SCN)_4$. Microcrystalline powder samples were loaded into a half piece of a gelatin capsule and topped with pure cotton. The whole assembly was inserted into a soda straw with both the top and bottom of the straw filled with pure cotton. Centering of sample in the magnetometer was performed at 10K with an applied magnetic field of 0.5 Tesla. Variable-temperature magnetic susceptibility experiments were measured with an applied field of 0.1 Tesla. Diamagnetic corrections on data were achieved using Pascal's constants[46] and the Bleaney-Bowers dimer equation[47] was fit to the χT product data. The exchange Hamiltonian is,

$$\widehat{H} = -2JS_1S_2$$

where, J is defined as the intermolecular exchange coupling between two radical spins.

4.4.3 Results and Discussion

4.4.3.1 X-ray Crystallography

The X-ray crystal structure of (PyVD)Pt(Cat) was performed at the UTEP X-ray facility. A dark blue needle shaped single crystal specimen of $C_{27}N_5O_3H_{38}$ was selected and placed on a Bruker APEX-II CCD diffractometer. The crystal was kept at 100.0 K during data collection. The crystallographic package Olex2 was used as the structure solution program, Intrinsic Phasing and defined with the SHELXL, SHELXT refinement package using Least Squares minimization.[48] [49] The structure was solved using direct, intrinsic phasing, charge flipping and difference Fourier techniques. All hydrogen atom positions were idealized and rode on the atom of attachment. Crystal data and structure refinement for $C_{27}N_5O_3PtH_{38}$ with a calculated molecular mass (M = 675.71 g/mol), is triclinic with space group P-1 and the unit cell parameters, $a = 13.6184(5)$ Å, $b = 14.1599(6)$ Å, $c = 15.2552(6)$ Å, $\alpha = 95.773(2)°$, $\beta = 105.175(2)°$, $\gamma = 100.460(2)°$, $V = 2757.77(19)$ Å3 $Z = 4$, $T = 100.0K$, $\mu(MoK\alpha) = 5.124$ mm^{-1}, $Dcalc$ = 1.627 g/cm^3, 190912 reflections measured ($3.744° \leq 2\Theta \leq 64.062°$), 19043 unique ($R_{int}$ = 0.1727, R_{sigma} = 0.0688) which were used in all calculations. The goodness of fitting value, final R_1 was 0.0411 ($I > 2\sigma$) I_0 and wR_2 was 0.0996.

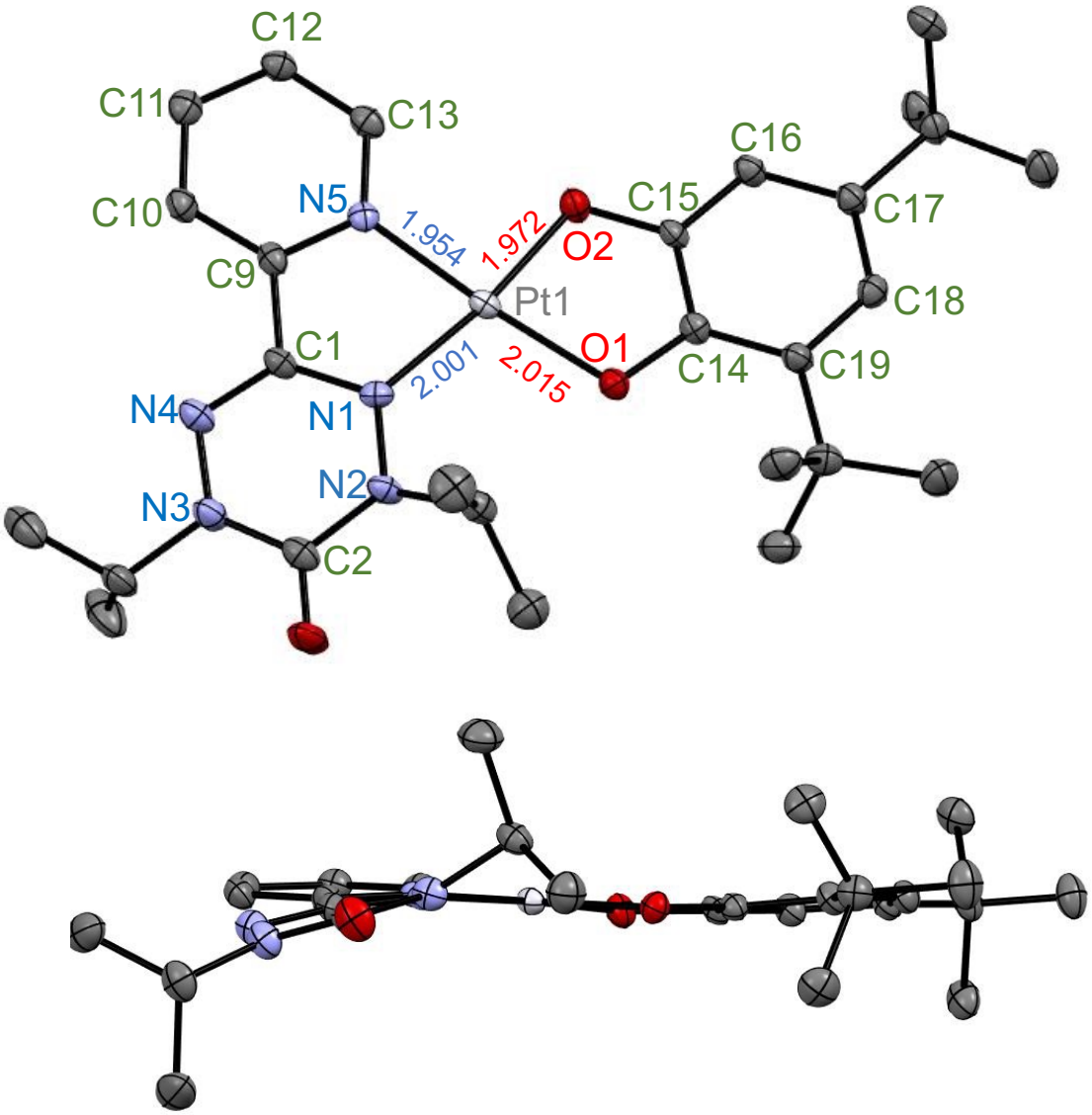

Figure 4.26: X-ray crystallographic structure of (PyVD)Pt(Cat); for clarity; carbon atoms are green color coded, oxygen atoms are red color coded, nitrogen atoms are blue color coded, and the platinum atom gray color coded. Bottom; depiction of the distortion from the planarity due to the steric interaction between isopropyl substituents of the VD and tertiary butyl group of catecholate.

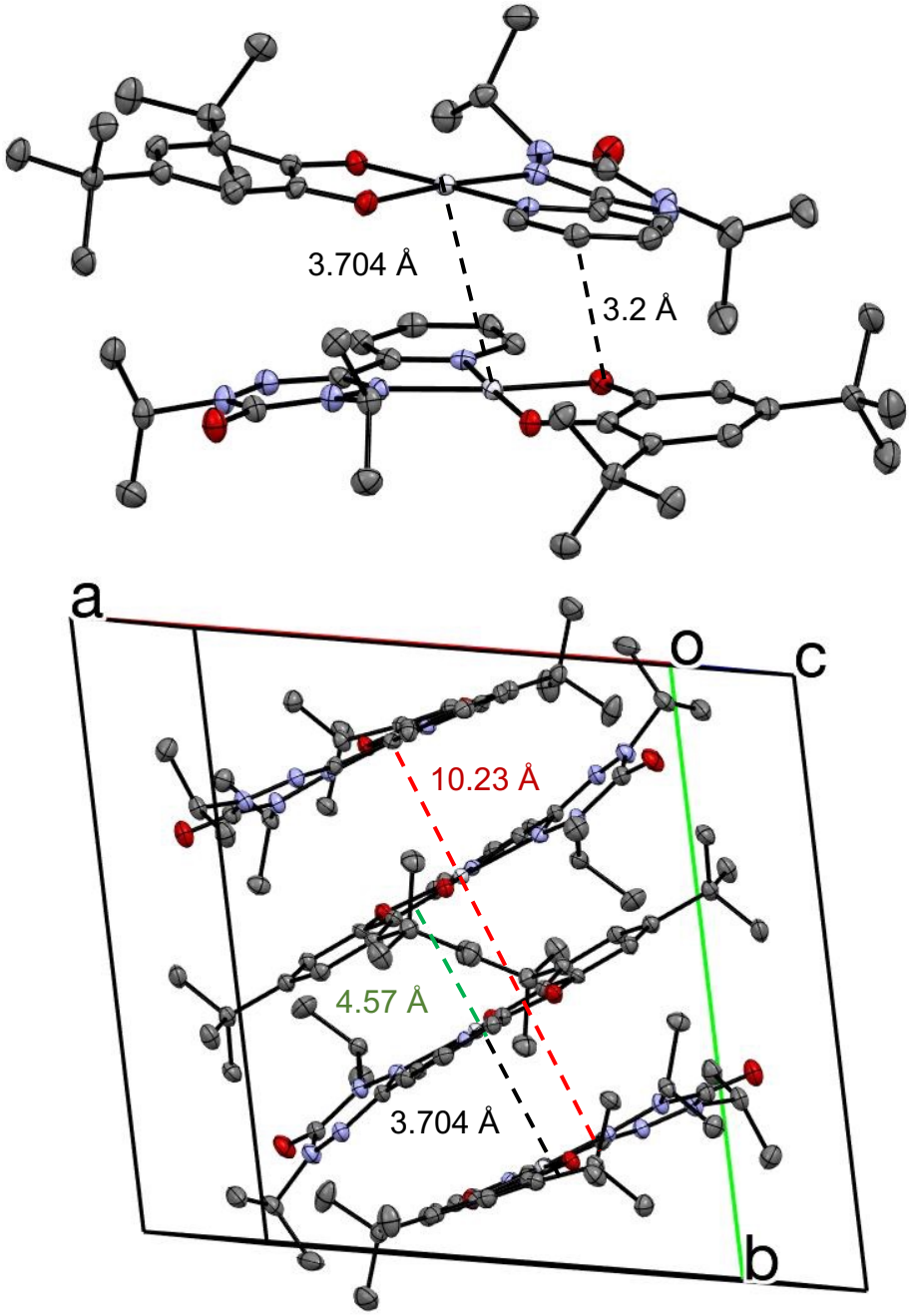

Figure 4.27: Depicting the crystal structure to illuminate the dimer interaction; (top) inter molecular interaction distance is shown by the black dotted line between intermolecular platinum atoms. The nature of crystal packing in one unit cell (bottom), red, green, and black dotted lines represent the distance between two dimers, the inter-dimeric distance, and the distance between two molecules in a dimer respectively. Four molecules are found to be packed in the unit cell.

The ORTEP diagram of (PyVD)Pt(Cat) is shown in Figure 4.*26*, and the crystal packing is depicted in Figure 4.27 showing weak intermolecular interactions between molecules. The intermolecular Pt-Pt distance between two dimeric molecules is 3.704 Å. The Pt-Pt interaction is negligible. There is a minimum possibility to experience any type of molecular stacking. The intermolecular Pt-Pt stacking of the precursor, (PyVD)$PtCl_2$, has also been reported with Pt-Pt intermolecular distance 3.48 Å and it was noted that there was an absence of a Pt-Pt interaction.[39] The crystal packing pattern shows the co-crystallization of four molecules in one triclinic crystal unit in Figure 4.27. The bond lengths of the two coordinating nitrogen atoms are different in (PyVD)Pt(Cat) as shown in Table 4.2. The Pt-N bond of the VD nitrogen is longer than the Pt-N bond of pyridyl nitrogen. This bonding effect is also reflected in Pt-O bond lengths. They are also not equal in length. The overall structure of (PyVD)Pt(Cat) deviates from a perfect square planar geometry. The bite angles of O1-Pt1-O2 (83°) and N1-Pt1-N5 (79°) are slightly deviated from the idealized value of 90° as shown in Table 4.3. The deviation from planarity of PyVD ligand is displayed by the torsion angles in Table 4.4. The pyridine ring is planar, but the VD ring deviates away from planarity by ~9°(N2-N1-C1-N4) as shown in Figure 4.26 and Table 4.3. The spin density on the four magnetic nitrogen atoms is different, contrasting two sets of nitrogen atoms in the free VD ring. In Table 4.2, Table 4.3, and Table 4.4, the selected crystallographic structural data have been summarized.

Table 4.11: Selected bond lengths obtained from X-ray crystallography for (PyVD)Pt(Cat)

Atoms	Atoms	Experimental bond Length /Å	Calculated bond Length /Å
Pt1	O1	2.008	2.015
Pt1	O2	1.954	1.972
Pt1	N1	2.001	2.018
Pt1	N5	1.993	1.995

Table 4.12: Selected bond angles observed in the X-ray crystallography for (PyVD)Pt(Cat)

Atoms	Atoms	Atoms	Angles (°)
O2	Pt1	O1	83.38
O2	Pt1	N1	171.81
O2	Pt1	N5	92.28
N1	Pt1	O1	104.53
N5	Pt1	O1	175.63
N5	Pt1	N1	79.83

Table 4.13: Selected torsion angles from the X-ray crystallography for (PyVD)Pt(Cat)

Atoms	Atoms	Atoms	Atoms	Angles (°)
Pt1	O1	C14	C15	-5.2
Pt1	O2	C14	C19	171.9
Pt1	O2	C15	C14	2.2
Pt1	O2	C15	C16	-175.7
Pt1	N2	N2	C2	-161.9
Pt1	N1	N2	C3	34.9
Pt1	N1	C1	N4	164.8
Pt1	N1	C1	C9	-13.7
Pt1	N5	C9	C1	0.0
Pt1	N5	C9	C10	179.6
Pt1	N5	C13	C12	179.4
N1	N2	C2	O3	177.5
N3	N4	C1	N1	-1.9
N2	N1	C1	N4	-8.3
N1	C1	C9	N5	8.9

4.4.3.2 Electronic Absorption Spectroscopy

Room temperature electronic absorption spectra were recorded on a HITACHI 4100 UV-vis-NIR spectrometer. Samples were prepared in acetonitrile solution which was purged with nitrogen gas. The MEC was calculated by the serial dilution method. The molar absorptivity value is less than that of (bpy)Pt(Cat), which can be explained by the weak coordination of the PyVD ligand with transition metal, thus resulting in relatively less orbital overlap contribution to the LLCT band compared to (bpy)Pt(Cat). This argument is supported by the longer Pt−N bond length[39] from the coordinating Pt atom and verdazyl to the Pt−N length of PyVD, as displayed in crystal structure and from the DFT optimized geometry. The CT band is red shifted by ~1 eV compared to (bpy)Pt(tbutCat).[19] The observed band features of the experimental data have been assigned with the help of TD-DFT computations. The absorption feature associated with the 10,477 cm^{-1} band is the promotion of an electron from the Cat HOMO to the VD SOMO. It is apparent that the wavefunctions of the HOMO and SOMO are very delocalized in these computations, indicating a large extent of mixing between the HOMO and SOMO. The second intense band feature observed at 17,700 cm^{-1} is similar in nature to the LLCT in the parent molecule, which can be described as resulting from a one electron promotion from the catecholate HOMO to the PyVD LUMO. Another band at 21,166 cm^{-1} is composed of a one electron promotion from the Cat HOMO-1 to the VD SOMO. CASSCF calculations were also performed by using a 5 electron, 5 orbital active space. These CASSCF computations indicate that predominantly SQ character (74%) in the ground state wavefunction, with only 21% VDZ radical character. The CASSCF orbitals in the active space describe a large mixing between two configurations and indicate that the CAT and

VDZ components of the molecule are highly mixed as indicated in Figure 4.28 and Figure 4.29.

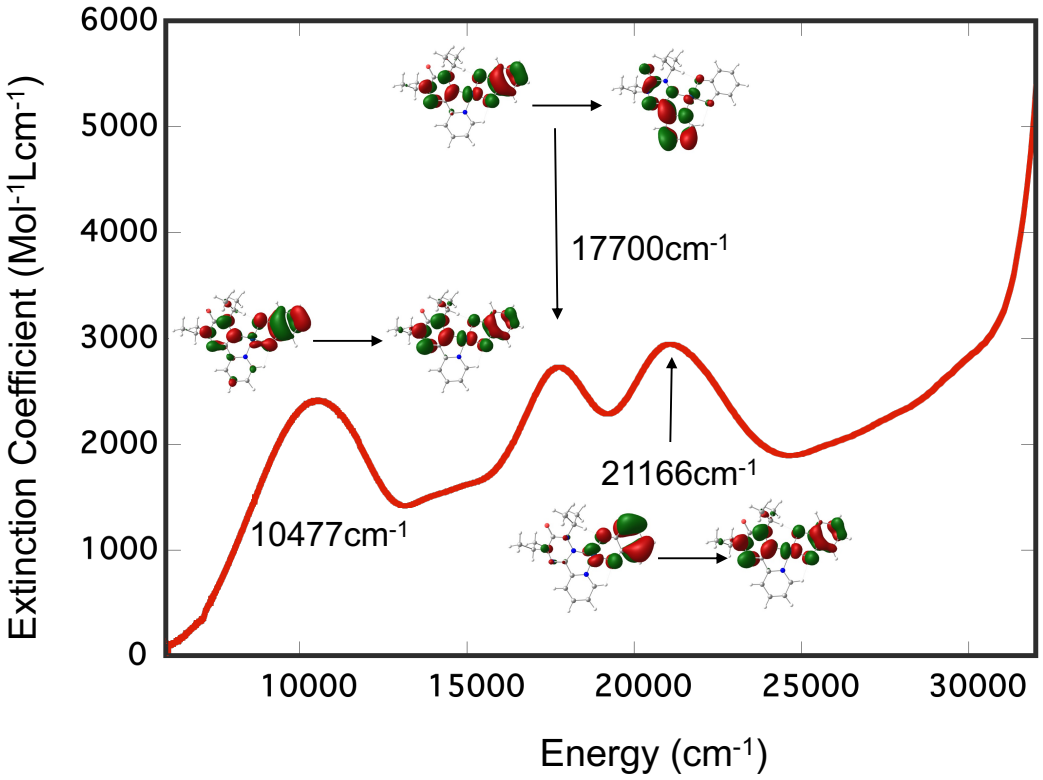

Figure 4.28: Electronic absorption spectrum of (PyVD)Pt(Cat) expressed in molar extinction coefficient vs energy on wavenumber. The sample solution was prepared in Acetonitrile. Inset: DFT calculated orbitals involved in one electron promotions for three visible features.

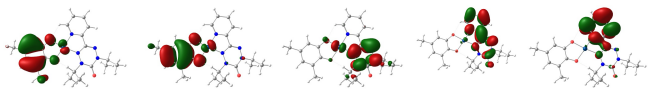

Ground state configuration	2	2	1	0	0	21%
	2	1	2	0	0	74%
First excited state configuration	2	1	1	1	0	34%
	2	2	1	0	0	14%
	2	1	2	0	0	42%

Figure 4.29: CASSCF results summary calculated using a (5e, 5O) active space. (Top) orbitals in the active space, (Bottom) electronic configuration in the ground state and first excited state.

4.4.3.3 Solvatochromic Effect

As observed in other reported diimine Pt complexes of dichalcogenolenes, (PyVD)Pt(Cat) also exhibits a solvatochromic effect on the lowest energy charge transfer bands has shown in Figure 4.***30***. The effect is defined as the shifting of the energy of a CT transition band ($\lambda_{\max}$) with various polarity of solvents. Solvatochromism is the effect of the solvent dipole moment rearrangement with the molecular dipole moment in the ground and excited states. Observed data has displayed a bathochromic shift of $\lambda_{\max}$ for the CT band in non-polar solvents (toluene and heptane) and hypsochromic shift in polar solvents (acetonitrile, dimethyl sulfoxide). This is also called a negative solvatochromic effect. The blue shift of the CT energy in polar solvent is because more energy is required to change the dipole moment of polar solvent molecules with the molecular dipole moment in the solvent shell after excitation, which were otherwise be in a different orientation in the ground state. The large solvatochromic effect suggests a more polar ground state compared to the excited state for the (PyVD)Pt(Cat) complex.[50] [51] The structureless broad charge transfer band present in more polar solvents starts to show vibronic features as the polarity of the solvent is lowered from acetonitrile to heptane. In toluene, the broad peak starts to split into two peaks and becomes more prominent in heptane. The electronic absorption spectra of (PyVD)Pt(Cat) in heptane clearly shows evidence for a vibronic structural feature based on an ~1580 cm^{-1} vibration. Comparing this with the computed molecular vibrational frequencies suggest this is due to a quinoidal vibrational mode of the catecholate donor (**Error! Reference source not found.**)

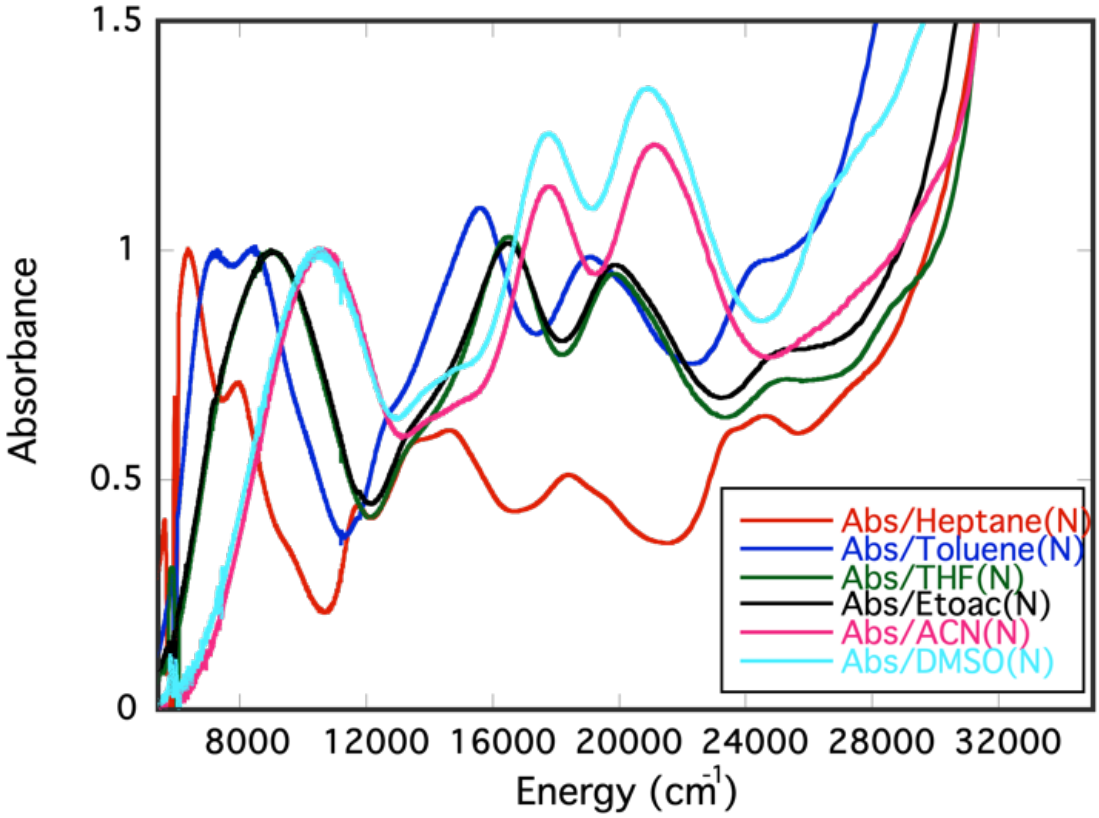

Figure 4.30: Solvatochromic effect for the (PyVD)Pt(Cat) complex using a series of solvents: heptane, toluene, tetrahydrofuran, ethyl acetate, acetonitrile, and dimethyl sulfoxide. The lowest energy charge transfer band has been remarkably shifted to lower energy on moving from polar solvents to non-polar solvents.

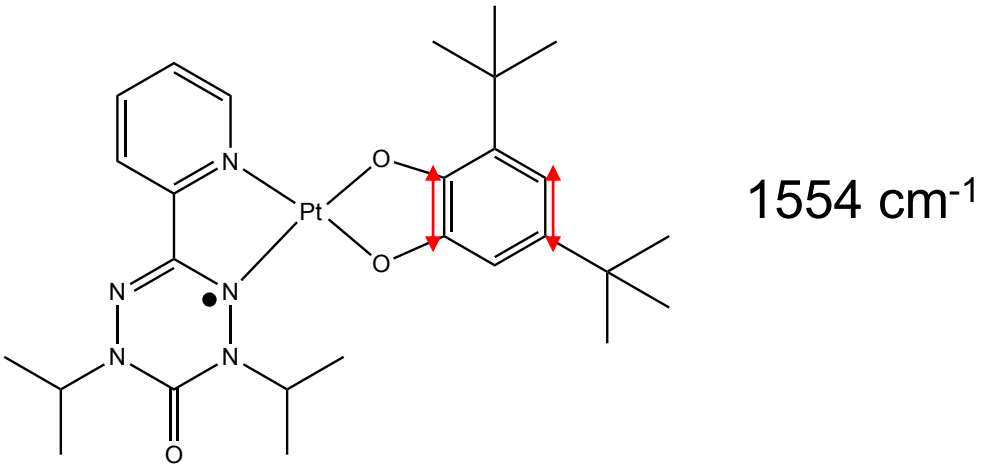

Figure 4.31: The quinoidal stretch shown by the red arrow on catecholate ring. From the frequency calculation, this is assigned as being responsible for the vibronic absorption feature observed at low energy region in heptane.

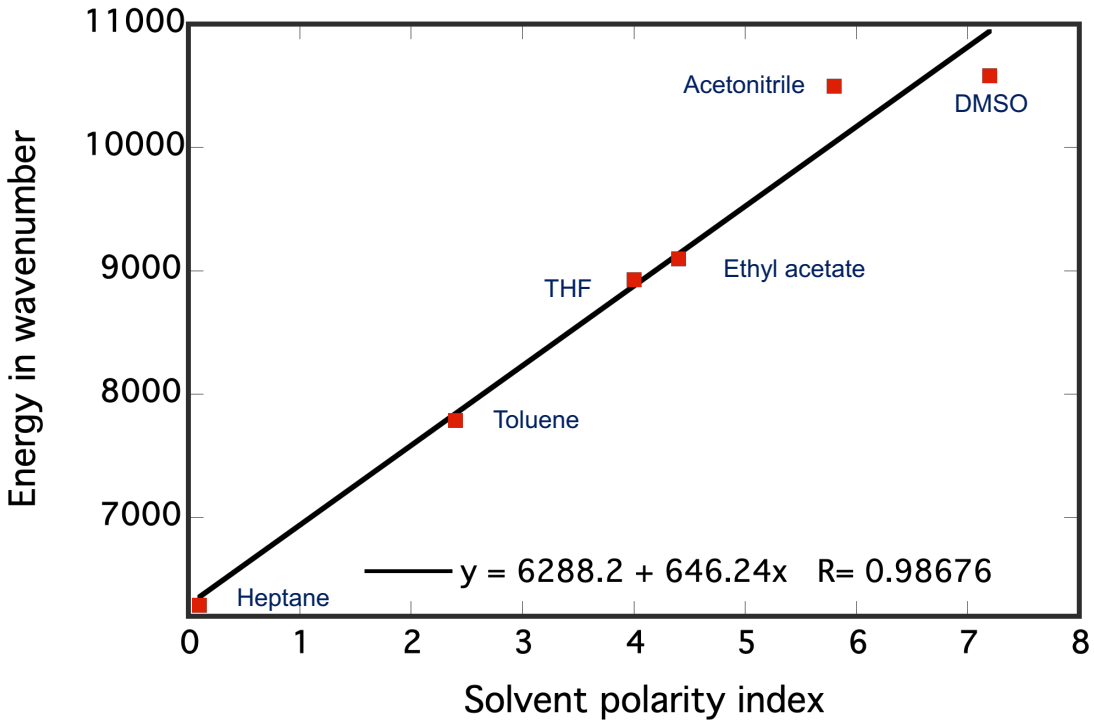

Figure 4.32: Solvent polarity index vs energy of lowest energy absorption maximum. (solvent parameters are adapted from ref 52)[52]

4.4.3.4 Electron Paramagnetic Resonance

Room temperature X-band (~9GHz) EPR spectra was recorded using Brucker EMX spectrometer using toluene as solvent. The experimental parameters were as follows: power attenuation 20dB, modulation amplitude of 2G and field modulation of 100 MHz. The EPR experimental spin Hamiltonian parameters were determined by the spectral simulation software EasySpin.[44] The experimental spin Hamiltonian parameters are presented in the inset of Figure 4.*35*. The parameters are spin value (S) =1/2, isotropic g value (g_{iso}) = 2.0295, line width (width at the half maximum) = 2.9 mT and the isotropic Pt hyperfine value (A_{iso}^{Pt}) = 230 MHz. The spectral feature of the complex indicates the significant amount of spin on the Pt metal. Deviation of 'g-value' from the free electron g_e (2.0023) is because of the large spin-orbit coupling constant of Pt. The Pt metal is a bridge to delocalize the spin from VD to Cat as shown in Figure 4.***33***.[39]

Experimental EPR spectral feature as shown in Figure 4.*35* reflects the occupation of the spin on the Pt center. Pt^{195} (I = ½) hyperfine of 230 MHz along with Pt^{196} (I = 0) single gaussian signal in the center has observed.[39] The ratio of intensity of the EPR signals resembles the natural abundance of Pt isotopes, I =0 (68.2%) and I =1/2 (33.8%).[53] Calculated total spin density map is included in Figure 4.33. This predicts 13% of the total VD radical spin on Pt and 30% on the catecholate ligand. The calculated result has been compared and presented to evaluate the extent of delocalization obtained from dipolar contribution on A anisotropy obtained from 77K EPR. As we can see in Figure 4.***34***, EPR spectrum of the (PyVD)Pt(Cat) complex is very different from the free VD radical, showing a nine line pattern. The difference of two spectrum is due to the delocalization of VD spin on Pt. Nitrogen hyperfine is not observed in 298K EPR signal since it is dominated by

large hyperfine value of Pt atom. Thus, simulation was carried out by using only the linewidth value. Literatures have reported the spin density on Pt ~7% for similar Pt hyperfine coupling constant value. [54] [53]

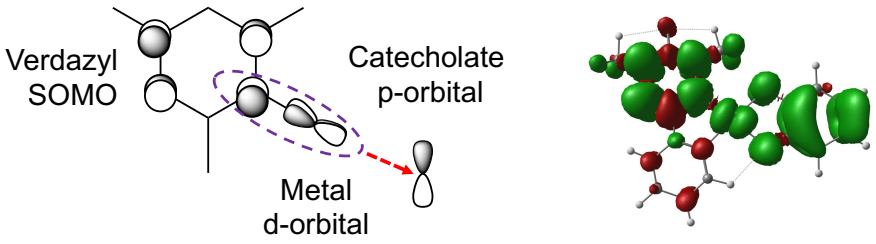

Figure 4.33: Diagrammatic representation of spin delocalization pathway (left). Spin density distribution map plotted on the optimized ground state geometry (right).[39]

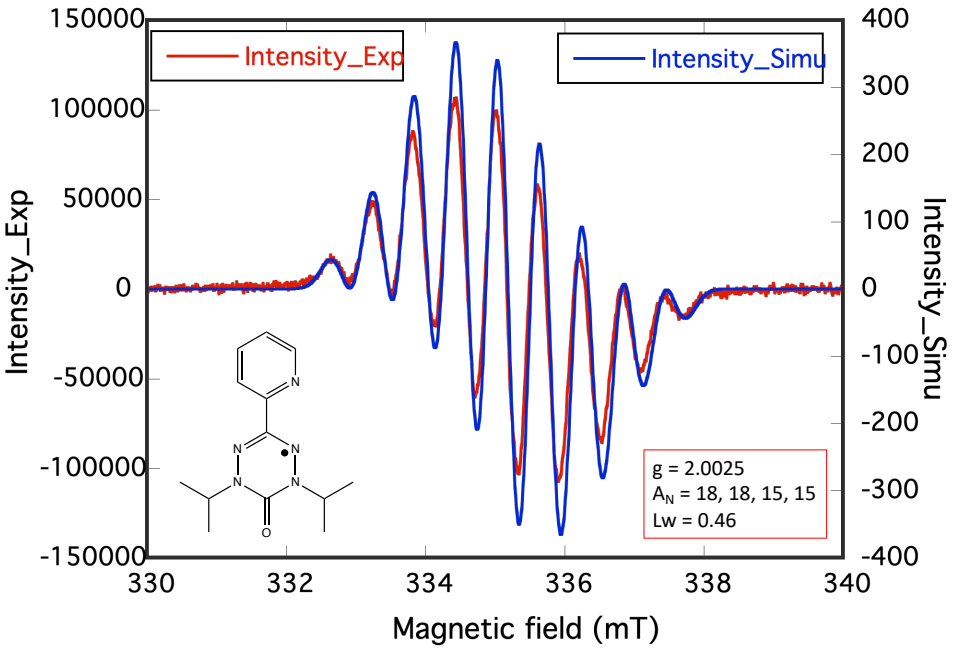

Figure 4.34: The 298K solution isotropic EPR data for the PyVD ligand recorded in DCM. Experimental (red) and simulation (blue). Simulation parameters are presented in the inset along with a bond line drawing of ligand PyVD.

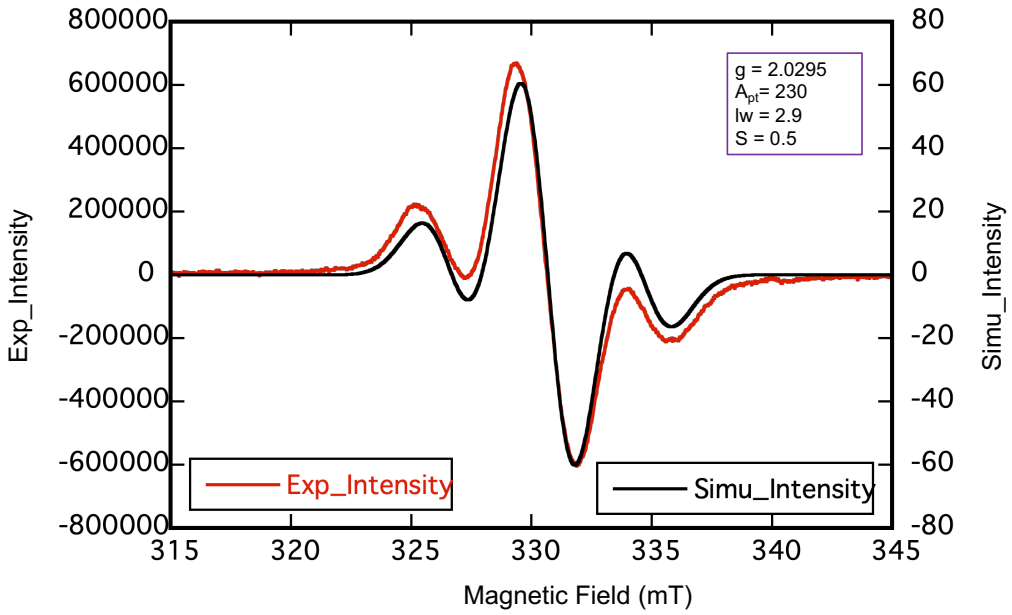

Figure 4.35: Room temperature solution electron paramagnetic resonance data of (PyVD)Pt(Cat) recorded in toluene. Experimental data (red) and simulated data (blue). Simulation parameters are presented in the inset.

Low temperature (77K) EPR data was recorded in frozen solution of 2-Me-THF and are presented in Figure 4.*36*. Experimental spin-Hamiltonian parameters are obtained from the best simulation of spectra as show in Table 4.5.

Table 4.14: 77K EPR-simulation spin Hamiltonian parameters

Nucleus	g-tensor (g_{ave} = 2.028), giso = 2.029)			A-tensor (MHz), A_{ave} = 225, Ai_{so}= 230		
Pt	g1	g2	g3	A1	A2	A3
	2.076	2.017	1.99	190	270	215
N1	-	-	-	0	0	55
N2	-	-	-	0	0	51

The (PyVD)Pt(Cat) molecule displays rhombic A and g tensor anisotropy because of the low symmetry environment (C_1) of the complex, and this allows for mixing of the Pt d_{xz}

orbital with Pt d_z^2 orbital. We note that the spin density localized any one of the five canonical d orbitals is expected to result in an axial Pt^{195} hyperfine tensor. The Pt^{195} hyperfine tensor is comprised of an isotropic Fermi contact term, the spin dipolar term and the orbital dipolar term. The isotropic term is proportional to the spin density at the magnetic nucleus. The anisotropic spin dipolar term comes from the spatial distribution of spin density around the magnetic nucleus. Hence, it can quantify the amount of spin on Pt in our system.[55] The simulation showed A_{Pt} = [190, 270, 215], which allows us to extract the spin dipolar term as (A_s) = [-35, +45, -10] MHz. With scaling to the spin dipolar term obtained from the calculation [-67, +91, -23], the amount of spin delocalized on Pt and Cat units is extimated to be ~7% and 15% respectively. This statement is also supported by the X-ray crystallographic structure of (PyVD)Pt(Cat) showing the pure catecholate bond lengths instead of the average between catecholate and SQ. Orca calculated EPR spin-Hamiltonian parameters result in higher nitrogen hyperfine couplings only along z-direction, which is in good agreement with the experimental data. The simulation was performed using two nitrogen atoms instead of four due to a very long processing time, but this is not ideal.

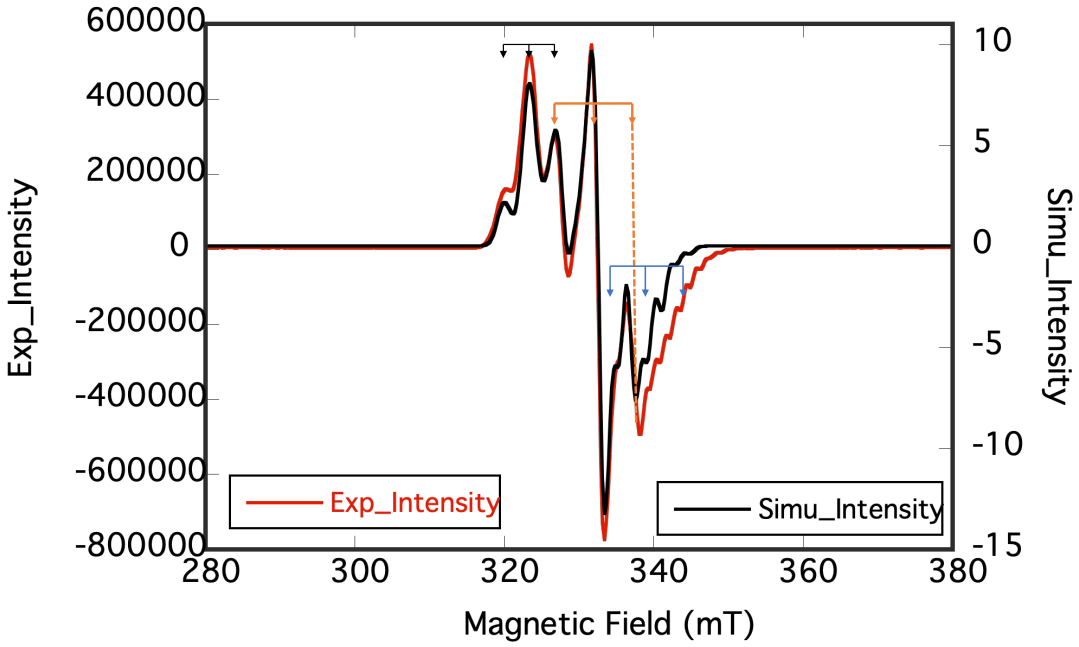

Figure 4.36: EPR spectrum of (PyVD)Pt(Cat) recorded at 77K in 2-methyl THF. (Red solid line) experimental, and (black solid line) simulated data sets. Black, brown, and blue arrows are indicating the three different Pt, A-tensor values. Simulated parameters are presented in text.

The A-tensor and g-tensor are not collinear, as expected for the C_1 symmetry. The relative orientation of the g- and A- tensors with the $\beta - LUMO$ is shown in Figure 4.37. Calculation has indicated the highest component of the Pt hyperfine to be along the d_{xz} orbital in $\beta - LUMO$ (depicted by the yellow arrow) in Figure 4.37, and is associated with the middle (g_{mid}) g-value. The middle hyperfine component is associated with the smallest (g_{min}) g-value. The smallest component of the Pt hyperfine, which goes through the nodal plane of the d_{xz} orbital, is associated with the highest g-value (g_{max}).

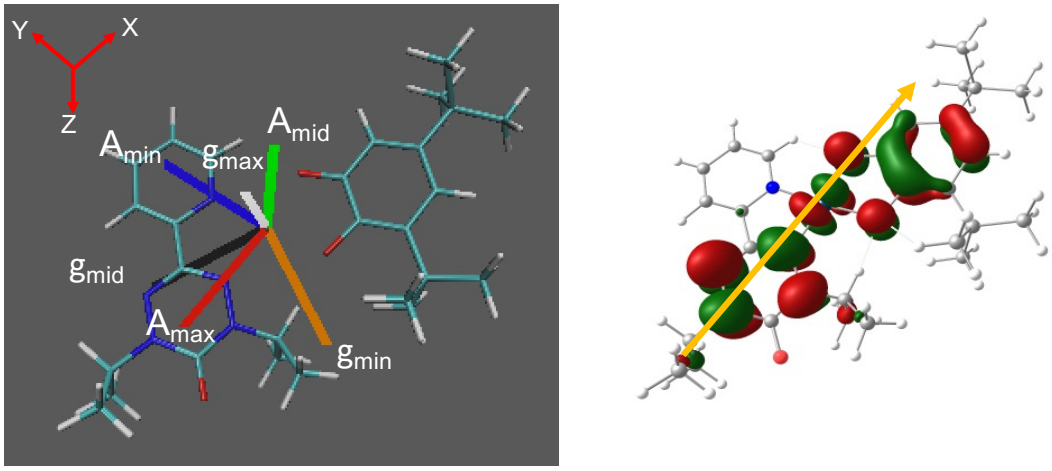

Figure 4.37: A-tensor and g-tensor orientations superimposed on the molecular frame. Molecular beta-LUMO wavefunction (right) with the yellow arrow pointing in the direction of the largest A-tensor component as represented by the red line in left figure.

The experimental method to quantify the amount of spin delocalization on the Cat ligand can be performed by appending a radical to the Cat donor ligand as in (PyVD)Pt(Cat-VD). We can then measure the exchange coupling between the appended radical spin and the PyVD spin, which should be J ~ 0 in the limit of no PyVD – VD exchange coupling. Delocalization of the PyVD spin onto the Cat will provide a mechanism for enhanced exchange coupling. The pairwise magnetic exchange interaction between SQ-VD spins is known to be J = 74 cm^{-1}, as determined by magnetic susceptibility measurements. This analysis will allow us to quantify the amount of spin delocalization from PyVD to the Cat moiety, since the spin density is proportional to the exchange coupling (details in section 4.6).[56] Another method to quantify the amount of spin delocalization can be estimated qualitatively by comparing the bond lengths of pure Cat and pure SQ radical. In the case of (PyVD)Pt(Cat), the bond lengths from the X-ray crystal structure show mostly pure catecholate bond distances, indicating only a small amount of spin delocalization on the Cat ligand.[56]

4.4.3.5 Magnetism

Variable-temperature magnetic susceptibility experiments were measured with an applied field of 0.1 tesla for Curie plots and temperature ranged from 300K to 0K, data is presented in Figure 4.***39*** for (PyVD)Pt(cat) and in Figure 4.***38*** for (PyVD)$PtCl_2$. Diamagnetic correction on data was achieved using Pascal's constants[46] and the plot of χT vs T was fit using Bleaney-Bowers dimer equation modified with mean field correction parameter (zJ') [47 57] with spin Hamiltonian:

$$\hat{H} = -2JS_1S_2$$

Where J is defined as the intermolecular exchange coupling between two radical spins. By fitting into the above equation, the g factor obtained was 1.97, which is comparable to g = 2.0297, the value obtained from the 298K EPR data simulation. The magnetic moment value (~0.35). This is the expected value for the pure mono-radical species (with measured inter-molecular VD exchange coupling value of $2J$ = −6.14 cm^{-1}). VD spins (S = ½, S = ½) show inter molecular anti-ferromagnetic coupling with each other in (PyVD)Pt(cat) complex. The possible pathway for the intermolecular anti-ferromagnetic exchange coupling is through the Cat oxygen and pyridine carbon, separated 3.2Å. This distance is shorter than the Pt-Pt distance. The exchange coupling value is half compared to the dichloro ($2J$ = −12.44 cm^{-1}) as shown in Figure 4.***38*** and Figure 4.***39***, which can be explained by the differences in the intermolecular distance between two molecules. They are 3.704 Å for (PyVD)Pt(Cat) and 3.48 Å for (PyVD)$PtCl_2$.[39]

The maximum χT value is 0.363 for (PyVD)Pt(Cat) Figure 4.39 and 0.371 for (PyVD)$PtCl_2$ Figure 4.38. These values are very close to the χT = 0.375 value for one

spin bearing system. In addition, this supports the purity of the target molecule. In both χT *vs* T plots, between 298K to 80K the signal plateaus nearly flat, indicating a constant value of χT caused by the rapid and constant ferro and anti-ferro magnetic exchange coupling of intermolecular spins. When the temperature is lowered below 80K, χT value starts to decrease, below 25K it decreases abruptly, and signal goes to zero at 0K. The precipitous decrease of χT value is because of weak inter molecular antiferromagnetic coupling between two VD radical spins. Inter-molecular antiferromagnetic interaction between Pt-Pt spins has been eliminated due to the absence of M-M stacking in crystal structure as shown in Figure 4.27Figure 4.27.

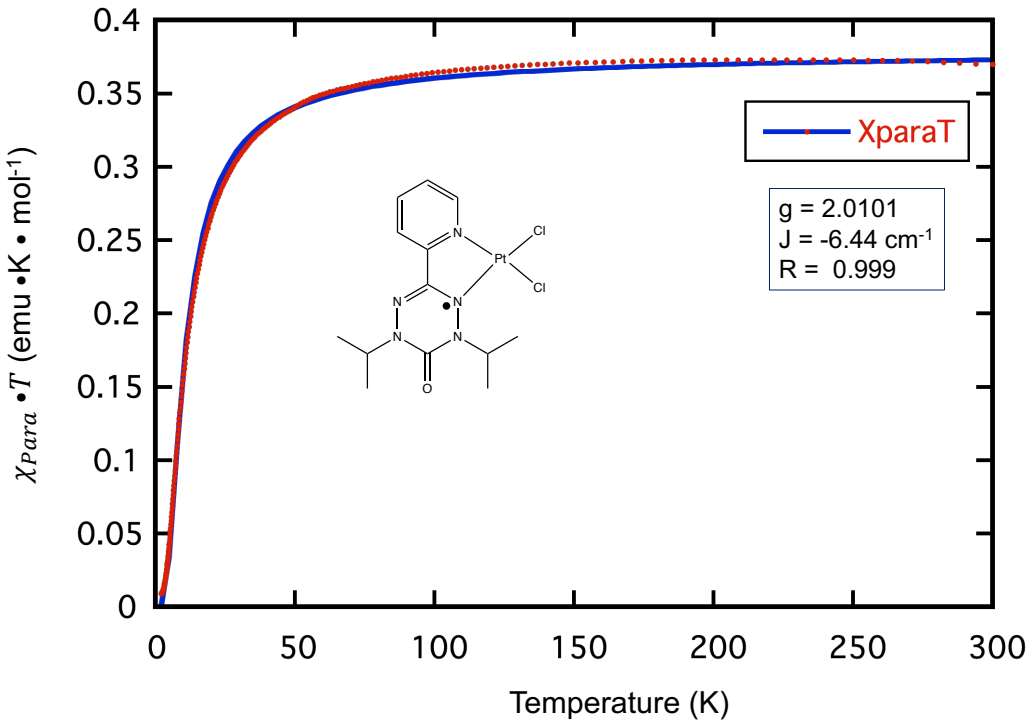

Figure 4.38: $\boldsymbol{\chi T}$ ***vs*** $\boldsymbol{T}$ plot for (PyVD)$PtCl_2$ recorded at variable temperature at 0.1 tesla applied magnetic field on microcrystalline solid sample. Red dots are the data points and blue solid line is the optimized fit to the data.

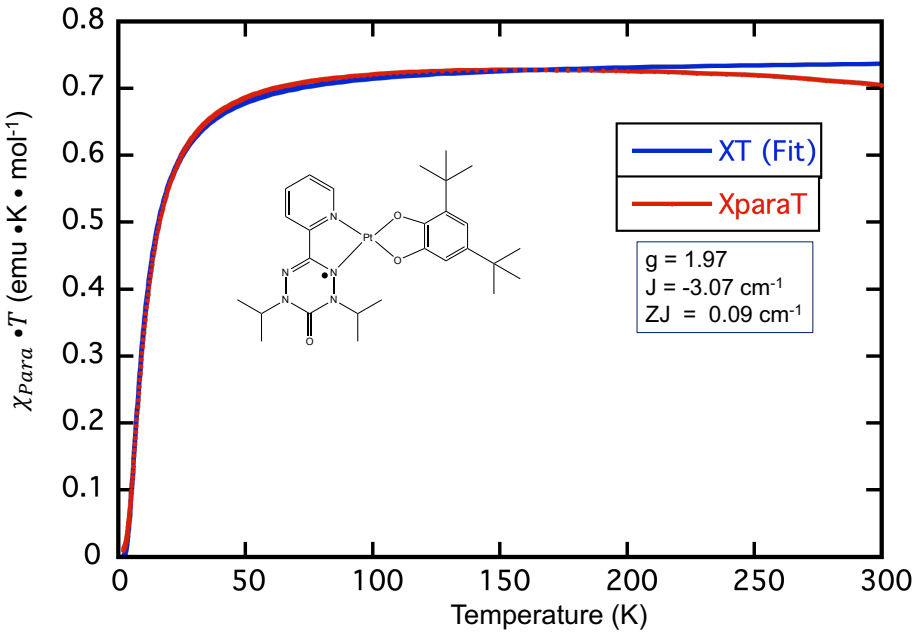

Figure 4.39: $\boldsymbol{\chi T\ vs\ T}$ plot for (PyVD)Pt(Cat) recorded at variable temperature at 0.1 tesla applied magnetic field on powder solid sample. Red dots are the data points and blue solid line is the optimized fit to the data.

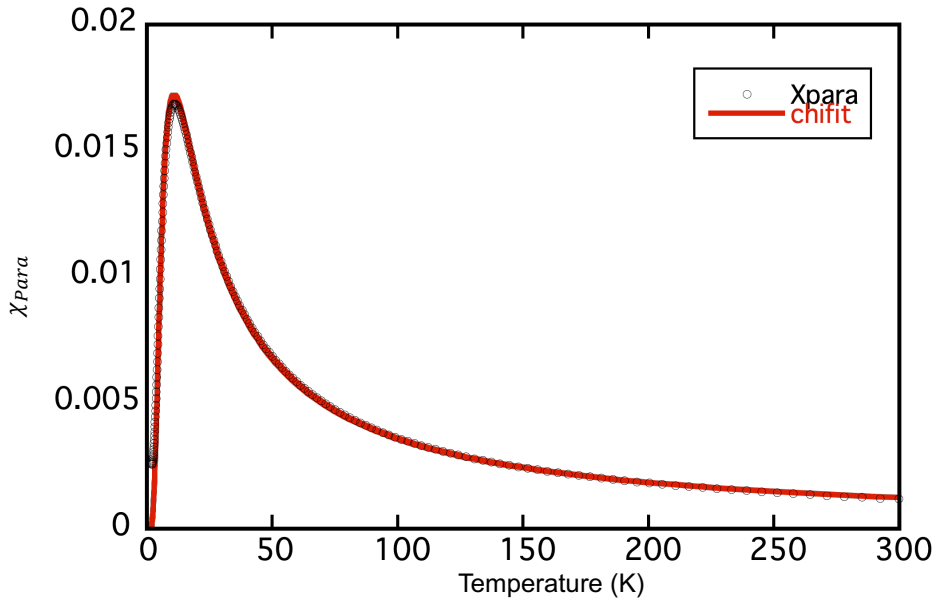

Figure 4.40: $\boldsymbol{\chi_{para}\ vs\ T}$ plot for (PyVD)Pt(Cat) recorded at variable temperature at 0.1 tesla applied magnetic field on powder form of sample. blue dots are the data points and red solid line is the optimized fit to the data

4.4.4 Conclusion

The complex (PyVD)Pt(Cat) has been successfully synthesized and characterized pure form. The first intense CT band is been red shifted relative to (bpy)Pt(Cat) due to the promotion of an electron from HOMO to VD SOMO. Since the radical on PyVD is directly coordinated to the Pt metal center, the radical spin is delocalized onto Pt and the catecholate. This is mediated by the Pt d_{xz} orbital. The extent of spin on Pt and Cat is estimated to be ~7% and 15% by comparing the experimental EPR spin-Hamiltonian parameter with those obtained by computation.

4.5. Synthesis, Characterization and Spectroscopy of 2-pyridine 1,5-diisopropyl 6-oxoverdazyl Platinum (II) Catecholate 1,5-diisopropyl 6-oxoverdazyl Catecholate; (PyVD)Pt(CatVD).

The purpose of the synthesis of the biradical transition metal complex is to quantify the amount of spin delocalization on the Cat ligand. More importantly this will allow us to study the degree of spin polarization, spin correlation and spin entanglement by optically exciting this system and observing spin polarization by transient EPR spectroscopy.

4.5.1 Synthesis and Characterization

The synthesis of (PyVD)Pt(CatVD) complex was done by using the modified synthetic procedure reported for non-radical donor-acceptor Pt (II) complexes[19]. 0.03 g (0.057 mmol) of (PyVD)$PtCl_2$ was dissolved in dry degassed THF. The solution of 0.012 g (0.114 mmol, 2.0 eq) of KOH was also dissolved in dry THF. The solution of 0.024 g (0.087 mmol, 1.5 eq) of 1,2 dihydroxy 3- verdazyl catecholate radical (CatVD) ligand in dry THF was prepared. The solution of base and ligand was mixed anaerobically to form

the salt of potassium (a green color solution). The deprotonated solution of CatVD was slowly added to the stirring solution of (PyVD)$PtCl_2$. The mixture turned bluish immediately. After 4 h solvent was removed. The dark purple colored product was purified by column chromatography using silica gel as adsorbent and 3:2 hexane: ethyl acetate as the eluent. The first bluish fraction was collected and concentrated to obtain pure crystalline compound. The yield was 0.009 g (24%) based on amount of (PyVD)$PtCl_2$ used.

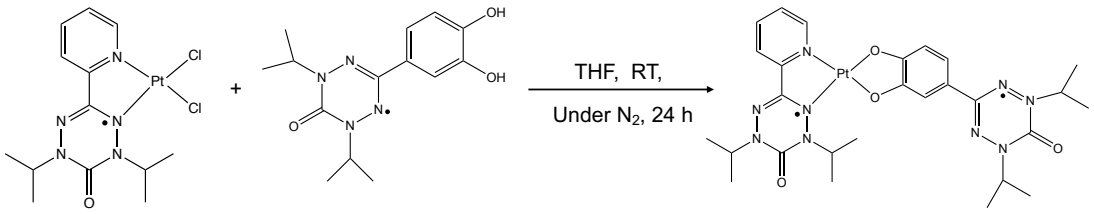

Pyridine verdazyl dichloro CatVD (PyVD)Pt(CatVD)

Characterization was done by MS, elemental analysis, and X-ray crystallography. ESI-MS data showed clean parent peak (m/z): calculated for [$C_{27}H_{35}N_9PtO_4$] 744.25, observed (M/z) for $[M+H]^+$ 744.23. The calculated composition percentage for [$C_{27}H_{35}N_9PtO_4$] with one and a half mole of methanol: C, 43.18; H, 2.21; N, 15.90; and observed percentage; C, 43.26; H, 4.74; N, 15.49. Detailed crystal structure and parameters have been presented in the X-ray crystallography section below.

4.6.2 X-ray Crystallography

The experimental details are given in section 4.4.3.1. An ORTEP drawing of X-ray crystal structure of (PyVD)Pt(CatVD) and crystal packing pattern in unit cell has presented in

Figure 4.41 and **Error! Reference source not found.**. The crystal data and structure refinement parameters are exhibited in Table 4.6. The Pt-Pt distance between two molecules within the dimer is 3.201Å. This distance is short enough to exhibit the Pt-Pt stacking despite not being directly superimposed as shown in Figure 4.43. Being the shortest distance between the molecules in the dimer, the Pt-Pt interaction is a possible pathway for intermolecular exchange coupling in this biradical complex. The bond lengths of catecholate coordinated to Pt and attached to the VD unit are closely related to the pure catecholate bond length [56] as shown in Table 4.7. Asymmetrical bond lengths of Pyridine Pt-N and VD Pt-N bond distances indicate the distortion of the square planar environment around the Pt center. The deviation is also depicted by the bite angles lowered to 80° from the ideal 90° as displayed in Table 4.17.

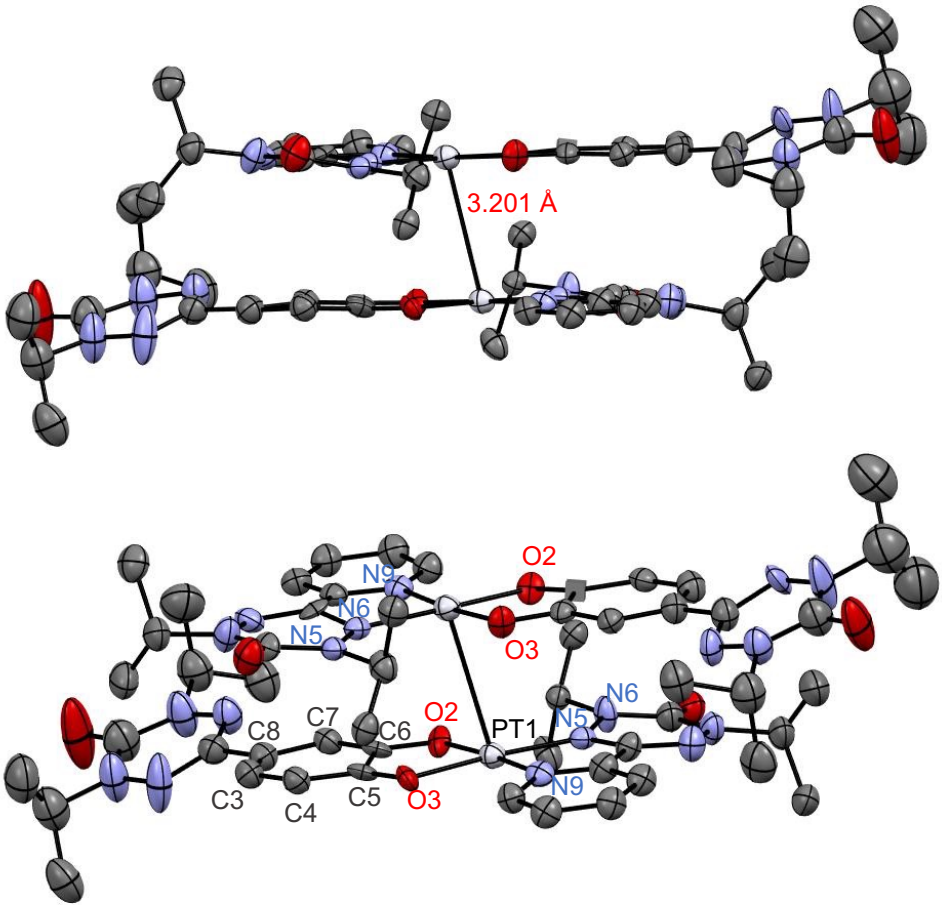

Figure 4.41: ORTEP drawing of X-ray crystallographic structure of (PyVD)Pt(CatVD). Elements are color coded by atom representative colors. Bottom: the labeling of selected atoms of interest.

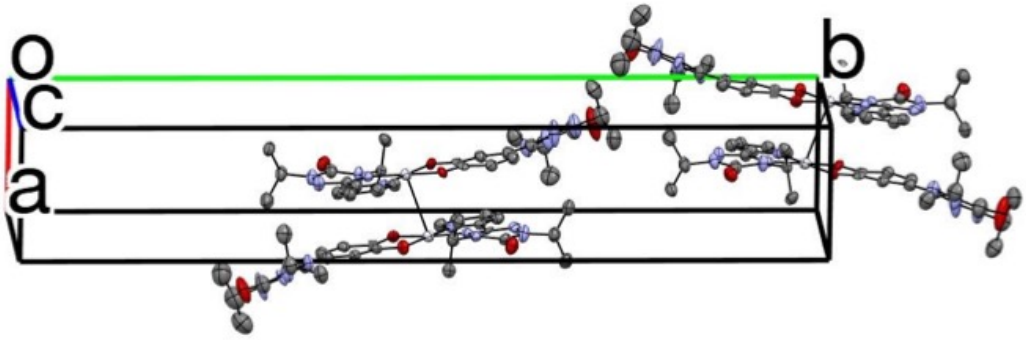

Figure 4.42: The nature of crystal packing in the unit cell. Two dimeric units associated with four individual molecules are packed in one unit cell of the crystal.

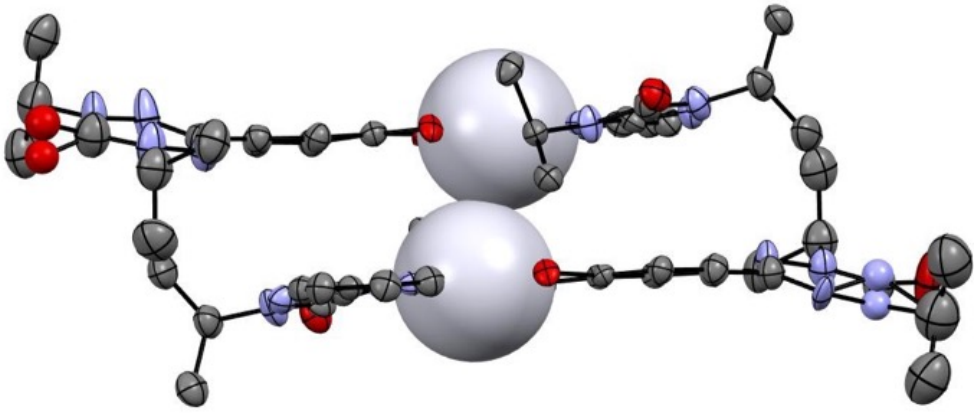

Figure 4.43: X-ray crystallographic structure of (PyVD)Pt(Cat) demonstrating the Pt-Pt (3.201Å) (gray colored solid sphere) intermolecular interaction in the dimeric unit.

Table 4.15: Crystal data and structure refinements.

Identification code	mo_05V01066MKRD_0m_a
Empirical formula	$C_{27}N_9O_4PtH_{35}$
Formula weight	744.73
Temperature/K	100.0
Crystal system	monoclinic
Space group	$P2_1$
a/Å	6.6652(4)
b/Å	38.5271(19)
c/Å	11.4400(6)
α/°	90
β/°	95.332(2)
γ/°	90
Volume/Å^3	2925.0(3)
Z	4
ρ_{calc}g/cm^3	1.691
μ/mm^{-1}	4.846
F(000)	1480.0
Radiation	MoKα (λ = 0.71073)
2Θ range for data collection/°	4.154 to 61.016
Index ranges	-9 ≤ h ≤ 9, -55 ≤ k ≤ 55, -16 ≤ l ≤ 16
Reflections collected	88166
Independent reflections	17856 [R_{int} = 0.0659, R_{sigma} = 0.0602]
Data/restraints/parameters	17856/281/346
Goodness-of-fit on F^2	1.205
Final R indexes [I>=2σ (I)]	R_1 = 0.1158, wR_2 = 0.2575

Final R indexes [all data]	R_1 = 0.1307, wR_2 = 0.2656
Largest diff. peak/hole / e Å^{-3}	8.98/-9.06
Flack parameter	0.47(4)

Table 4.16: Selected bond length from the X-ray crystal structure of (PyVD)Pt(CatVD).

Atom	Atom	Experimental bond Length /Å	Calculated bond Length /Å
Pt1	O2	1.993	2.006
Pt1	O3	1.995	1.986
Pt1	N6	2.010	2.004
Pt1	N9	2.025	1.997
C3	C4	1.42	1.40
C4	C5	1.36	1.39
C5	C6	1.41	1.41
C6	C7	1.40	1.40
C7	C8	1.42	1.39
C8	C3	1.32	1.41
C5	O2	1.33	1.344
C6	O3	1.26	1.340

Table 4.17: Selected bond angles from the X-ray crystal structure of (PyVD)Pt(CatVD).

Atom	Atom	Atom	Angles (°)
O2	Pt1	O3	82.4
N6	Pt1	N5	80.8
O2	Pt1	N9	175.0
N6	Pt1	O3	173.3
C6	O3	Pt1	108.2

Table 4.18: Selected torsion angles from the X-ray crystal structure of (PyVD)Pt(CatVD).

Atoms	Atoms	Atoms	Atoms	Angles (°)
O2	C5	C6	C7	177.4
O2	C5	C6	O3	7

C6	C5	O2	Pt1	-6
C4	C5	O2	Pt1	-176.8

4.5.3 Results and Discussion

4.5.3.1 Electron Absorption Spectroscopy

Room temperature electron absorption data were recorded in acetonitrile and are presented in Figure 4.44. Tentative computationally assisted band assignments have been performed by comparing TD-DFT results with observed experimental data. The MEC was calculated by dissolving 0.010 g of complex in 25 ml of solution, followed by applying the serial dilution method. The MEC is 3,833 mol• L^{-1}•cm^{-1} for the lowest energy band that is observed at 10,460 cm^{-1}. This band is assigned to originate from the promotion of an electron from the donor HOMO to the VD SOMO. The energy of this transition has been red shifted by 1 eV compared to the parent (bpy)Pt(cat) complex.[19] This energy is similar to the energy of the same transition in (PyVD)Pt(Cat). This shows that there is a minimal effect of the appended VD radical on the electronic structure of the complex. Molecular orbitals obtained from the computations show that the chromophoric SOMO does not extend to the appended VD SOMO. The energy of the CT band has been blue shifted only by a small amount (200 cm^{-1}) compared to (PyVD)Pt(Cat). The second lowest energy peak is observed at 17,777 cm^{-1} and likely corresponds to the ILCT transition, having an MEC of 5,650 mol•L^{-1}•cm^{-1}. This transition is associated with the promotion of an electron from the donor HOMO to the acceptor LUMO. This transition is similar to that found in (bpy)Pt(cat) (the LLCT band) in terms of energy and molar absorptivity.[19] The electronic transition at 21,025 cm^{-1} is suggested to derive from both

VD SOMOs as donors and PyVD, to the LUMO acceptor orbital, as can be seen in the inset of Figure 4.44.

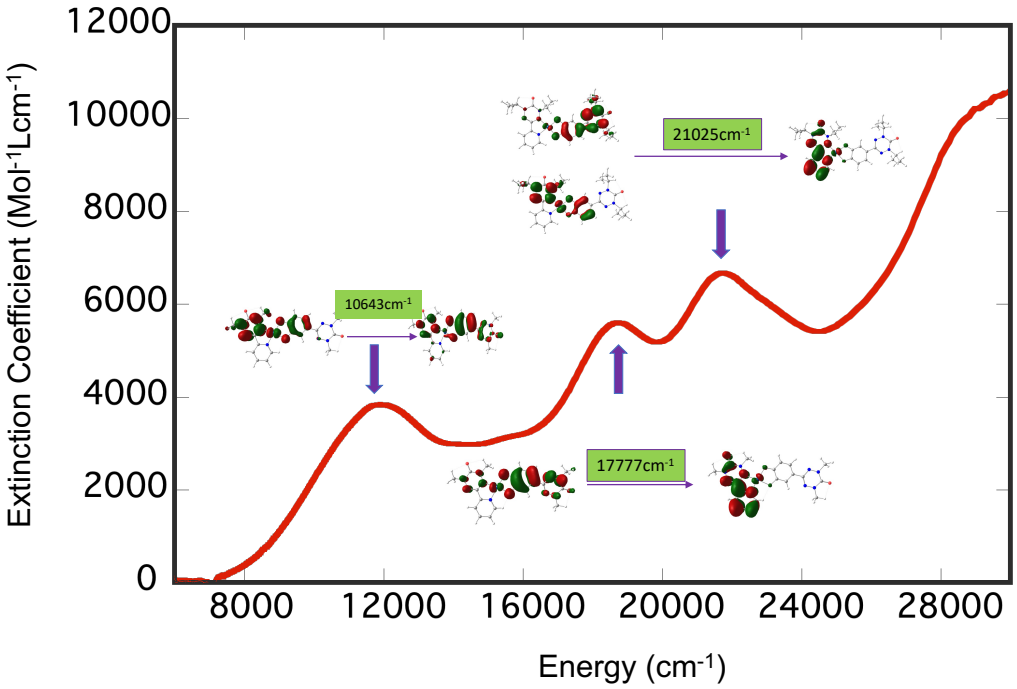

Figure 4.44: EAS data recorded at 298K in acetonitrile. Orbitals involved have been shown on respective peaks by purple arrows.

4.5.3.2 Electron Paramagnetic Resonance Spectroscopy

The 298K X-band solution EPR spectrum was recorded using a Brucker EMX EPR spectrometer as shown in Figure 4.45. The data were recorded with a power attenuation of 20dB and amplitude modulation of 2G. The isotropic EPR spectrum was simulated by using EasySpin software [44] to determine spin-Hamiltonian parameters. The simulated parameters are g = 2.0305, linewidth = 2.5 mT, and the isotropic Pt hyperfine value (A_{iso}) = 232 MHz. These values are similar to those of (PyVD)Pt(Cat) and indicate a similar

amount of VD spin delocalized on to the Pt ion.[54] The g-value deviates from the free electron g value (g_e), and this is the result of the high spin orbit coupling constant of Pt. We can see the residual signal from the free VD radical on the high-field side of the spectrum in Figure 4.45. A DFT calculated spin density map is depicted in the inset of Figure 4.45 and shows the effects of delocalization of the spin density on the Cat. The frozen solution EPR data indicates that the two radical spins are exchange coupled ferromagnetically in an S=1 ground state as shown by the half-field transition in Figure 4.46. The spin density map has shown the delocalization of spin from coordinated VD to catecholate. The spin of the appended VD radical is mostly localized due to nodal character on the bridge head carbon atom.

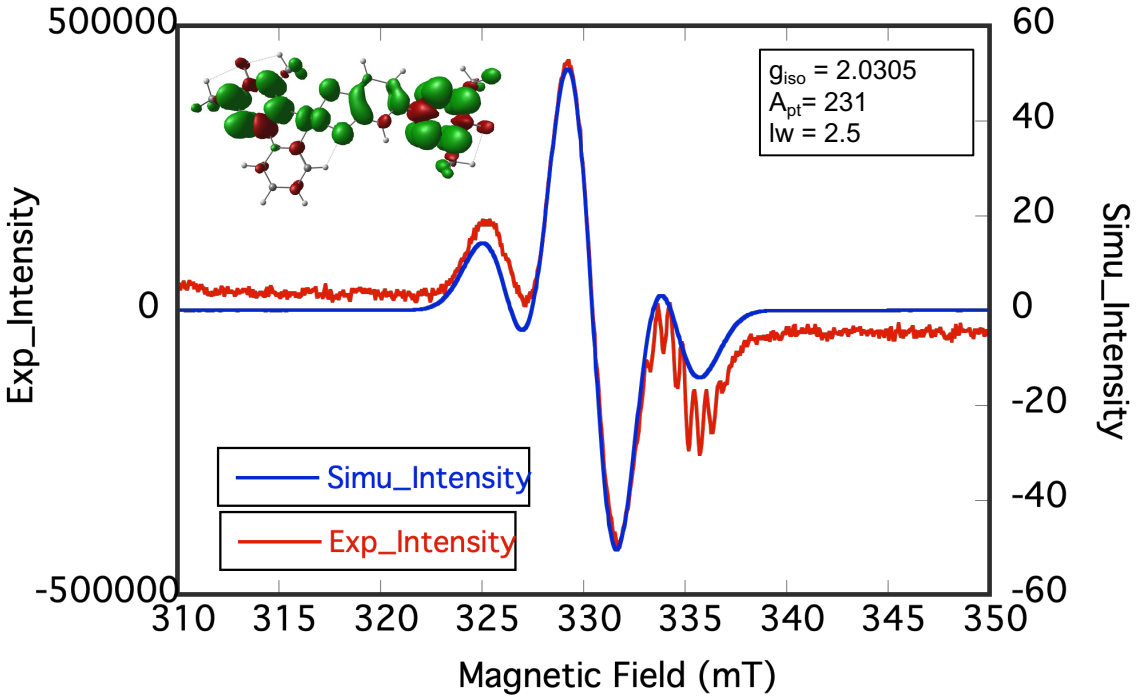

Figure 4.45: X-band 298K solution EPR data of (PyVD)Pt(CatVD) recorded in toluene, experimental data (red) and simulated data (blue). Only A_{pt} value was used during simulation. Simulation parameters and spin density map are presented in set.

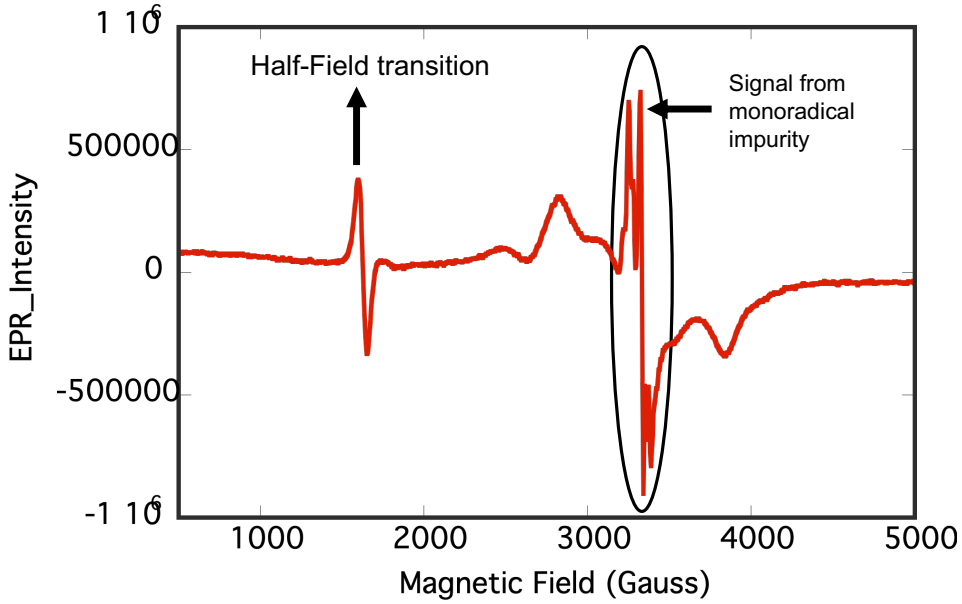

Figure 4.46: X-band 77K EPR data collected in frozen solution. Black bold arrow indicating a half field transition.

4.5.3.3 Magnetism

Variable temperature magnetic susceptibility data has been collected (details in (section 4.4.3.3). The maximum value for the χT product that we obtain ($\chi T = 0.465$) is less than the expected value for two uncorrelated spins ($\chi T = 0.75$). To gain further insight, a proper analysis of the observed magnetic data is needed. This can be accomplished by using a suitable exchange Hamiltonian that considers all the possible pairwise magnetic exchange couplings in this system, including intra- and inter-molecular exchange interactions. This system exhibits the possibility of having multiple exchange couplings between radical spins because of the relatively close interacting molecules within the dimer, as is seen in the X-ray crystal structure displayed in Figure 4.43. This remains a future goal for this project.

4.6 Conclusion

The low temperature (77K) EPR data shows evidence for ferromagnetic exchange coupling between the two radical spins in the ground state. The magnetic susceptibility data will need to be re-collected and properly analyzed, but it will provide important insight into the nature of the magnetic exchange coupling. This will quantify the spin delocalization on the Cat donor from PyVD, as the spin density is proportional to the exchange coupling. Future work with modified molecules and attempting to change the appended radical from VD to NN is in progress. This will allow us to fully understand the extent of the radical-radical coupling in this molecular framework. There is also the potential of extended study by separating the radical spins further by adding a bridge fragment on donor part of the molecule. These represent future aspects of the current project.

Chapter 4: References

1. Wolf, S. A. Spintronics: A Spin-Based Electronics Vision for the Future. *Science* **294**, 1488–1495 (2001).
2. Shultz, D. A. & Kirk, M. L. Molecular spintronics: a web themed issue. *Chem. Commun.* **50**, 7401 (2014).
3. Herrmann, C. & Elmisz, J. Electronic communication through molecular bridges. *Chem. Commun.* **49**, 10456 (2013).
4. Sanvito, S. Molecular spintronics. *Chem. Soc. Rev.* **40**, 3336 (2011).
5. Lehmann, J., Gaita-Ariño, A., Coronado, E. & Loss, D. Quantum computing with molecular spin systems. *J Mater Chem* **19**, 1672–1677 (2009).

6. Stamp, P. C. E. & Gaita-Ariño, A. Spin-based quantum computers made by chemistry: hows and whys. *J Mater Chem* **19**, 1718–1730 (2009).
7. Baart, T. A., Fujita, T., Reichl, C., Wegscheider, W. & Vandersypen, L. M. K. Coherent spin-exchange via a quantum mediator. *Nat. Nanotechnol.* **12**, 26–30 (2017).
8. Pal, A. K. & Bose, I. Entanglement in a molecular three-qubit system. *J. Phys. Condens. Matter* **22**, 016004 (2010).
9. Manriquez, J. M., Yee, G. T., McLean, R. S., Epstein, A. J. & Miller, J. S. A Room-Temperature Molecular/Organic-Based Magnet. *Science* **252**, 1415–1417 (1991).
10. Stein, B. W., Tichnell, C. R., Chen, J., Shultz, D. A. & Kirk, M. L. Excited State Magnetic Exchange Interactions Enable Large Spin Polarization Effects. *J. Am. Chem. Soc.* **140**, 2221–2228 (2018).
11. Nielsen, M. A. & Chuang, I. L. *Quantum computation and quantum information*. (Cambridge University Press, 2010).
12. Timco, G. A. *et al.* Engineering the coupling between molecular spin qubits by coordination chemistry. *Nat. Nanotechnol.* **4**, 173–178 (2009).
13. Wasielewski, M. R. *et al.* Exploiting chemistry and molecular systems for quantum information science. *Nat. Rev. Chem.* **4**, 490–504 (2020).
14. Cummings, S. D. & Eisenberg, R. Tuning the excited-state properties of platinum (II) diimine dithiolate complexes. *J. Am. Chem. Soc.* **118**, 1949–1960 (1996).
15. Hissler, M. *et al.* Platinum diimine complexes: towards a molecular photochemical device. *Coord. Chem. Rev.* **208**, 115–137 (2000).

16. Zuleta, J. A., Burberry, M. S. & Eisenberg, R. Platinum(II) diimine dithiolates. New solution luminescent complexes. *Coord. Chem. Rev.* **97**, 47–64 (1990).

17. Stiefel, E. I. & Karlin D., K. Dithiolene Chemistry: Synthesis, Properties, and Applications,. *Prog Inorg Chem* **52**, (2004).

18. Paw, W. *et al.* Luminescent platinum complexes: tuning and using the excited state. *Coord. Chem. Rev.* **171**, 125–150 (1998).

19. Yang, J. *et al.* Ligand Control of Donor–Acceptor Excited-State Lifetimes. *Inorg. Chem.* **53**, 4791–4793 (2014).

20. Sandrini, D., Maestri, M., Balzani, V., Chassot, L. & Von Zelewsky, A. Photochemistry of the orthometalated cis-bis[2-(2-thienyl)pyridine]platinum(II) complex in halocarbon solvents. *J. Am. Chem. Soc.* **109**, 7720–7724 (1987).

21. Zuleta, J. A., Bevilacqua, J. M., Proserpio, D. M., Harvey, P. D. & Eisenberg, R. Spectroscopic and theoretical studies on the excited state in diimine dithiolate complexes of platinum(II). *Inorg. Chem.* **31**, 2396–2404 (1992).

22. Best, J. *et al.* Structure and Ultrafast Dynamics of the Charge-Transfer Excited State and Redox Activity of the Ground State of Mono- and Binuclear Platinum(II) Diimine Catecholate and Bis-catecholate Complexes: A Transient Absorption, TRIR, DFT, and Electrochemical Study. *Inorg. Chem.* **49**, 10041–10056 (2010).

23. Teki, Y., Miyamoto, S., Iimura, K., Nakatsuji, M. & Miura, Y. Intramolecular Spin Alignment Utilizing the Excited Molecular Field between the Triplet (*S* = 1) Excited State and the Dangling Stable Radicals (*S* = 1/2) as Studied by Time-Resolved Electron Spin Resonance: Observation of the Excited Quartet (*S* = 3/2) and Quintet

(*S* = 2) States on the Purely Organic π-Conjugated Spin Systems. *J. Am. Chem. Soc.* **122**, 984–985 (2000).

24. Ito, A. *et al.* Excited-State Dynamics of Pentacene Derivatives with Stable Radical Substituents. *Angew. Chem. Int. Ed.* **53**, 6715–6719 (2014).
25. Chernick, E. T. *et al.* Electron Donor−Bridge−Acceptor Molecules with Bridging Nitronylnitroxide Radicals: Influence of a Third Spin on Charge- and Spin-Transfer Dynamics. *J. Am. Chem. Soc.* **128**, 4356–4364 (2006).
26. Kirk, M. L. *et al.* Metal Ion Control of Photoinduced Electron Spin Polarization in Electronic Ground States. *J. Am. Chem. Soc.* **143**, 10519–10523 (2021).
27. Tichnell, C. R. *et al.* Wave Function Control of Charge-Separated Excited-State Lifetimes. *J. Am. Chem. Soc.* **141**, 3986–3992 (2019).
28. Kuhn, R. & Trischmann, H. Surprisingly Stable Nitrogenous Free Radicals. *Angew. Chem. Int. Ed. Engl.* **2**, 155–155 (1963).
29. Koivisto, B. D. & Hicks, R. G. The magnetochemistry of verdazyl radical-based materials. *Coord. Chem. Rev.* **249**, 2612–2630 (2005).
30. Brook, D. J. R., Lynch, V., Conklin, B. & Fox, M. A. Spin Delocalization in the Copper(I) Complexes of Bis(verdazyl) Diradicals. *J. Am. Chem. Soc.* **119**, 5155–5162 (1997).
31. Gilroy, J. B., McKinnon, S. D. J., Koivisto, B. D. & Hicks, R. G. Electrochemical Studies of Verdazyl Radicals. *Org. Lett.* **9**, 4837–4840 (2007).
32. McKinnon, S. D. J., Patrick, B. O., Lever, A. B. P. & Hicks, R. G. Verdazyl radicals as redox-active, non-innocent, ligands: contrasting electronic structures as a

function of electron-poor and electron-rich ruthenium bis(β-diketonate) co-ligands. *Chem Commun* **46**, 773–775 (2010).

33. Martin Trent Lemaire. Synthesis and Coordination Chemistry of Chelating Verdazyl Radicals. (1996).
34. Brook, D. J. R. *et al.* Coordination Chemistry of Verdazyl Radicals: Group 12 Metal (Zn, Cd, Hg) Complexes of 1,4,5,6-Tetrahydro-2,4-dimethyl-6-(2‘-pyridyl)-1,2,4,5-tetrazin-3(2 *H*)-one (pvdH $_3$) and 1,5-Dimethyl-3-(2‘-pyridyl)-6-oxoverdazyl (pvd). *Inorg. Chem.* **39**, 562–567 (2000).
35. Barclay, T. M., Hicks, R. G., Lemaire, M. T. & Thompson, L. K. Structure and magnetic properties of a nickel(ii) complex of a tridentate verdazyl radical: strong ferromagnetic metal-radical exchange coupling. *Chem. Commun.* 2141–2142 (2000) doi:10.1039/b006520j.
36. Hicks, R. G., Lemaire, M. T., Thompson, L. K. & Barclay, T. M. Strong Ferromagnetic and Antiferromagnetic Exchange Coupling between Transition Metals and Coordinated Verdazyl Radicals. *J. Am. Chem. Soc.* **122**, 8077–8078 (2000).
37. Kahn, O., Prins, R., Reedijk, J. & Thompson, J. S. Orbital symmetries and magnetic interaction between copper(II) ions and the o-semiquinone radical. Magnetic studies of (di-2-pyridylamine)(3,5-di-tert-butyl-o-semiquinonato)copper(II) perchlorate and bis(bis(3,5-di-tert-butyl-o-semiquinonato)copper(II)). *Inorg. Chem.* **26**, 3557–3561 (1987).
38. Brook, D. J. R., Richardson, C. J., Haller, B. C., Hundley, M. & Yee, G. T. Strong ferromagnetic metal–ligand exchange in a nickel bis(3,5-dipyridylverdazyl) complex. *Chem. Commun.* **46**, 6590 (2010).

39. McKinnon, S. D. J., Gilroy, J. B., McDonald, R., Patrick, B. O. & Hicks, R. G. Magnetostructural studies of palladium(II) and platinum(II) complexes of verdazyl radicals. *J Mater Chem* **21**, 1523–1530 (2011).

40. Hicks, R. G., Koivisto, B. D. & Lemaire, M. T. Synthesis of Multitopic Verdazyl Radical Ligands. Paramagnetic Supramolecular Synthons. *Org. Lett.* **6**, 1887–1890 (2004).

41. Barclay, T. M., Hicks, R. G., Lemaire, M. T. & Thompson, L. K. Weak Magnetic Coupling of Coordinated Verdazyl Radicals through Diamagnetic Metal Ions. Synthesis, Structure, and Magnetism of a Homoleptic Copper(I) Complex. *Inorg. Chem.* **40**, 6521–6524 (2001).

42. Brook, D. J. R. & Yee, G. T. Radical−Radical Interaction through a Saturated Link: Methylenebis-6-oxoverdazyl. *J. Org. Chem.* **71**, 4889–4895 (2006).

43. Paré, E. C., Brook, D. J. R., Brieger, A., Badik, M. & Schinke, M. Synthesis of 1,5-diisopropyl substituted 6-oxoverdazyls. *Org. Biomol. Chem.* **3**, 4258 (2005).

44. Stoll, S. & Schweiger, A. EasySpin, a comprehensive software package for spectral simulation and analysis in EPR. *J. Magn. Reson.* **178**, 42–55 (2006).

45. Kirk, M. L., Shultz, D. A., Habel-Rodriguez, D., Schmidt, R. D. & Sullivan, U. Hyperfine Interaction, Spin Polarization, and Spin Delocalization as Probes of Donor−Bridge−Acceptor Interactions in Exchange-Coupled Biradicals †. *J. Phys. Chem. B* **114**, 14712–14716 (2010).

46. Bain, G. A. & Berry, J. F. Diamagnetic Corrections and Pascal's Constants. *J. Chem. Educ.* **85**, 532 (2008).

47. O'Conner, C. J. Progress in Inorganic Chemistry. in vol. 29 203–283 (1982).

48. Sheldrick, G. M. Crystal structure refinement with *SHELXL*. *Acta Crystallogr. Sect. C Struct. Chem.* **71**, 3–8 (2015).

49. Dolomanov, O. V., Bourhis, L. J., Gildea, R. J., Howard, J. A. K. & Puschmann, H. *OLEX2* : a complete structure solution, refinement and analysis program. *J. Appl. Crystallogr.* **42**, 339–341 (2009).

50. Shafaatian, B. & Heidari, B. Synthesis, characterization, crystal structure, solvatochromism, fluorescence and electrochemical studies of new organometallic platinum complexes, kinetic investigation of oxidative addition reaction. *J. Organomet. Chem.* **780**, 34–42 (2015).

51. Barigelletti, F., Juris, A., Balzani, V., Belser, P. & Von Zelewsky, A. Temperature dependence of the bis(2,2'-bipyridine)dicyanoruthenium(II) and bis(2,2'-bipyridine)(2,2'-isobiquinoline)ruthenium(II) luminescence. *J. Phys. Chem.* **91**, 1095–1098 (1987).

52. Adams, C. J. *et al.* Photophysical Properties of Platinum(II)−Acetylide Complexes: the Effect of a Strongly Electron-Accepting Diimine Ligand on Excited-State Structure. *Inorg. Chem.* **47**, 8242–8257 (2008).

53. Weinstein, J. A. *et al.* Probing the Electronic Structure of Platinum(II) Chromophores: Crystal Structures, NMR Structures, and Photophysical Properties of Six New Bis- and Di- Phenolate/Thiolate Pt(II)Diimine Chromophores. *Inorg. Chem.* **45**, 4544–4555 (2006).

54. Mason, D. N., Deacon, G. B., Yellowlees, L. J. & Bond, A. M. Electrochemical and chemical oxidation of the antitumour agent [Pt{((p-HC6F4)NCH2)2}(py)2] –

detection of platinum(iii) intermediates. *Dalton Trans.* 890–900 (2003) doi:10.1039/b210815a.

55. Mtei, R. P. *et al.* Spectroscopic and Electronic Structure Studies of a Dimethyl Sulfoxide Reductase Catalytic Intermediate: Implications for Electron- and Atom-Transfer Reactivity. *J. Am. Chem. Soc.* **133**, 9762–9774 (2011).
56. Kirk, M. L. *et al.* Ferromagnetic Nanoscale Electron Correlation Promoted by Organic Spin-Dependent Delocalization. *J. Am. Chem. Soc.* **131**, 18304–18313 (2009).
57. Case, F. H. THE PREPARATION OF 1,1'- AND 3,3'-BIISOQUINOLINE [1]. *J. Org. Chem.* **17**, 471–472 (1952).

Appendix A: Additional information for Chapter 2: Optimized Geometry of the Complex Studied for Molecular Conductance

XYZ Coordinate of Optimized Geometry of SQ-Py-Thp-NN [ZnBC32N9H32SO4]

C	9.512140000	1.042404000	-1.290359000
N	8.543182000	0.243677000	-0.793176000
N	7.363747000	0.913830000	-0.768760000
C	7.596939000	2.138259000	-1.248426000
C	8.949049000	2.273551000	-1.601770000
B	8.621485000	-1.206318000	-0.252407000
N	7.640736000	-2.091977000	-1.056147000
N	6.320991000	-1.781393000	-1.073165000
C	5.705448000	-2.716931000	-1.800301000
C	6.637286000	-3.654580000	-2.275534000
C	7.856167000	-3.216284000	-1.773528000
Zn	5.762479000	-0.119948000	0.096146000
N	6.954700000	-0.777439000	1.637621000
N	8.185479000	-1.207399000	1.248828000
C	8.888443000	-1.597641000	2.331937000
C	8.101103000	-1.420487000	3.463123000
C	6.896644000	-0.902036000	2.968303000
O	4.803351000	1.706613000	0.424492000
C	3.534139000	1.602465000	0.350559000
C	2.646046000	2.717656000	0.523148000
C	1.293914000	2.499743000	0.413897000

C	0.729412000	1.204094000	0.142545000
C	1.571959000	0.112823000	-0.031859000
C	2.974637000	0.264973000	0.064266000
C	-0.740671000	1.085408000	0.052600000
C	-3.520557000	0.997703000	-0.160276000
C	-2.783606000	-0.199423000	-0.100224000
C	-8.717551000	-0.083672000	-0.109935000
N	-8.938235000	-1.327279000	0.388401000
C	-10.377079000	-1.746918000	0.226139000
C	-11.069953000	-0.354084000	0.037622000
N	-9.909138000	0.486502000	-0.444374000
O	-8.040223000	-2.140697000	0.774972000
O	-10.091361000	1.649847000	-0.920704000
C	-12.188803000	-0.305677000	-1.003172000
C	-11.546704000	0.297398000	1.348180000
C	-10.808193000	-2.544138000	1.457782000
C	-10.417975000	-2.649724000	-1.020269000
C	3.237690000	4.070136000	0.813304000
O	3.810555000	-0.696518000	-0.094228000
H	5.998721000	-0.614746000	3.500605000
H	8.361558000	-1.634862000	4.489467000
H	9.896578000	-1.972966000	2.221885000
H	9.742214000	-1.626933000	-0.342714000
H	8.853881000	-3.621431000	-1.874479000
H	6.452957000	-4.522973000	-2.891685000
H	4.632862000	-2.664999000	-1.932647000
H	10.526933000	0.680652000	-1.385369000
H	9.444775000	3.138151000	-2.019288000
H	6.786070000	2.852413000	-1.303008000
H	1.198696000	-0.879344000	-0.265010000
H	0.597206000	3.323391000	0.533812000
H	-3.293049000	-1.158889000	-0.153831000
H	-13.047855000	-0.892077000	-0.659475000
H	-12.504015000	0.732476000	-1.135882000
H	-11.870501000	-0.686597000	-1.976203000
H	-11.815390000	1.337139000	1.139173000
H	-12.425745000	-0.218975000	1.746647000
H	-10.762028000	0.294205000	2.111369000
H	-11.844536000	-2.880489000	1.345384000
H	-10.725049000	-1.964143000	2.379591000
H	-10.163590000	-3.421739000	1.553461000
H	-10.095981000	-2.115495000	-1.919673000
H	-11.425682000	-3.042989000	-1.187354000
H	-9.735749000	-3.489998000	-0.860493000
C	-4.974313000	1.034745000	-0.285497000
C	-5.762149000	2.070812000	-0.759182000
S	-5.958862000	-0.329542000	0.200650000
C	-7.143554000	1.786686000	-0.743318000
H	-5.352986000	3.002016000	-1.136764000
C	-7.427832000	0.519760000	-0.253715000
H	-7.924851000	2.454698000	-1.081929000

H	3.849465000	4.044753000	1.723579000
H	2.455361000	4.825107000	0.937185000
H	3.905410000	4.389418000	0.003082000
C	-1.403207000	-0.158266000	0.012944000
H	-0.844236000	-1.085954000	0.073528000
N	-1.444799000	2.238854000	0.018145000
C	-2.766670000	2.187738000	-0.077442000
H	-3.279868000	3.149350000	-0.072800000

XYZ Coordinate of Optimized Geometry of SQ-Thp-Py-NN ZnBC32N9H32SO4

C	9.285193000	0.056288000	-1.684761000
N	8.236987000	-0.453901000	-1.002844000
N	7.191400000	0.408815000	-1.055589000
C	7.588674000	1.465437000	-1.769362000
C	8.913628000	1.291640000	-2.200315000
B	8.111599000	-1.772786000	-0.199306000
N	6.936591000	-2.597826000	-0.774939000
N	5.689777000	-2.064967000	-0.790478000
C	4.871821000	-2.990615000	-1.297454000
C	5.594226000	-4.148986000	-1.628289000
C	6.904568000	-3.852407000	-1.275104000
Zn	5.509472000	-0.150178000	0.060795000
N	6.694224000	-0.711971000	1.645180000
N	7.798583000	-1.423977000	1.292363000
C	8.502107000	-1.740326000	2.398896000
C	7.845155000	-1.223682000	3.509008000
C	6.715457000	-0.587217000	2.977041000
O	4.889017000	1.856229000	0.016454000
C	3.619478000	1.960253000	0.061521000
C	2.940914000	3.227687000	0.048817000
C	1.568384000	3.236201000	0.103439000
C	0.781752000	2.031046000	0.171930000
C	1.424991000	0.794399000	0.177945000
C	2.831459000	0.711770000	0.121629000
C	-4.485379000	1.080765000	0.170471000
C	-5.639575000	1.867796000	-0.049407000
C	-7.057693000	0.067689000	0.041162000
C	-4.699888000	-0.299779000	0.327118000
C	-8.437140000	-0.418402000	-0.036433000
N	-8.878562000	-1.591425000	0.490155000
C	-10.309621000	-1.875569000	0.095489000
C	-10.796806000	-0.448256000	-0.306208000
N	-9.480240000	0.224702000	-0.641856000
O	-8.202967000	-2.460652000	1.126714000
O	-9.457881000	1.291714000	-1.313641000
C	-11.718556000	-0.379261000	-1.522638000
C	-11.398335000	0.366540000	0.853231000
C	-11.036381000	-2.517974000	1.276763000
C	-10.231521000	-2.872049000	-1.075512000

C	3.765976000	4.482661000	-0.031088000
O	3.487894000	-0.391854000	0.122922000
H	5.923103000	-0.050916000	3.483706000
H	8.140847000	-1.297946000	4.545452000
H	9.417798000	-2.309856000	2.318874000
H	9.135058000	-2.397412000	-0.257234000
H	7.809613000	-4.440707000	-1.342719000
H	5.219937000	-5.066741000	-2.058777000
H	3.815602000	-2.773715000	-1.387292000
H	10.215017000	-0.491815000	-1.753266000
H	9.513625000	1.964243000	-2.796328000
H	6.905779000	2.290130000	-1.924034000
H	0.867686000	-0.135999000	0.246350000
H	1.053222000	4.192387000	0.072338000
H	4.364607000	4.501000000	-0.950480000
H	3.134597000	5.376498000	-0.010112000
H	4.478595000	4.535882000	0.800917000
H	-3.861907000	-0.966782000	0.515668000
H	-5.539618000	2.942690000	-0.197499000
H	-12.681032000	-0.848131000	-1.290344000
H	-11.890639000	0.668679000	-1.779762000
H	-11.290282000	-0.871868000	-2.398451000
H	-11.503676000	1.405585000	0.526645000
H	-12.386128000	-0.015152000	1.131070000
H	-10.754910000	0.351520000	1.738655000
H	-12.073034000	-2.741983000	1.002351000
H	-11.038457000	-1.876925000	2.161102000
H	-10.532686000	-3.451305000	1.539808000
H	-11.231808000	-3.178050000	-1.397877000
H	-9.685094000	-3.758348000	-0.739169000
C	-3.163202000	1.691227000	0.231518000
C	-2.834785000	3.015943000	0.460234000
S	-1.705204000	0.745435000	-0.001867000
C	-1.445744000	3.267803000	0.457565000
H	-3.576612000	3.782621000	0.657472000
C	-0.666502000	2.142735000	0.228960000
H	-1.025431000	4.248500000	0.651072000
H	-9.701460000	-2.448398000	-1.934570000
C	-5.986137000	-0.816538000	0.266126000
H	-6.179041000	-1.872246000	0.411180000
N	-6.875871000	1.395187000	-0.107071000

XYZ Coordinate of Bridge Fragments (phenylene with di-thiol group) C6H6S2

6	-10.494485000	-0.035605000	2.893727000
6	-9.107450000	-0.022656000	2.894321000
6	-8.414243000	1.177805000	2.894027000
6	-9.096361000	2.385589000	2.893092000
6	-10.486572000	2.372210000	2.892467000
6	-11.177818000	1.175145000	2.892801000

1	-8.551258000	-0.945726000	2.895023000
1	-7.336747000	1.157501000	2.894566000
1	-11.036701000	3.299209000	2.891669000
1	-12.255686000	1.188235000	2.892304000
16	-8.273560000	3.967303000	2.892775000
16	-11.453107000	-1.538890000	2.894052000
1	-7.023393000	3.520479000	2.891271000
1	-10.441184000	-2.398297000	2.895063000

C8H14S2 (Octane Bridge with Sulfur Atoms)

C	-1.638037000	-0.272340000	0.039292000
C	-1.118120000	0.418081000	-1.232185000
C	0.966966000	-0.245621000	0.037004000
C	-1.093127000	-1.709248000	0.087961000
H	-1.536506000	-2.300554000	-0.709726000
H	-1.580157000	1.395502000	-1.333551000
C	-1.114857000	0.498041000	1.264614000
H	-1.414188000	-0.163120000	-2.103747000
H	-1.393531000	-2.171899000	1.024285000
H	-1.560033000	0.098507000	2.172331000
H	-1.423165000	1.538162000	1.191360000
C	0.453618000	-1.692410000	-0.046562000
C	0.431569000	0.390790000	1.331965000
C	0.427633000	0.547845000	-1.164487000
H	0.912356000	-2.289876000	0.735560000
H	0.758510000	-2.127939000	-0.996518000
H	0.871763000	1.374911000	1.471631000
H	0.736134000	-0.216292000	2.181072000
H	0.879300000	0.181110000	-2.083202000
H	0.723027000	1.588892000	-1.064630000
S	2.800498000	-0.178905000	0.118414000
S	-3.472400000	-0.245508000	0.125154000
H	3.057545000	-0.822616000	-1.017709000
H	-3.718451000	-0.875663000	-1.020971000

C5NH5S2(Pyridine Bridge Ring with Sulfur Atoms)

C	-3.056106000	-4.482364000	-0.000033000
C	-1.665202000	-4.485194000	-0.000045000
C	-1.009765000	-3.269980000	-0.000182000
C	-1.749611000	-2.095109000	-0.000298000
C	-3.131781000	-2.216784000	-0.000256000
N	-3.763563000	-3.373889000	-0.000131000
H	0.067936000	-3.245835000	-0.000194000
H	-1.107862000	-5.405409000	0.000045000
H	-3.756728000	-1.337361000	-0.000354000
S	-4.038229000	-5.965897000	0.000156000
S	-1.034732000	-0.463478000	-0.000478000
H	-3.036339000	-6.838747000	0.000254000
H	0.240096000	-0.834013000	-0.000726000

C4H4S3 (Thiophene Bridge with Sulfur Atoms)

C	0.942698000	0.823402000	-3.232456000
C	2.286815000	0.857253000	-3.232693000
C	2.815272000	2.197379000	-3.232463000
C	1.856024000	3.139525000	-3.231816000
S	0.267142000	2.427936000	-3.231668000
H	2.908105000	-0.021409000	-3.233132000
H	3.869061000	2.415499000	-3.232702000
S	1.998817000	4.904679000	-3.231250000
S	-0.157720000	-0.564127000	-3.232728000
H	3.326482000	4.942243000	-3.229836000
H	0.786969000	-1.497760000	-3.233902000

C9NH7S (pyridine-Thiophene Bridge with Sulfur Atoms)

C	-0.702361828	0.086565179	0.033986399
C	-1.509063635	1.198205102	-0.283297646
C	-3.452236202	0.025159336	-0.023689608
C	-1.370435976	-1.115057798	0.318836609
H	-0.804709952	-2.006305736	0.581175655
H	-1.036499695	2.144165167	-0.547214245
C	0.758696440	0.208056037	0.057920471
C	1.521806430	1.324066296	0.322450255
S	1.798597331	-1.162074234	-0.288565952
C	2.925248604	1.086362802	0.254348724
H	1.087439186	2.282508160	0.587799960
C	3.229202507	-0.210142926	-0.061826685
H	3.676341487	1.847081826	0.441395010
C	-2.761199175	-1.148114654	0.283368454
H	-3.303042562	-2.064571368	0.501851188
N	-2.842490008	1.184352538	-0.304751213
H	-4.541658929	0.035734525	-0.048216396
H	4.204060159	-0.666488839	-0.179059285

C12H10S2 (Di-phenylene bridge Ring with Sulfur Atoms)

C	-5.859189000	1.993239000	0.850752000
C	-4.476143000	1.988418000	0.847154000
C	-3.751498000	2.813818000	-0.010511000
C	-4.466864000	3.647189000	-0.865561000
C	-5.851856000	3.660744000	-0.867939000
C	-6.559916000	2.831578000	-0.008609000
H	-6.392490000	1.335591000	1.517921000
H	-3.954048000	1.315281000	1.507202000
H	-3.938121000	4.314141000	-1.526742000
H	-6.371861000	4.327152000	-1.536410000
C	-2.261432000	2.803260000	-0.011762000
C	-1.540800000	2.797606000	1.180528000
C	-1.542602000	2.800505000	-1.204513000
C	-0.156981000	2.796124000	1.183500000

H	-2.065893000	2.824034000	2.121206000
C	-0.158091000	2.786001000	-1.211108000
H	-2.068632000	2.782268000	-2.144994000
C	0.546739000	2.788433000	-0.014694000
H	0.374175000	2.815400000	2.121054000
H	0.365913000	2.762418000	-2.152492000
S	-8.340680000	2.793930000	0.053627000
S	2.328360000	2.743782000	0.054944000
H	-8.575574000	3.632292000	-0.948613000
H	2.570341000	3.187375000	-1.173098000

C8H6S4 (Di-thiophene Bridge Ring with Sulfur Atoms)

C	-1.495438000	-0.157395000	-0.040437000
C	-0.188419000	-0.087606000	0.304988000
C	0.374411000	1.216065000	0.116310000
C	-0.514701000	2.109340000	-0.363973000
S	-2.063766000	1.372825000	-0.634811000
H	0.363757000	-0.919819000	0.705427000
H	1.395495000	1.467844000	0.341283000
C	-2.390628000	-1.316221000	0.037085000
C	-3.729609000	-1.325626000	0.235267000
S	-1.776695000	-2.932118000	-0.137979000
C	-4.287123000	-2.645140000	0.248639000
H	-4.312820000	-0.433524000	0.382791000
C	-3.363795000	-3.609571000	0.058211000
H	-5.331194000	-2.854562000	0.399251000
S	-0.193999000	3.795071000	-0.793845000
S	-3.637779000	-5.356802000	0.090863000
H	-0.774522000	4.373302000	0.255964000
H	-3.562539000	-5.586399000	-1.218729000

Appendix B: Mass Spectrometry Data of Chapter 3 and Chapter 4

1. (biq)Pt(bdt); Full Spectrum and Isotope Pattern

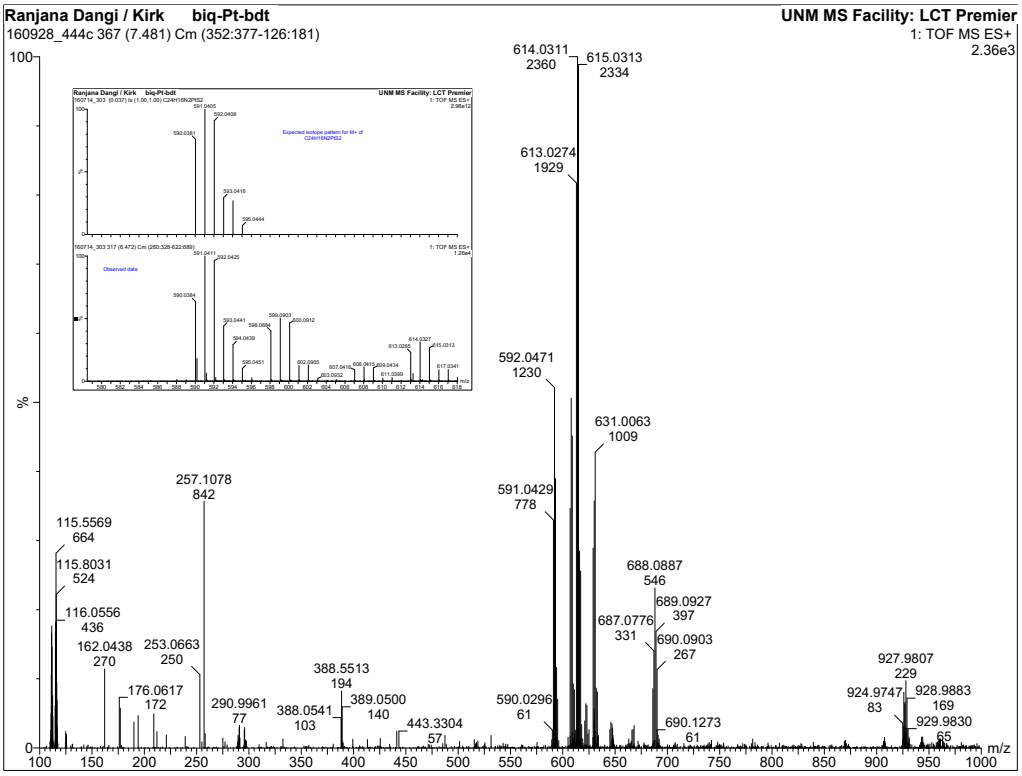

2. (bmbpy)Pt(bdt); Full Spectrum and Isotope Pattern

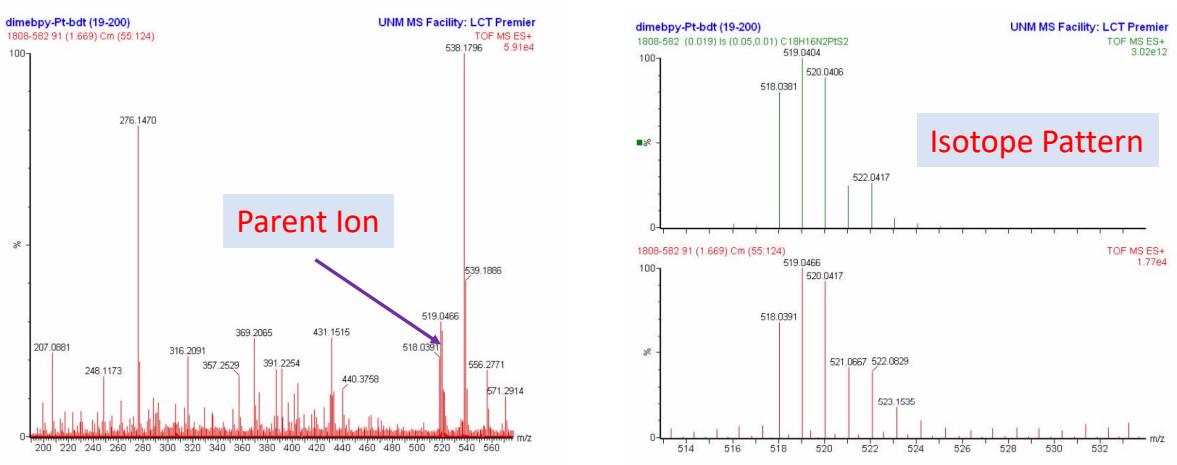

3. (i-biq)Pt(bdt) Full Spectrum and Isotope Pattern

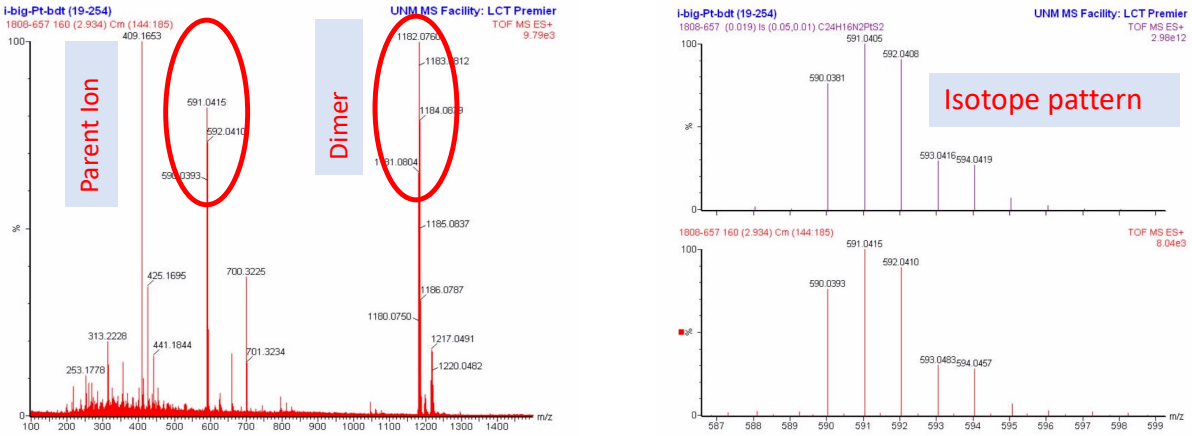

4. (PyVD)Pt(Cat) Full Spectrum and Isotope Pattern

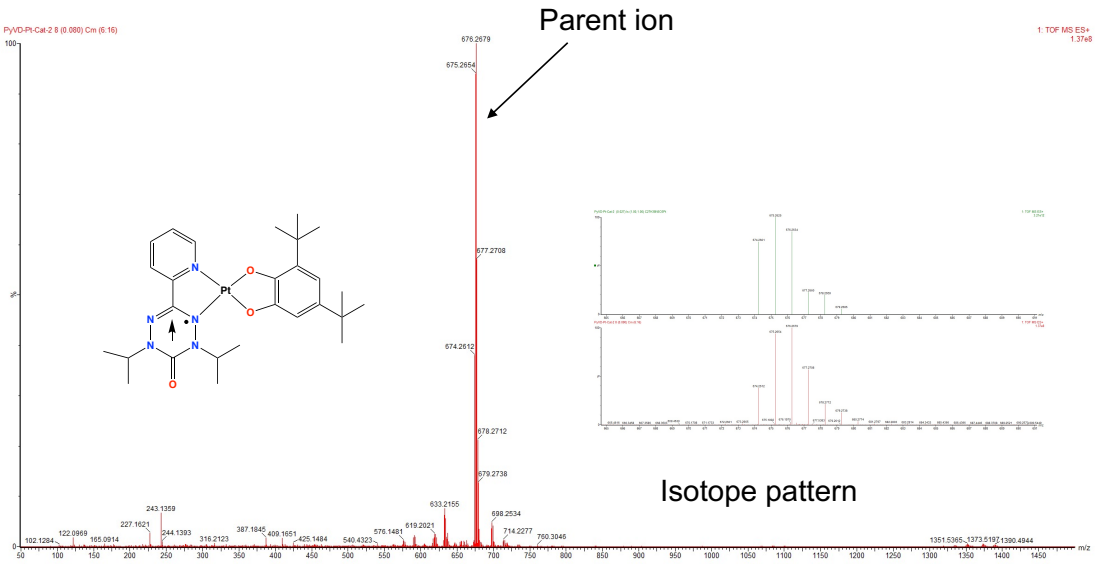
Parent ion
Isotope pattern
676.2679
675.2654
677.2708
674.2612
678.2712
679.2738
633.2155
698.2534
619.2021
714.2277
576.1481
750.3046
540.4323
425.1484
409.1651
387.1845
316.2123
244.1393
243.1359
227.1621
165.0914
122.0969
102.1284
1351.5365
1373.5197
1390.4944
m/z

5. (PyVD)Pt(CatVD) Full Spectrum and Isotope Pattern

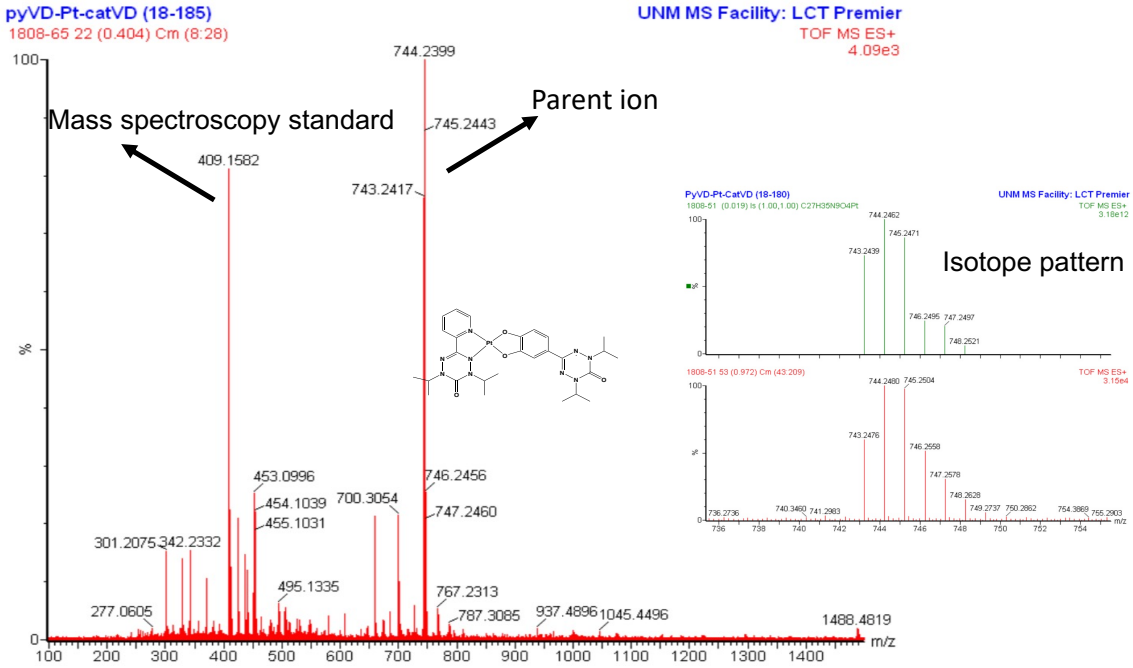

Appendix C: NMR Spectroscopy for Chapter 3 Molecules

1. (biq)Pt(bdt) Room Temperature Proton NMR

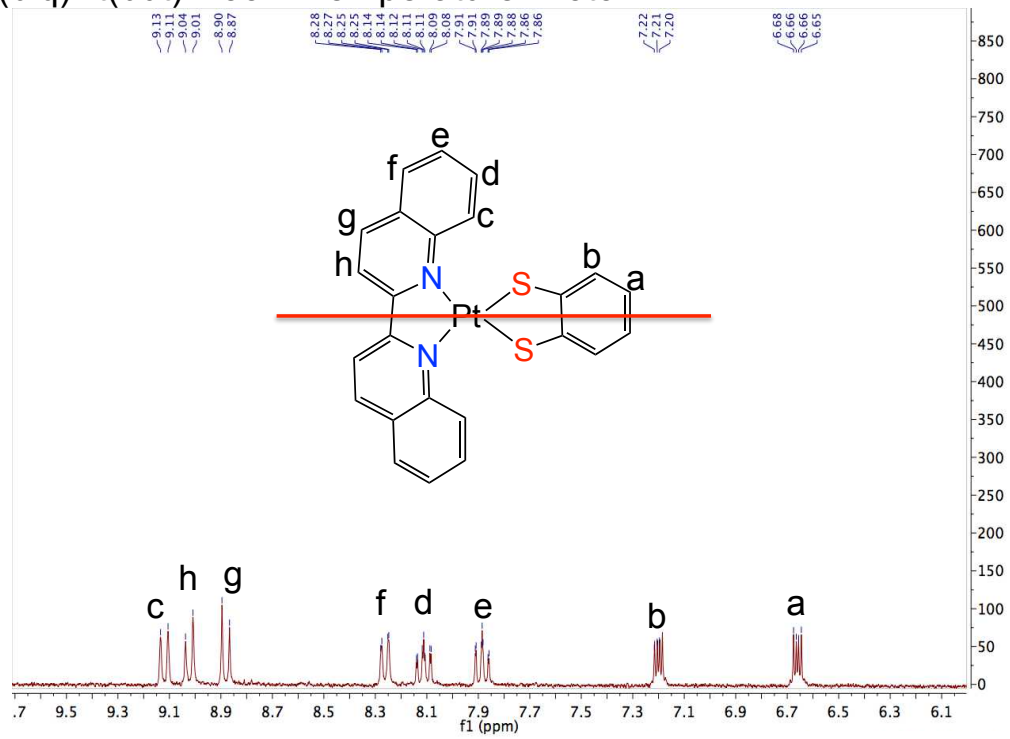

2. (dmbpy)Pt(bdt) Room Temperature Proton NMR

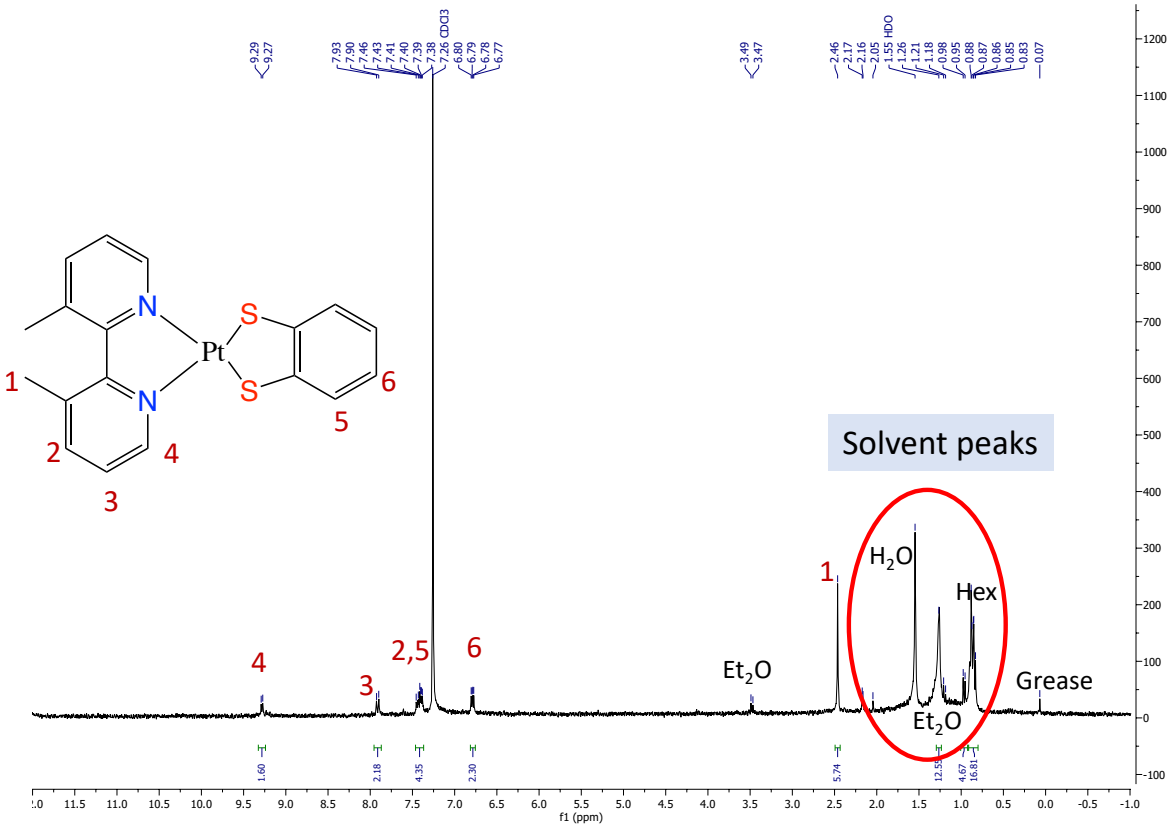

3. (bdt)Pt(i-biq) Room Temperature Proton NMR

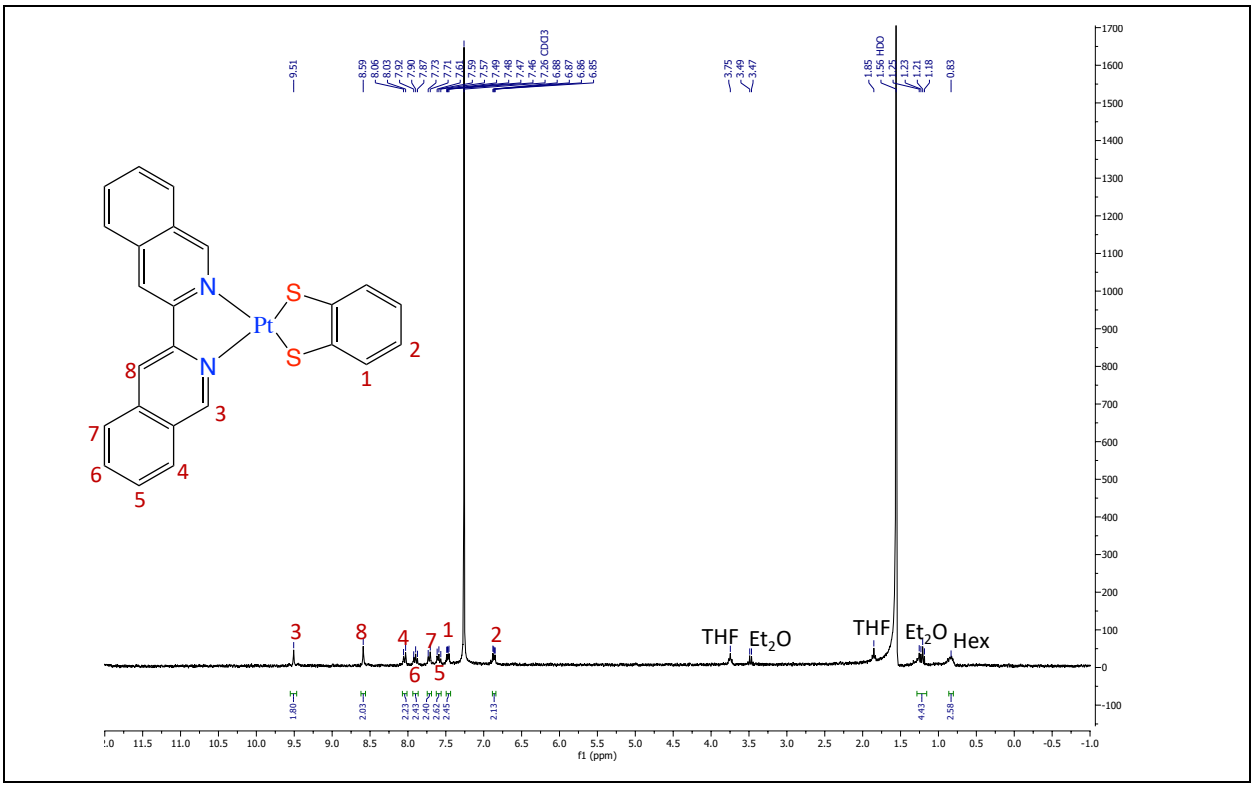

Appendix D: X-ray Crystal Structure and Refinement Parameters

1. (dmbpy)$PtCl_2$ X-ray Crystallography Data

Table 1 Crystal data and structure refinement.

Identification code	mo_fgFB101a_0m_a
Empirical formula	$C_{12}H_{12}Cl_2N_2Pt$
Formula weight	450.23
Temperature/K	100.0
Crystal system	monoclinic
Space group	$P2_1/n$
a/Å	10.136(2)
b/Å	15.269(3)
c/Å	8.025(2)
α/°	89.97(3)
β/°	84.88(3)
γ/°	89.81(3)
Volume/Å^3	1237.1(5)
Z	4
ρ_{calc}g/cm^3	2.417
μ/mm^{-1}	11.750

F(000)	840.0
Crystal size/mm^3	? × ? × ?
Radiation	MoKα (λ = 0.71073)
2Θ range for data collection/°	4.83 to 101.218
Index ranges	-21 ≤ h ≤ 21, -33 ≤ k ≤ 32, -9 ≤ l ≤ 16
Reflections collected	32554
Independent reflections	12884 [R_{int} = 0.0503, R_{sigma} = 0.0593]
Data/restraints/parameters	12884/0/156
Goodness-of-fit on F^2	1.002
Final R indexes [I>=2σ (I)]	R_1 = 0.0360, wR_2 = 0.0616
Final R indexes [all data]	R_1 = 0.0600, wR_2 = 0.0677
Largest diff. peak/hole / e Å^{-3}	4.62/-4.29

Table 2 Fractional Atomic Coordinates (×10^4) and Equivalent Isotropic Displacement Parameters (Å^2×10^3) for mo_fgFB101a_0m_a. U_{eq} is defined as 1/3 of of the trace of the orthogonalised U_{IJ} tensor.

Atom	***x***	***y***	***z***	**U(eq)**
Pt1	5476.3(2)	6295.5(2)	3431.3(2)	9.33(2)
Cl2	7675.3(5)	6456.9(4)	2489.1(8)	16.31(9)
Cl1	5531.2(5)	7667.8(3)	4640.6(7)	14.20(8)
N2	3545.6(17)	6075.7(11)	4124(2)	10.2(2)
N1	5255.1(17)	5121.5(11)	2349(2)	11.0(3)
C12	2786(2)	6594.6(13)	5175(2)	11.4(3)
C2	6087(2)	3775.6(14)	1164(3)	15.8(4)
C11	1410(2)	6499.2(14)	5338(3)	13.0(3)
C7	2987.5(19)	5425.7(12)	3232(2)	9.8(3)
C10	834(2)	5961.1(14)	4217(3)	13.1(3)
C1	6271(2)	4630.8(14)	1693(3)	13.5(3)
C8	1621.8(19)	5431.7(13)	3087(3)	10.9(3)
C4	3755(2)	3906.1(13)	2145(3)	12.0(3)
C3	4845(2)	3410.5(15)	1455(3)	15.3(3)
C9	953(2)	5001.4(14)	1686(3)	14.4(3)
C6	3985.0(19)	4793.2(12)	2483(2)	9.7(3)
C5	2482(2)	3420.5(14)	2622(3)	15.4(3)

Table 3 Anisotropic Displacement Parameters (Å^2×10^3) for mo_fgFB101a_0m_a. The Anisotropic displacement factor exponent takes the form: -2π^2[h^{2}a*^{2}U$_{11}$+2hka*b*U$_{12}$+…].

Atom	**U_{11}**	**U_{22}**	**U_{33}**	**U_{23}**	**U_{13}**	**U_{12}**
Pt1	7.07(2)	9.86(2)	11.03(3)	1.72(2)	-0.67(2)	-0.74(2)
Cl2	8.37(16)	16.59(19)	23.4(2)	2.92(17)	1.56(16)	-1.75(14)
Cl1	12.31(18)	11.62(17)	18.7(2)	-0.33(15)	-1.76(16)	-1.97(14)

Table 3 Anisotropic Displacement Parameters ($Å^2×10^3$) for mo_fgFB101a_0m_a. The Anisotropic displacement factor exponent takes the form: $-2π^2[h^2a^{*2}U_{11}+2hka^*b^*U_{12}+…]$.

Atom	U_{11}	U_{22}	U_{33}	U_{23}	U_{13}	U_{12}
N2	9.6(6)	10.2(5)	10.5(6)	0.1(5)	-0.3(5)	-0.7(5)
N1	8.9(6)	12.3(6)	11.5(6)	1.4(5)	0.1(5)	-0.2(5)
C12	10.4(7)	12.2(7)	11.5(7)	-1.2(6)	-0.5(6)	0.2(5)
C2	12.7(7)	16.6(8)	17.7(9)	-1.8(7)	1.0(7)	3.9(6)
C11	11.9(7)	13.6(7)	12.9(7)	-0.1(6)	1.8(6)	1.3(6)
C7	8.5(6)	12.0(6)	9.0(6)	1.1(5)	-0.8(5)	0.1(5)
C10	8.3(7)	15.4(8)	15.1(8)	1.3(6)	1.8(6)	0.0(6)
C1	10.2(7)	14.4(7)	15.1(8)	1.2(6)	2.3(6)	2.4(6)
C8	7.8(6)	12.8(7)	12.3(7)	0.6(6)	-1.3(5)	0.3(5)
C4	11.8(7)	11.6(6)	12.7(7)	-0.6(6)	-1.1(6)	0.3(6)
C3	16.2(8)	13.6(8)	16.2(9)	-2.1(6)	-1.8(7)	0.9(7)
C9	11.2(7)	18.5(8)	14.2(8)	-0.5(7)	-4.6(6)	-0.6(6)
C6	8.7(6)	11.6(6)	8.8(6)	0.6(5)	-0.1(5)	0.4(5)
C5	13.9(8)	13.6(7)	18.9(9)	0.9(7)	-2.9(7)	-1.9(6)

Table 4 Bond Lengths for mo_fgFB101a_0m_a.

Atom	Atom	Length/Å	Atom	Atom	Length/Å
Pt1	Cl2	2.3030(8)	C2	C3	1.379(3)
Pt1	Cl1	2.3126(8)	C11	C10	1.387(3)
Pt1	N2	2.0154(17)	C7	C8	1.399(3)
Pt1	N1	2.0144(18)	C7	C6	1.484(3)
N2	C12	1.346(3)	C10	C8	1.407(3)
N2	C7	1.377(3)	C8	C9	1.516(3)
N1	C1	1.341(3)	C4	C3	1.409(3)
N1	C6	1.378(3)	C4	C6	1.406(3)
C12	C11	1.397(3)	C4	C5	1.509(3)
C2	C1	1.392(3)			

Table 5 Bond Angles for mo_fgFB101a_0m_a.

Atom	Atom	Atom	Angle/˚	Atom	Atom	Atom	Angle/˚
Cl2	Pt1	Cl1	88.81(4)	N2	C7	C8	119.75(17)
N2	Pt1	Cl2	175.44(5)	N2	C7	C6	112.50(16)
N2	Pt1	Cl1	95.57(6)	C8	C7	C6	127.73(18)
N1	Pt1	Cl2	95.63(6)	C11	C10	C8	120.70(19)
N1	Pt1	Cl1	174.82(5)	N1	C1	C2	121.51(19)
N1	Pt1	N2	79.94(7)	C7	C8	C10	117.22(18)
C12	N2	Pt1	124.08(14)	C7	C8	C9	124.86(18)
C12	N2	C7	120.76(17)	C10	C8	C9	117.49(18)

Table 5 Bond Angles for mo_fgFB101a_0m_a.

Atom	Atom	Atom	Angle/°	Atom	Atom	Atom	Angle/°
C7	N2	Pt1	114.39(13)	C3	C4	C5	117.27(19)
C1	N1	Pt1	123.62(14)	C6	C4	C3	116.94(19)
C1	N1	C6	120.41(17)	C6	C4	C5	125.46(18)
C6	N1	Pt1	115.59(13)	C2	C3	C4	121.4(2)
N2	C12	C11	120.38(19)	N1	C6	C7	113.06(16)
C3	C2	C1	118.43(19)	N1	C6	C4	120.57(17)
C10	C11	C12	118.56(19)	C4	C6	C7	125.78(17)

Table 6 Torsion Angles for mo_fgFB101a_0m_a.

A	B	C	D	Angle/°	A	B	C	D	Angle/°
Pt1	N2	C12	C11	167.36(15)	C7	N2	C12	C11	-2.0(3)
Pt1	N2	C7	C8	-154.74(15)	C1	N1	C6	C7	-179.84(17)
Pt1	N2	C7	C6	23.9(2)	C1	N1	C6	C4	8.5(3)
Pt1	N1	C1	C2	171.15(17)	C1	C2	C3	C4	5.2(3)
Pt1	N1	C6	C7	7.0(2)	C8	C7	C6	N1	158.41(19)
Pt1	N1	C6	C4	-164.66(15)	C8	C7	C6	C4	-30.4(3)
N2	C12	C11	C10	-10.0(3)	C3	C2	C1	N1	-5.4(3)
N2	C7	C8	C10	-16.5(3)	C3	C4	C6	N1	-8.4(3)
N2	C7	C8	C9	155.69(19)	C3	C4	C6	C7	-178.93(19)
N2	C7	C6	N1	-20.1(2)	C6	N1	C1	C2	-1.4(3)
N2	C7	C6	C4	151.13(19)	C6	C7	C8	C10	165.10(19)
C12	N2	C7	C8	15.6(3)	C6	C7	C8	C9	-22.7(3)
C12	N2	C7	C6	-165.81(17)	C6	C4	C3	C2	1.5(3)
C12	C11	C10	C8	8.5(3)	C5	C4	C3	C2	-172.3(2)
C11	C10	C8	C7	4.6(3)	C5	C4	C6	N1	164.9(2)
C11	C10	C8	C9	-168.25(19)	C5	C4	C6	C7	-5.7(3)

Table 7 Hydrogen Atom Coordinates (Å×10^4) and Isotropic Displacement Parameters (Å^2×10^3) for mo_fgFB101a_0m_a.

Atom	*x*	*y*	*z*	U(eq)
H12	3187.69	7028.17	5809.64	14
H2	6799.17	3451.09	614.85	19
H11	880.89	6796.53	6197.14	16
H10	-102.74	5949.68	4211.39	16
H1	7137.12	4872.42	1587.47	16
H3	4721.91	2812.41	1184.99	18
H9A	1624.94	4735.17	888.02	22
H9B	454.75	5443.03	1111.84	22
H9C	345	4547.65	2151.68	22

Table 7 Hydrogen Atom Coordinates (Å×10^4) and Isotropic Displacement Parameters (Å^2×10^3) for mo_fgFB101a_0m_a.

Atom	*x*	*y*	*z*	U(eq)
H5A	1952.62	3745.73	3498.65	23
H5B	2686.55	2836.67	3038.85	23
H5C	1980.39	3363.96	1639.04	23

Single crystals of $C_{12}H_{12}Cl_2N_2Pt$ [mo_fgFB101a_0m_a] were []. A suitable crystal was selected and [] on a Bruker APEX-II CCD diffractometer. The crystal was kept at 100.0 K during data collection. Using Olex2 [1], the structure was solved with the SHELXT [2] structure solution program using Intrinsic Phasing and refined with the SHELXL [3] refinement package using Least Squares minimisation.

1. Dolomanov, O.V., Bourhis, L.J., Gildea, R.J, Howard, J.A.K. & Puschmann, H. (2009), J. Appl. Cryst. 42, 339-341.
2. Sheldrick, G.M. (2015). Acta Cryst. A71, 3-8.
3. Sheldrick, G.M. (2015). Acta Cryst. C71, 3-8.

Crystal structure determination of [mo_fgFB101a_0m_a]

Crystal Data for $C_{12}H_{12}Cl_2N_2Pt$ (*M* =450.23 g/mol): monoclinic, space group $P2_1/n$ (no. 14), *a* = 10.136(2) Å, *b* = 15.269(3) Å, *c* = 8.025(2) Å, *β* = 84.88(3)°, *V* = 1237.1(5) Å^3, *Z* = 4, *T* = 100.0 K, μ(MoKα) = 11.750 mm^{-1}, *Dcalc* = 2.417 g/cm^3, 32554 reflections measured (4.83° ≤ 2Θ ≤ 101.218°), 12884 unique (R_{int} = 0.0503, R_{sigma} = 0.0593) which were used in all calculations. The final R_1 was 0.0360 (I > 2σ(I)) and wR_2 was 0.0677 (all data).

2. (PyVD)Pt(Cat) X-ray Crystal Parameters

Table 1 Crystal data and structure refinement for mo_V00926NMMY_0m_a.

Identification code	mo_V00926NMMY_0m_a
Empirical formula	$C_{27}N_5O_3PtH_{38}$
Formula weight	675.71
Temperature/K	100.0
Crystal system	triclinic
Space group	P-1
a/Å	13.6184(5)
b/Å	14.1599(6)
c/Å	15.2552(6)
α/°	95.773(2)
β/°	105.175(2)
γ/°	100.460(2)

Volume/Å^3	2757.77(19)
Z	4
ρ_{calc}g/cm^3	1.627
μ/mm^{-1}	5.124
F(000)	1348.0
Crystal size/mm^3	? × ? × ?
Radiation	MoKα (λ = 0.71073)
2Θ range for data collection/°	3.744 to 64.062
Index ranges	-20 ≤ h ≤ 20, -21 ≤ k ≤ 21, -22 ≤ l ≤ 22
Reflections collected	190912
Independent reflections	19043 [R_{int} = 0.1727, R_{sigma} = 0.0688]
Data/restraints/parameters	19043/0/669
Goodness-of-fit on F^2	1.030
Final R indexes [I>=2σ (I)]	R_1 = 0.0411, wR_2 = 0.0825
Final R indexes [all data]	R_1 = 0.0693, wR_2 = 0.0996
Largest diff. peak/hole / e Å^{-3}	2.60/-3.10

Table 3 Anisotropic Displacement Parameters (Å^2×10^3) for mo_V00926NMMY_0m_a. The Anisotropic displacement factor exponent takes the form: -2π^2[h^{2}a*^{2}U$_{11}$+2hka*b*U$_{12}$+…].

Atom	*x*	*y*	*z*	U(eq)
Pt1	5135.6(2)	3738.4(2)	5820.4(2)	15.16(4)
O1	5717(2)	3950(2)	7195(2)	18.4(6)
O2	6527(2)	4447(2)	5873(2)	20.4(6)
O3	1811(3)	1587(2)	6448(2)	28.7(7)
N1	3685(3)	2956(2)	5575(2)	16.7(7)
N2	3148(3)	2642(3)	6194(3)	19.7(7)
N3	1951(3)	1510(3)	4987(3)	22.8(8)
N4	2354(3)	1907(3)	4348(3)	21.8(7)
N5	4659(3)	3593(2)	4453(2)	15.9(6)
C1	3199(3)	2593(3)	4681(3)	17.9(8)
C2	2263(3)	1886(3)	5911(3)	22.4(9)
C3	3377(4)	3317(3)	7075(3)	22.3(9)
C4	3543(4)	2807(4)	7913(4)	31.9(11)
C5	2533(4)	3903(4)	6993(4)	34.5(11)
C6	1127(4)	612(3)	4630(3)	26.3(10)
C7	1625(5)	-247(4)	4499(5)	40.6(14)
C8	351(4)	711(4)	3755(4)	34.7(12)
C9	3710(3)	3014(3)	4038(3)	18.6(8)
C10	3289(4)	2859(3)	3090(3)	20.6(8)
C11	3868(4)	3289(3)	2559(3)	21.9(8)

C12	4846(3)	3867(3)	2992(3)	19.8(8)
C13	5228(3)	4010(3)	3945(3)	19.9(8)
C14	6696(3)	4517(3)	7455(3)	16.4(7)
C15	7133(3)	4767(3)	6749(3)	16.5(7)
C16	8123(3)	5339(3)	6930(3)	18.9(8)
C17	8711(3)	5707(3)	7836(3)	18.8(8)
C18	8260(3)	5485(3)	8533(3)	19.3(8)
C19	7267(3)	4898(3)	8378(3)	18.7(8)
C20	9807(3)	6337(3)	8012(3)	19.5(8)
C21	9744(4)	7244(3)	7538(4)	25.6(9)
C22	10483(4)	5745(4)	7617(4)	26.8(10)
C23	10349(4)	6689(4)	9037(3)	27.2(10)
C24	6813(4)	4656(3)	9172(3)	22.8(9)
C25	7550(4)	5133(4)	10116(3)	31.9(11)
C26	5787(4)	4996(4)	9068(3)	26.8(10)
C27	6612(4)	3550(4)	9159(4)	29.2(10)
Pt2	5748.0(2)	1592.0(2)	4649.9(2)	14.89(4)
O00C	9768(3)	3409(3)	6039(2)	27.3(7)
O4	5988(2)	1735(2)	3421(2)	17.9(6)
O5	4325(2)	966(2)	3901(2)	18.9(6)
N6	7118(3)	2227(2)	5572(2)	14.7(6)
N7	8022(3)	2779(3)	5462(3)	19.4(7)
N8	8895(3)	2783(3)	7009(3)	20.0(7)
N9	8002(3)	2339(3)	7169(3)	19.0(7)
N10	5410(3)	1338(2)	5808(2)	15.9(6)
C28	7177(3)	2095(3)	6453(3)	16.6(7)
C29	8953(3)	3019(3)	6163(3)	20.6(8)
C30	7977(3)	3055(3)	4547(3)	19.4(8)
C31	8314(4)	4150(3)	4597(3)	24.3(9)
C32	8589(4)	2481(4)	4070(4)	27.9(10)
C33	9843(3)	2958(3)	7790(3)	22.1(9)
C34	9612(4)	3353(4)	8661(3)	28.1(10)
C35	10269(4)	2043(4)	7865(4)	31.2(11)
C36	6195(3)	1613(3)	6589(3)	17.4(8)
C37	6072(3)	1446(3)	7436(3)	19.4(8)
C38	5099(4)	990(3)	7475(3)	22.1(9)
C39	4288(3)	704(3)	6669(3)	21.6(9)
C40	4465(3)	887(3)	5843(3)	18.6(8)
C41	5094(3)	1373(3)	2733(3)	17.5(8)
C42	4206(3)	981(3)	2996(3)	17.3(8)
C43	3244(3)	639(3)	2355(3)	19.4(8)
C44	3134(3)	674(3)	1419(3)	20.2(8)
C45	4029(4)	1014(3)	1163(3)	21.4(8)
C46	5019(3)	1355(3)	1795(3)	18.5(8)
C47	2058(3)	326(3)	722(3)	23.5(9)

C48	2046(4)	528(5)	-242(4)	38.9(13)
C49	1288(4)	844(5)	1028(4)	38.1(13)
C50	1695(4)	-774(4)	674(4)	38.7(13)
C51	5984(3)	1693(3)	1467(3)	20.2(8)
C52	5741(4)	1537(4)	421(3)	27.3(10)
C53	6439(4)	2784(3)	1818(3)	25.2(9)
C54	6802(4)	1103(3)	1842(3)	25.8(9)

Table 4 Bond Lengths for mo_V00926NMMY_0m_a.

Atom	Atom	Length/Å	Atom	Atom	Length/Å
Pt1	O1	2.008(3)	Pt2	O4	2.009(3)
Pt1	O2	1.954(3)	Pt2	O5	1.965(3)
Pt1	N1	2.001(4)	Pt2	N6	2.008(3)
Pt1	N5	1.993(4)	Pt2	N10	1.990(3)
O1	C14	1.359(5)	O00C	C29	1.217(5)
O2	C15	1.355(5)	O4	C41	1.357(5)
O3	C2	1.211(5)	O5	C42	1.351(5)
N1	N2	1.397(5)	N6	N7	1.392(5)
N1	C1	1.351(6)	N6	C28	1.359(5)
N2	C2	1.397(5)	N7	C29	1.389(6)
N2	C3	1.493(6)	N7	C30	1.476(5)
N3	N4	1.359(5)	N8	N9	1.358(5)
N3	C2	1.380(6)	N8	C29	1.384(6)
N3	C6	1.483(6)	N8	C33	1.471(6)
N4	C1	1.309(5)	N9	C28	1.310(5)
N5	C9	1.352(5)	N10	C36	1.343(6)
N5	C13	1.338(5)	N10	C40	1.346(5)
C1	C9	1.458(6)	C28	C36	1.463(6)
C3	C4	1.518(7)	C30	C31	1.523(6)
C3	C5	1.522(7)	C30	C32	1.527(6)
C6	C7	1.517(7)	C33	C34	1.521(6)
C6	C8	1.508(7)	C33	C35	1.515(7)
C9	C10	1.387(6)	C36	C37	1.384(6)
C10	C11	1.381(6)	C37	C38	1.383(6)
C11	C12	1.384(6)	C38	C39	1.387(7)
C12	C13	1.389(6)	C39	C40	1.384(6)
C14	C15	1.406(6)	C41	C42	1.409(6)
C14	C19	1.414(6)	C41	C46	1.404(6)
C15	C16	1.383(6)	C42	C43	1.383(6)
C16	C17	1.396(6)	C43	C44	1.403(6)
C17	C18	1.394(6)	C44	C45	1.393(6)
C17	C20	1.535(6)	C44	C47	1.529(6)
C18	C19	1.400(6)	C45	C46	1.403(6)
C19	C24	1.538(6)	C46	C51	1.539(6)

C20	C21	1.540(6)	C47	C48	1.523(7)
C20	C22	1.543(6)	C47	C49	1.524(7)
C20	C23	1.530(6)	C47	C50	1.535(7)
C24	C25	1.529(7)	C51	C52	1.527(6)
C24	C26	1.533(7)	C51	C53	1.540(6)
C24	C27	1.536(7)	C51	C54	1.537(6)

Table 5 Bond Angles for mo_V00926NMMY_0m_a.

Atom	Atom	Atom	Angle/°	Atom	Atom	Atom	Angle/°
O2	Pt1	O1	83.38(12)	O5	Pt2	O4	83.36(12)
O2	Pt1	N1	171.81(13)	O5	Pt2	N6	171.69(13)
O2	Pt1	N5	92.28(14)	O5	Pt2	N10	91.97(13)
N1	Pt1	O1	104.53(13)	N6	Pt2	O4	104.82(13)
N5	Pt1	O1	175.63(13)	N10	Pt2	O4	174.61(13)
N5	Pt1	N1	79.83(14)	N10	Pt2	N6	79.94(14)
C14	O1	Pt1	110.3(2)	C41	O4	Pt2	110.6(2)
C15	O2	Pt1	112.2(3)	C42	O5	Pt2	111.7(2)
N2	N1	Pt1	129.6(3)	N7	N6	Pt2	130.9(3)
C1	N1	Pt1	114.7(3)	C28	N6	Pt2	114.7(3)
C1	N1	N2	115.3(3)	C28	N6	N7	114.4(3)
N1	N2	C2	121.1(4)	N6	N7	C30	117.5(3)
N1	N2	C3	116.1(3)	C29	N7	N6	122.0(4)
C2	N2	C3	120.6(4)	C29	N7	C30	120.4(4)
N4	N3	C2	124.5(4)	N9	N8	C29	123.8(4)
N4	N3	C6	115.3(4)	N9	N8	C33	115.7(3)
C2	N3	C6	120.2(4)	C29	N8	C33	120.4(4)
C1	N4	N3	115.1(4)	C28	N9	N8	115.9(4)
C9	N5	Pt1	116.1(3)	C36	N10	Pt2	116.6(3)
C13	N5	Pt1	124.0(3)	C36	N10	C40	119.4(4)
C13	N5	C9	119.9(4)	C40	N10	Pt2	123.9(3)
N1	C1	C9	114.5(4)	N6	C28	C36	114.5(4)
N4	C1	N1	127.3(4)	N9	C28	N6	127.5(4)
N4	C1	C9	118.2(4)	N9	C28	C36	118.0(4)
O3	C2	N2	121.7(4)	O00C	C29	N7	122.1(4)
O3	C2	N3	123.1(4)	O00C	C29	N8	122.2(4)
N3	C2	N2	115.2(4)	N8	C29	N7	115.7(4)
N2	C3	C4	113.2(4)	N7	C30	C31	112.0(4)
N2	C3	C5	108.9(4)	N7	C30	C32	110.4(4)
C4	C3	C5	113.6(4)	C31	C30	C32	113.0(4)
N3	C6	C7	109.4(4)	N8	C33	C34	109.5(4)
N3	C6	C8	111.3(4)	N8	C33	C35	110.4(4)
C8	C6	C7	111.8(5)	C35	C33	C34	113.4(4)
N5	C9	C1	113.4(4)	N10	C36	C28	113.7(4)

N5	C9	C10	121.6(4)	N10	C36	C37	122.3(4)
C10	C9	C1	125.0(4)	C37	C36	C28	124.0(4)
C11	C10	C9	119.0(4)	C38	C37	C36	118.5(4)
C10	C11	C12	118.8(4)	C37	C38	C39	119.3(4)
C11	C12	C13	120.1(4)	C40	C39	C38	119.4(4)
N5	C13	C12	120.6(4)	N10	C40	C39	121.1(4)
O1	C14	C15	116.9(4)	O4	C41	C42	116.6(4)
O1	C14	C19	124.1(4)	O4	C41	C46	123.9(4)
C15	C14	C19	119.0(4)	C46	C41	C42	119.4(4)
O2	C15	C14	117.0(4)	O5	C42	C41	117.6(4)
O2	C15	C16	120.9(4)	O5	C42	C43	121.0(4)
C16	C15	C14	122.1(4)	C43	C42	C41	121.5(4)
C15	C16	C17	120.0(4)	C42	C43	C44	120.0(4)
C16	C17	C20	118.6(4)	C43	C44	C47	119.5(4)
C18	C17	C16	117.7(4)	C45	C44	C43	117.9(4)
C18	C17	C20	123.7(4)	C45	C44	C47	122.7(4)
C17	C18	C19	124.0(4)	C44	C45	C46	123.4(4)
C14	C19	C24	120.8(4)	C41	C46	C51	121.5(4)
C18	C19	C14	117.2(4)	C45	C46	C41	117.5(4)
C18	C19	C24	122.0(4)	C45	C46	C51	120.9(4)
C17	C20	C21	110.0(4)	C44	C47	C50	109.3(4)
C17	C20	C22	109.5(3)	C48	C47	C44	113.0(4)
C21	C20	C22	108.9(4)	C48	C47	C49	107.8(4)
C23	C20	C17	112.4(4)	C48	C47	C50	108.2(4)
C23	C20	C21	107.5(4)	C49	C47	C44	109.3(4)
C23	C20	C22	108.5(4)	C49	C47	C50	109.3(5)
C25	C24	C19	112.8(4)	C46	C51	C53	110.0(4)
C25	C24	C26	107.7(4)	C52	C51	C46	112.8(4)
C25	C24	C27	107.5(4)	C52	C51	C53	107.7(4)
C26	C24	C19	110.5(4)	C52	C51	C54	107.6(4)
C26	C24	C27	109.4(4)	C54	C51	C46	108.8(4)
C27	C24	C19	108.8(4)	C54	C51	C53	109.8(4)

Table 6 Torsion Angles for mo_V00926NMMY_0m_a.

A	B	C	D	Angle/˚	A	B	C	D	Angle/˚
Pt1	O1	C14	C15	-5.2(4)	Pt2	O4	C41	C42	0.0(4)
Pt1	O1	C14	C19	171.9(3)	Pt2	O4	C41	C46	-179.0(3)
Pt1	O2	C15	C14	2.2(5)	Pt2	O5	C42	C41	3.6(4)
Pt1	O2	C15	C16	-175.7(3)	Pt2	O5	C42	C43	-175.4(3)
Pt1	N1	N2	C2	-161.9(3)	Pt2	N6	N7	C29	-168.8(3)
Pt1	N1	N2	C3	34.9(5)	Pt2	N6	N7	C30	7.5(5)

Pt1	N1	C1	N4	164.8(4)	Pt2	N6	C28	N9	172.3(4)
Pt1	N1	C1	C9	-13.7(5)	Pt2	N6	C28	C36	-6.9(4)
Pt1	N5	C9	C1	0.0(5)	Pt2	N10	C36	C28	2.1(5)
Pt1	N5	C9	C10	179.6(3)	Pt2	N10	C36	C37	-177.7(3)
Pt1	N5	C13	C12	179.4(3)	Pt2	N10	C40	C39	178.0(3)
O1	C14	C15	O2	2.1(6)	O4	C41	C42	O5	-2.4(5)
O1	C14	C15	C16	-179.9(4)	O4	C41	C42	C43	176.6(4)
O1	C14	C19	C18	-178.8(4)	O4	C41	C46	C45	-176.0(4)
O1	C14	C19	C24	2.1(6)	O4	C41	C46	C51	4.2(6)
O2	C15	C16	C17	176.3(4)	O5	C42	C43	C44	179.1(4)
N1	N2	C2	O3	177.5(4)	N6	N7	C29	O00C	171.9(4)
N1	N2	C2	N3	-2.1(6)	N6	N7	C29	N8	-7.8(6)
N1	N2	C3	C4	-134.9(4)	N6	N7	C30	C31	125.0(4)
N1	N2	C3	C5	97.7(4)	N6	N7	C30	C32	-108.1(4)
N1	C1	C9	N5	8.9(5)	N6	C28	C36	N10	3.2(5)
N1	C1	C9	C10	-170.6(4)	N6	C28	C36	C37	-177.0(4)
N2	N1	C1	N4	-8.3(6)	N7	N6	C28	N9	-7.4(6)
N2	N1	C1	C9	173.2(3)	N7	N6	C28	C36	173.3(3)
N3	N4	C1	N1	-1.9(7)	N8	N9	C28	N6	0.7(6)
N3	N4	C1	C9	176.6(4)	N8	N9	C28	C36	180.0(4)
N4	N3	C2	O3	171.2(4)	N9	N8	C29	O00C	-179.2(4)
N4	N3	C2	N2	-9.2(6)	N9	N8	C29	N7	0.5(6)
N4	N3	C6	C7	79.3(5)	N9	N8	C33	C34	-44.3(5)
N4	N3	C6	C8	-44.7(6)	N9	N8	C33	C35	81.1(5)
N4	C1	C9	N5	-169.7(4)	N9	C28	C36	N10	-176.1(4)

N4	C1	C9	C10	10.8(7)
N5	C9	C10	C11	1.7(6)
C1	N1	N2	C2	10.1(6)
C1	N1	N2	C3	-153.2(4)
C1	C9	C10	C11	-178.7(4)
C2	N2	C3	C4	61.7(5)
C2	N2	C3	C5	-65.6(5)
C2	N3	N4	C1	11.3(6)
C2	N3	C6	C7	-100.4(5)
C2	N3	C6	C8	135.5(5)
C3	N2	C2	O3	-19.9(7)
C3	N2	C2	N3	160.5(4)
C6	N3	N4	C1	-168.5(4)
C6	N3	C2	O3	-9.1(7)
C6	N3	C2	N2	170.5(4)
C9	N5	C13	C12	1.2(6)
C9	C10	C11	C12	-0.5(6)
C10	C11	C12	C13	-0.3(7)
C11	C12	C13	N5	0.0(6)
C13	N5	C9	C1	178.3(4)
C13	N5	C9	C10	-2.1(6)
C14	C15	C16	C17	-1.6(6)
C14	C19	C24	C25	179.8(4)
C14	C19	C24	C26	-59.6(5)
C14	C19	C24	C27	60.6(5)
N9	C28	C36	C37	3.7(6)
N10	C36	C37	C38	-0.8(6)
C28	N6	N7	C29	10.9(5)
C28	N6	N7	C30	-172.7(4)
C28	C36	C37	C38	179.5(4)
C29	N7	C30	C31	-58.5(5)
C29	N7	C30	C32	68.3(5)
C29	N8	N9	C28	3.0(6)
C29	N8	C33	C34	139.1(4)
C29	N8	C33	C35	-95.5(5)
C30	N7	C29	O00C	-4.4(7)
C30	N7	C29	N8	175.9(4)
C33	N8	N9	C28	-173.4(4)
C33	N8	C29	O00C	-2.9(7)
C33	N8	C29	N7	176.8(4)
C36	N10	C40	C39	0.2(6)
C36	C37	C38	C39	0.8(6)
C37	C38	C39	C40	-0.4(6)
C38	C39	C40	N10	-0.1(6)
C40	N10	C36	C28	-179.9(4)
C40	N10	C36	C37	0.2(6)
C41	C42	C43	C44	0.1(6)
C41	C46	C51	C52	175.4(4)
C41	C46	C51	C53	-64.3(5)
C41	C46	C51	C54	56.1(5)

1.359	C14	C19	C18	-1.8(6)	C42	C41	C46	C45	5.0(6)
C15	C14	C19	C24	179.1(4)	C42	C41	C46	C51	-174.7(4)
C15	C16	C17	C18	-0.7(6)	C42	C43	C44	C45	3.2(6)
C15	C16	C17	C20	179.8(4)	C42	C43	C44	C47	-177.8(4)
C16	C17	C18	C19	1.7(7)	C43	C44	C45	C46	-2.5(6)
C16	C17	C20	C21	60.0(5)	C43	C44	C47	C48	172.8(4)
C16	C17	C20	C22	-59.6(5)	C43	C44	C47	C49	52.8(6)
C16	C17	C20	C23	179.7(4)	C43	C44	C47	C50	-66.7(5)
C17	C18	C19	C14	-0.4(7)	C44	C45	C46	C41	-1.7(6)
C17	C18	C19	C24	178.6(4)	C44	C45	C46	C51	178.1(4)
C18	C17	C20	C21	-119.5(5)	C45	C44	C47	C48	-8.3(6)
C18	C17	C20	C22	120.9(5)	C45	C44	C47	C49	-128.4(5)
C18	C17	C20	C23	0.3(6)	C45	C44	C47	C50	112.1(5)
C18	C19	C24	C25	0.8(6)	C45	C46	C51	C52	-4.3(6)
C18	C19	C24	C26	121.4(5)	C45	C46	C51	C53	116.0(4)
C18	C19	C24	C27	-118.4(5)	C45	C46	C51	C54	-123.6(4)
C19	C14	C15	O2	-175.1(4)	C46	C41	C42	O5	176.6(4)
C19	C14	C15	C16	2.8(6)	C46	C41	C42	C43	-4.4(6)
C20	C17	C18	C19	-178.9(4)	C47	C44	C45	C46	178.6(4)

Table 7 Hydrogen Atom Coordinates (Å×10^4) and Isotropic Displacement Parameters (Å^2×10^3) for mo_V00926NMMY_0m_a.

Atom	*x*	*y*	*z*	U(eq)
H3	4045.13	3787.48	7141.92	27
H4A	2879.82	2397.41	7912.74	48
H4B	3804.41	3292.84	8471.86	48
H4C	4050.98	2400.97	7897.38	48
H5A	2471.66	4217.73	6443.67	52

H5B	2718.14	4399.2	7539.35	52
H5C	1866.46	3468.25	6943.47	52
H6	746.3	500.48	5102.47	32
H7A	1082.21	-844.89	4288.2	61
H7B	2110.31	-297.64	5083.81	61
H7C	2004.19	-152.37	4038.74	61
H8A	687.65	739.88	3260.59	52
H8B	98.49	1307.96	3848.49	52
H8C	-237.69	149.27	3585.59	52
H10	2612.76	2464.01	2810.21	25
H11	3598.99	3190.75	1908.29	26
H12	5256.35	4165.46	2637.9	24
H13	5900.62	4406.7	4237.99	24
H16	8402.4	5481.34	6437.14	23
H18	8649.25	5749.1	9149.57	23
H21A	9436.62	7041.71	6873.95	38
H21B	10446.18	7645.2	7659.36	38
H21C	9309.81	7620.55	7780.13	38
H22A	10153.03	5526.91	6957.31	40
H22B	10547.52	5178.58	7930.29	40
H22C	11176.08	6153.59	7712.59	40
H23A	11047.94	7079.13	9115.67	41
H23B	10405.65	6126.79	9357.8	41
H23C	9941.83	7086.41	9293.15	41
H25A	8207.7	4915.27	10207.77	48
H25B	7228.53	4948.94	10595.66	48
H25C	7686.31	5841.56	10148.65	48
H26A	5925.33	5706.76	9133.55	40
H26B	5475.17	4781.6	9544.95	40
H26C	5306.06	4716.04	8460.36	40

H27A	6119.18	3223.5	8569.92	44
H27B	6319	3387.88	9661.09	44
H27C	7269.7	3334.54	9238.22	44
H30	7230.82	2861.11	4168.73	23
H31A	8200.14	4310.8	3973	36
H31B	9054.69	4363.83	4933.7	36
H31C	7902.95	4480.67	4915.86	36
H32A	8494.51	2622.93	3440.95	42
H32B	8335.37	1783.83	4051.51	42
H32C	9330.67	2667.71	4410.39	42
H33	10380.4	3467.95	7666.3	26
H34A	9267.11	3897.98	8547.22	42
H34B	10265.06	3578.53	9156.03	42
H34C	9153.64	2838.91	8841.06	42
H35A	10448.82	1851.57	7301.47	47
H35B	9740.95	1519.29	7950.84	47
H35C	10894.1	2167.66	8392.42	47
H37	6641.17	1641.06	7978.47	23
H38	4988.58	873.75	8048.04	26
H39	3616.85	386.4	6683.8	26
H40	3909.62	689.74	5290.47	22
H43	2655.49	379.24	2548.7	23
H45	3965.21	1015.71	528.17	26
H48A	2494.96	160.83	-474.25	58
H48B	2304.25	1224.37	-222.14	58
H48C	1332.29	327.5	-649.34	58
H49A	1525.1	1548.02	1071.11	57

H49B	1245.64	690.05	1630.92	57
H49C	599.22	628.21	579.21	57
H50A	988.3	-993.21	255.85	58
H50B	1696.4	-920.19	1289.27	58
H50C	2168.88	-1112.39	447.94	58
H52A	5431.56	849.56	177.56	41
H52B	6386.27	1728.79	250.86	41
H52C	5249.78	1933.93	164.1	41
H53A	7074.16	2984.38	1634.56	38
H53B	6606.64	2904.18	2490.27	38
H53C	5926.88	3158.02	1553.2	38
H54A	6510.51	410.55	1610.54	39
H54B	6994.91	1210.2	2515.63	39
H54C	7421.13	1314.13	1639.19	39

Crystal structure determination

Crystal Data for $C_{27}N_5O_3PtH_{38}$ (M =675.71 g/mol): triclinic, space group P-1 (no. 2), a = 13.6184(5) Å, b = 14.1599(6) Å, c = 15.2552(6) Å, α = 95.773(2)°, β = 105.175(2)°, γ = 100.460(2)°, V = 2757.77(19) Å^3, Z = 4, T = 100.0 K, μ(MoKα) = 5.124 mm^{-1}, *Dcalc* = 1.627 g/cm^3, 190912 reflections measured (3.744° ≤ 2Θ ≤ 64.062°), 19043 unique (R_{int} = 0.1727, R_{sigma} = 0.0688) which were used in all calculations. The final R_1 was 0.0411 (I > 2σ(I)) and wR_2 was 0.0996 (all data).

3. (PyVD)Pt(CatV) Crystallography Data

Table 1 Crystal data and structure refinement for mo_05V01066MKRD_0m_a.

Identification code	mo_05V01066MKRD_0m_a

Empirical formula	$C_{27}N_9O_4PtH_{35}$
Formula weight	744.73
Temperature/K	100.0
Crystal system	monoclinic
Space group	$P2_1$
a/Å	6.6652(4)
b/Å	38.5271(19)
c/Å	11.4400(6)
α/°	90
β/°	95.332(2)
γ/°	90
Volume/Å^3	2925.0(3)
Z	4
ρ_{calc}g/cm^3	1.691
μ/mm^{-1}	4.846
F(000)	1480.0
Crystal size/mm^3	? × ? × ?
Radiation	MoKα (λ = 0.71073)
2Θ range for data collection/°	4.154 to 61.016
Index ranges	-9 ≤ h ≤ 9, -55 ≤ k ≤ 55, -16 ≤ l ≤ 16
Reflections collected	88166
Independent reflections	17856 [R_{int} = 0.0659, R_{sigma} = 0.0602]
Data/restraints/parameters	17856/281/346
Goodness-of-fit on F^2	1.205
Final R indexes [I>=2σ (I)]	R_1 = 0.1158, wR_2 = 0.2575
Final R indexes [all data]	R_1 = 0.1307, wR_2 = 0.2656
Largest diff. peak/hole / e Å^{-3}	8.98/-9.06
Flack parameter	0.47(4)

Table 2 Fractional Atomic Coordinates (×10^4) and Equivalent Isotropic Displacement Parameters (Å^2×10^3) for mo_05V01066MKRD_0m_a. U_{eq} is defined as 1/3 of of the trace of the orthogonalised U_{IJ} tensor.

Atom	*x*	*y*	*z*	U(eq)
Pt1_1	5301.1(17)	4988.9(3)	2624.3(9)	30.1(2)
O1_1	4860(40)	4040(7)	5990(30)	55(7)
O2_1	5730(30)	5414(4)	1686(15)	28(4)
O3_1	5630(30)	5330(4)	3960(14)	30(4)
O4_1	7460(110)	7350(20)	6920(70)	180(30)
N1_1	4820(30)	4532(5)	3397(19)	22(4)
N2_1	4610(40)	4444(6)	4530(20)	33(5)
N3_1	4690(50)	3853(7)	4100(30)	47(7)
N4_1	4600(50)	3928(8)	2950(30)	43(6)

Table 2 Fractional Atomic Coordinates ($\times 10^4$) and Equivalent Isotropic Displacement Parameters ($Å^2 \times 10^3$) for mo_05V01066MKRD_0m_a. U_{eq} is defined as 1/3 of of the trace of the orthogonalised U_{IJ} tensor.

Atom	*x*	*y*	*z*	U(eq)
N5_1	5260(30)	4676(6)	1249(19)	24(4)
N6_1	7670(70)	6832(12)	4350(40)	74(11)
N7_1	7750(100)	7121(17)	5030(70)	140(20)
N8_1	6500(70)	6784(13)	6530(40)	84(13)
N9_1	6040(60)	6524(10)	5770(40)	66(10)
C1_1	4720(60)	4104(9)	4930(30)	43(8)
C2_1	4830(40)	4248(7)	2640(20)	22(5)
C3_1	4540(40)	4741(7)	5370(20)	35(7)
C4_1	2890(40)	4693(9)	6200(30)	43(7)
C5_1	6620(40)	4805(9)	5990(30)	46(8)
C6_1	4730(50)	3479(7)	4480(30)	55(10)
C7_1	2860(50)	3310(13)	3850(40)	74(14)
C8_1	6720(50)	3330(12)	4170(40)	63(11)
C9_1	4900(50)	4336(8)	1450(30)	31(6)
C10_1	4810(60)	4101(9)	510(30)	43(8)
C11_1	5070(60)	4220(11)	-620(40)	51(9)
C12_1	5430(60)	4564(10)	-790(30)	48(8)
C13_1	5480(60)	4795(10)	140(30)	48(8)
C14_1	5940(30)	5686(4)	2373(14)	10(3)
C15_1	5830(40)	5644(4)	3564(16)	29(6)
C16_1	5970(50)	5928(5)	4316(16)	35(6)
C17_1	6320(60)	6259(5)	3882(19)	43(8)
C18_1	6570(60)	6303(5)	2700(20)	47(8)
C19_1	6240(40)	6032(6)	1914(16)	29(6)
C20_1	6660(60)	6562(9)	4710(30)	43(7)
C21_1	7290(140)	7080(30)	6250(90)	140(30)
C22_1	9150(70)	7405(15)	4700(40)	98(18)
C23_1	7730(90)	7550(20)	3700(60)	130(30)
C24_1	11220(70)	7299(18)	4360(60)	110(20)
C25_1	5540(90)	6773(16)	7660(50)	100(20)
C26_1	3300(90)	6840(20)	7430(80)	140(30)
C27_1	5970(90)	6411(14)	8150(50)	88(17)
Pt1_2	10706.0(18)	5279.5(3)	2550.2(9)	31.8(2)
O1_2	11150(50)	6229(8)	-790(30)	62(8)
O2_2	10190(30)	4860(4)	3479(15)	34(5)
O3_2	10480(30)	4942(4)	1215(14)	28(4)
O4_2	8380(70)	2911(12)	-1700(40)	109(14)
N1_2	11060(40)	5749(7)	1780(20)	36(6)

Table 2 Fractional Atomic Coordinates ($\times 10^4$) and Equivalent Isotropic Displacement Parameters ($Å^2 \times 10^3$) for mo_05V01066MKRD_0m_a. U_{eq} is defined as 1/3 of of the trace of the orthogonalised U_{IJ} tensor.

Atom	*x*	*y*	*z*	U(eq)
N2_2	11390(50)	5818(7)	630(20)	44(7)
N3_2	11420(50)	6410(8)	1110(30)	52(8)
N4_2	11360(50)	6340(9)	2250(30)	53(8)
N5_2	10870(40)	5597(7)	3950(20)	36(6)
N6_2	8350(60)	3428(10)	900(40)	64(10)
N7_2	8050(60)	3170(11)	120(40)	74(11)
N8_2	9570(60)	3472(10)	-1300(30)	64(9)
N9_2	9950(50)	3746(8)	-570(30)	47(7)
C1_2	11290(60)	6161(11)	250(40)	52(9)
C2_2	11110(60)	5990(9)	2570(30)	38(7)
C3_2	11430(40)	5523(8)	-210(20)	39(7)
C4_2	9350(40)	5472(12)	-840(40)	61(11)
C5_2	13110(40)	5576(9)	-1010(30)	41(7)
C6_2	11510(60)	6791(8)	820(40)	68(12)
C7_2	9460(50)	6940(12)	1030(40)	64(11)
C8_2	13300(60)	6970(15)	1500(50)	97(19)
C9_2	11050(50)	5929(8)	3780(30)	37(7)
C10_2	11190(60)	6176(11)	4680(40)	51(9)
C11_2	10910(70)	6048(12)	5780(40)	58(10)
C12_2	10590(60)	5699(10)	5970(40)	52(9)
C13_2	10600(50)	5477(9)	5040(30)	40(7)
C14_2	9850(20)	4634(3)	2646(11)	-1(3)
C15_2	10180(50)	4626(4)	1505(16)	31(6)
C16_2	10010(50)	4325(5)	840(16)	40(7)
C17_2	9630(60)	4010(5)	1362(19)	43(8)
C18_2	9640(50)	3991(4)	2577(18)	33(6)
C19_2	9720(50)	4276(7)	3275(18)	41(7)
C20_2	9540(80)	3711(13)	550(40)	65(12)
C21_2	8590(90)	3176(16)	-1010(60)	87(16)
C22_2	7390(110)	2836(15)	670(60)	140(30)
C23_2	5190(110)	2910(30)	840(80)	190(40)
C24_2	8700(120)	2740(30)	1770(80)	190(40)
C25_2	10340(60)	3499(12)	-2490(30)	67(14)
C26_2	9900(90)	3857(12)	-3020(50)	91(17)
C27_2	12580(60)	3422(15)	-2250(50)	89(17)